Thèse de doctorat

Pour obtenir le grade de Docteur de

l'UNIVERSITE POLYTECHNIQUE HAUTS-DE-FRANCE

Discipline et spécialité : Molécules et Matière Condensée

Présentée et soutenue par

Maxime LAGNY

Le 11/04/2019, à Saint-Louis

Ecole doctorale :

Sciences de la Matière, du Rayonnement et de l'Environnement (ED SMRE 104)

Equipe de recherche, Laboratoire :

Laboratoire des Matériaux Céramiques et Procédés Associés (LMCPA - EA 2443)
Institut franco-allemand de recherches de Saint-Louis (ISL)

Céramiques transparentes Er :YAG à gradient de dopage élaborées par SPS et frittage réactif

JURY

Président du jury

- Bernard, Frédéric. Professeur, Université de Bourgogne, Dijon, FRA

Rapporteurs

- Kupp, Elizabeth. Professeur, Penn State University, Pennsylvania, USA
- Montanaro, Laura. Professeur, Politecnico di Torino, Torino, ITA

Examinateur

- Messing, Gary. Professeur, Penn State University, Pennsylvania, USA

Directrice de thèse

- Leriche, Anne. Professeur, LMCPA, Université polytechnique Hauts-de-France, Maubeuge, FRA

Co-encadrants

- Boehmler, Judith. Docteur, ISL, Saint-Louis, FRA
- Lemonnier, Sébastien. Docteur, ISL, Saint-Louis, FRA
- Lorgouilloux, Yannick. Docteur, LMCPA, Université polytechnique Hauts-de-France, Maubeuge, FRA

Membres invités

- Cambier, Francis. Professeur, Belgian Ceramic Research Center, Mons, BEL
- Vivet, Aurélien. Docteur, Baïkowski, La Balme-De-Sillingy, FRA

CC BY ND

A Thesis Submitted in Fulfilment of the Requirement for

the Degree of Doctor of Philosophy of

the University POLYTECHNIQUE HAUTS-DE-FRANCE

Speciality : Molecules and Condensed Matter

Presented by

Maxime LAGNY

11th April 2019, in Saint-Louis

Doctoral School :

Materials, Radiation and Environmental Sciences (ED SMRE 104)

Research team, Laboratory :

Laboratory of Ceramic Materials and Associated Processes (LMCPA - EA 2443)

French-German research institute of Saint-Louis (ISL)

Transparent Er :YAG ceramics with doping gradient processed by SPS and reactive sintering

COMMITTEE

President

- Bernard, Frédéric. Professor, University of Bourgogne, Dijon, FRA

Reviewers

- Kupp, Elizabeth. Professor, Penn State University, Pennsylvania, USA
- Montanaro, Laura. Professor, Politecnico di Torino, Torino, ITA

Examiner

- Messing, Gary. Professor, Penn State University, Pennsylvania, USA

Thesis director

- Leriche, Anne. Professor, LMCPA, University polytechnique Hauts-de-France, Maubeuge, FRA

Thesis supervisors

- Boehmler, Judith. PhD, ISL, Saint-Louis, FRA
- Lemonnier, Sébastien. PhD, ISL, Saint-Louis, FRA
- Lorgouilloux, Yannick. PhD, LMCPA, University polytechnique Hauts-de-France, Maubeuge, FRA

Invited members

- Cambier, Francis. Professor, Belgian Ceramic Research Center, Mons, BEL
- Vivet, Aurélien. PhD, Baïkowski, La Balme-De-Sillingy, FRA

CC BY ND

Acknowledgments

I sincerely thank my supervisors Anne Leriche and Yannick Lorgouilloux for their support and encouragements that went far beyond what was required when the time to complete this work was short. Thank you for your advices and for all the discussions that we have had during these 3 years. I hope to keep in touch with you. Your kindness and your welcome to the LMCPA lab and your help allowed me to finish this work.

I thank Mrs Montanaro, professor at the Politecnico di Torino, and Mrs Kupp, professor at the Penn State University, for accepting to be the examinators of this thesis and review my work. I also want to thank Mr Gary Messing, professor at the Penn State University and Mr Frederic Bernard, professor at the Université de Dijon, for accepting to be in my thesis jury.

This thesis was not conducted alone and I would like to thank Judith Böhmler and Sébastien Lemonnier for their supervision, the French-german research institute of Saint Louis (ISL) and **people who directly or indirectly participated to make this thesis go well.** I want to thank two intern students, Camille Rage and Nicolas Lorinet who contributed to a part of this PhD thesis. I especially want to thank everyone who has supported me during these years and I really hope to keep in touch with you.

Speaking of support, I would like to thank all my family and the "Bidal Family", without your understanding and your presence, this whole step would have been impossible. I would also like to thank friends who supported me from the first day to the last.

Last but not least, Clémentine, thank you for your patience, your love and your foolproof support. With you, even in the most difficult moments, you have always been my light. Now a page is turning, a new chapter is beginning and I know that it is with you, we will write the next ones, my love.

Tell me and I forget.
Teach me and I remember.
Involve me and I learn.

Benjamin Franklin

Contents

Introduction **1**

I Bibliography **3**

1. Laser . . . 3
   1.1. Applications of High Energy Lasers (HELs) . . . 3
   1.2. Laser System . . . 3
   1.3. Active media . . . 4
      1. Laser effect . . . 4
      2. Laser categories . . . 5
         1 Gaseous lasers . . . 5
         2 Dye lasers . . . 5
         3 Solid state lasers . . . 5
   1.4. Solid-state lasers . . . 6
      1. Gain media for solid state laser . . . 6
         1 Glass materials . . . 6
         2 Single crystals . . . 6
         3 Polycrystalline ceramics . . . 8
      2. Transparent ceramics (TCs) for laser application . . . 11
         1 YAG & Er^{3+}:YAG . . . 13
         2 Requirements for transparency . . . 17
2. Fabrication of transparent polycrystalline ceramics by ceramic powder processing . . . 25
   2.1. Precursors & ceramic powders . . . 25
      1. Ceramic powder syntheses . . . 25
         1 Solid state reaction methods . . . 25
         2 Wet chemical routes . . . 26
      2. Powder characteristics . . . 27
         1 Size and morphology of particles . . . 27
         2 Agglomeration state . . . 28
         3 Purity . . . 29
         4 Stoichiometry . . . 30
         5 Commercial YAG powders . . . 30
         6 Sintering . . . 32
         7 Sintering aids . . . 33
         8 Post-treatments . . . 33
3. Composite doping structure . . . 34
   3.1. Composite processing methods . . . 35

1. Dry pressing . . . 35
2. Slip Casting . . . 35
3. Tape casting . . . 36
4. Crystal bonding . . . 36
5. Polycrystalline bonding . . . 37

II Influence of the stoichiometry and sulfur impurity on transparency of YAG ceramics processed by SPS 39

1. Introduction . . . 40
2. Experimental . . . 42
   2.1. Starting powders . . . 42
   2.2. Characterization . . . 42
   2.3. Sulfur removal procedure . . . 42
   2.4. Stoichiometry correction procedure . . . 43
   2.5. Sintering . . . 43
3. Results and discussion . . . 43
   3.1. Sulfur removal procedure . . . 43
      1. Washing treatments . . . 50
   3.2. Y/Al ratio adjustment . . . 58
4. Conclusion . . . 65
5. Complementary work . . . 66
   5.1. Longer SPS holding time . . . 66
      1. Pre-calcination of the powder mixture . . . 68
      2. Conclusion about complementary work . . . 73

III Development of YAG ceramics by Solid State Reactive Sintering (SSRS) 75

1. Introduction . . . 76
2. Experimental . . . 77
3. Results and discussion . . . 81
   3.1. Characterization of powder mixtures . . . 81
   3.2. Evolution of phase composition after thermal treatment of powder mixtures . . . 85
      1. Influence of a holding time on the formation of YAG phase . . . 88
      2. Study on compacted specimens: densification, dilatometry and phase evolution . . . 90
4. Conclusion . . . 99

IV Er:YAG composite ceramics processed by Spark Plasma Sintering 101

1. Introduction . . . 107
2. Experimental . . . 108
3. Results and discussion . . . 109
   3.1. Powder assembly . . . 109
   3.2. Presintered samples . . . 114
   3.3. Fully dense ceramics . . . 115
   3.4. Limitations and advantages . . . 119
4. Conclusion . . . 126
5. Acknowledgment . . . 126

Conclusions and perspectives **127**

A Appendix **131**

B SEM observations of powders after thermal and chemical treatments. **133**

C XRD enlargement of 35-45 ° 2 θ for samples A to F **135**

D Yttria and alumina supplier technical data **137**

E Enlargement of EDX map results of the number 3, 4, 6, 10, 22, 28, 30 and 31 conditions **141**

F Determination of the porosity and relative density by Archimedes method **145**

G Polishing procedure **147**

List of Tables **149**

List of Figures **151**

Communications **157**

Bibliography **159**

Glossary

HEL High Energy Laser.
HIP Hot Isostatic Press.

ICP-OES Inductively Coupled Plasma Optical Emission Spectrometry.
ILT In-Line Transmission.

PC Polycrystalline Ceramic.

SEM Scanning Electron Microscope.
SPS Spark Plasma Sintering.

Abstract: The realization of transparent Er:YAG ceramics for laser application requires a perfect transparency that implies a high quality of the used powder and a perfect control of the manufacturing processes. However, the quality of the starting powder is sometimes insufficient and its characteristics are not suitable in terms of stoichiometry, impurities or particle morphology. In this case, a pre-treatment of the powder and the use of sintering aids are necessary to obtain transparency. In order to prepare transparent ceramics, the first part of this work consisted in correcting the main defects of two experimental YAG powders. In the first powder, a high level of sulfur was measured and the objective was to eliminate this impurity by chemical and thermal treatments, while keeping the structural characteristics and particle size of the starting powder. In the second powder, the measured stoichiometry showed an yttrium deficiency of 5.3 mol% and the purpose was to correct the Y/Al ratio by addition of yttria. In a second part, in order to overcome the problems of non-reproducibility of the quality of YAG commercial powders, the possibility of obtaining YAG transparent ceramics by reactive sintering from alumina and yttria powders was investigated. The last part of this study concerned the development of transparent ceramics with doping gradients by three approaches having in common the use of SPS sintering. The first involved the assembly of fully dense ceramics; the second, pre-sintered ceramics and finally, the last approach a stack of powder layers. The measurement of Erbium ion diffusion through the interface made it possible to compare these different approaches.
Key words: Er:YAG, Transparent ceramics, Spark Plasma Sintering, Commercial powder, Reactive sintering, Doping gradient, Laser

Résumé : La réalisation de céramiques transparentes de type Er:YAG pour application laser nécessite une transparence parfaite ce qui implique une grande qualité de la poudre utilisée et une parfaite maîtrise des procédés de fabrication. Afin d'obtenir une céramique transparente, la première partie de cette thèse a consisté à corriger le principal défaut de deux poudres de YAG experimentales. Dans la première poudre, un taux de soufre élevé a été mesuré et l'objectif a été d'éliminer cette impureté par des traitements chimiques et thermiques, tout en gardant les caractéristiques structurales et granulométriques de la poudre de départ. La seconde poudre présentait un déficit en yttrium et le but a été de corriger ce déséquilibre par l'ajout d'yttrine. Dans un deuxième temps, afin de s'affranchir des problèmes de non-reproductibilité de la qualité des poudres commerciales de YAG, la possibilité d'obtenir des céramiques transparentes YAG par frittage réactif à partir de poudres d'alumine et d'yttrine a été étudiée. Lors de cette étude, le mélange, la stœchiométrie, la compaction, la densification et les transformations de phase ont été suivis dans le but de réaliser une carte de frittage de ce mélange. La dernière étude concerne l'obtention de céramiques transparentes à gradient de dopage suivant trois approches ayant pour point commun l'emploi de la technique de frittage SPS. La première a consisté en l'assemblage de céramiques déjà totalement densifiées, la deuxième, de céramiques pré-frittées et enfin, la dernière, d'un empilement de lits de poudres. Les mesures de diffusion des ions Erbium à travers l'interface ont permis de comparer ces différentes approches.
Mots clefs: Er:YAG, Céramiques transparentes, Spark Plasma Sintering, Poudres commerciales, Frittage réactif, Gradient de dopage, Laser

Laboratoire de rattachement : Laboratoire des Matériaux Céramiques et Procédés Associés, Campus universitaire de Maubeuge. Boulevard Charles de Gaulle, 59600 Maubeuge.

Introduction

Transparent ceramics have been of great interest because of their many applications in fields such as ballistic protection or optical devices. In this second area, polycrystalline transparent ceramics represent a serious alternative to single crystals as laser amplifying media. Indeed, laser performances are limited due to the formation of thermal lenses in the bulk material caused by a high temperature gradient which impacts the quality of the laser beam and output power. In addition, the synthesis of single crystals by Czochralski of Stockbarger-Bridgman methods requires a long time. In addition, doping concentration of single crystals with active ions is limited and sometimes the segregation of dopants can be observed and leads to a decrease in laser performance.

In order to solve these problems, PCs have been studied to replace single crystals as gain media. PCs have high thermomechanical properties that allow them to resist high thermal gradients, high transparency and above all they can be synthesized in a few hours by ceramic powder processing. Therefore, they are less expensive to produce. Of all the advantages of PCs, the most interesting is the possibility of having a higher doping content, which leads to a higher power output. It is also possible to create a composite doping structure to further improve the heat dissipation in the material during use, which is more complex for single crystals.

Anyway, these studies led to mastering SPS parameters to obtain highly transparent Er: YAG ceramics with commercial powders. The quality of YAG commercial powders highly depends on the supplier synthesis route. As highlighted by the literature and the two previous theses, non-homogeneity between powder batches leads to different aspects of the final ceramics. Then, a control of the powder characteristics is recommended to ensure the final quality of the PCs. Another way to manufacture a YAG ceramic is to synthesize the powder by Solid State Reactive Sintering (SSRS) from precursors like alumina and yttria. This solution allows to use very pure, fine and reproducible commercial powders. With this method, highly transparent ceramics can be obtained and present good laser performances.

Given the literature and conclusions of previous theses, many topics have been defined to improve the laser performance of Er: YAG polycrystalline ceramics:

- Understand the impact of stoichiometry and of the level of impurities in YAG powders on the transparency of obtained ceramics.
- Determine a simple and fast procedure for mixing alumina and yttria powders to obtain a YAG phase after sintering.
- Establish sintering trajectories corresponding to a reactive mixture of alumina and yttria powders.
- Develop a fast method to obtain a transparent ceramic with doping gradient by SPS.

On these considerations, this thesis has been divided into four parts:

- Chapter 1 presents the state of the art on transparent ceramics, especially Er:YAG obtained by ceramic powder processing and their laser performances.
- Chapter 2 focuses on the treatment of YAG and Er:YAG experimental powders to correct all deleterious defects to improve the quality of the transparent ceramic. These results are presented in the form of an article.
- Chapter 3 is devoted to another processing route based on Solid State Reactive Sintering (SSRS) of commercial yttria and alumina powders to overcome the problems of commercial YAG powders availability.
- Chapter 4 concerns the realization of doping gradients by SPS to enhance laser performances and reduce the overheating phenomenon in the ceramics.

Chapter I

Bibliography

1. Laser

LASER stands for "Light Amplification by Stimulated Emission of Radiation". In other terms, light is amplified by means of a gain medium that contains active ions. The Laser term can be used to define the whole system that produces the laser beam.

1.1. Applications of High Energy Lasers (HELs)

High Energy Laser (HEL) are used in a wide variety of applications, due to a large spectrum of emission when high temperature or/and precision are required. Their high output powers are specially needed for military applications as weapons [1]. HELs are commonly used to detect intrusion and to eliminate threats in defense situation. For these applications, high output power is needed to counter the beam attenuation due to interaction with atmosphere [2]. HELs are further used for spatial communication and in industry for metal welding, heat-treatment and precision machining. They also find use in the medical domain for surgery and for skin recovery or dental surgery [3–5].

1.2. Laser System

A laser system is composed of a pump source and an optical resonator (Fig. I.1). The role of the pump source is to provide energy, which initiates the laser effect in the gain medium. Multiple pump sources exist depending on the type of pumping: optical, electrical or gaseous. The initial energy is transferred to the optical cavity, the gain medium. The gain medium is the active part of lasers. It amplifies the light intensity in order to obtain an intense laser beam at the output of the laser system. The phenomenon of emission and amplification which takes place is described in the section 1.3.1. Amplified light bounces back and forth between two reflective mirrors at the end of the optical resonator. When the light has enough energy, it passes through the partially reflective mirror and escapes from the optical cavity. At the output, the light coming out is spatially and temporally coherent[1] and forms a beam (Fig. I.1).

[1] coherence: a fixed phase relationship between the electric field values at different locations or at different times [6].

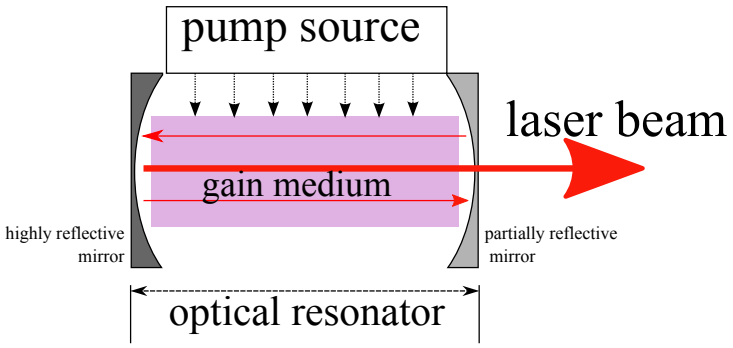

Figure I.1: Scheme of laser system principle.

1.3. Active media

1. *Laser effect*

The amplification of light occurs in the active medium of a laser system by means of energy level transitions of active ions. Energy diagrams representing these phenomena are reported in Fig. I.2. With the help of an external source of energy, the active ions absorb energy and are thus excited. In other words: quantum incident energy has to be sufficient to promote the ions from the ground state to a higher level, a discrete level of energy.

In the first case, the return to ground state is due to the metastability of the excited state and during transition the ion emits a radiation whose intensity is proportional to the difference of energy between the excited level and the ground state. This phenomeon can be described by the case a in the Fig. I.2.

In the second case (case b Fig. I.2), an incident photon meets an ion in an excited state. This induces a transition of the excited ion to the ground state and thereby leads to the formation of two photons which are emitted in the same mode in terms of frequency, direction and polarization state. This phenomenon is called “stimulated emission”. This description corresponds to the ideal case where the two photons have the same characteristics but sometimes reabsorption phenomenon can occur and lead to energy losses.

For a laser system, the population of created photons has thus to be higher than the

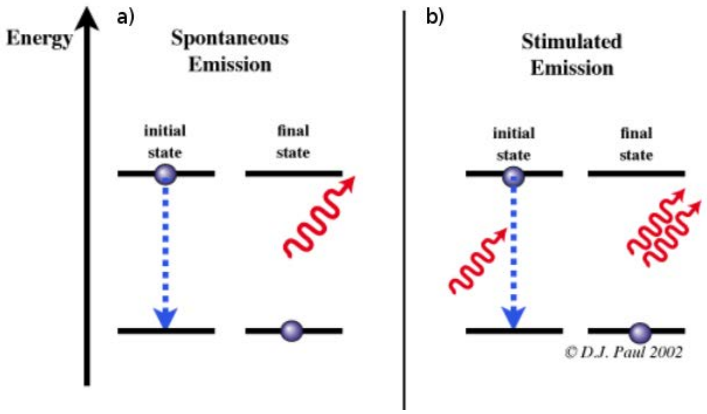

Figure I.2: Principle of (left) spontaneous emission and (right) stimulated emission [7].

provided one supplied by the pump source.

2. Laser categories

Lasers can be classified in different categories depending on nature of their gain medium, which can be either gaseous, liquid dye or solid [8].

1 Gaseous lasers In the first category are gaseous lasers. Here, the gain medium is composed of a gas such as helium neon (He-Ne), argon (Ar) or carbon dioxide (CO_2). The CO_2 lasers are commonly used in industry to cut materials, in the medical field for surgery or even in the holographic domain. These lasers have a large emission range from the UV to IR wavelengths with an output power comprised between mW and kW. Their power is limited due to the low concentration of active ions in the gain medium and they need high current and voltage to ignite a laser beam [9].

2 Dye lasers Dye lasers are constituted by a solvated organic medium. This medium is colored and this coloration depends on the wavelength range needed for a specific application. These lasers allow oscillation threshold relatively low and spectral range between 210 and 900 nm. They are particularly used in spectroscopy. They are attractive because they have a high homogeneity and they enable the possibility to have an efficient cooling when the cavity is used. Depending on the risk of leakage and the difficulty of producing this type of laser system, dye lasers do not have a great success [8].

3 Solid state lasers Solid state lasers, which will be more detailed in the following section 1.4.1, are generally composed by a solid matrix which is either glass, single crystal or Polycrystalline Ceramic (PC). Besides the advantage it presents in terms of thermal stability and laser beam quality, this category of lasers combines the possibility to obtain a high output power with a good stability. They also have large spectral domain of output wavelength (325 nm -3.3 pm), which provides a large possibility of applications. Nevertheless, solid lasers are limited by thermal gradients that can appear during use and their output power still needs to be increased. Improvements by new laser systems, designs or radial gradient can be obtained to reach higher output power. These improvements will be more detailled in the section 1.4.1 (paragraph Issues of single crystal in the laser field).

1.4. Solid-state lasers

1. Gain media for solid state laser

The gain media of solid state lasers are single crystals, glasses or ceramic materials. Each of the mentioned materials has its drawbacks and advantages, which are discussed in the following and listed in Table I.1.

1 Glass materials Glass materials has the advantages of low temperature fabrication and time-saving process. In addition the size of glass specimen is only limited by the furnace. On the other side, the low distance arrangement in glass induces a non-homogeneous surrounding of all active ions which causes broadening[2] of the beam and thus low quality laser beam. Moreover, even if the glass material is cheaper to produce than single crystal, its thermo-mechanical properties are very low. For these reasons, glass material is preferably used as optical fiber.

2 Single crystals Single crystals are the most famous solid materials for the gain medium. Single crystals have a continuous crystal lattice and thanks to the perfect organization of atoms, defects creation associated with grain boundaries does not exist. This particular property gives to single crystals specific mechanical, optical and electrical properties and they are mainly used in the optical field for their ability to be transparent in large range of wavelengths.

Single crystals are grown by the Bridgman-Stockbarger [11, 12] or the Czochralski [13–15] methods. The Bridgman method consists in melting a polycrystalline material and slowly cooling it down to produce the crystallized phase at the bottom of the melted sample (Fig. I.3). The second method (Czochralski) consist in introducing a seed crystal at the contact of the melted material in a crucible. The seed crystal and a rotation of the crucible can be used to obtain a better homogeneity. Then, the seed is slowly pulled upwards to form the crystal between the liquid and solid phase. The pulling rate and the rotation speed of the seed are controlled to obtain a larger single crystal, with a cylindrical shape. The length of the ingot depends on the volume of the melted sample allowed by the crucible and the pulling mechanism of the chamber. Finally, the obtained sample forms a ingot of crystal and will be cut to a laser slab to be used (see Fig. I.3).

[2]Definition: "increase in the linewidth of an atomic transition caused by effects which cause different radiating or absorbing atoms (or ions) to interact with different wavelength components" from [10]

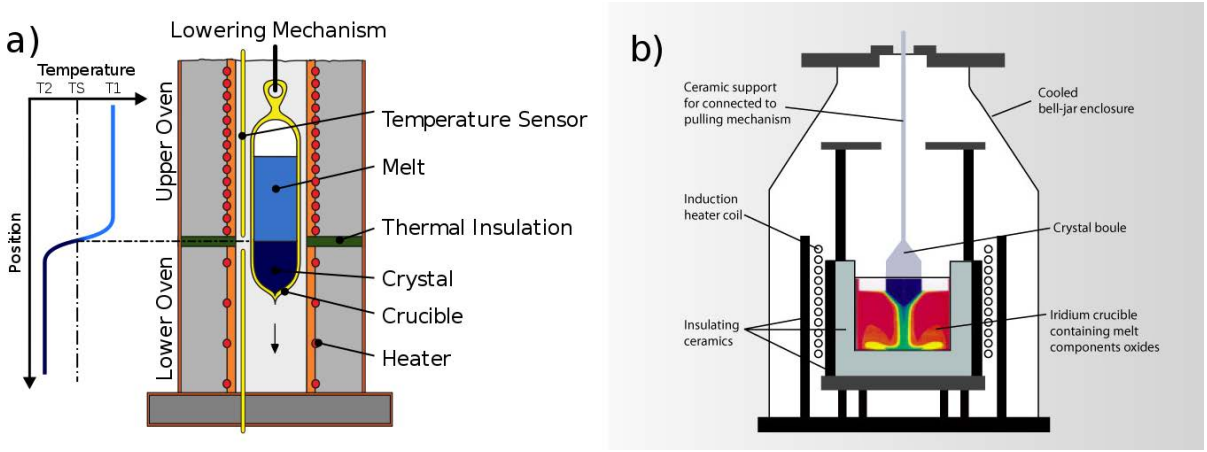

Figure I.3: Crystal growth by a) Bridgman-Stockbarger [16] and b) by Czochraslki [17].

Both techniques have the handicap that process takes a lot of time. Normally, for a piece of single crystal few weeks (2-3 weeks) of fabrication are needed (see table I.1). Moreover, the preparation of the laser slab needs to cut the piece to the right dimensions which leads to a loss of material. In addition, high doping concentrations are difficult to obtain without dopant ion segregation. For example, beyond 1.5 at% of Nd in YAG, highly doped single crystals are hardly obtained by crystal growing [18]. Generally, rare earth (RE) ions have a low solubility and poor homogeneity in the single crystal material [19]. The replacement of the doped ion into the single crystal lattice is extremely difficult when the doping rate is high. The replaced atoms should be similar in term of ionic radius, otherwise doping will induce changes and deformation of the crystal lattice and hence disturb the crystallinity. The influence of ionic radius of dopant in YAG can be shown through the example of Nd^{3+}:YAG and Er^{3+}:YAG, where Y^{3+} has an ionic radius of 89.2 pm, Nd^{3+} of 99.5 pm and Er^{3+} of 88.1 pm [20, 21]. In Nd^{3+}:YAG doping limit is reached with 1 to 1.5 at% Nd^{3+} , whereas Er^{3+}:YAG crystal can be doped up to 50 at% by Er^{3+}. For this reason, the substitution of atoms in the lattice is highly limited by crystal organization and strongly dependent on the matrix material[3] [22, 23].

Issues of single crystals in the laser field During lasing, large thermal gradients are created between the center and the surface of the gain medium, which is generally cooled. As a result, thermal lensing effect appears on the edges of the laser slab. This intrinsic phenomenon finds its origin in the endface deformation by longitudinal expansion, the radial temperature gradient of the refractive index and the photo-elastic effect [24]. The most the temperature difference inside the laser slab is elevated, the most thermal lense effect is pronounced. This effect was often observed and confirmed by Marc Eichhorn in Er^{3+}:YAG-SSHCL [25]. In the extreme, thermal lenses effects are so important that they can lead to fracture of the laser slab.

For instance, the experimental setup in Fig. I.4a) illustrates the decrease of the slope efficiency when the Highly Reflective (HR) mirror radius curvature is high (Fig. I.4b)). The most the curvature is elevated, more the contribution of thermal lenses is taken into

[3]Ion sizes are available in Table I.3.

account, and decreases the slope efficiency.

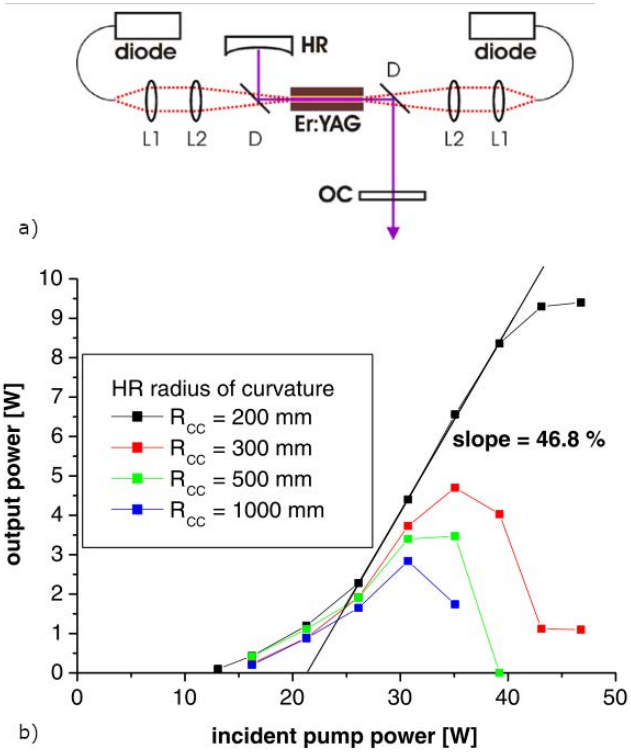

Figure I.4: a) Experimental setup b) CW output power versus incident pump power with different HR curvatures from [25].

Single crystals need a longer processing step to have same dimension as polycrystalline ceramics. Furthermore, the iridium crucibles used for these methods are very expensive [26]. Among solutions, polycrystalline ceramics allowed to improve laser performances.

3 Polycrystalline ceramics Aside from glass and single crystals, polycrystalline ceramics can be used as gain media in solid state laser. (Table I.1). They present the advantage to be processed at lower temperature than single crystal and in a few hours in case of Field Assisted Sintering Technique (FAST). These specificities make them easier and cheaper to produce compared to single crystals [27]. The process is generally faster than the Czochralski and Bridgmann-Stockbarger methods and a similar size of specimen can be synthesized in few hours (see table I.1). On contrary to the other host matrix candidates, polycrystalline ceramics can have a high doping concentration which is useful in order to reach higher output power [28]. Comparatively, a ceramic with higher doping will develop higher output power than the single crystal, due to limited doping concentration. In other words, ceramics are interesting to replace single crystal thanks to the possibility of higher doping amounts. These performances were measured by Shoji *et al.* and represented in the Fig. I.5.

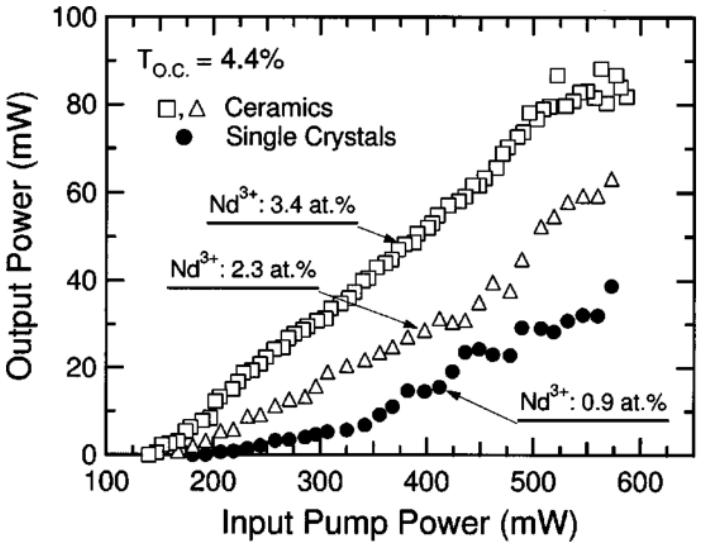

Figure I.5: Dependence of the output power on the input pump power for the 0.9 at. % Nd:YAG single crystal and the 3.4 and 2.3 at. % Nd:YAG ceramics [28].

A 2.3 at.% doped Nd^{3+}:YAG ceramics results in a higher output power than a 0.9 at.% doped Nd^{3+}:YAG single crystal at the same input power [28].

Concerning thermo-mechanical stresses and thermal lenses issues, good thermal conductivity is important for an optimal heat dissipation in the cavity. Taira *et al.* reported that the thermal conductivity of polycrystalline ceramic is similar to a YAG single crystal (Fig. I.6), but the ceramics have the advantage to sustain the power laser operation [18]. As reported in Table I.1, the thermal shock parameter is more important for ceramics, which is very interesting to whistand higher temperature gradient.

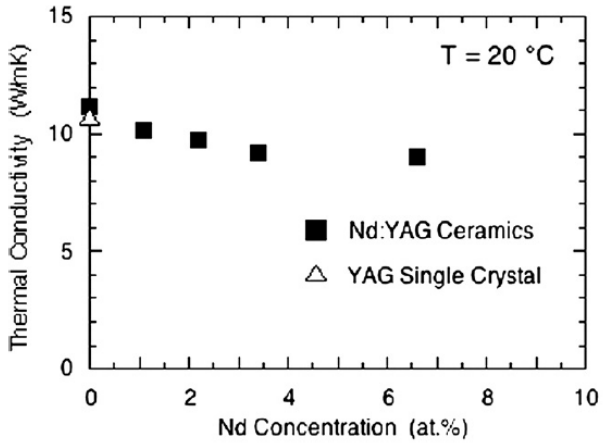

Figure I.6: Thermal conductivity of polycrystalline ceramics doped with different Nd concentration and single crystal from [29].

		Glass	Single crystals	Polycrystalline ceramics
Processing route	Fabrication temperature	Low	High	Low
	Processing / mass production	Easy / already done	Hard / hard	Easy / possible
	Fabrication time	Hours	Weeks	Hours
Size of sample	Dimension limitations	By the furnace	By the crucible (max =23 cm)	By the furnace
Dopant incorporation	Doping rate	Limited	Low	High
	Homogeneity	Bad	Bad	High
Thermo mechanical properties	Thermal conductivity ($W\,m^{-1}\,K^{-1}$)	1.3 [30]	10[31]	10.7[32] 12-14[33]
	Thermal expansion coefficient ($10^{-6}\,K^{-1}$)	9[30]	∼7[30]	8[30]
	Young modulus (GPa)	86[30]	280±7[31]	280±11[31]
	Toughness ($MPa\,m^{1/2}$)	0.45[30]	∼1[31]	1.6[31]
	Thermal shock parameter ($W\,m^{1/2}$)	0.5[30]	3.6[30]	5.35[30]
Optical properties	Optical quality	High	High	High

Table I.1: Comparison of process and properties of glasses, single crystals and ceramics for solid state laser applications (from [34]. Experimental values were taken for Nd^{3+} doped materials.

2. Transparent ceramics (TCs) for laser application

The first use of polycrystalline ceramics as laser sources was shown in 1964 by Hatch *et al.* with a Dy^{2+}:CaF_2 hot-pressed ceramic [35]. Later, in 1973, Greskovich *et al.* reported an Nd^{3+}doped ceramic Y_2O_3 [36], which was able to produce a laser oscillation at room temperature with a low slope efficiency of 0.1%. Since then, the research on transparent ceramics has continuously grown. In the 80s, Y_2O_3 ceramics became more popular and were highly developed by industry for light bulbs, rocket windows or missiles domes [37–39]. In the 90s, Ikesue *et al.* reported the development of transparent polycrystalline Nd^{3+}:YAG ceramic with same spectroscopic performances as single crystal [40]. In 2004, Lu *et al.* reported output powers of a pressureless sintered Nd^{3+}:YAG of 100 W and 103 W, which is comparable to a single crystal [41]. After the 2000s, the Konoshima Company reached the kW output power barrier using ceramics [40, 42] and finally in 2010, three teams reached the actual record of a polycrystalline ceramic of 100 kW (Fig. I.7)[43].

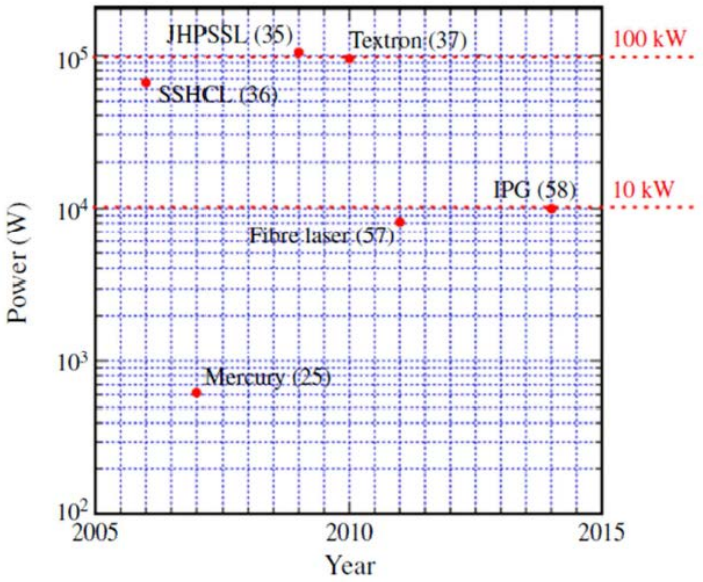

Figure I.7: Evolution of the power for diode-pumped solid-state laser versus years: Mercury, SSHCL, Textron, JHPSSL and four combined fiber laser from [43].

As singles crystals, laser gain medium based on ceramic materials have same overheating issues when used for HELs. To reduce the heat accumulation, a solution is to better manage the heat distribution in the volume during lasing operation and the ceramic processing opens possibilities. Indeed, the development of polycrystalline ceramic bulks exhibiting a doping gradient can be very efficient. Thanks to this specificity, interest in polycrystalline ceramics has drastically grown. As shown by Ikesue and Aung, a multilayer ceramic doped and undoped, in two and three layers or clad core configurations (Fig. I.8) can reduce the heat accumulation in the material [44, 45].

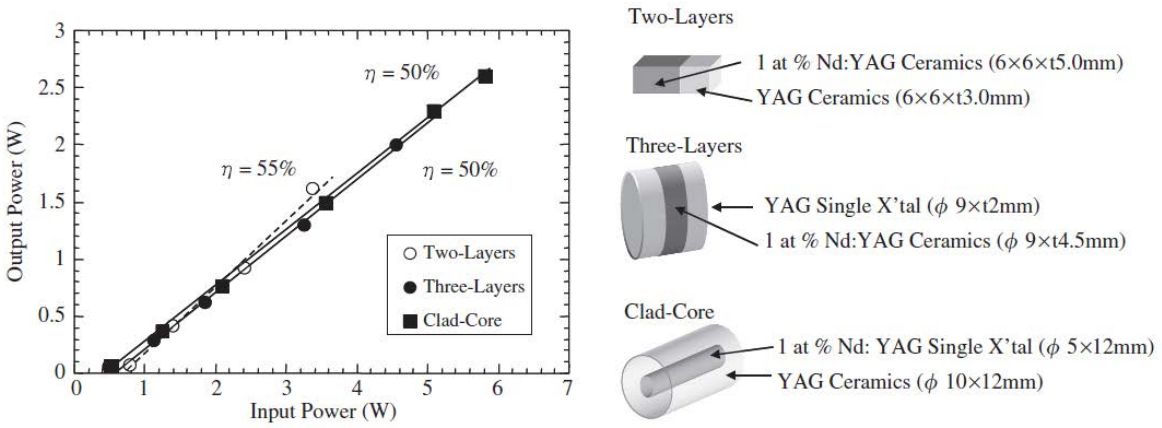

Figure I.8: Comparison between output power of different configurations of composite gradient PCs: two-layers, three-layers and clad-core [46].

The improvement concerning the laser performance is high and increased by a factor 10. A homogeneous doped Nd^{3+}:YAG slab showed an output power which is close to the milliWatt range, whereas the output power for a multilayer ceramic laser slab is close to the Watt range (Fig. I.8)[46]. In addition to better laser performances, Ikesue *et al.* report that a longer sintering favors the ion diffusion and contributes to obtain a smoother gradient in the ceramic. It leads to a better laser beam during laser tests in cavity [46].

Globally, the use of multilayer of active ions with a smooth gradient contributes to enhance laser performances and reduce the heat creation due to a better heat distribution [45].

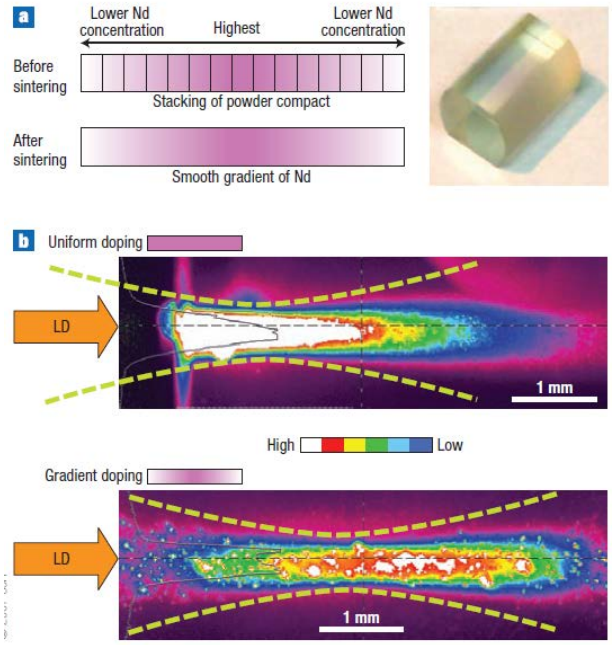

Figure I.9: a) Schematic distribution of Neodymium ions in a heterogeneous doping profile b) Comparison of thermal distribution between conventional Nd:YAG single crystal with uniform doping of Neodymium sample (top) and a smooth gradient doped sample by neodymium ions in a ceramic material (bottom) from [45].

In the Fig.I.9, the temperature gradient is elevated in the homogeneously doped single crystal. In the second example of Fig.I.9 a ceramic with a doping gradient is shown, with the highest concentration of active ions at the center of the specimen. The formation of such a smooth gradient of Nd^{3+} ions is possible by stacking green bodies with different concentrations of active ions and sintering them together. Finally a radial gradient specimen was obtained, and leads to a better distribution of the heat inside the volume [45]. Diffusion of dopant ions is not sufficient to lead a smooth gradient. So, only a good procedure to stack multiple green bodies with different amount of dopant ion is required to achieve this goal. Further architectures which increase laser output power are reported in the literature [47].

These architectures (Fig. I.10) optimize the light trajectory in the ceramics to maximize the yield of the laser beam. The above mentioned output powder of 100 kW was recorded using a Konoshima ceramics as a heat capacity laser (Lawrence Livermore Labs), end pumped slab laser (Northrop Grumman Corp.) and thinzag slab laser (Textron). These configurations are presented in the figure I.10. Records are presented in the figure I.7 [43].

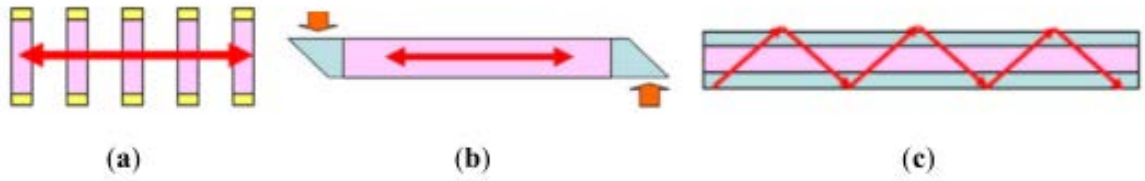

Figure I.10: Three different solid state configurations for laser demonstration from [47] corresponding to (a) heat capacity laser (Lawrence Livermore Labs), (b) end pumped slab laser (Northrop Grumman Corp.) and (c) thinzag slab laser (Textron).

1 YAG & Er^{3+}:YAG

YAG host matrix Host matrices are the matrix of the medium where the active ions are located. Generally the host matrices can be divided into two types of material: non-oxides (fluorides and chacolgenides) and oxides (garnets, sesquioxides) [20]. To find the best material as host matrix, the thermal expansion coefficient has to be low, in order to prevent risks of laser beam degradation. In fact, a high thermal expansion coefficient can induce big differences of thermal expansion along various directions, which can lead to failure of the gain medium in worst cases. Then to improve the heat dissipation, thermal conductivity must be high enough to avoid creation of high thermal gradient between hot and cold parts in the material. In certain cases, the active cavities are cooled down to keep a stable temperature.

To keep optimal performances, it is recommended to use material composed of a cubic lattice which allows a better In-Line Transmission . The following table I.2 summarizes different properties of solid matrices used in the literature for solid state lasers.

Material	Structure	Thermal expansion coefficient ($10^{-6}\,K^{-1}$)	Thermal conductivity ($W\,m^{-1}\,K^{-1}$)	Melting point (°C)
$Y_3Al_5O_{12}$	Cubic Ia-3d	8.2[33]	12-13[33]	1920 [48]1940[49]
Y_2O_3	Cubic Ia3	8.5[50]	27[48]	2430[48]
Sc_2O_3	Cubic Ia	6.4[48]	16.5[50]	2430[48]
Lu_2O_3	Cubic Ia	8[50]	12.2[50]	2450[48]

Table I.2: Properties of the most widely used solid matrices as gain medium for laser applications.

Table I.2 shows the main differences between $Y_3Al_5O_{12}$, Y_2O_3, Sc_2O_3 and Lu_2O_3 ceramics. Y_2O_3 has largely higher thermal conductivity value than others which constitutes a very interesting material as gain medium. Scandium oxide (Sc_2O_3) offers the lowest thermal expansion but in order to choose a material which is a compromise between the process facility, a high thermal conductivity and low thermal expansion coefficient, YAG is preferred. Y_2O_3 and Lu_2O_3 are investigated in the literature but fabrication process is more difficult due to their high melting point.

Er^{3+} Dopant The dopant ion is responsible for the laser effect and emits at a particular wavelength in a laser cavity when it is associated with a matrix. The most popular dopant ions are neodymium Nd^{3+}, ytterbium Yb^{3+} and erbium Er^{3+}. The particularity of these ions is to absorb and emit in a monochromatic way. In the case of Er^{3+}, it has the advantage to emit at 1.6 µm. This wavelength corresponding to an eye-safe laser, since the radiation is absorbed by the aqueous humor of human eye. The intensity of the laser beam is considerably decreased when it is absorbed by the aqueous environment. Thus, the emission does not impact the retina and allows many more applications in civil or military domains. Other emissions are dangerous for the skin and eyes and can lead to damages without noticing.

The "eye-safe" emission can reduce the necessary protective equipment when the laser is used, and explains the popularity in dental surgery. Other applications can be found in the literature for telecommunication, target catching, destruction of missiles [9, 20, 51].

Er:YAG Gain medium Up to date, most lasers using Er:YAG as gain medium contain a single crystal often obtained by the Czochralski method. The great interest for this laser is thanks to its good experimental and numerical spectroscopy properties. These properties were measured by Eichhorn *et al.* [52–54]. Multiple configurations were tested to combine an adapted matrix to the Erbium ion (YAG, YALO, YLF, Y_2O_3)[4]. The ion Er^{3+} shows interesting spectroscopic results when it is integrated in a YAG host matrix [1]. In fact, the main feature of this gain medium is to possess several energy multiplets linked to transitions from the $^4I_{13/2}$ level to the $^4I_{15/2}$ level leading to a 1.6 µm emission.

[4]YALO and YLF stands for $YAlO_3$ and $YLiF_4$, these are matrices commonly used as host with the Er^{3+} ion.

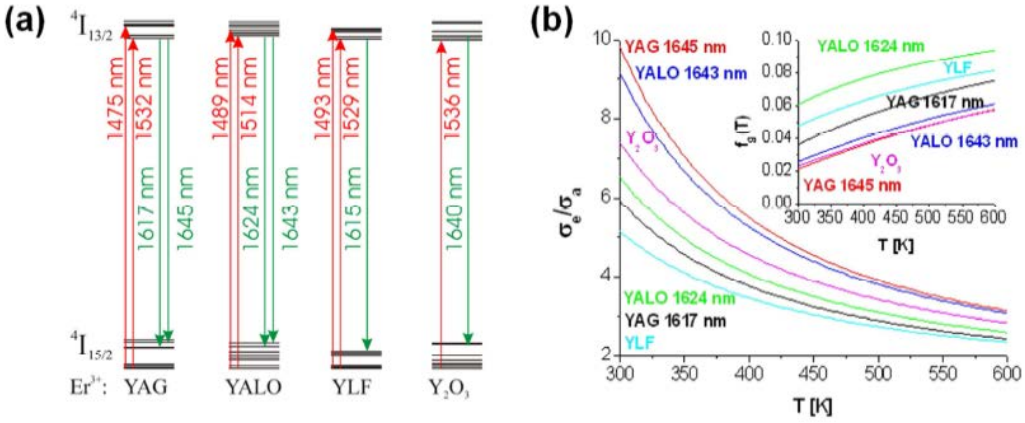

Figure I.11: a) Energy-level diagrams for different host matrices doped with Er^{3+} ion. b) Calculation of emission-to-absorption cross section ratio and lower laser level population of Er^{3+} in different hosts as a function of the crystal temperature from [1].

Fig. I.11 shows the energy diagrams proposed for different host matrices. It is worthy to notice that in the case of Er^{3+} doping for the YAG host matrix, there is an energy gap between the lower level of laser transition and the fundamental level which induces the decrease of energy losses by re-absorptions. On the contrary, other host matrices proposed here (YALO,YLF, Y_2O_3) are most prone to re-absorption losses. Moreover, according to the Boltzmann statistic, the thermal population of ions is lower for the YAG matrix and tends to stay more easily at this level [1].

Furthermore, in Fig. I.11. for pumping at 1645 µm, the YAG doped with Er^{3+} ion has the highest emission-to-absorption cross ratio (σ_e/σ_a) whatever the temperature. σ_e/σ_a is the ratio between emission coefficient and the absorption coefficient and expresses that the emission is always important in comparison to the absorption in a large range of temperature. This reveals that the Er^{3+}:YAG is the most promising combination for a host matrix and a doping ion compared to others proposed here.

On top of that, the properties of Y^{3+}ion, one of the YAG elements, are similar to those of Er^{3+}(Table I.3).

Ion	Ionic radius (pm)	Atomic radius (pm)	Covalent radius (pm)	Pauli electronegativity	Solubility in YAG (at%)
Y^{3+}	89.2[20]	180[20]	190[20]	1.29[55]	-
Er^{3+}	88.1[20]	175[20]	189[20]	1.38[55]	up to 50[56]
Eu^{3+}	95[21]	185[57]	198[58]	1.37[55]	>50[56]
Nd^{3+}	99.5[21]	185[57]	201[58]	1.33[55]	0.9-11[56]
Ce^{3+}	103.4[21]	185[57]	204[58]	1.29[55]	0.5-1.2[56]
Yb^{3+}	100.8[57]	175[57]	187[58]	1.41[55]	up to 50[59]

Table I.3: Comparison between Y^{+3} ion characteristics and rare earth candidates for replacement in YAG matrix as active ion.

Thanks to electronic structure and smaller size, the Er^{3+}ion allows the replacement of Y^{3+}in the matrix. In the case of doping, the doping amount Er^{3+} in YAG host can be high, up to 50 at.%, higher than for Ce^{3+} Nd^{3+} or Yb^{3+} doping. This capacity of a doping rate can be used to vary the emission wavelength from 1.64 to 2.94 µm (see table I.4.).

The lowest doping rates are generally used for high power needed for outside applications such as satellite communications, telemetry or teledection. In the case of high doping, the emission at 2.94 µm is more strongly absorbed by water, which decreases the penetration in aqueous environments. A possible use of this emission is for cosmetic, reconstructive or dental surgery.

	50 at% Er:YAG	0.1-1 at% Er:YAG
Emission wavelength	2.94 µm	1.64 µm
Laser transition	$^4I_{11/2} \rightarrow {}^4I_{13/2}$	$^4I_{13/2} \rightarrow {}^4I_{15/2}$
Pumping wavelength	600-800 nm	1.5 µm
Applications	Medicine	Telecommunications

Table I.4: Spectroscopy comparison between high and low doping from [22].

The choice of the Er:YAG material has been made according to the desired application of this work. Thanks to the good thermo-mechanical properties, the cubic structure and a relative lower melting point, the YAG matrix is a good candidate as solid host matrix. The ions responsible for the laser effect are the Er^{3+} ions, because they enable to have a high rate of doping in the YAG matrix and especially they allow a safer use thanks to lasing wavelenghts. To conclude, combination between Er^{3+} and YAG enables high spectroscopic performances.

2 Requirements for transparency

Obtaining the transparency To get a higher transparency, special focus has to be on reducing the reflection, absorption and scattering effect in the considered material. These effects will be defined in the following with their effects.

Theoretical notions for transparency

Transmittance & transmission The transmittance of a material is defined by the fraction of incident light transmitted through it. To compare the transmittance of a material, it is interesting to compare the real transmittance from the theoretical transmittance (Th). Th can be calculated as follows:

$$T_h = \frac{2n_1 n_2}{(n_1^2 + n_2^2)} \tag{I.1}$$

The refractive index for the air is approximated at n_2=1 but refractive index of YAG material n_1 is in function of the wavelength considered by the following equation:

$$n^2 - 1 = \frac{C_1\lambda}{\lambda^2 - C_2} + \frac{C_3\lambda}{\lambda^2 - C_4} \tag{I.2}$$

The C_i coefficients for YAG is $C_1 = 2.28200$, $C_2 = 0.01185$, $C_3 = 3.27644$,$C_4 = 282.734$ [60, 61].

The real transmittance T_r is measured by a spectrophotometer and dividing the incident light I by the transmitted light I_0 at the output:

$$T_r = \frac{I}{I_0} = \frac{(1 - r - s)^2\, e^{-\alpha x}}{1 - r^2(1 - s)^2 e^{-2\alpha x}} \tag{I.3}$$

With s the surface diffusion, x the sample thickness in cm, r the Fresnel reflection and α the absorption coefficient in cm^{-1}.

Finally, the T_r is affected by the thickness, and to compare all samples between them, the normalization by the thickness can be calculated as follows:

$$T_n = T_h \left(\frac{T_r}{T_h}\right)^{\frac{e_n}{e_r}} \tag{I.4}$$

The specimen transmission T_r is normalized by the theoretical transmission of the material T_h and for a given thickness e_n (in mm), where e_r is the thickness of the specimen.

The criteria for transparency is the RIT : Real In-line Transmittance. The light is collected 1 meter after the sample at a very low angle ($\approx 0.5^\circ$) to avoid the interference and scattered light from the sample.

There is no relationship between the optical qualification observed with naked eye and the measurement of transmission when the specimen is qualified as transparent, but A.Goldstein gives some ranges to judge a transparent ceramic based on the percentage of In-Line Transmission (ILT) [62]:

- 0-20%: opaque
- 20-50%: translucent
- 50-75%: transparent

- 75- to theoretical: highly transparent

Then, particular conditions during the shaping, sintering and the post-treatment are crucial to obtain an optimal result on the transparency. Nevertheless, the transparency can be precisely measured with a spectrophotometer at different wavelengths and the optical quality can be judged subjectively by naked eye. In this current work, a ceramic is qualified as transparent when the observer can read through whatever the distance between the sample and the background. For a translucent sample, the image through it is clear when it is on contact of the background and smeared if the distance between the sample and the background is increased [63].

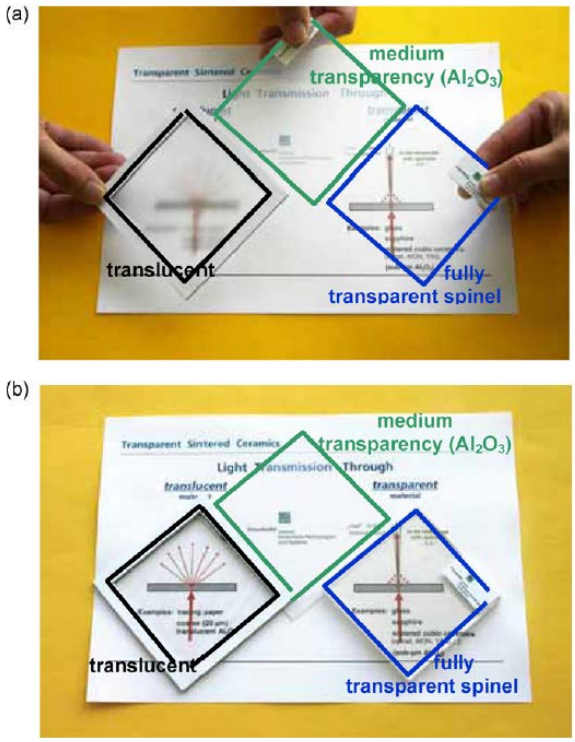

Figure I.12: Comparison of different transparencies depending on the positioning for a translucent material, a medium transparency from Al_2O_3 ceramic and a fully transparent spinel from [64].

An example is presented in Fig. I.12 where differences between translucent, medium transparency of Al_2O_3 ceramic and transparent spinel ceramic are shown.

To better understand origins of transparency loss, phenomena like reflection, absorption and scattering of the light are described in following paragraphs. To be more precise, a part of the light which is not totally transmitted through the ceramic is reflected, refracted, diffracted, absorbed and /or scattered (Fig. I.13).

Reflection The reflection of a light beam is due to the change of the beam into the opposite direction. The light which is neither absorbed nor transmitted is reflected. The reflection phenomena occur when the light changes in medium of propagation. The total reflection r_s can be calculated by this expression [64, 66]:

$$r_s = \frac{2r}{1+r} \tag{I.5}$$

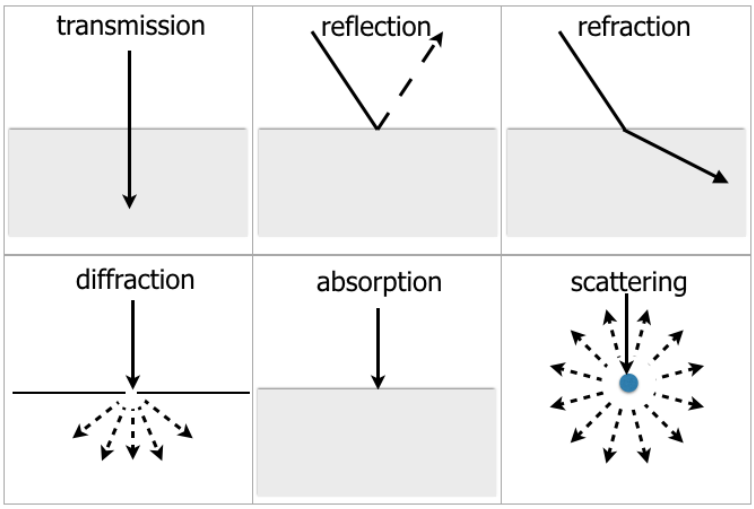

Figure I.13: Phenomena which take place when light hits a surface (From [65]).

where r is the Fresnel reflection.

Scattering The scattering effect is a phenomenon related to the deviation of the light by the material. In the case of PCs, it is due to the presence of secondary phases or porosity. The scattering is produced by the same causes than the refraction or the absorption, and these causes are explained in the following.

Absorption The phenomenon of absorption is due to the loss of the intensity of transmitted light other than reflection or refraction. Absorption (a) decreases proportionally according to the number of defects present in the materials and can be calculated by:

$$a = (1 - r_s) \exp(-\alpha d) \tag{I.6}$$

Where

- r_s is the total reflection coefficient,
- α the absorption coefficient in cm^{-1},
- and d, the thickness of the sample in cm.

Ceramic defects which cause a transparency loss Several parameters have to be considered to reduce defects in the ceramic and reach the highest transparency. Parameters which can be responsible of a loss of transparency are presented in the Fig. I.14:

1. Surface roughness
2. Grain boundary
3. Triple point
4. Porosity
5. Secondary phases
6. Impurities

All these defects have to be controlled at all steps of the ceramic processing. Sometimes, some type of defects can be removed with a post-treatment after the sintering like in the case of porosity. An optimized procedure tends to find best conditions to avoid all these defects. Surface roughness can be improved by a polished surface treatment but in the

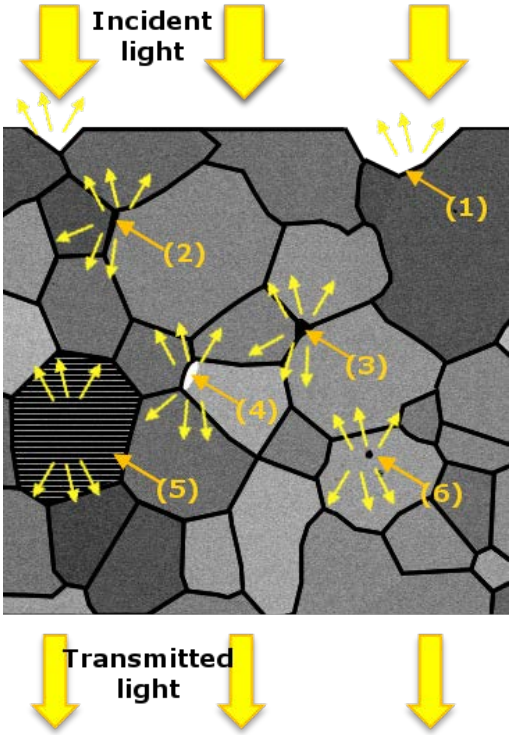

Figure I.14: Ceramic defects which cause a loss of transparency.

case of other defects (grain boundary, impurity, porosity ...), only an high quality powder, and adapted processing could avoid formation of these.

Secondary phases The presence of secondary phases induces the change of the refractive index locally. This region can be more or less important in certain cases, depends on the chemical composition of this phase and creates an area where the incident light is scattered.

For the YAG case, the stoichiometry has to be scrupulously respected and molar ratio between yttrium and aluminum has to be $R = Y/Al = 0.6$ as predicted by the phase diagram Fig. I.15.

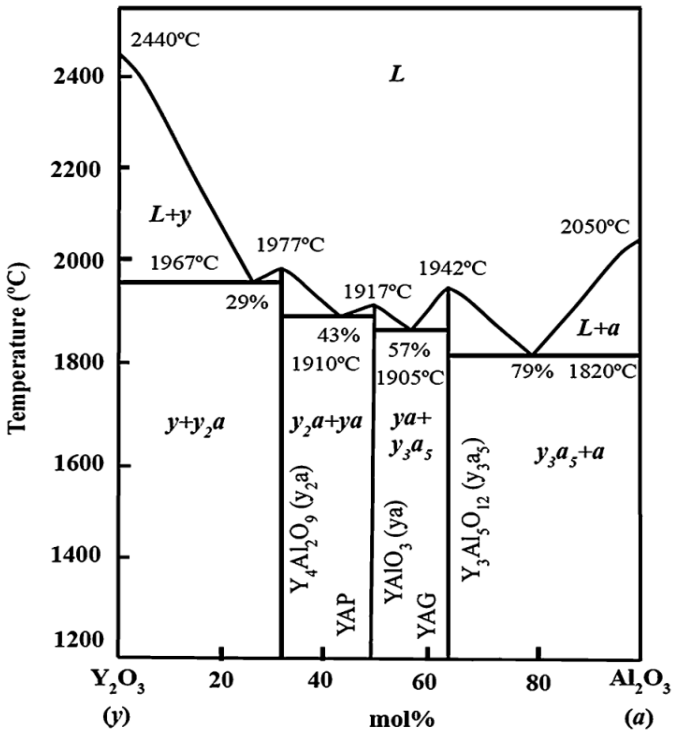

Figure I.15: Phase diagram for system Y_2O_3-Al_2O_3 from [49].

The employment of sintering aids like LiF is generally used as cleanser to avoid carbon pollution and finish the densification step. LiF is particularly helpful, with a low volatilization temperature (<1000 ° C). It prevents the carbon from the graphite tools (i.e. during SPS process) to penetrate into the ceramic before reaching the sintering temperature. Unfortunately, the sintering aid can also react with current phases and disturb the stoichiometry. These deleterious reactions form secondary phases and impact the final transmission as reported in Katz *et al.* study [67].

Porosity The porosity is the formation of the small cavities at the microscopic scale during the compaction procedure of the powder into a green body. It is the most important sources of transparency loss in PCs [68]. After the sintering, a residual porosity can be present and impacts the transparency, being responsible of most scattering effects. The scattering effect by the porosity can be calculated as follow:

$$\gamma_{pore} = \frac{3pC_{sca,p}}{4\pi r_p^2} \tag{I.7}$$

With p the total porosity, $C_{sca,p}$ is the scattering cross section of a spherical pore and r_p the pore radius.

$C_{sca,p}$ was defined by Apetz *et al.* [66] :

$$C_{sca,p} = \frac{8\pi^3 r_p^4}{\lambda_m^2}\left(\frac{\Delta n}{n}\right)^2 \tag{I.8}$$

With $\triangle n$ the difference between refractive index of the material and the porosity (air or gas) and λ_m the wavelength of the considered light.

The scattering can be approximated by the Rayleigh theory for small pores compared to higher wavelength (few nm) as described in this equation :

$$I \propto I_0 \left(\frac{D^6}{\lambda^4} \right) \tag{I.9}$$

Where I is the intensity of the scattered light, I_0 the intensity of the incident light, D the spherical diameter (approx.) of the scattering center and λ the wavelength of the incident light.

Here, pores have to be as small as possible to prevent the scattering phenomenon. Simulation of porosity in YAG made by Pabst *et al.* indicated a decrease of the transmission when the porosity reaches 0.001% (10 ppm) [69] (Fig. I.16). For a practical case, Ikesue *et al.* showed a similar slope efficiency for a ceramic (compared to a single crystal) with a residual porosity of 150 ppm [70]. More recently, Boulesteix *et al.* have shown that the residual porosity has to be below 18 ppm for laser application and above this amount, scattering effects drastically impact laser performances [71]. So, from numerical considerations and practical observations, the residual porosity has to be as low as possible in order to achieve good laser performances.

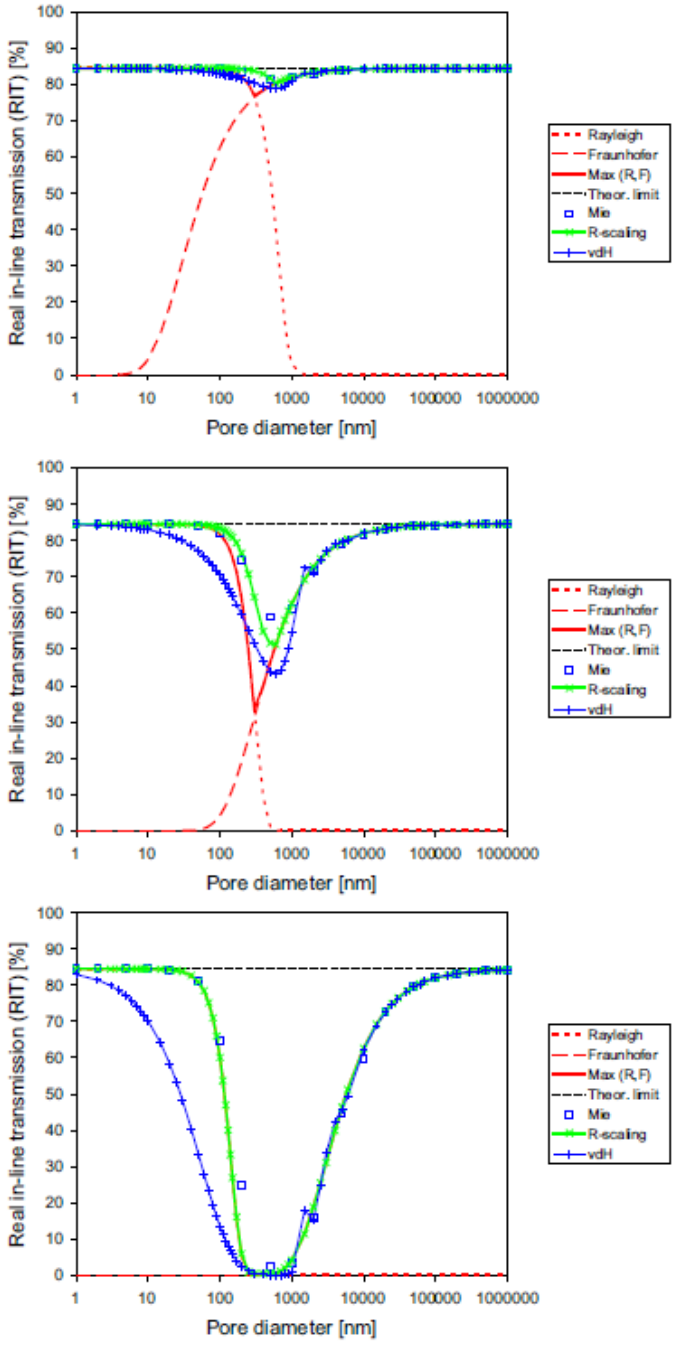

Figure I.16: Simulation of RIT in function of the pore size diameter for YAG ceramics for 10, 100 and 1000 ppm of residual porosity (from top to bottom). Wavelength considered: 1031 nm. Several expressions were considered for the simulation: R-scaling, Rayleigh, Fraunhofer, maximum function, van de Hust, and Mie solution from [69].

Grain boundary In a single phase ceramic, all grains have the same composition but the crystallographic orientations can be different.

A loss of transmission can be caused by difference of the refractive indices inside the material or by different crystallographic orientations [27] and composition. Two cases are possible: if the material is birefringent and anisotropic, then it induces a loss of the transparency. In this case, the loss of transparency is due to the grain boundary γ_{gb}. This

is proportional to the grain size multiplied by the square of the variation of the refractive index as showed in the following equation from [66]:

$$\gamma_{gb} = 3\frac{\pi^2 r_g}{\lambda_0^2}\Delta n^2 \tag{I.10}$$

with λ_0=$\lambda_m n$ and r_g the grain size.

If the material is isotropic, the refractive index is not dependent on the crystallographic orientation (i.e. n is the same in all directions)[68]. So, the grain boundary has to be as small as possible to avoid to be not assimilated as another medium with different refractive index.

Studies conducted by Yoshimura *et al.* [72] have shown that for a birefringent material, the RIT increases when the grain size is high due to a reduction of grain boundary number. Nevertheless, a basic model based on approximated Mie and Rayleigh-Debye theories shows that a transparent Al_2O_3 ceramics can be obtained even with an elevated number of grain boundaries [66].

To obtain a highly transparent ceramic, all scattering effects have to be avoided. During the synthesis, some parameters can be adjusted to improve optical results. All kinds of defects that were described previously are now summarized in the following table (table I.5).

Defects impacting ceramic transparency	Goal	Procedure to goal achievement
Surface roughness	Obtain a flat surface	Polishing and surface treatment (after the sintering)
Porosity	below 10 ppm	Increase the green body density and homogeneity before sintering. Use of pressure assisted sintering to obtain a full densification. Avoid formation of agglomerates in the powder.
Secondary phase	Y/Al=0.6	Control the formation of YAG and avoid formation of secondary phase during the sintering.
Purity	>99.999%	Select commercial YAG or synthesize highly pure powder. Avoid pollution contamination from crucible of graphite environment.

Table I.5: Summary of requirements for highly transparent samples.

2. Fabrication of transparent polycrystalline ceramics by ceramic powder processing

The processing of polycrystalline transparent ceramics using the powder processing method consists in sintering a compact powder to obtain a ceramic with a high density. To reach the highest transparency, the full compaction is needed and each step has to be optimized in this goal. Most important parameters are listed in next paragraphs and considered in a global approach. More generally, powder is chosen depending on the desired characteristics (particle size, purity ...) and can undergo some pre-treatments to optimize the future behavior during compaction and sintering. For example, the spray drying method is used to modify the shape of powder agglomerate in order to enhance the green density and the reactivity during the sintering. Freeze dried powder is able to provide a high green density and therefore improve the sintering [73]. In some cases, the commercial powder has to be treated in solvent to remove impurities. Globally, after choosing/synthesizing a powder, formation of green body is necessary to perform sintering. So, compaction with uniaxial or isostatic pressure can be applied to form a green body. To achieve in fabrication of compact sample, the ratio between the diameter and the height has to be lower than 5, and the lower ratio, the lower gradient density [74]. Then a sintering consists in heating up the temperature in a furnace with the possibility to have different atmospheres and pressures to densify the sample by shrinkage effect.

In this section, various syntheses of ceramic powder methods will be presented and a literature survey of the powder characteristics and processing parameters influencing the ceramic transparency will be described.

2.1. Precursors & ceramic powders

1. Ceramic powder syntheses

Syntheses To synthesize a ceramic powder, different routes are possible: (i) physical and (ii) chemical methods. Physical route can be processed by mechanical milling (a commonly used method), vacuum vapor condensation and the physical vapor deposition. These two last methods are not suitable to produce large quantities of powder and will not be discussed in the following.

Chemical methods are more adapted to fabricate transparent ceramics. Two types of chemical routes can be involved here: the solid state reaction and the wet chemical route.

1 Solid state reaction methods Here solid state reaction can be decomposed in 3 methods: chemical decomposition, chemical reaction between solid species and chemical reduction.

The chemical reaction is often used in calcination step for chemical precipitation or coprecipitation methods. But more generally, this method consists in decomposition and reaction between precursors such as hydroxides, oxalates or nitrates at elevated temperature. By this method, magnesia can be obtained from magnesium carbonate by forming CO_2 gas [75].

Reaction between solids can be used to obtain complex oxides powder such as $MgAl_2O_3$ spinel starting from MgO and Al_2O_3 powder [75]. Solid state reaction method is also

used to obtain YAG [76], Lutethium Aluminum Garnet (LuAG) [77], or $MgAl_2O_4$ [78, 79] powder.

In case of YAG, the YAG powder can be synthesized by several steps from Al_2O_3 and Y_2O_3 powders*:

1. Formation of YAM between 900 and 1100 °C:

$$2Y_2O_3 + Al_2O_3 \rightarrow Y_4Al_2O_9(YAM) \tag{I.11}$$

2. Formation of YAP between 1100 and 1250 °C:

$$Y_4Al_2O_9 + Al_2O_3 \rightarrow 4YAlO_3(YAP) \tag{I.12}$$

3. Formation of YAG between 1400 and 1600 °C:

$$3YAlO_3 + Al_2O_3 \rightarrow Y_3Al_5O_{12}(YAG) \tag{I.13}$$

**These temperature ranges can be slightly influenced by the particle size.*

Each of these three reactions needs alumina to form the next phase. Solid State Reactions (SSR) is involved through a powder calcination after a chemical synthesis (co-precipitation, sol-gel) in order to reach the YAG phase. SSR method can be used during the ball milling process to initiate reaction between precursors [80, 81]. The other solution is to let precursors react together inside the green body during the sintering. This method is called Solid State Reactive Sintering (SSRS).

The first YAG ceramics for laser application were fabricated from alkoxide precursors by calcination of these precursors to obtain the starting powder [40]. Since, numerous approaches in the literature reported this technique to form YAG or other transparent ceramic material.

To be more effective, the mixture has to be homogeneous between species. Ball milling method is often used to ensure a dispersed mix and a homogeneous result, but the main disadvantage is to potentially generate a contamination in the powder. The goal of ball-milling is to refine the powder.

2 Wet chemical routes To synthesize ceramic precursor powder, several methods can be used: chemical precipitation/coprecipitation [82, 83], spray drying [84], spray pyrolysis [85], freeze drying [86], gel methods (sol-gel [87], pechini method [88], citrate gel method [89], glycine nitrate process [90]) and non aqueous liquid reaction [91].

- Chemical precipitation/coprecipitation method is a well-known method used to synthesize nanocrystalline powder [92]. This method uses a metal salt solution mixed with a precipitant solution. The precipitation can be controlled by various parameters such as pH value, the temperature and concentration of the solution. After the precipitation, the precipitant is dried and calcined in air, and particle powder size is highly dependent of the calcination temperature [75].
- The spray drying technique consist in obtaining fine droplets of precursor solution by a fluid atomizer and sprayed into a drying chamber. In this chamber, the temperature can be fixed at 300 °C, which is sufficient to dry and obtain a powder but, not to start solid state reactions. Optimal conditions allow to obtain agglomerated spherical particles with a primary particle size under 100 nm [75].

- Hydrothermal synthesis involves to heat up the reactant, the metal salt (oxide or hydroxide precursor) or metal powder in a solvent, between the boiling and the liquid-vapor critical point to start hydrothermal reaction. Several parameters such as the pH value, time and additives can be used to favor some final powder characteristics. Hydrothermal synthesis has been used in a study to obtain Al_2O_3 powder with a high purity and 100% of α-Al_2O_3. Particle size was mostly between 40 and 100 µm [93].
- The spray pyrolysis is a derived method of spray drying but the drying chamber is heated in an oxidizing atmosphere. By this method, the solution of injected precursors is calcined and decomposed in the chamber. This technique has the advantage to control the morphology of powder by adjusting experimental conditions [75]. Although multiple phases are present (*i.e.* YAG,YAM,YAP, Al_2O_3 and Y_2O_3), the stoichiometry Y/Al is respected. An additional calcination allows to form the final YAG phase [94]. Compared to the SSR reaction method which forms the final YAG phase by calcination, the high heating rate and short heating time of the spray pyrolysis tend to form in majority kinetic products (intermediate phases).
- Freeze drying is also derived from the spray drying method where metal salt droplets obtained by an atomizer are frozen rapidly. The solvent is evaporated in a vacuum cooled chamber and leads to formation of spherical agglomerates of powder. The primary particle size is estimated between 10 to 500 nm. This method was used to obtain very fine particles [86, 95, 96].
- Gel methods imply formation of viscous semi-rigid gel by formation of polymeric structure. The gel is calcined to obtain the ceramic powder. This method allows the formation of complex oxides with a high homogeneity. For example, YAG ceramic can be fabricated by sol-gel [97], Yb^{3+}:Lu_2O_3, $MgAl_2O_4$ and Ce:YAG by Pechini [98–100], and $Yb^{3+}Y_2O_3$ ceramic by citrate gel method [101].
- In non aqueous liquid reaction, the most famous method is the flame spray pyrolysis that leads to produce highly pure and fine particle powder. A precursor solution is atomized by a nozzle with high velocity oxygen. The solvent is evaporated instantly by the flame and precursors react at the same time. Lu_2O_3 or YAG can be obtained by this procedure [91, 102] which leads to the formation of particles having a mean size of 10-20 nm [103]. The main disadvantage is the same as encountered by the spray pyrolysis, which is to form kinetic products and not the final phase. The stoichiometry is conserved but multiple phases are present such as alumina, yttria, YAM and YAP. Sometimes YAG was not formed due to high heating rate of the procedure.

2. Powder characteristics

Powders for advanced ceramics such as transparent ceramics have to respect many requirements in terms of phase composition, stoichiometry, purity, size and morphology of particles.

1 Size and morphology of particles The size and the morphology of particles are relevant parameters to take into account for transparent ceramic achievement. Indeed, the compaction and the sintering depend on these parameters. Smaller powder particle size

provides a higher reactivity (around 50 nm) when bigger particle size (100 nm) decreases the reactivity implying higher temperatures for the solid state reaction. [104]. Moreover, a particle size population over 100 nm will induce the porosity formation with abnormal grain growth [105]. In one hand, small particles are preferable to favor the sintering and eliminate the porosity and in other hand, larger particles facilitate the compaction and the green density [106]. So a compromise between high sinterable powder and a high green density has to be found.

The size distribution of a population of particles in also important. A large distribution will form heterogeneities: formation of porosity and large and small grains in the microstructure. A large distribution leads to a very difficult pore closure during the sintering and post-treatment [104]. To avoid heterogeneities, a narrow distribution of particle size is more indicated [75].

The morphology of particles strongly depends on the powder synthesis route and shape of particles impacts directly the green density and therefore the densification of the ceramic.

In fact, more the morphology of particles is rounded, more the density in the compaction process is elevated. When the roughness of particle raises, the compaction is low [107] as illustrated by the Fig. I.17.

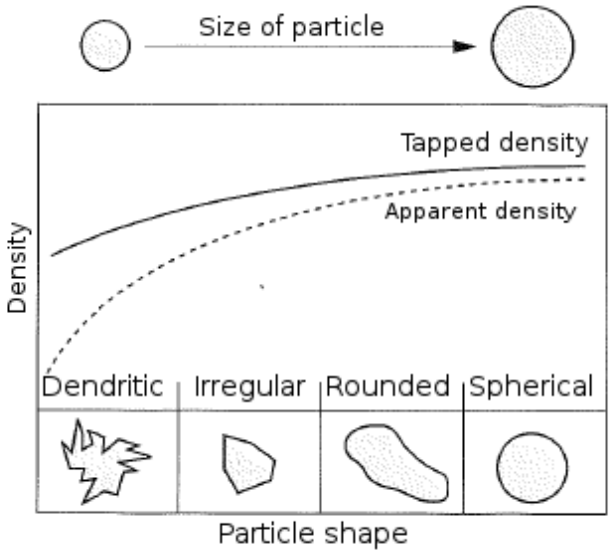

Figure I.17: Size and morphology influence on apparent and tapped density, adapted from [107].

2 Agglomeration state The agglomeration state is always considered in literature by reporting granulometry results and Scanning Electron Microscope (SEM) images of powder. There are two types of agglomerates: soft and hard agglomerates. Soft agglomerates result from Van der Waals forces which link particles between each other. This sort of agglomerates is not detrimental to the sintering as reported by Mroz *et al.* [108].

Hard agglomerates are formed by ionic and covalent forces and induce residual porosity in the material, which is difficult to remove during the processing.

Two types of pores are caused by agglomerates: intra-agglomerates (between particles) and inter-agglomerates pores (between agglomerates) as presented in the Fig. I.18. by [109].

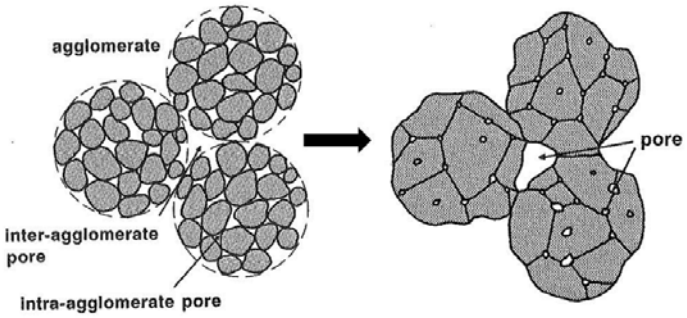

Figure I.18: Intergranular and intra granular pores formation from [109].

Liu *et al.* studied the effect of ball milling on powder used to fabricate Nd^{3+}:YAG transparent ceramic. Thereby, the agglomerates of the powder were broken and the size of particles reduced. The impact of the ball milling parameters of powder on optical transmission of the ceramics was shown in Fig. I.19. An optimal ball milling time of 12 hours was determined resulting in an optical transmission of 83% at 1064 nm [110].

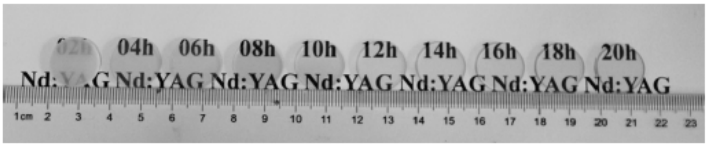

Figure I.19: Influence of ball-milling on optical result for Nd:YAG from [110].

3 Purity Purity mainly depends on the fabrication method of powder [111]. Regarding the literature for transparent ceramic, it is largely admitted to use powder with level of purity higher than 99.99% [112, 113].

Some research teams produce their own powders to control the stoichiometry, purity, agglomeration state, size and the morphology of particles. When powders are synthesized by chemical reaction, a thermal treatment, is applied to remove side-products (organics) in order to purify the powder and start reactions between species. This step uses low temperatures (600-800 $^{\circ}$C) [114, 115] to limit the sintering and grain growth. A relevant example reported by Rubat du Merac *et al.* shows the impact on transmittance and the microstructure with two different powder purities. He has highlighted the formation of amorphous phase from impurities segregated at grain boundaries in triple junctions [116].

In order to avoid the formation of amorphous phases at grain boundaries and triple junctions, some cleaning treatment of the powder is proposed in a patent published in 2013 [117]. The patent describes the cleaning of spinel powder and the reduction of sulfur impurity from 820 to 520 ppm. The cleaning treatment resulted in an optical transmission of 80%.

Villalobos *et al.* have also reported an acid-based procedure to clean powder from impurity. They have succeeded to reduce all metal impurities, the sulfur amount (from 660 to 380 ppm) to obtain high transparent spinel [118]. After the treatment, the authors coated particle powder with LiF and obtained after sintering, a ceramic with an absorption of 80 ppm/cm (100000 ppm/cm without treatment).

4 Stoichiometry The stoichiometry of the starting powder is extremely important for synthesizing YAG ceramics. In this case, the Al_2O_3-Y_2O_3 system is considered and the molar ratio between yttrium and aluminum (Y/Al=0.6) has to be respected to obtain the final YAG phase. Slight deviation from the stoichiometry has a drastic impact on the transparency and mechanical properties.

For example, Zarzecka-Napierala *et al.* have reported that an aluminum excess of 5%, was sufficient to form α-alumina secondary phase in YAG [119]. At the contrary, an aluminum deficit implies an increase of the fracture toughness maybe due to formation of YAP phase. Secondly, authors also reported a higher hardness value when the ceramic is stoichiometric (R=Y/Al=0.6) compared to non stoichiometric (aluminum deficit).

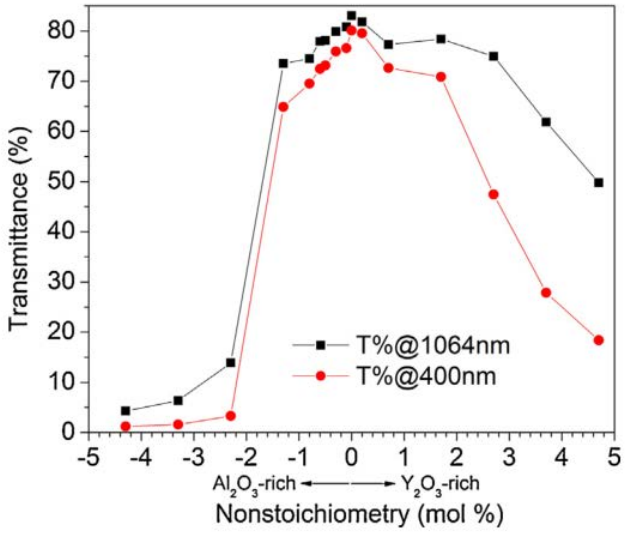

Figure I.20: Transmittance measurements versus the stoichiometry default in the YAG system. x corresponds to the stochiometry shift of $Y_{3(1+x)}Al_5O_{12}$ formula from [120].

In 2015, Liu *et al.* shown the direct influence of the stoichiometric shift of Al_2O_3-Y_2O_3 system on transmission results. They report that the alumina excess is more harmful on transmission than the excess of yttria. The excess limits were 0.6 and 1.7 mol% for alumina and yttria respectively (Fig. I.20). According to the authors, the decrease of the transmission results above these limits is due to formation of optical scattering centers (micro-pores and secondary phases) which are caused by the non-stoichiometry. To their opinion, this porosity is irreversible and could not be removed by any treatment [120].

5 Commercial YAG powders Synthesis of Er:YAG polycrystalline ceramics can be developed from YAG commercial powders. Several suppliers of alumina and yttria exist but few propose YAG powders. Nanocerox and Baikowski are able to provide two different YAG powders which were thoroughly analyzed by Katz *et al.* [20, 121].

Nanocerox company uses Flame Spray Pyrolysis method [102] to synthesize the YAG powder and as discussed before, provides a powder with small particle size (∼50 nm - Fig. I.21) and a multiphasic composition where YAP is the major phase followed by YAG, YAM and Al_2O_3. By this synthesis route, particles are spherical with a very low level of impurity (<10 ppm).

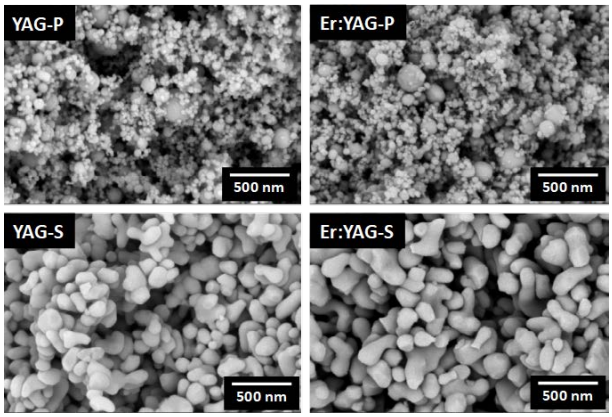

Figure I.21: SEM pictures of Er:YAG and YAG powders from Nanocerox (Er:YAG-P and YAG-P) and Baikowski (Er:YAG-S and YAG-S) suppliers.

The Baikowski powders are based on sulfate precursors to synthesize the powder [122]. This powder is totally different from the Nanocerox powder and possesses round-shaped large particle (∼250 nm - Fig. I.21) with a YAG major phase followed by YAP, YAM and Y_2O_3 phases.

The shape and the size of powder, the agglomeration state, the phase composition and the sulfur content of the powder for each supplier are summarized in Table I.6 by Katz *et al.* [121]. In this table, powders were named as function of their synthesis route YAP-P and Er:YAG-P for the pyrolysis route (Nanocerox) and YAP-S and Er:YAG-S for the sulfate synthesis path (Baïkowski).

	Particle size (nm)	Particle shape	S_{BET} (m^2/g)	Agglomerate size distribution	Phase composition	S content (ppm)
YAG-P	55	Spherical	23	Narrow/ monomodal	YAP+ YAG+ YAM+ Al_2O_3	<10
Er:YAG-P	52	Spherical	21	Narrow/ monomodal	YAP+ YAG+ YAM+ Al_2O_3	<10
YAG-S	208	Round-shaped	9	Large/ multimodal	YAG+ YAP+ YAM+ Y_2O_3	522
Er:YAG-S	271	Round-shaped	7	Large/ multimodal	YAG+ YAP+ YAM+ Y_2O_3	207

Table I.6: Powder characteristics of Er:YAG-P, and YAG -P from Nanocerox and Er:YAG-S and YAG-S for Baikowski powders. S_{BET} correspond to specific surface of particles measured by BET method. From [121].

Er:YAG-S and YAG-S powders are not totally suitable to produce highly transparent ceramics for laser application due to a high level of sulfur impurity [118]. These impurities contribute to increase the absorption phenomena and decrease the transparency. This

sulfur level can be decreased by a pre-treatment of the powder and the use of LiF as sintering aid can play a cleanser role [116, 123] to further improve the transparency.

An attempt to decrease the sulfur level in Baikowski powder is presented in the Chapter 2.

To conclude, the ideal powder for transparent ceramic should present: a narrow particle size distribution, spherical or at least near-spherical particles with a grain size under the micron, no agglomeration, a high purity and a single phase [75].

6 Sintering The sintering stage can be defined by the transformation of a powder compact called green body into a solid by applying a thermal treatment at a temperature lower than the melting point of the major component. In other words, sintering is the replacement of the solid-gas to solid-solid interfaces accompanied by the decrease of the porosity. During the sintering step, grains were formed, the porosity decreases and volatile species escape from the bulk material. The sintering process is frequently accompanied by the shrinkage effect. The holding time is also important to let the time to have a complete shrinkage and obtain a coherent solid. There are several methods to sinter samples and each of them presents advantages and drawbacks. Sintering methods can be separated in two types: with pressure/electrical assisted-sintering and without.

The densification process can be assisted by application of a pressure, which can allow in parallel to reduce both the time and temperature. The well-known techniques that use pressure assistance are Spark Plasma Sintering (SPS) [124–126], Hot-Press (HP) [127–129] and Hot Isostatic Press (HIP) [130–132].

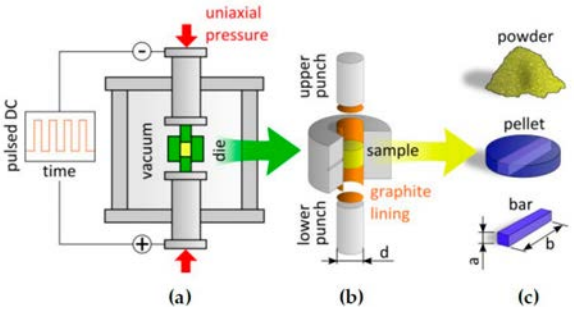

Figure I.22: (a) SPS setup and (b) scheme of the SPS die and the result of compacted powder after sintering. For instance, (c) a slab of the ceramic can be cut to laser applications. From [133].

In the SPS process, an uniaxial pressure is applied by the punches during the cycle as illustrated in Fig. I.22. Heating is achieved by Joule effect, the graphite punches, die and, in some cases, the sample, being thrown away by an electrical current of high intensity and low voltage. More precisely if the sample has a conductive character, then it can be directly heated by Joule effect otherwise it is heated by thermal conduction from the punch and die [134].

The Hot Isostatic Press (HIP) is a press where the pressure is isostatic and controlled by gas atmosphere. HIP is frequently used as an additional post-treatment to eliminate residual porosity [135].

The natural sintering is performed in a furnace without application of pressure, but where different atmospheres or vacuum can be applied. Sintering in air has the advantage

to avoid oxygen vacancies formation during the consolidation [136]. However, sintering under vacuum allows to reduce the porosity and to lower the temperatures of sintering [137]. Vacuum sintering is frequently followed by an annealing step in air or oxygen, which reduces oxygen vacancies formed in the reductive atmosphere under vacuum conditions [68, 138, 139].

7 Sintering aids Sintering aids are additives that are used to help the densification of the material and obtain a fully dense sample after the sintering [140, 141]. Frequently used sintering aids are SiO_2 [142–144], LiF [145–147] or MgO [141, 148]. The sintering aids increase the reactivity and thus lower the sintering temperature [149]. If ceramics are sintered under pressure like in Spark Plasma Sintering (SPS) or hot press, graphite tools and furnace are often used. In this case, LiF is generally chosen since it was shown in the literature that it can prevent the carbon pollution, due to the tools and furnace [20]. It acts as a cleanser, meaning it eliminates impurities by reacting with impurities and evaporating from the ceramics at high temperatures [150–152]. In addition, LiF promotes the densification by enhancing grain growth in the ceramic, this allows to reach the high transparency [67].

Katz *et al.* described the importance to adapt the SPS cycle to the LiF characteristics like wetting temperature and evaporation temperature. The application of the uniaxial pressure was optimized to let the LiF derived species escape from the ceramic before the densification process ended [20, 153]. If the LiF is entrapped in the ceramic, it can react with residual phases such as Y_2O_3 and form YF_3 which will disturb the stoichiometry [20, 67]. Same side effects were observed with $MgAl_2O_4$ ceramics with LiF [152, 154–156]. An optimized powder preparation process and sinter cycle are highly recommended because they prevent the formation of opaque area in the ceramic [157].

8 Post-treatments As mentioned above, HIP can be used to finish the densification by removing residual porosity. Pores localized between grains can be successfully eliminated, whereas the intragranular pores are impossible to remove by HIP-treatment. HIP post-treatment is most effective when the sample has higher density than 92 % of the theoretical value [158]. Nevertheless, HIP treatment could induce gas bubbles (pores) in the ceramics at triple junction as observed by Zhang *et al.* [132]. In their publication, Nd:YAG specimens were sintered by two methods: the first was a high vacuum sintering and the second method was composed of high vacuum sintering followed by HIP post-treatment. Ceramics were observed by SEM after each step and revealed formation of pores located in the triple junction after HIP treatment with annealing in Fig. I.23-D. Gas chromatography-mass measurements revealed that bubbles were composed by Ar gas as shown in Fig. I.23-E.

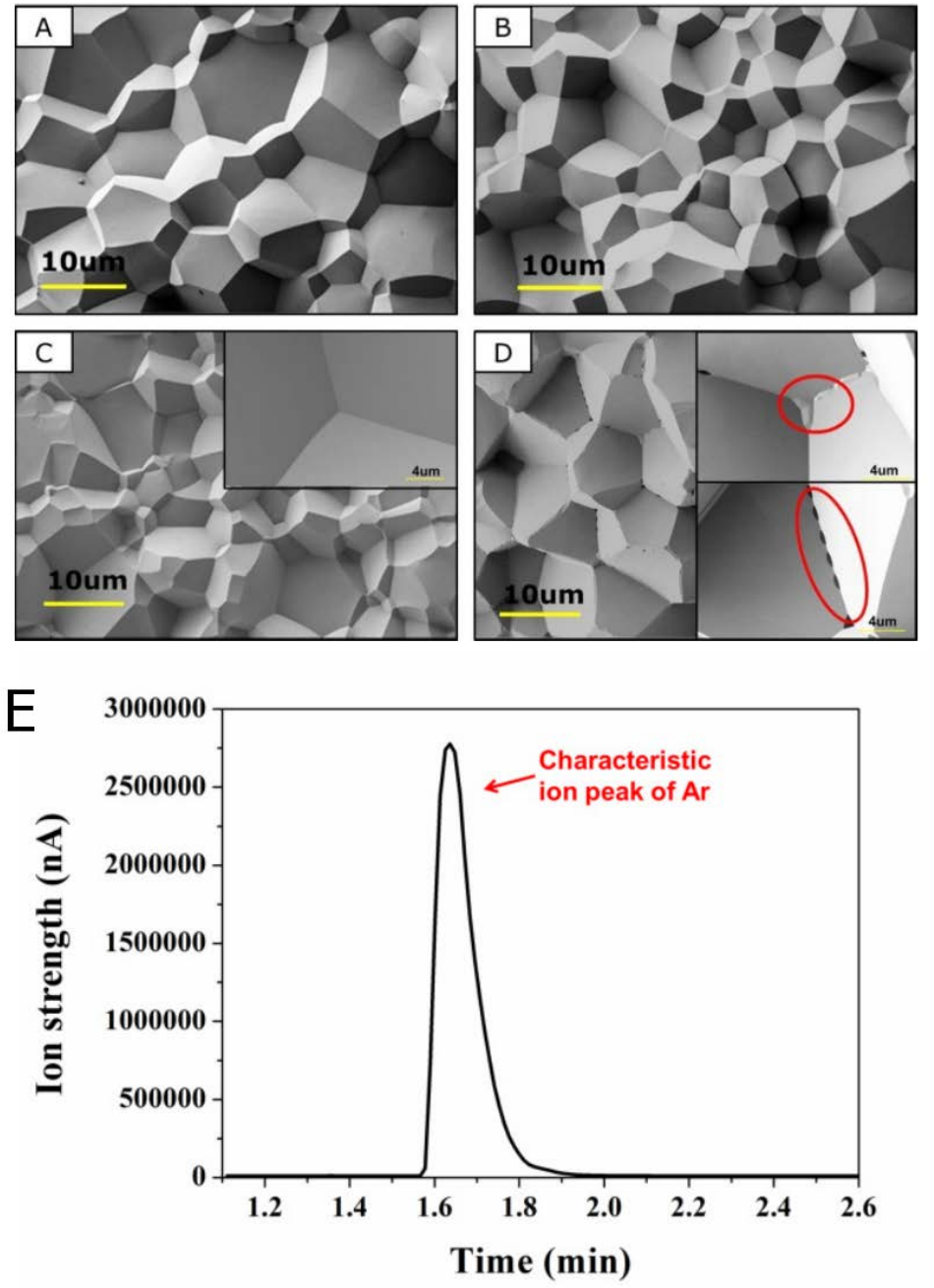

Figure I.23: SEM micrographs of Nd:YAG fracture surfaces. (A) Vacuum sintered before annealing, (B) HIP-sintered specimen before annealing (C) Vacuum sintered specimen after annealing (D) HIP-sintered specimen after annealing (E) gas chromatography-mass measurement of HIPed specimen from [132].

3. Composite doping structure

Composite with dopant gradients allows the the improvement of the laser performances of polycrystalline ceramics. In this part, the main methods to fabricated composite ceramics are presented. Beside the fabrication of composite architecture within the process, attention was also paid to the bonding process of two dense materials.

3.1. Composite processing methods

1. Dry pressing

Dry pressing is the most common used shaping technique to form doping gradients [40, 46, 159–163]. Thereby, powders with different at% of dopant are used to shape green bodies with a dopant ions gradient. It is possible to apply a vibration after the filling of each powder into the die, to smooth the surface of the powder layer before adding a new one [143, 164]. Instead of the vibration, pressure can also be applied on each layer to pre-compact the powder [162]. Dry pressing leads to layer-by-layer composite designs. Fig. I.24 shows an example of Nd:YAG/YAG transparent polycrystalline ceramics fabricated by cold pressing at 67 MPa and a sintering under vacuum [143].



Figure I.24: Polycrystalline multilayer ceramic obtained by dry pressing method. Effect of HIP treatment under 200 MPa was shown on sintered ceramics (from left to right): 1750 ° C 4h, 1650 ° C 4h and as-sintered (9.5 mm diameter, 1.5 mm thick) from [143].

2. Slip Casting

The slip casting, among dry pressing, is one of the well-known methods to produce highly transparent ceramics [165, 166]. This method consists in preparing a slurry containing at least 70 wt% of dry matter in a liquid (water or organic liquid) and pouring the stabilized slurry into a porous mold (usually in plaster). After powder deposition on the mold wall, the green body is dried and an uniaxial or/and cold isostatic pressing can be applied to increase the green density up to 50-55% of theoretical density. Slip cast were pre-sintered, mirror polished and stacked together before the full densification of ceramics [167, 168].

Co-stacked sample of Nd^{3+}:YAG/YAG from slip-casting method are presented in the Fig. I.25.

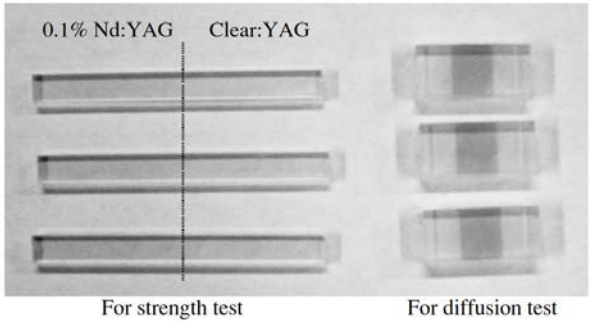

Figure I.25: Composite 0.1% Nd:YAG/YAG obtained by slip casting method from [167].

3. Tape casting

Green ceramic sheets are processed by tape casting technique. Slurry of ceramic powder with binder and plasticizers is prepared in organic liquid and poured on the tape casting bench. The evaporation of solvent from the slurry has to be controlled in order to avoid creation of cracks within the sheet [169–172]. This technique allows to fabricate large, thin sheets of tape casted ceramic with an excellent homogeneity [170]. Tape casting offers the possibility to stack co-casted specimens together. For example, Kupp *et al.* fabricated YAG/0.25at%Er:YAG/0.5at%Er:YAG multilayer ceramics using tape casting before sintering (Fig. I.26) [170].

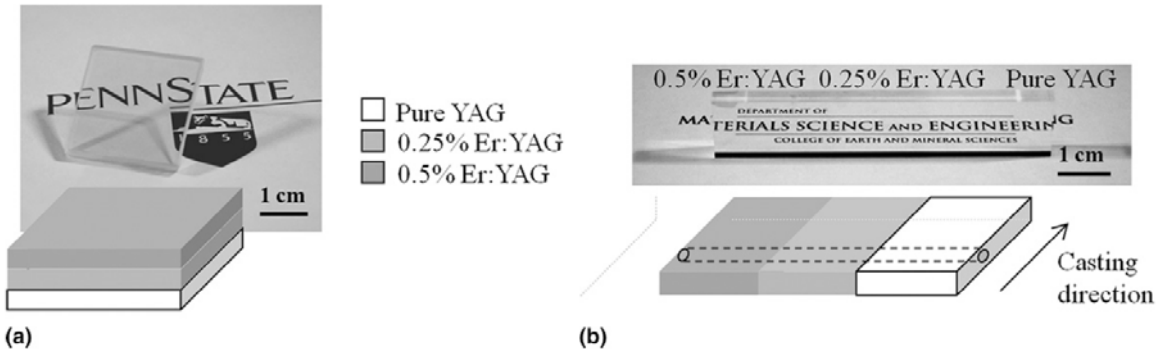

Figure I.26: Schematics of tape cast composites (a) stacked and (b) co-cast with corresponding pictures specimen from [170].

4. Crystal bonding

The crystal bonding technique involves the use of a crystal in contact with a polycrystalline ceramic[5]. The two parts were stacked and heated together (1700-1840 ° C) and the crystal grew in the direction of the polycrystalline ceramic (Fig. I.27). Authors indicated that no precise polishing treatment was required to achieved an "almost-perfect" bonding. This route leads to an expensive and a time-intensive process due to preparation of single crystal and good optical polycrystalline ceramic although the optical quality seems elevated (not communicated) [46].

[5]Bonding between two crystals also used for laser application, we only consider the use of PCs.

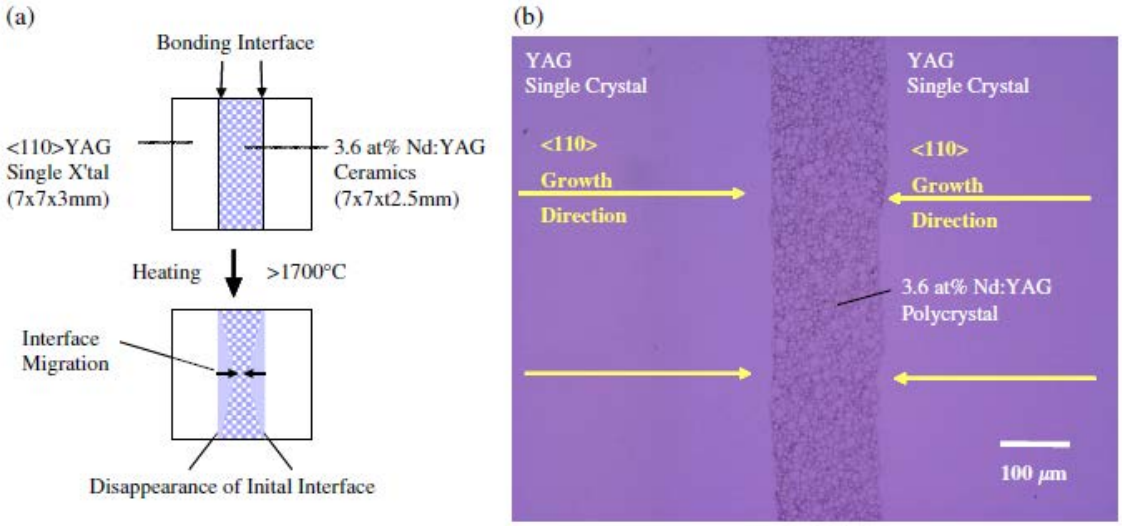

Figure I.27: (a) Schematic diagram of layer-by-layer composite before and after the bonding. (b) Cross observation of the specimen after thermal treatment at 1720 ° C 5h from [46].

5. Polycrystalline bonding

The bonding between two fully dense polycrystalline ceramics is composed by preparation of the surface of two ceramics that will be in contact [143, 164, 173–175]. Surfaces are thoroughly mirror polished [174] and optionally sputtering etching can be used to hydrophilize the surface of the ceramic [175].

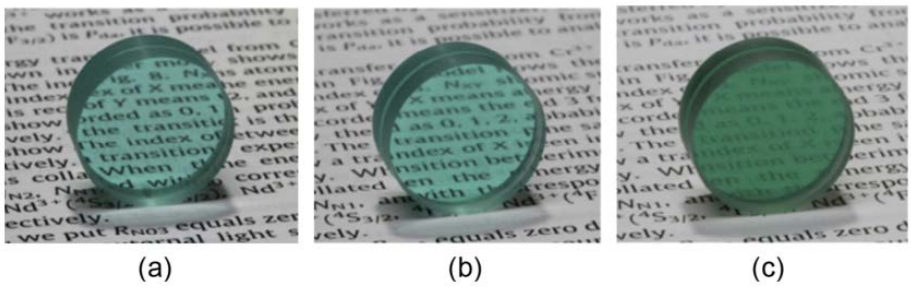

Figure I.28: Composite ceramics Yb:YAG from fully dense sample after heat treatment (when ceramics were in contact) in high vacuum furnace at (a) 1400 ° C 10h (b) 1400 ° C 50h and (c) 1600 ° C 50h from [175].

Obtained samples can present a high transparency (not indicated) but conditions of the bonding have to be managed to avoid creation of defects at the interface (Fig. I.28-(c)).

Regarding the literature, it appears that composite ceramics have a huge potential to replace the single crystal as gain medium but many efforts have to be done to manage all parameters (powder, sintering, bonding...) to obtain the same optical quality. Obtaining a high transparent ceramic is not sufficient, the amount of defects (residual porosity, impurities in grain boundaries...) has to be as low as possible, and in theory all procedure steps have to be well controlled to reach this result.

Additionally, composite doping structures add a higher level of complexity. Several

methods lead to obtain doped gradient ceramics but procedures discussed before imply a good expertise and a long process to manage.

Spark plasma sintering has shown in recent years a huge interest for fabrication of highly transparent ceramics in a short period of time (few hours). Recent report indicated promising results to obtain highly transparent Er^{3+}:YAG fabricated by SPS followed by HIP post-treatment. This first promising result showed an homogeneous doped ceramics with a slope efficiency of 31% and a high transparency [176]. To pursue in this objective, the second achievement is to obtain a doping gradient structure for a polycrystalline ceramics by SPS. Up to date, no study was reporting on fabrication of composite transparent ceramics. This part will be addressed in this manuscript.

Chapter II

Influence of the stoichiometry and sulfur impurity on transparency of YAG ceramics processed by SPS

Preface

It is well-known that, to prepare transparent ceramics, scattering defects such as secondary phases and grain boundary impurities have to be avoided. It is thus necessary to use highly pure and stoichiometric powders. Concerning transparent YAG ceramics, very few suppliers of powders with the required properties exist. Some extra-pure and stoichiometric (Y/Al = 0.60) powders are available, but are very expensive due to complex synthesis procedures. Some much cheaper YAG powders are suitable for some applications (photoluminescence...), but not to prepare gain media for solid state lasers. A laser YAG ceramic has to be fully transparent, and powder defects such as sulfur (a few hundreds of ppm) and a slight deviation from stoichiometry (Y/Al = 0.60±0.03) are very deleterious to the optical properties of the YAG samples. To study the effect of these defects and develop treatments to enhance the powder properties, two industrial experimental powders have been selected, each of them with a particular flaw.

This chapter has been divided into two parts:

- The first part of this chapter is presented as an article on treatments applied to two industrial experimental YAG powders. The first powder posses the stoichiometric correct ratio (Y/Al=0.6) but presented a high sulfur level (>660 ppm). Several chemical and thermal treatments were used to reduce the sulfur content without modifying the sinterability, the particle size, the crystalline phases and the stoichiometry.
- The second powder had a lower sulfur level but presented a non-stoichiometry, with a Y/Al ratio of 0.57. The effect on transparency of Y_2O_3 addition, to balance the Y/Al ratio, was studied.
- The second part is composed of complementary work that aimed at exploring if improvement strategies proposed at the end of the article could be successful.

Influence of the stoichiometry and sulfur impurity on transparency of YAG ceramics processed by SPS

Abstract

Transparent YAG ceramics achievement requires fully dense and chemically homogeneous materials. These properties strongly depend on stoichiometry, purity, particle size and crystallinity of the starting powder. In this work, two industrial experimental YAG powders were chosen to study the influence of their main defects on transparency and develop procedures to correct these defects. The first powder presents an yttrium deficit shown by the shift of the theoretical stoichiometry: Y/Al=0.57 instead of 0.60. The second powder contains over 600 ppm of sulfur impurity. In the first case, different quantities of Y_2O_3 were added to the YAG powder to get close to the correct Y/Al ratio. Different grades of optical quality of the sintered ceramics were obtained and thoroughly analyzed. As expected, the best results were obtained for the Y/Al ratio of 0.60.

In the second case, thermal treatments at 950, 1000 and 1200 °C and chemical washing by acid and basic solutions were applied to the powder to decrease impurities and especially the sulfur content. The characterization of the sintered ceramics revealed that: thermal treatments allowed to reduce the sulfur content but induced a particle size increase; washing with acid solutions modified the Y/Al ratio and caused the formation of secondary phases; washing with sodium hydroxide led to a pollution by sodium.

1. Introduction

Over the past few years, High Energy Lasers (HELs) have been developed for optical, surgery and ballistic applications [1, 52, 177]. The current limitation of HELs is due to a thermal gradient that appears in single crystals when they are employed as gain media, which leads to thermomechanical stresses [45, 178]. To enhance laser performances, transparent ceramics are expected to replace single crystals thanks to their good thermomechanical properties with a less expensive process than single crystals. Despite successful fabrication of ceramic Er^{3+}:YAG laser slabs by SPS with an in-line transmission and a lifetime comparable to a single crystal, the output power varied much with the laser slab position, which indicates a heterogeneous ceramic [176].

To obtain a highly transparent ceramic, some requirements have to be taken into account. The final specimen must contain a single phase with a cubic structure and a full densification is required to avoid scattering losses [71, 179]. The quality of the starting powder is crucial and some characteristics have to be tightly controlled such as the purity, the stoichiometry to prevent secondary phases and inclusions in the final ceramic and the morphology and grain size distribution to enhance the powder compaction [62, 71, 116]. These characteristics have to be optimized according to sintering parameters to reach the highest transparency. Surface roughness, porosity, secondary phases and impurities have to be avoided during the procedure because they impact the optical quality and therefore the laser performances [176].

The effect of non-stoichiometry in YAG powder was highlighted by Liu *et al.* [120]. Multiple deviations of the stoichiometry were tested by these authors. They showed that alumina and yttria begin to have an impact on transmission for small excesses: 0.6 mol% for alumina and 1.7 mol% for yttria. The highest transmittance (83.1 % @ 1064 nm) was obtained for the theoretical Y/Al=0.60 molar ratio. The loss of transparency is also accompanied by a decrease of average grain size and by the presence of an Al_2O_3 secondary

phase for Al_2O_3-excess, and by an increase of average grain size in the case of Y_2O_3-excess. Porosity also tends to increase when the excess of alumina and yttria increases [120].

Level of impurities also has a dramatic impact on ceramic transparency, particularly when impurities are segregated at grain boundaries, and induces secondary phase formation [116]. Low concentrations of impurities impact the color [116] of the specimen and high concentrations cause absorption phenomena in the 1-2 µm range [3, 118, 123, 180–183]. Particular attention has to be paid to the complete elimination of impurities that are introduced during the powder synthesis (like sulfur) and additives such as binders and dispersants prior to the densification. Thus the sintering procedure has to be adapted in order to enable their volatilization. In the case of SO_x species, which possess a high vaporization temperature (1050 ° C-1250 ° C), the pressure applied in SPS or in Hot Press has to be adjusted to help the elimination of residual species before finishing the densification [116].

Residual porosity in the ceramic specimens has a harmful impact on laser performances as shown by Ikesue *et al.* Authors reported a similar slope efficiency as the single crystal when the concentration of residual pores is lower than 150 ppm [70]. Boulesteix *et al.* have shown that the residual porosity has to be below 18 ppm for a 1at%Nd:YAG polycrystalline ceramic used for laser applications [71]. Lower pore concentrations lead to higher performances as shown by Konoshima: an output power of 25 kW was obtained for an estimated porosity of 1 ppm [184]. Difference of refractive index between ceramic and gas in the pores induces scattering sites that have a larger impact than secondary phases [185]. To eliminate the residual porosity, it is necessary to limit the porosity formed during compaction, which highly depends on the powder quality and particle morphology and size. Simulations made by Pabst *et al.* on porosity and pore size in YAG ceramics revealed that porosity of 0.0001% has practically no influence on Real In-line Transmission (RIT) whatever the pore size. For higher pore concentration (0.001%), results indicated a large decrease of the RIT when pore size is similar to the wavelength of light [69].

In some cases, powder synthesis involves temperatures as high as 700-1200 ° C resulting in neck formation between particles. These necks participate to reduce the sinterability and induce formation of pores due to bad particle organization inside the green body during compaction.

As mentioned, the quality of the powder is thus very important and the quality of the final ceramic highly depends on the starting powder. But few suppliers are able to provide a high quality powder with a low level of impurity and these powders are very expensive due to a costly process.

There are two routes to obtain a high quality nanopowder with a high reproducibility: the synthesis of very pure powder (>99.99%) by a wide variety of methods (coprecipitation, sol-gel, colloid/solution reaction, hydrothermal synthesis, nitrate melt cooling, etc.) [62] or the cleaning and/or the correction of the actual defect of a commercial powder. Concerning the cleaning, Villalobos *et al.* have performed an acid pre-treatment of a spinel commercial powder that decreased the sulfur content from 660 down to 380 ppm. This pre-treatment combined with use of LiF as a sintering aid allowed to reduce the absorption loss between 1-2 µm from 100,000 ppm/cm down to 75 ppm/cm [118, 186].

In this article, we propose to investigate the influence of YAG powder defects such as Y/Al ratio and sulfur impurity on the transparency of ceramics prepared with these

powders. Several chemical and thermal treatments were applied to reduce the sulfur content on a first batch of industrial experimental powder. For the second batch, the goal was to adjust the Y/Al stoichiometry by Y_2O_3 addition. In both cases powders were characterized before and after treatment and the effect of powder improvement on ceramic transparency was studied.

2. Experimental

2.1. Starting powders

Two batches of YAG experimental powder supplied by Baïkowski (France) were used in this study. The first batch (#21998), called thereafter BY, has a deficit in yttrium and the second (#20238), called thereafter BS, has a high level of sulfur. Data are presented in Table II.1.

Batch	Y/Al	Sulfur content (ppm)±41
BY	0,568	324
BS	0,604	622

Table II.1: Y/Al molar ratio and sulfur content in the starting powders.

2.2. Characterization

Powders were thoroughly analyzed by XRD (D8 Advance, Bruker) using a Cu Kα radiation (λ=0,15406 nm) to identify phases. Semi-quantification of phases was performed by the EVA software (Bruker) by comparing intensity of the highest peak of each phase. Specific Surface Area (SSA) was measured by nitrogen adsorption according to the BET method (ASAP 2020, Micromeritics). SEM (NNS 450, FEI Company) observations were done to determine the morphology and grain size of powders and sintered ceramics. The mean grain size was calculated by intercept method. The value obtained was corrected by the mandelsen coefficient k=1.56 [187]. Inductively Coupled Plasma Optical Emission Spectrometry (ICP-OES) (Perkin Elmer) was used to determine the sulfur content and the Y/Al molar ratio of the powder. After sintering, samples were annealed at 1100 °C during 1 hour and mirror polished afterwards. Archimedes method was used to obtain the density of samples after sintering. In-Line Transmission (ILT) measurements of ceramics were performed from 1000 to 3000 nm with a UV-vis-IR spectrophotometer (Cary 7000 UMS, Agilent Technologies).

2.3. Sulfur removal procedure

Two kinds of treatment, either chemical or thermal, were applied on the powder with high sulfur content (BS). For thermal treatments an alumina crucible containing 20 g of the BS powder was placed in a conventional furnace. Temperatures from 950 to 1200 °C for 3 h in air and 950 to 1000 °C under vacuum for 3 to 12 h were applied. A vacuum pump was used throughout the treatment to keep pressure as low as 2.10^{-3} bar.

The second kind of treatment consisted in washing the powder with different acid or basic aqueous solutions. In 200 mL glass beakers 150 mL of 1 mol/L solutions (NaOH, NH_4OH, HCl and HNO_3) or of deionized water were added to 20 grams of powder. Each

suspension was stirred overnight at 30 °C. Then, the mixture was centrifuged at 3000 rpm and the supernatant was discarded, while the powder was washed three times with deionized water. After the last centrifugation, the supernatant was removed and the paste was dried in an oven during 6 h at 100 °C. The dried powder was manually ground in a mortar to break soft agglomerates.

2.4. Stoichiometry correction procedure

The BY powder contained an yttrium molar deficit, corresponding to x=5.33 mol%, equivalent to a Y/Al ratio of 0.568, as revealed by ICP-OES. A composition correction was performed by adding a Y_2O_3 commercial powder (Alfa Aesar, 99.995%) to the BY powder through manual mixing and grinding. Therefore, 10 g samples of YAG powder were mixed with varied Y_2O_3 powder amounts to obtain different molar ratios: Y/Al=0.580, 0.590, 0.600, 0.612, 0.632, named after as B,C,D,E and F (Fig. II.17) whereas A stands for the untreated sample).

2.5. Sintering

Sintering of ceramics was performed by SPS (HP D 125, FCT systeme GmbH, Rauenstein, Germany). Treated powders (either to reduce the sulfur content or to correct the Y/Al ratio) were mixed with 0.25 wt% LiF. For each sample, the powder was poured into the graphite die with a 30 mm inner diameter of the SPS device. Graphite foils (Papyex®) were placed between the graphite die and the powder. Pre-compaction was applied by uniaxial pressure at 100 kg/cm². Samples were sintered for 2 h at 1450 °C with a pressure of 85 MPa during the second part of the cycle as described elsewhere [67]. A pyrometer focused on the upper die monitored the temperature during the cycle.

3. Results and discussion

3.1. Sulfur removal procedure

ICP-OES analyses on 3 samples taken from the industrial experimental BS powder showed an average sulfur content of 662 ± 41 ppm and a Y/Al ratio of around 0.604 ± 0.014. The specific surface area (SSA) was 9.3 ± 0.2 m²/g, which corresponds to an average particle size of 141 nm for round shaped particles. To characterize the homogeneity of the as received batch, semi-quantification of the crystalline phases was performed by XRD on 9 samples and revealed that the major phase was indeed the yttrium aluminum garnet (YAG, $Y_3Al_5O_{12}$) (91 ± 1 %) phase, followed by yttria (5 ± 1 %), yttrium aluminum perovskite (YAP, $YAlO_3$) (2 ± 1 %) and monoclinic yttrium aluminum oxide (YAM, $Y_4Al_2O_9$) (2 ± 1 %). Detailed results are given as supporting informations (Fig. A.1 and table A.1 in appendix A).

Untreated BS powder exhibited an elongated and rounded particle shape with an average size of 173.7 ± 3.5 nm (min: 81 nm, max: 257 nm) (Fig. II.1).

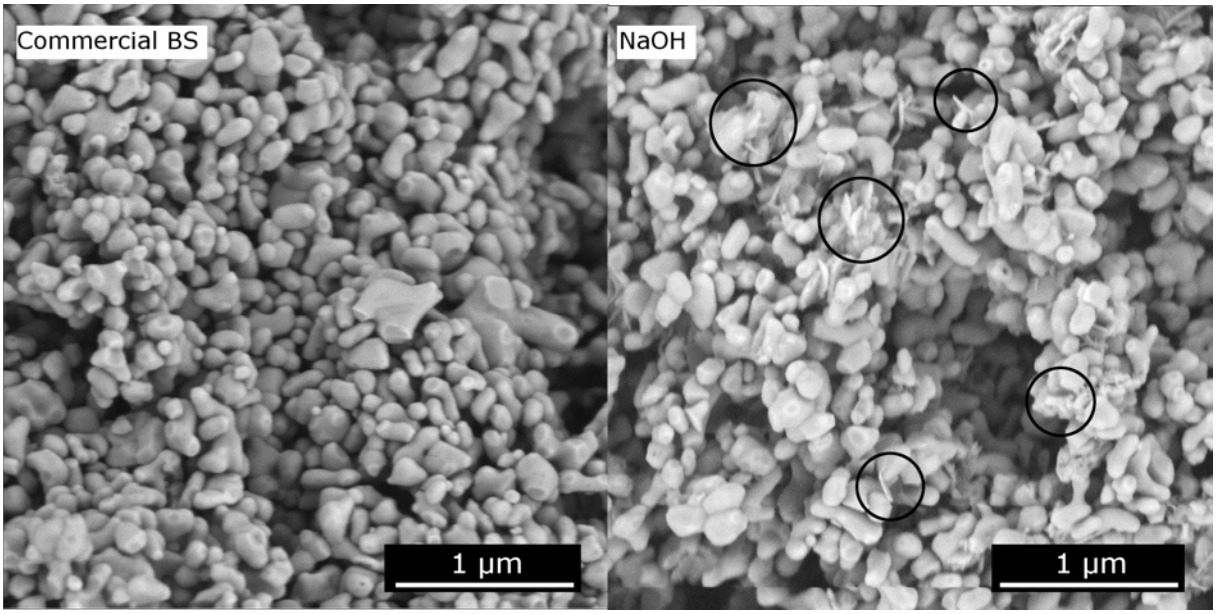

Figure II.1: SEM pictures of the untreated commercial BS powder (left) and of the powder washed with a NaOH solution (right). Black circles indicate flake-like particles.

Thermal treatments allowed to decrease the sulfur content but induced an increase of particle size, as shown by SSA measurements (Table II.2). SEM images are presented in appendix B.1.

Conditions	SSA (m^2/g)	Particle size D_{BET} (nm)	Sulfur content (ppm)±40
BS powder	9.29	141	662
950 ° C 3h in air	8,46	155	469
1200 ° C 3h in air	6,77	194	361
950 ° C 3h vac.	8,99	146	456
950 ° C 12h vac.	8,60	153	533
1000 ° C 3h vac.	8,54	154	354
1000 ° C 12h vac.	8,55	154	240

Table II.2: BS powder characteristics after thermal treatments (vac. : under vacuum).

A first general tendency can be highlighted: a decrease of the sulfur content with treatment temperature increase, whatever the atmosphere.

For thermal treatments in air the decrease of sulfur content (from 662 to 469 and 361 ppm) was accompanied by particle growth (SSA from 9.29 down to 6.77 m^2/g for 1200 ° C 3h). SEM observation also confirmed the increase of particle size and showed neck formation between particles for the sample treated at the higher temperature under air: 1200 ° C for 3h (Fig. B.1 in appendix). The influence of the atmosphere could be observed for samples treated at 950 ° C for 3h, either in air or under vacuum. After both treatments, the sulfur amount decreased to the same extent (~460 ppm), but SSA remained significantly higher under vacuum (8.46 m^2/g under air, 8.99 m^2/g under vacuum). Concerning treatment duration, for a treatment at 1000 ° C under vacuum, the

sulfur amount decreased from 3 to 12h as could be expected. Surprisingly at 900 °C, results were opposite: 456 ppm after 3h, but 533 ppm after 12h. Most certainly, the value measured for the longer duration must has been incorrect, as it was higher than values obtained for 3h both in air and under vacuum. For all these treatments under vacuum (950 °C 3h and 12h and 1000 °C 3h and 12h) SSA were similar and higher than 8.5 m^2/g. The best conditions seemed to be 1000 °C during 12h under vacuum. With these conditions, while maintaining a high SSA, the sulfur content dropped from 662 to 240 ppm. The benefit of treating powder under vacuum was visible when comparing the sample treated at 950 °C 3h in air with the one treated at 1000 °C 12h under vacuum. The obtained powders had similar SSA (8.46 and 8.55 m^2/g) whereas the sulfur amount decreased by 29% in air versus almost 64% under vacuum.

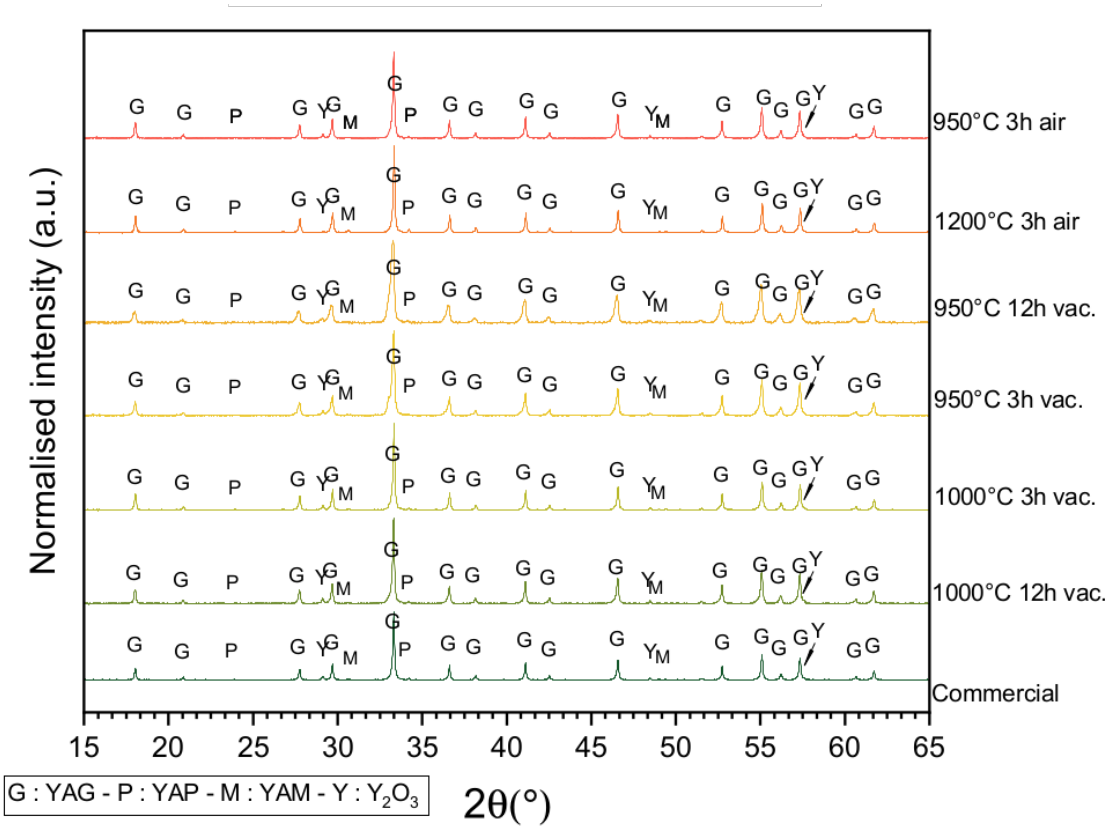

Figure II.2: X-Ray Diffraction patterns of BS powder as-received and after various thermal treatments.

As shown by XRD results (Fig. II.2) thermal treatments in these conditions did not affect the crystalline phase proportions. YAG, YAP, YAM and Y_2O_3 phases present in the powder were still detected after every thermal treatment.

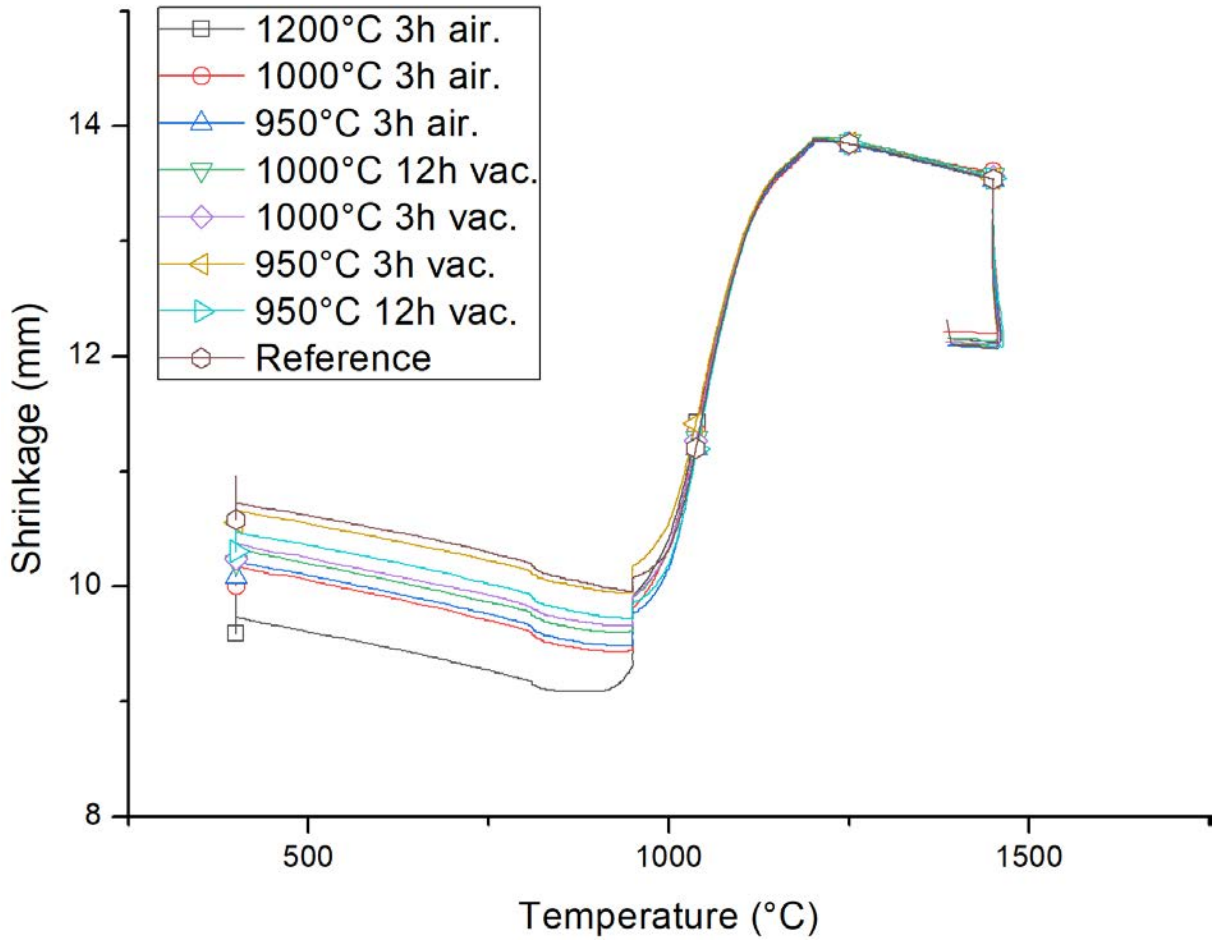

Figure II.3: Shrinkage curves of samples prepared with thermally treated powders during sintering by SPS.

The following of sample shrinkage during SPS experiments (Fig. II.3) showed that sinterability of treated powders remained similar, as the temperatures of beginning and end of densification did not change. Yet these results confirmed that the treatments in air modified some powder characteristics like agglomeration state, which induced a lower green density and therefore a higher shrinkage (Fig. II.3). The most important shrinkage was observed for the sample prepared with the powder treated at 1200 °C for 3h, which is in agreement with the necks formed between particles that are visible on the SEM pictures (Fig. B.1 in appendix). These necks may have contributed to a bad organization of particles during the cold compaction occurring at the beginning of the SPS cycle. Afterwards with the help of temperature and pressure, it seems that full densification was reached at the end of the SPS cycle.

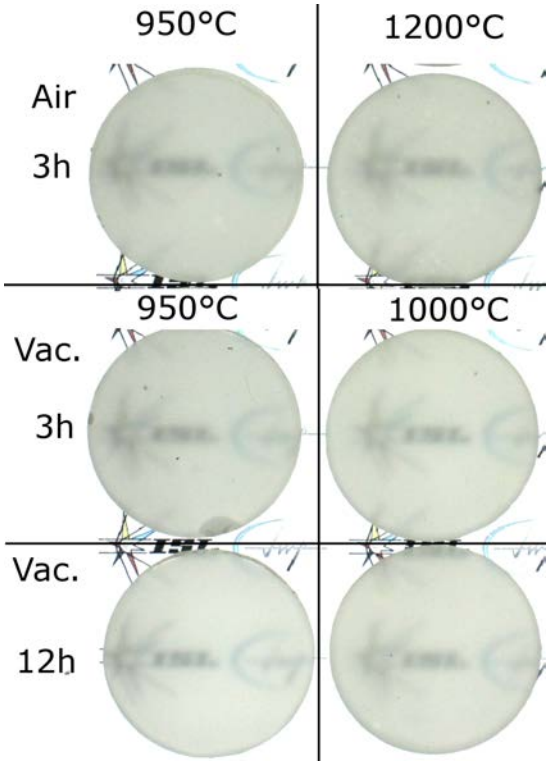

Figure II.4: Visual aspect of polished YAG ceramics prepared with thermally treated powders after SPS sintering. Diameter of samples: 30 mm. Thickness of samples: 2.7 mm.

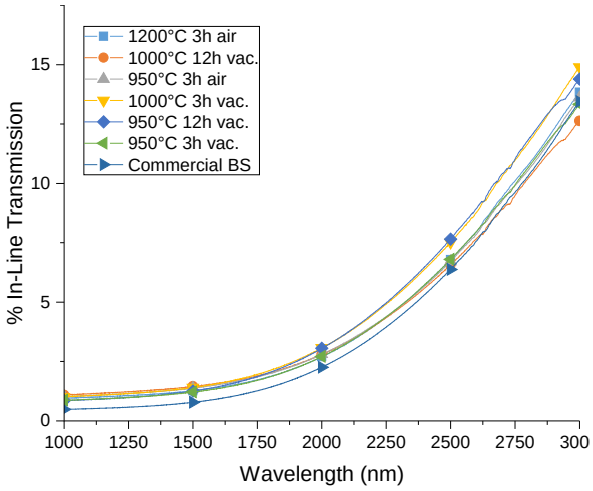

Figure II.5: In-Line Transmission of YAG ceramics prepared with thermally treated powders after SPS sintering.

Fig. II.4 shows photographs of samples obtained after thermal treatment of powders and SPS sintering and the corresponding ILT measurements were plotted in Fig. II.5. Thermal treatments did not significantly improve the transparency of sintered samples even for the specimen with the lowest sulfur content (240 ppm for 1000 ° C 3h under vacuum). Thermally treated specimens were only slightly better than the reference specimen.

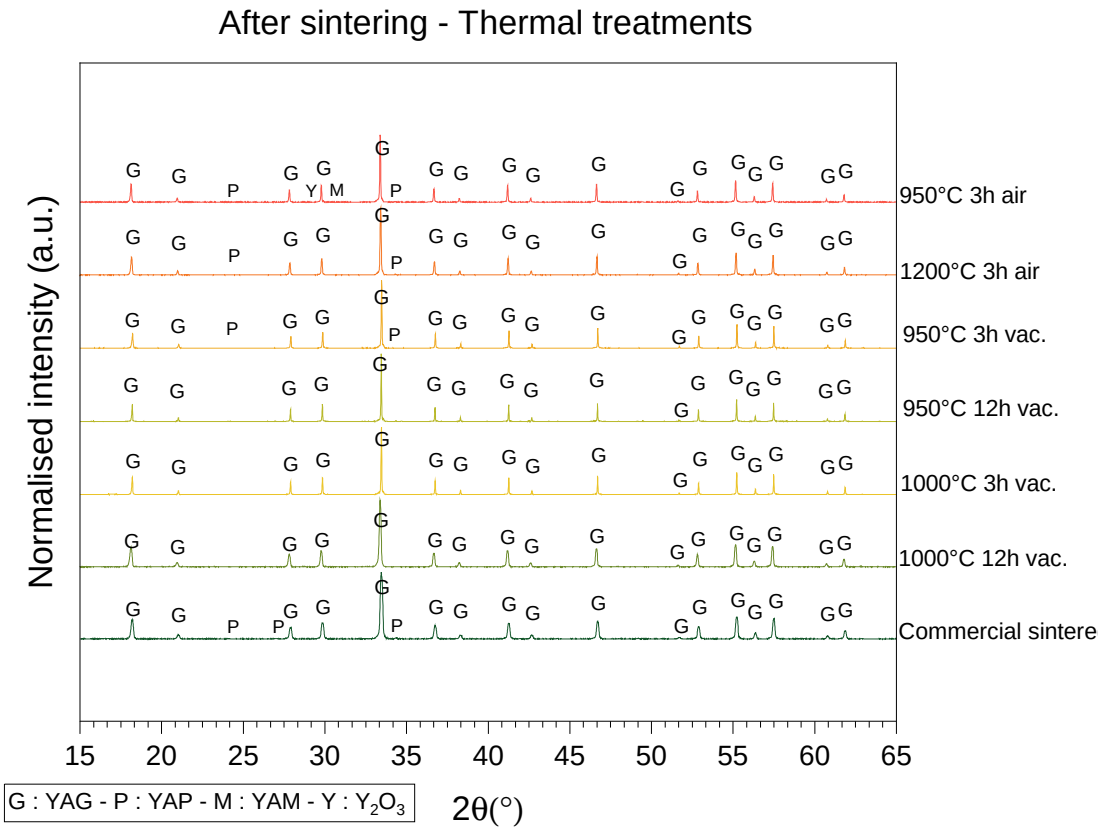

Figure II.6: X Ray Diffraction patterns of YAG ceramics prepared with thermally treated powders after SPS sintering.

XRD patterns (Fig. II.6) indicated the presence of only YAG and YAP phases in the sintered sample of the BS powder. During SPS sintering, except for the powder treated at 950 ° C for 3h in air, the Y_2O_3 and YAM phases (Fig. II.2) reacted and were not detectable by XRD after sintering. Most powders treated under vacuum (950 ° C 12h and 1000 ° C 3h and 12h) contained only the YAG phase after SPS, whereas other treated powders (1200 ° C 3h in air, 950 ° C 3h under vacuum) led to sintered samples composed of YAG and a small amount of YAP. A very small amount of additional Y_2O_3 and YAM phases was still observable in the 950 ° C 3h air sample. Treatments of powders under vacuum seemed to be helpful to initiate reactions between precursor phases (Y_2O_3, YAM and YAP) and contributed to obtain pure YAG samples after sintering.

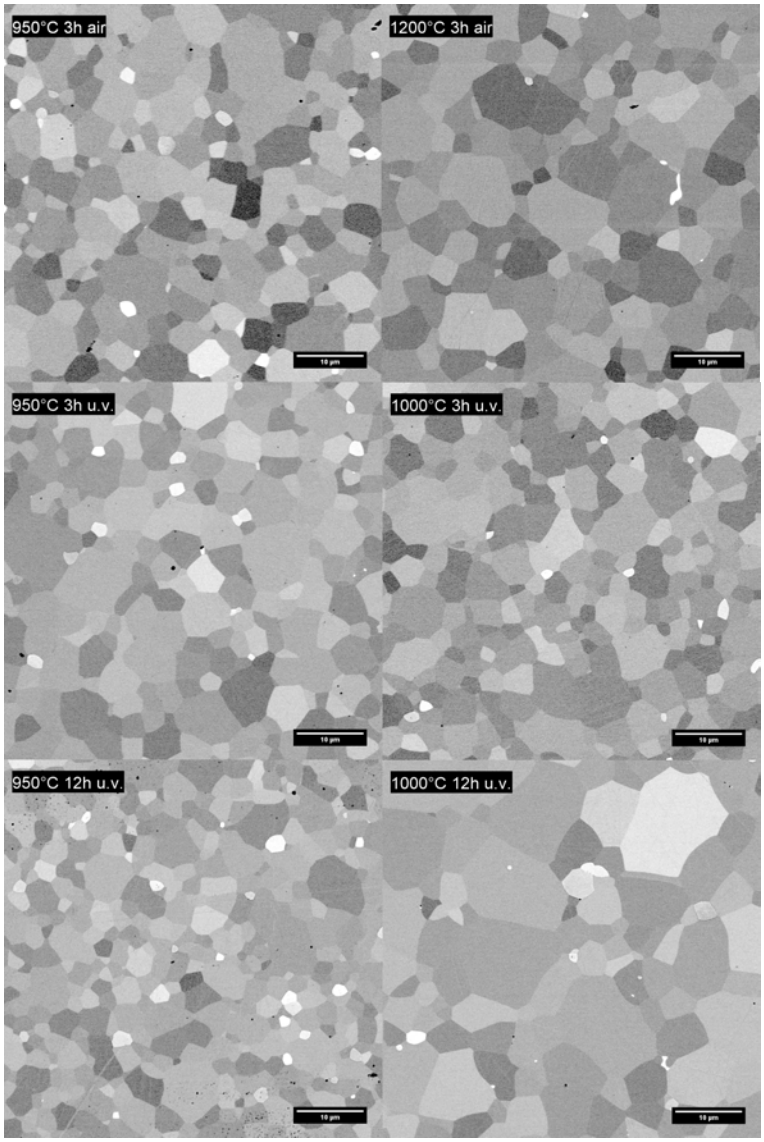

Figure II.7: Surface observations by SEM of raw polished YAG ceramics prepared with thermally treated powders after SPS.

Microstructure analysis of specimens prepared with thermally treated powders showed an increase of the grain size with temperature and holding time without presence of porosity. For example in the case of 3 hour treatments in air, the corresponding average grain sizes were 5.45 µm and 9.98 µm for 950 and 1200 ° C respectively (Fig. II.7). No pores were found in the microstructure and density measurements revealed only one sintered sample that did not reach the full densification (950 ° C 3h in air -99.6% of the theoretical density).

For such fully dense YAG ceramics the reason for non-transparency can be the presence of two kinds of impurities: either chemical, like sulfur, or crystalline, like Y_2O_3, YAM and YAP phases. For some treated powders (950 and 1200 ° C 3h air, 950 ° C 3h vac.) and for the as-received BS powder, XRD showed the presence of small amounts of YAP and/or Y_2O_3 and YAM after SPS (Fig.II.6), which must be deleterious to transparency. However, for the 3 other powders treated under vacuum (950 ° C 12h, 1000 ° C 3h and

12h), only pure YAG phase was observed in the sintered samples. For them, either sulfur was responsible for the non-transparency even though its amount was much reduced by the thermal powder treatment, or secondary phases were still present but in quantities to low to be detected by XRD.

1. Washing treatments

Washing solution	SSA (m^2/g)	Particle size D_{BET} (nm)	Sulfur content (ppm)±40	Y/Al molar ratio
Industrial experimental BS powder	9.29	141	662	0.604
Dionized Water	9.33	141	583	0.611
NaOH	9.65	136	267	0.613
NH_4OH	9.39	140	356	0.600
HCl	9.57	137	703	0.575
HNO_3	9.52	138	680	0.568

Table II.3: BS powder characteristics after chemical treatments.

Washing treatment with deionized water contributed to slightly reduce the sulfur content down to 583 ppm while maintaining the same specific surface area, Y/Al stoichiometry and phase proportions as in the starting powder (Table II.3 and Fig. II.8). On the contrary, acidic solution treatments reduced the Y/Al ratio down to 0.58 for HCl and 0.57 for HNO_3 and did not allow to reduce the sulfur content.

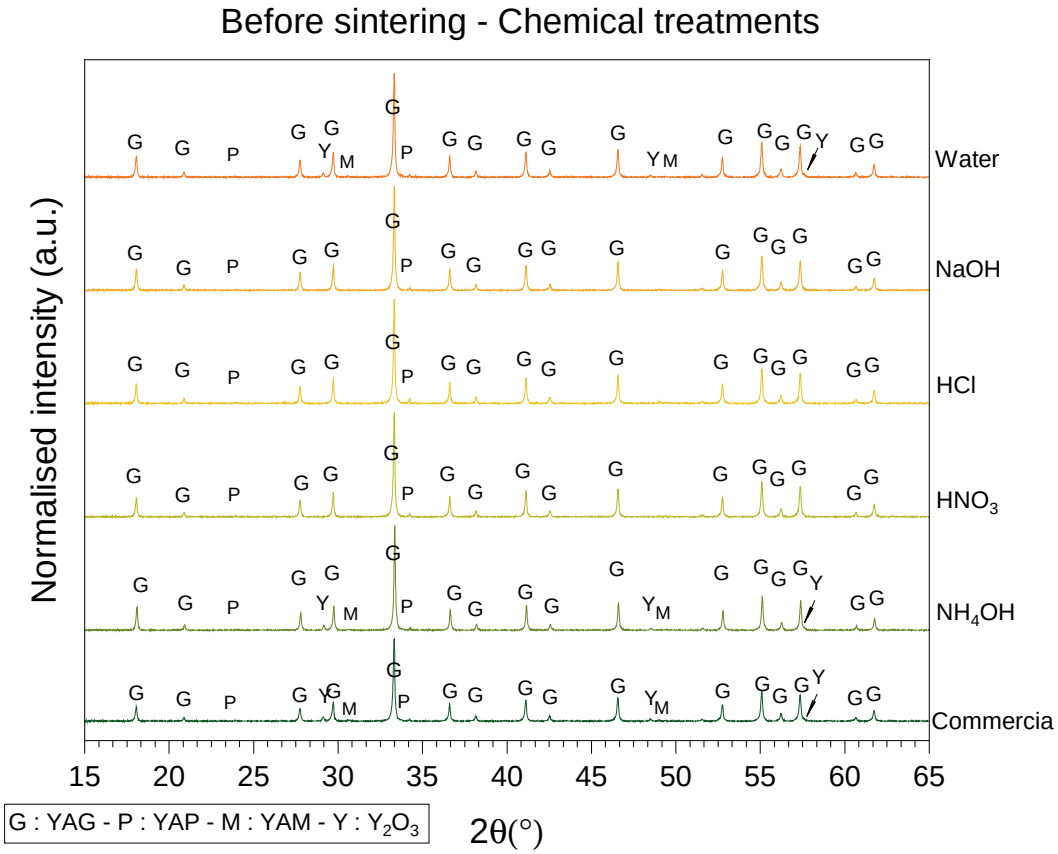

Figure II.8: X-Ray Diffraction patterns of the powders after washing treatments.

XRD patterns of these two treated powders revealed the presence of only YAG and YAP phases among the four phases present in the BS powder (Fig. II.8). Powder treated by alkaline solutions (NaOH, NH_4OH) led to values for the specific surface area and the Y/Al ratio similar to the BS powder, but the sulfur content decreased to 267 and 356 ppm respectively. XRD results (Fig. II.8) indicated the presence of the same phases (YAG, Y_2O_3, YAP and YAM) as in the reference BS powder for NH_4OH treatment. The sample treated with NaOH was on the contrary composed of YAG and YAP phases only. This NaOH treatment thus induced dissolution of YAM and Y_2O_3 phases, as with the acidic HCl and HNO_3 solutions. A thorough study of NaOH treated powder by SEM highlighted the presence of flake-like particles in addition to the initial powder particles (Fig. II.1). EDX analysis revealed the presence of sodium in the flake-like particles (Fig. II.13).

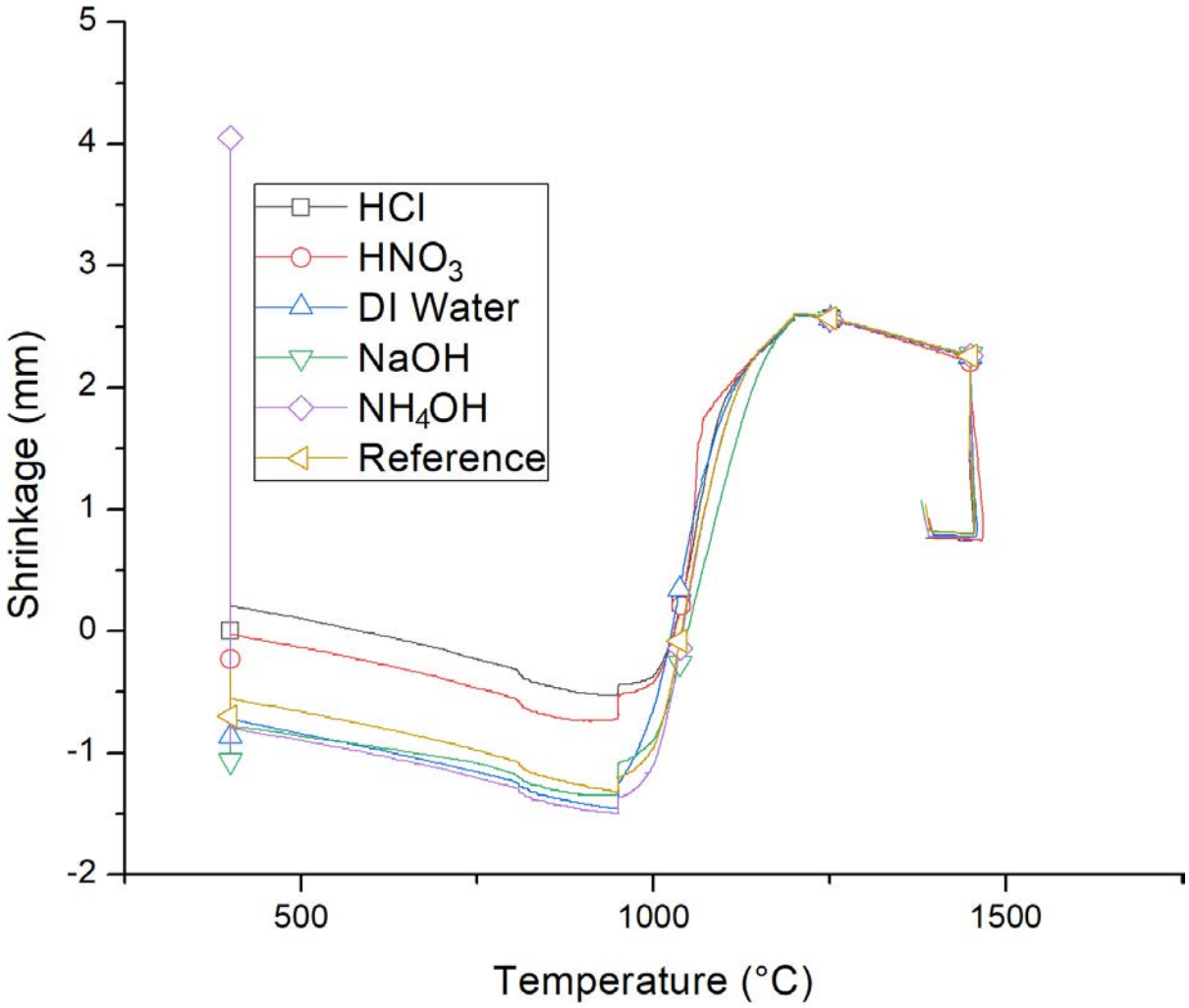

Figure II.9: Shrinkage curves of samples prepared with chemically treated powders during sintering by SPS.

The sintering behavior of the chemically treated powders during SPS treatment is presented on Fig. II.9.

No significant modification of sinterability of treated powders could be observed, as the temperatures of beginning and end of densification remained unchanged. However a higher green density was reached for the powders treated with acidic solutions, which shows a better flowability after these treatments. Other chemical conditions led to a shrinkage similar to the untreated BS powder.

After sintering, XRD showed the YAG and YAP phases in the untreated powder and samples treated with NaOH and NH_4OH solutions. Yttria and YAM phases disappeared during sintering, which shows that these phases reacted to form YAP and YAG. Sintered samples of powders treated with water and acidic solutions only presented a single YAG phase (Fig. II.10).

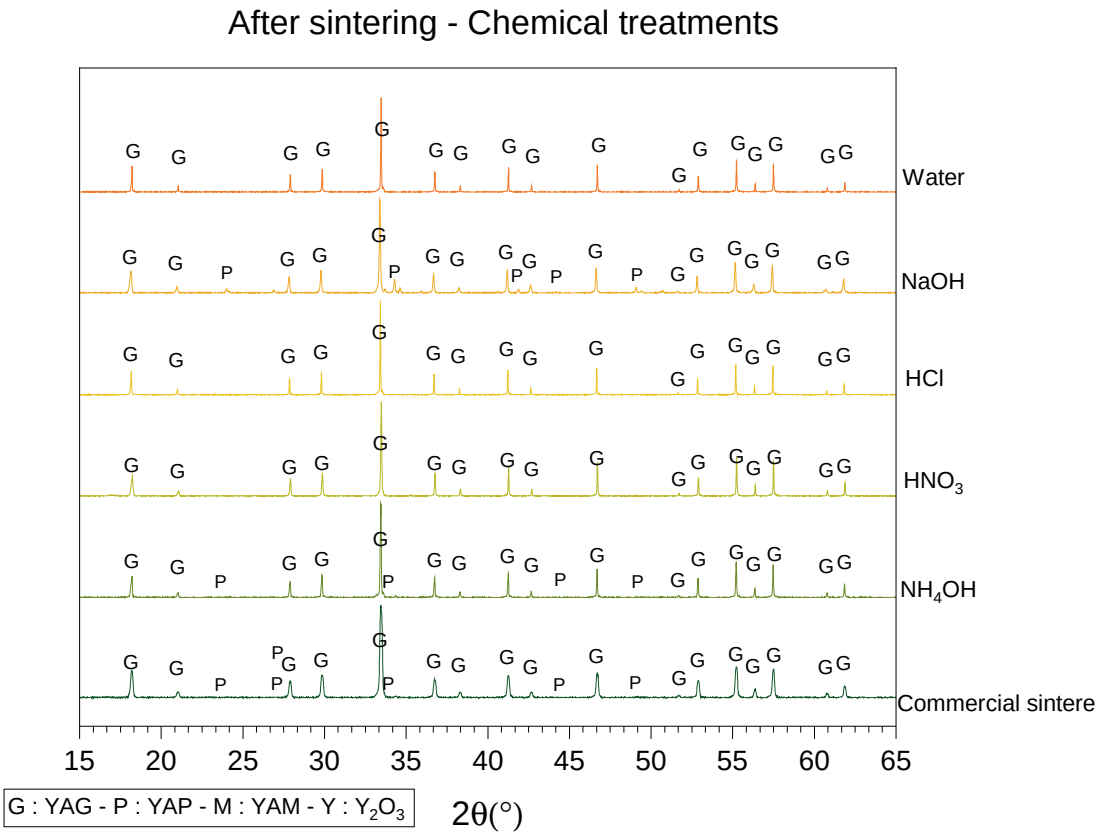

Figure II.10: X-Ray Diffraction patterns of YAG ceramics prepared with chemically treated powders after SPS sintering.

Fracture of specimen were observed by SEM and revealed an homogeneous microstructure for the reference, NH_4OH and deionized water samples.

Fracture observations of specimens, where the powder had been washed with NaOH, HNO_3 and HCl, revealed a strong chemical contrast when using the BSE (backscattered electrons) detector. Firstly, deviation from the Y/Al stoichiometry impacted the microstructure in the case of HCl and HNO_3 conditions. Surface observation by SEM showed black grains between lighter YAG grains (Fig. II.11).

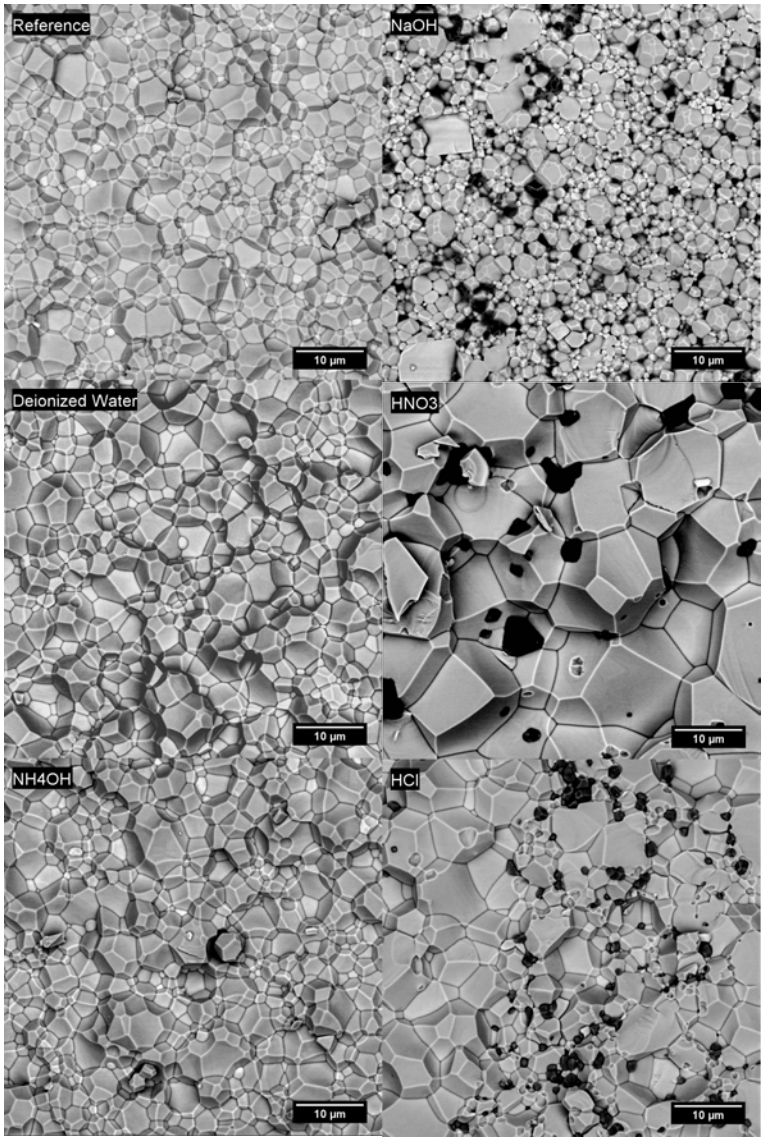

Figure II.11: SEM fracture observations of samples prepared with chemically treated powders after SPS.

EDX analysis confirmed that the black grains in Fig. II.11 were mainly composed of Al-rich phase. Intensities of peaks were not representative and it is difficult to associate ratios of elements detected with corresponding phases. As mentioned before, the two acidic treatments led to a dissolution of the Y-rich phases Y_2O_3 and YAM and in the case of YAM, alumina must have been released and crystallized during sintering although it was not detected by XRD (Fig. II.8). In very low proportions Al_2O_3 secondary phases cannot be detected by XRD [120]. This excess of alumina phase plays an inhibitor role and contributes to slow down the elimination of porosity during sintering and could explain the low optical quality of the final specimens (Fig. II.14) [115, 149]. As demonstrated by Kim acid treatments were efficient to remove impurities in $MgAl_2O_4$ powder but it depended on the phase composition of the starting powder. The authors explained that single element oxide phases (such as Al_2O_3, MgO, Y_2O_3...) are soluble in certain acids [188]. This solubility allows dissolving these phases and removing impurities present in

a commercial powder. If the powder was only composed of a highly stable phase in acidic solution (*e.g.* YAG or $MgAl_2O_4$), the washing treatment was effective. But in the case of multiphase compositions, acidic solutions tended to dissolve Y-rich phases and therefore disturbed the Y/Al ratio. Dissolution of YAG, YAP and YAM phases by acidic solutions and its impact on the stoichiometry is yet not well known. Fractures of the HNO_3 specimen showed larger grain sizes compared to other conditions, maybe due to the shift of stoichiometry (Y/Al=0.57) to the Al-rich region.

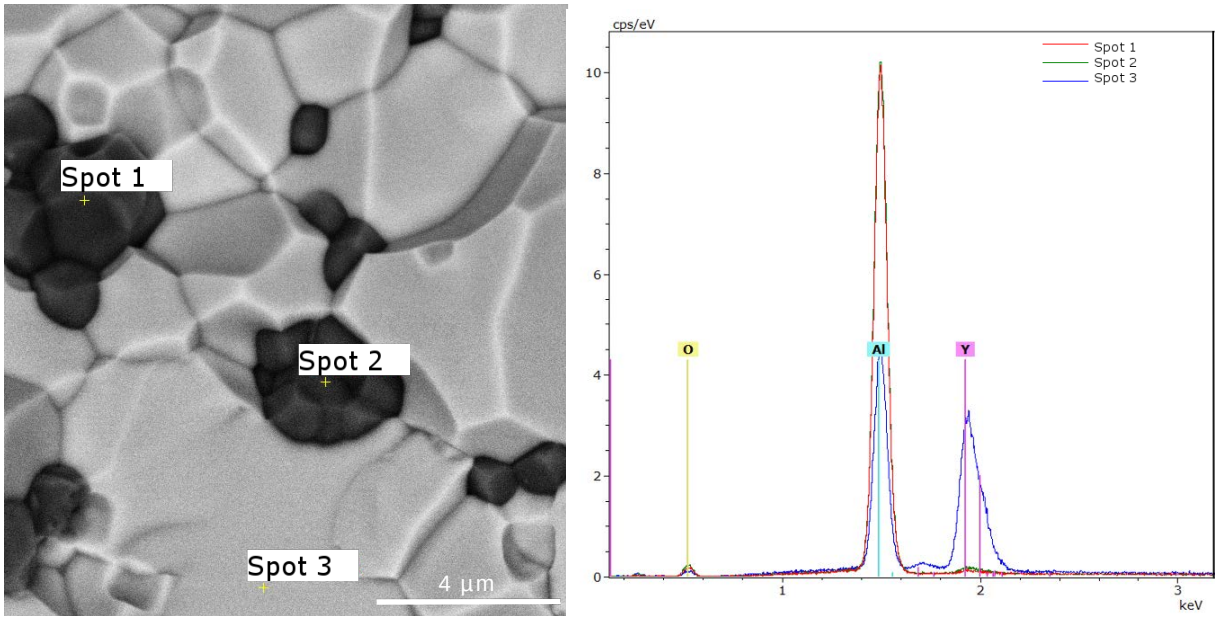

Figure II.12: EDX analysis of the HCl-treated sample after sintering.

Secondly, although YAG and YAP were the only phases detected by XRD on the sintered specimen of powder treated in NaOH condition (Fig. II.10), EDX analysis revealed the presence of Na in the specimen after sintering (Fig. II.13). Na pollution was retained inside the powder and induced an opaque sample (Fig. II.14).

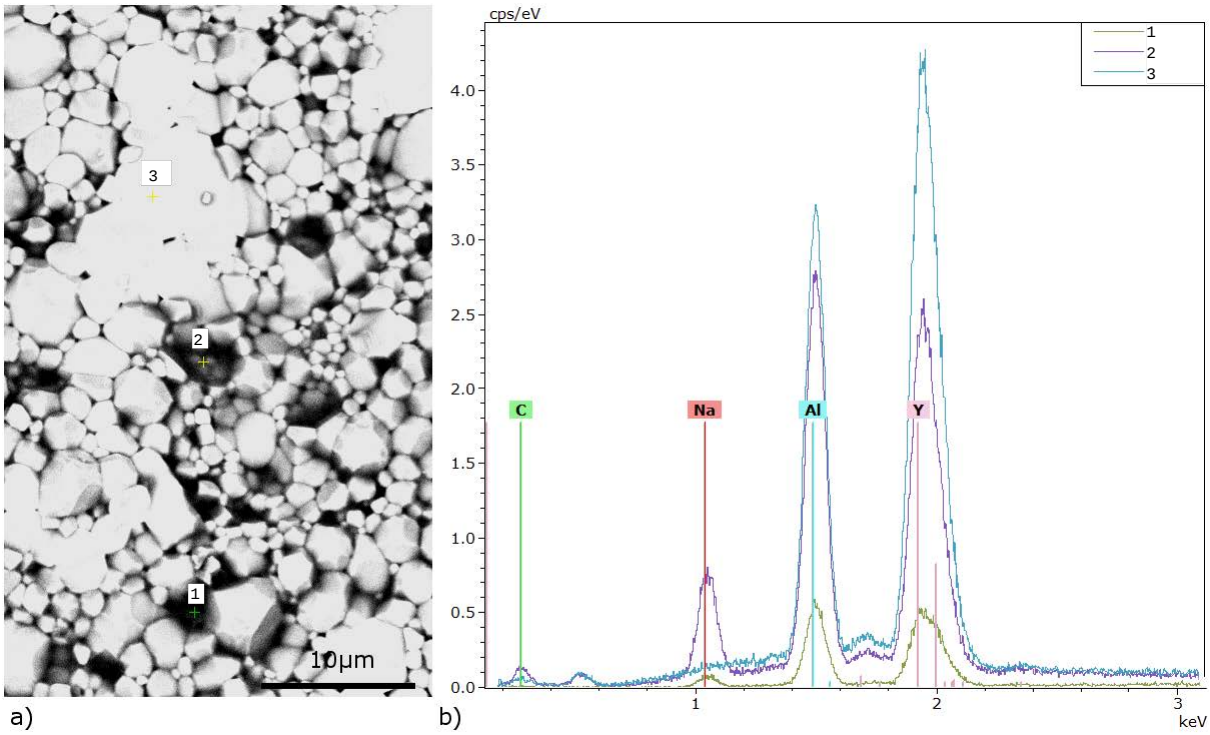

Figure II.13: EDX analysis of the NaOH treated sample after sintering. a) SEM picture of the sample fracture b) EDX measurements.

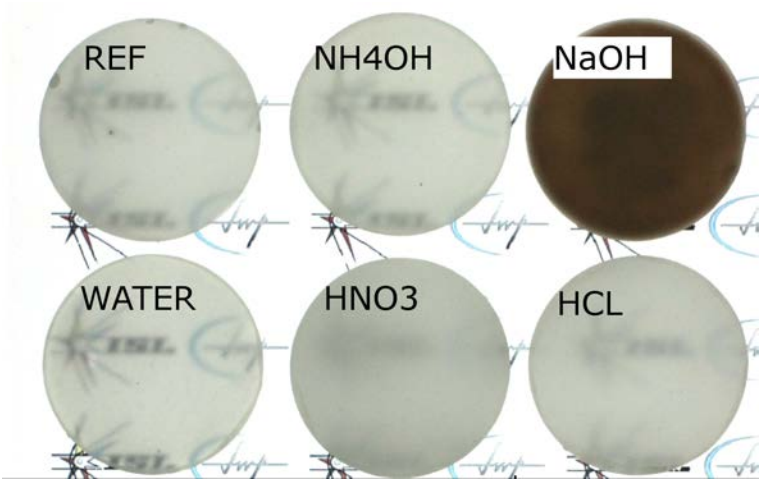

Figure II.14: Sintered specimens obtained with chemically treated powders. Diameter: 30mm. Thickness: 2.7 mm.

Only the sample obtained from powder washed with water had an improved optical quality (Fig. II.14) (+13.2% @ 3000 nm), as confirmed by the ILT measurements (Fig. II.15). This result can be explained by the role of water as a cleaner. Deionized water could be have a slightly acid pH due to reaction with carbon dioxide contained in the atmosphere which could favour the elimination of sulfur. Further investigations on pH of cleaning water have to be done to confirm this hypothesis

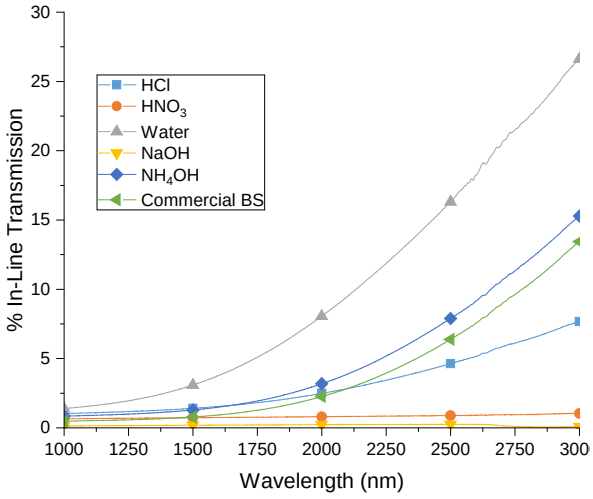

Figure II.15: In-Line Transmission of YAG SPS after chemical treatment.

Moreover, fracture observation of this water-treated specimen was free of defect with a homogeneous grain size and its XRD pattern presented only YAG phase. The water treatment did not induce important sulfur elimination during the washing itself (Table II.3), but this treatment enhanced the behavior of the obtained powder during compaction and/or sintering. The flowability of powders might have been improved by the treatment leading to a more homogeneous and denser green body.

In addition to the defects mentioned above (presence of YAP in the sintered ceramics after basic solution treatments, Y/Al ratio modification after acidic solution treatments and sodium impurity when using NaOH), it has to be mentioned that other residual secondary phases could be present in the sintered samples although these phases were not detected by XRD nor seen by SEM. Excess of yttria could induce precipitation of YAP phase between YAG grains while an excess of alumina could lead to precipitation of Al_2O_3 [120, 185] and XRD cannot detect yttria and alumina below 2 mol% and 1 mol% respectively [189]. More recently a study of Liu revealed the limit of XRD detection was 1.3 mol% for Y_2O_3 and 0.7 mol% for Al_2O_3 [120]. Even a few tenths of a percent of these phases can drastically impact the optical quality of ceramics [190, 191]. Consequently, a particular attention has to be paid to the modification of the Y/Al ratio and the formation of secondary phases when a chemical treatment is applied to a powder.

3.2. Y/Al ratio adjustment

SEM observations of the BY and yttria powders indicated agglomerates of particles around 90 µm and 144 µm respectively (Fig. II.16). The average particle size was estimated at around 650 nm for the BY powder due to two populations of particles: the first around 1 µm composed of hard agglomerates visible in Fig. II.16 and the second population around 0.1 to 0.3 µm. Yttria particle size was estimated at 85 nm of length. XRD analysis of BY powder exhibited the presence of YAG as the main phase and traces of YAP and Al_2O_3 phases (Fig. II.16 -c). Yttria was the only phase detected in the Yttria commercial powder (Fig. II.16-d).

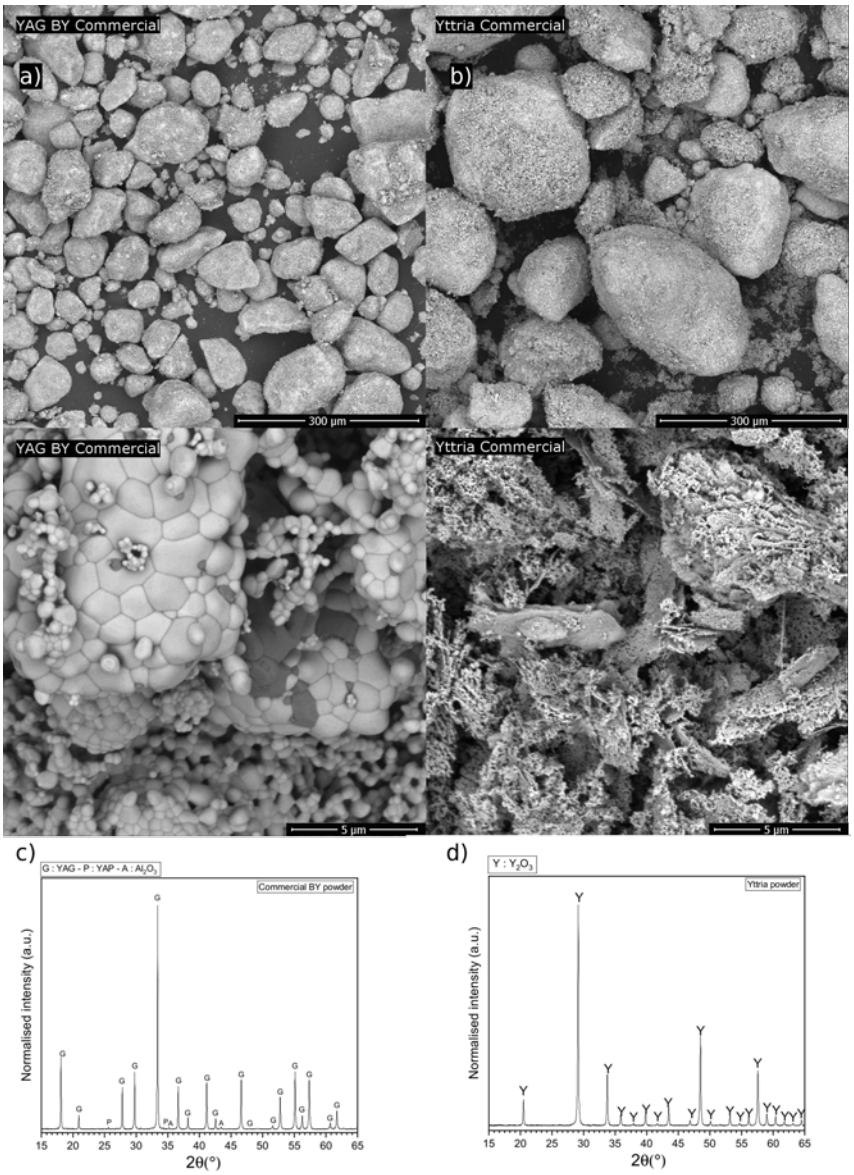

Figure II.16: SEM observation of the BY (a) and yttria (b) powders and their X Ray Diffraction patterns (c and d).

Fig. II.17 shows pictures of YAG ceramics with various Y/Al ratios sintered at 1450 ° C

by SPS. All fully dense samples were mirror polished on both sides. Sintered specimens were named A to F corresponding to the respective ratios 0.568, 0.580, 0.590, 0.600, 0.610, 0.630. Specimen A was the ceramic obtained from the unmodified BY powder with the ratio of 0.568. XRD allowed to follow the evolution of secondary phase quantities in the sintered samples (Fig. II.18). A focus on some particular diffraction peaks in the 33-45 ° C region is given as SI (Fig. C.1).

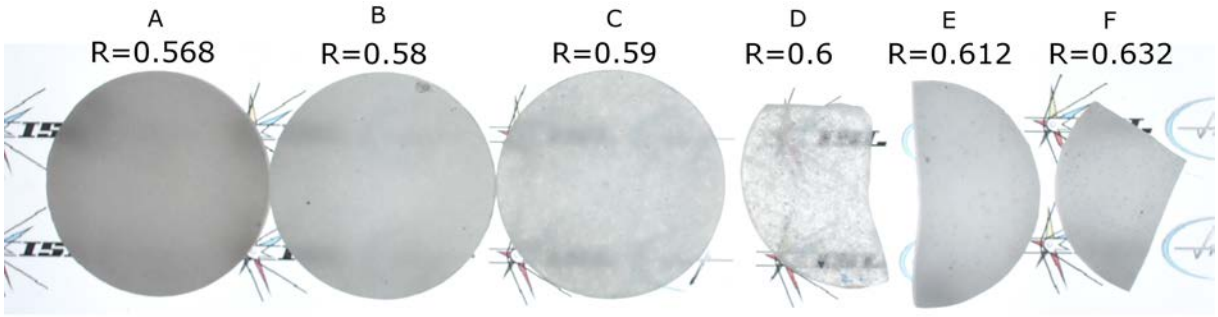

Figure II.17: Sintered specimens obtained after optimized SPS cycle with different amounts of Y_2O_3 added to the BY powder. (Ratios were calculated starting from the measured Y/Al ratio of the BY powder and the amount of yttria added).

Sample A showed the presence of YAG and a very small amount of alumina (Fig. II.18). Fracture of sample A presented a heterogeneous microstructure composed of two populations of grains: the majority was composed of YAG grains and a small population of black micrograins embedded in YAG grains (Fig. II.19). Thorough observations of the specimen by EDX revealed a high concentration of aluminum in black grains (Fig. II.20). Same behavior was reported for Al_2O_3-excess YAG ceramics: alumina micrograins were formed in the YAG microstructure due to the low solubility of Al_2O_3 in YAG ($\sim 0.2\%$) [120, 189].

As the Y/Al ratio got closer to the stoichiometry, B, C and D ceramics were composed of YAG exclusively, according to XRD results. However, some Al-rich grains were still visible in samples B and C, as shown on Fig.II.19 for sample C. For the theoretical stoichiometric Y/Al ratio (sample D), the microstructure was homogeneous without presence of secondary phase in SEM and XRD observations. The optical observation of ceramic D (Fig. II.17) though indicated the presence of opaque areas probably corresponding to secondary phases in very small quantities, although they were not detected by XRD nor visible in SEM pictures.

The two last specimens E and F, with Y/Al ratio higher than 0.6, contained YAG and YAP as a minor phase (Fig.II.18). According to results obtained by Liu *et al.*, excess of yttria leads to a local precipitation of YAP phase when the excess is higher than 1.7 mol% which must have been the case for sample E (2 mol% of yttria excess) and F [120, 185]. Yet, SEM revealed an homogeneous microstructure for ceramics E and F (Fig. II.19). After a second analysis of sample E by EDX, larger grains correspond to the YAP phase and have small spherical porosities at grain boundaries (Fig. II.21).

When yttria was added into the BY powder, the proportion of Al_2O_3 micrograins decreased as shown for samples B and C. Yttria reacted with alumina to form YAG, as revealed by XRD scans of B, C and D ceramics (Fig. II.18).When reaching the theoretical Y/Al=0.6 ratio, no alumina was detected anymore and sample D seemed to contain only

pure YAG. It was thus the sample with the best optical properties (Fig. II.17). As the Y/Al ratio increased above 0.6, other secondary phases, such as YAP were formed, which led to worse optical properties (samples E and F in Fig. II.18). Indeed for Y/Al ratios higher than 0.6, yttria and YAG can react to form the Y-rich phase YAP (Y/Al=1 in YAP) [189, 190]. Whether the secondary phase was alumina (samples A, B and C) or YAP (samples E and F), the difference of refractive index between alumina or YAP and YAG induced the formation of scattering sites [185] that caused the loss of transparency in these samples.

Even with the stoichiometric Y/Al ratio of YAG, sample D was not fully transparent, as shown in Fig. II.17. Some secondary phases must have been present in this sample, but in amounts so low that they were not detectable neither by XRD nor SEM. As the BY powder was composed of multiple phases (YAG, YAP, Al_2O_3), if added yttria was not homogeneously dispersed, it may have reacted not only with alumina, but also with other phases. When yttria is locally in excess, it can react to form antisite defects and when in large excess it can induce precipitation of YAP when it reacts with YAG [189, 190], which of course causes a loss of transparency. To improve reaction between alumina contained in BY powder and the added yttria, a thermal pretreatment of the powder mixture with continuous stirring could be useful. A second solution would be to add an extra holding step at high temperature during SPS sintering to help the Al^{3+} ions diffusion through the bulk material and enhance their reaction with yttria.

Anyway it is necessary to have a homogeneous mixture of the two powders (yttria and BY powder) to enhance reactions between alumina and yttria and avoid side reactions leading to other secondary phases. A grinding of the BY powder mixed with yttria could be interesting not only to reduce the size of agglomerates and maybe obtain smaller particles, which would increase powder reactivity, but also for homogenization of the mixture. The challenge would be to have an efficient communition without adding more impurities to the mixture.

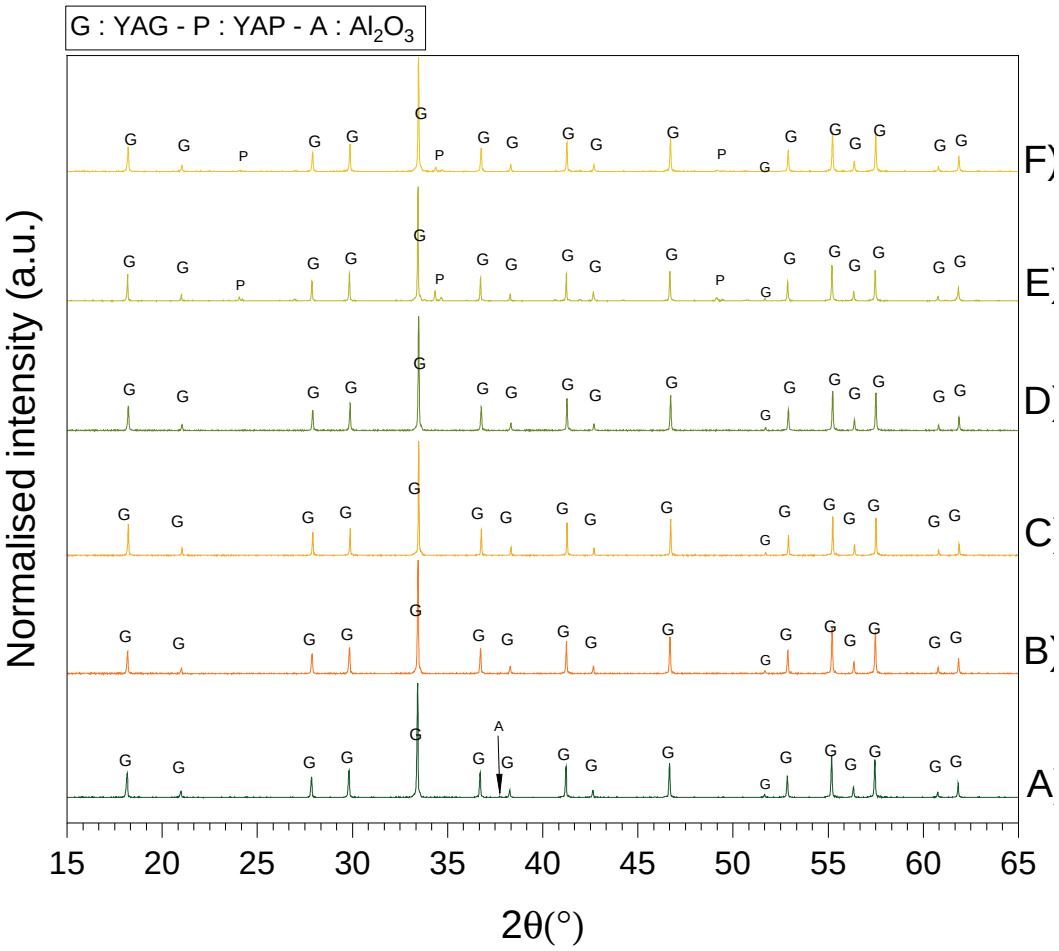

Figure II.18: XRD patterns of A, B, C, D, E and F samples.

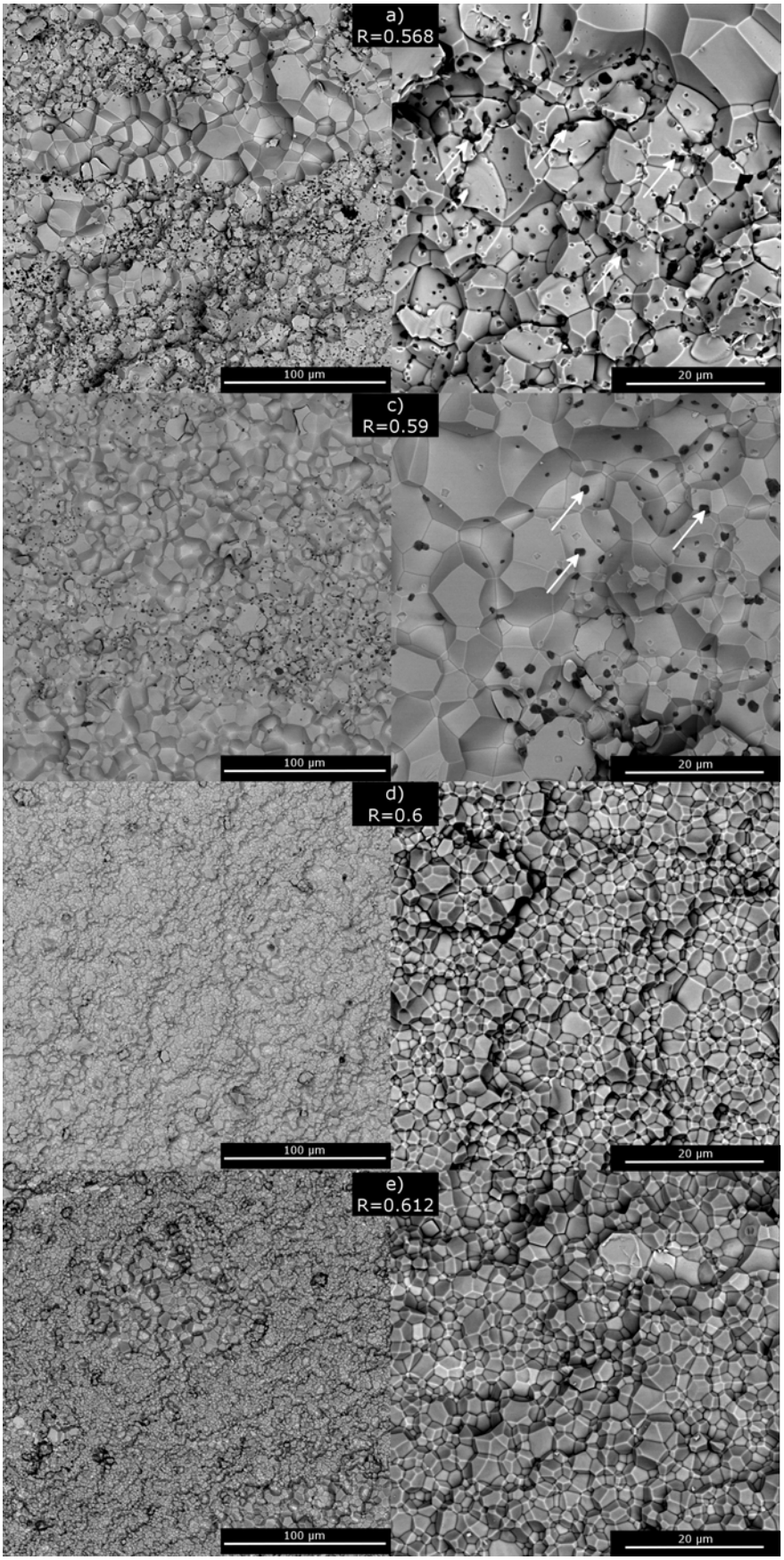

Figure II.19: SEM fracture surface of A,C,D and E of sintered samples at two magnifications. Inter-granular fracture in all conditions. Arrows show areas of Al-rich phase embedded in YAG grain.

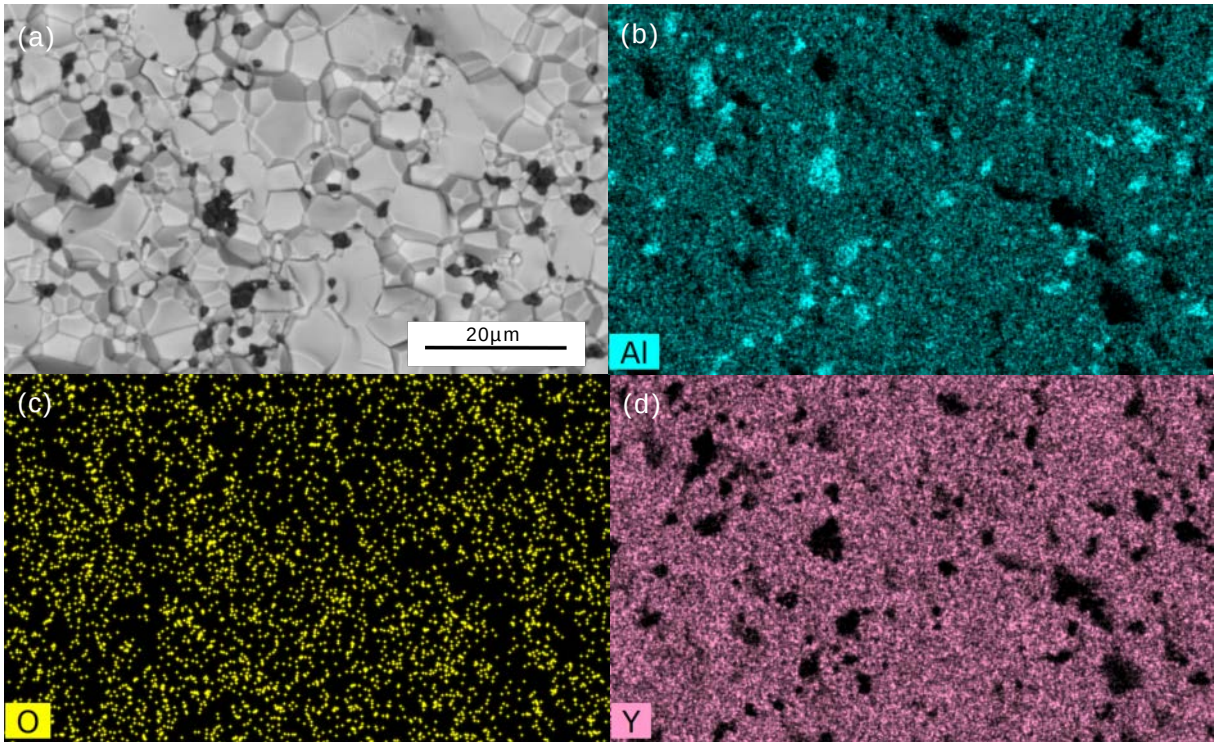

Figure II.20: EDX measurement of the sample A fracture. (a) SEM image (b) Al (c) O (d) Y element map.

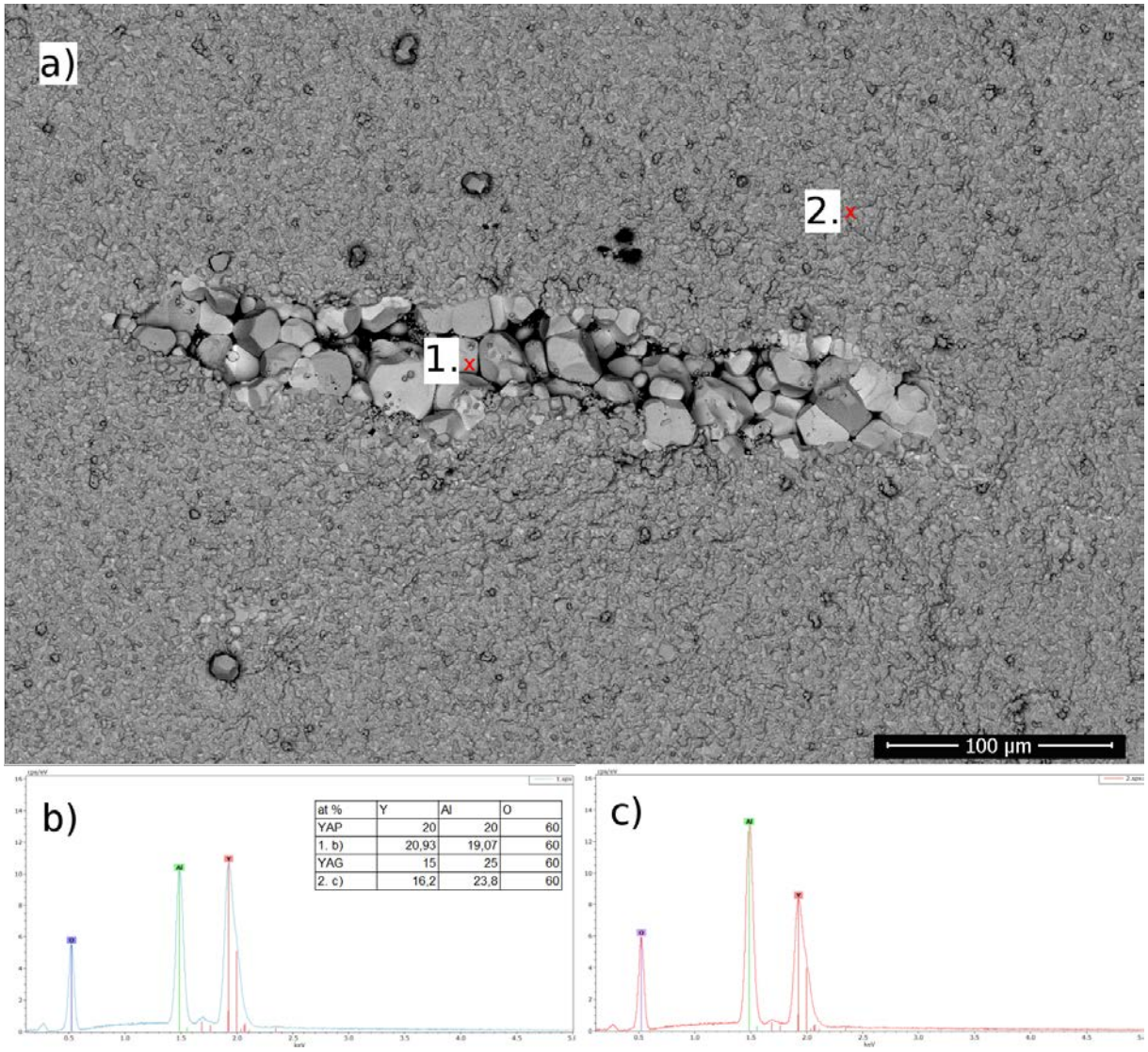

at %	Y	Al	O
YAP	20	20	60
1. b)	20,93	19,07	60
YAG	15	25	60
2. c)	16,2	23,8	60

Figure II.21: a) SEM fracture observation of the sample E and EDX profiles for the YAP (b) and YAG (c) grains. Table summarizes atomic percentages obtained from EDX measures for yttrium, aluminum and oxygen elements.

4. Conclusion

The aim of this study was to understand the impact of impurities and Y/Al ratio in industrial experimental YAG powders on transparency of ceramics prepared with these powders. In the case of sulfur removal, two kinds of processes were tested: i) thermal treatments at various temperatures (from 950 to 1200 °C) under air or vacuum, and ii) washing with different acidic and basic solutions. Thermal treatments were efficient to remove sulfur but caused aggregation which led to lower green densities and prevented total elimination of the porosity during sintering. Among various solutions used for chemical treatments (deionized water or NaOH, NH_4OH, HCl and HNO_3 solutions), the best results were obtained for the water treatment. Although the sulfur content was not significantly reduced (583 ppm instead of 662 ppm in the untreated powder), optical quality was clearly enhanced. Further investigations will be necessary to understand the impact of water on powder properties (compaction behavior among others) and if water plays a role during sintering.

Concerning Y/Al ratio adjustment, addition of yttria to a industrial experimental YAG powder with an yttrium deficit proved effective. The best optical quality was reached for the sample with a theoretical Y/Al ratio corresponding to pure stoichiometric YAG. This part of the study showed that homogeneity of the yttria and BY powder mixture has to be optimized to avoid secondary phases. This work showed that improvement of powder properties is difficult, as a treatment used to correct one defect may often lead to apparition of other defects. For example, use of a sodium hydroxide solution for washing allowed strongly reducing the sulfur impurity content, but induced pollution by sodium that could be deleterious to the transparency of the final ceramic. From all the results of this work, the parameters that seemed to need particular attention were Y/Al ratio, as secondary phases were formed even for slight deviations from stoichiometry, and compaction behavior of the powders, as low flowability (due to agglomeration for example) led to low green densities and thus to remaining porosity in the obtained ceramics. Scattering sites like secondary phases and pores had much more influence on optical properties than sulfur impurities.

5. Complementary work

When adjusting the Y/Al ratio by addition of Y_2O_3 to the BY YAG powder, even in the case of stoichiometric Y/Al= 0.6 ratio, the sample was not fully transparent (Fig.II.17, part 3.2). Some opaque areas were observed probably corresponding to secondary phases in very small quantities, as they were not detectable by XRD. To avoid these heterogeneities in the final ceramic, it is necessary to improve homogeneity of the initial powder mixture. Two approaches were investigated to improve homogeneity of the YAG-yttria mixtures. As the best optical properties of the previous study were obtained for Y/Al ratios 0.590 and 0.600, these two conditions were selected. The first approach involved a longer SPS step to help Solid State Reactive Sintering Reactions (SSRS) occurring at high temperature. The second way consisted in calcining the powder before SPS treatment. In both cases, the aim was to enhance reaction between added yttria and the alumina secondary phase.

5.1. Longer SPS holding time

A longer holding time during SPS treatment, 4h at 1450 °C instead of 2h, was applied to let more time for the diffusion of Al^{3+} and Y^{3+} ions, so as to enhance reactions between alumina and yttria and thus obtain a homogeneous transparency of the samples. Same ratios as samples C and D (0.590 and 0.600, Fig.II.17, part 3.2) were used to get a comparative study of microstructure and XRD results with 2 and 4 hours of holding time.

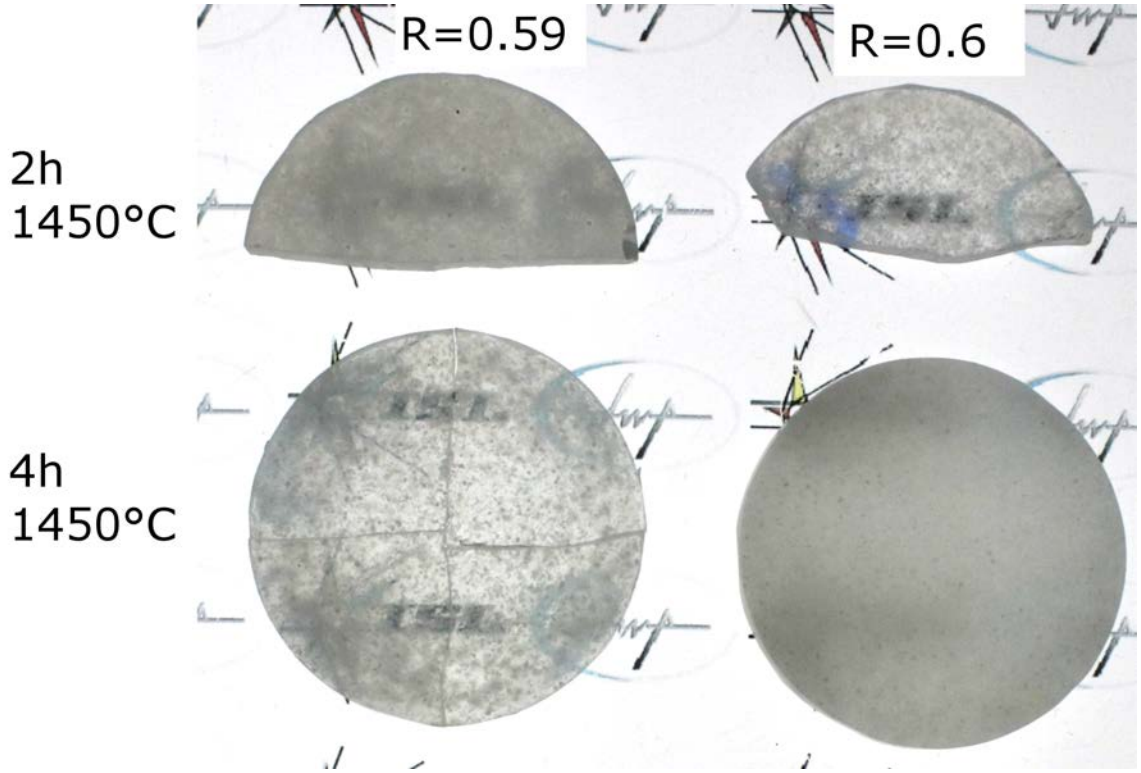

Figure II.22: Visual comparison between polished sample sintered during 2 and 4 hours by SPS.

After SPS sintering, for the 0.590 ratio, the extra holding time (4h) significantly im-

proved the transparency compared to the sample with shorter time at 1450 ° C (Fig. II.22). The 4h sintered sample with Y/Al = 0.590 seemed to be even more transparent than the 2h sintered stoichiometric sample (Y/Al = 0.600), even though this latter sample had the highest transparency of the previous series (Fig. II.17, part 3.2).

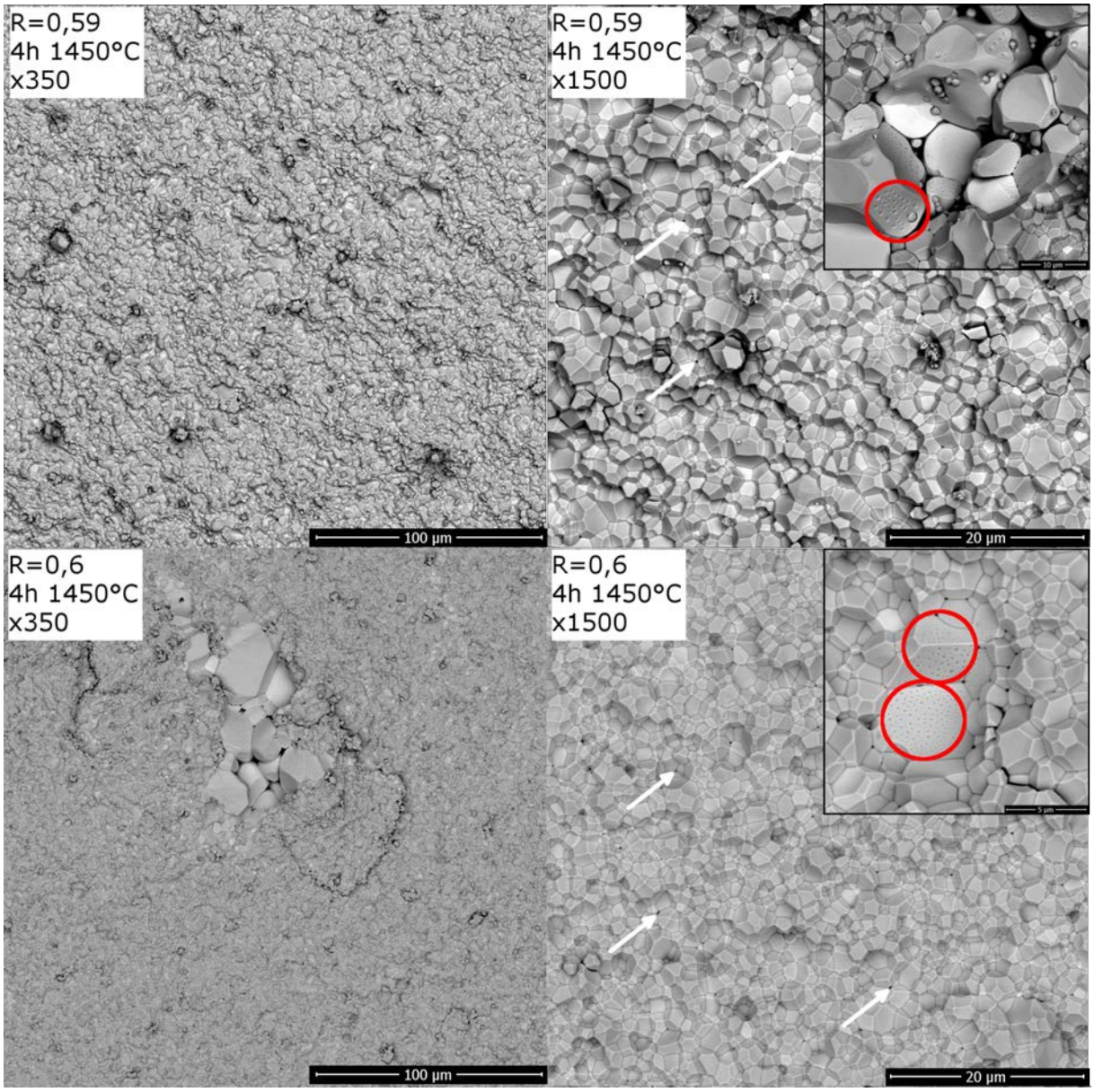

Figure II.23: SEM fracture observations of samples sintered at 1450 ° C during 4h. White arrows show the porosity at triple points. Red circles indicate small spherical pores on YAG grain surfaces in the inset.

SEM observations of these samples showed inter-granular fractures for both Y/Al ratios (Fig. II.23). For the 0.590 ratio, SEM analyses revealed a homogeneous microstructure in the sample, but little porosity was found at triple points (highlighted by white arrows in Fig. II.23). Nevertheless no black micrograins of Al_2O_3 were observed in the microstructure in these conditions whereas they were visible in the sample sintered for 2h at 1450 ° C (Fig. II.19). On the one hand, the additional time helped to eliminate Al_2O_3 micrograins but on the other hand porosity was found in the microstructure. Considering the optical

properties of both samples with Y/Al = 0.590, porosity seemed to be much less deleterious than the alumina secondary phase.

Surprisingly, in the case of the 0.600 ratio, the sample with 4h of holding time was more opaque than the sample sintered for 2h. SEM fracture observation indicated a heterogeneous microstructure with large grains of approximately 20 µm corresponding to formation of YAP phase as observed for the previous sample E in Fig. II.21.

For both Y/Al ratios, in samples sintered for 4h, very small spherical marks were present on YAP grains, as can be seen in the insets on Fig. II.23. These small spherical pores results to the formation of YAP phase (identical to the sample E Fig. II.19)

These results were also observed in literature when 5%wt of LiF was mixed with a powder before sintering by SPS [67]. SEM observations revealed the same characteristics as observed here. Due to a bad distribution of LiF inside the YAG powder, globules are formed on the grain surface that were trapped between grains [67]. Moreover, YF_3 is formed when the LiF is trapped into the microstructure resulting to deviate the stoichiometry and form locally YAP grain.
In summary, formation of large YAP grains are mainly due to a deviation of stoichiometry as showed by Liu *et al.* [120]. Nevertheless, in the case of the Y/Al ratio is respected, LiF disturb locally the stoichiometry, especially when the sintering aid is remained into the microstructure. This forms opaque area in transparent samples as observed by Katz *et al.* [67].

Concerning the optical quality, as already mentioned, increase of holding time led to better results for Y/Al = 0.590 but worse results for Y/Al = 0.600. According to the Y/Al ratio, the optimal holding time seemed to vary, indicating a modification of the mixture reactivity when changing the yttria-YAG powder ratio.

1. Pre-calcination of the powder mixture

To promote reaction between added yttria and alumina present as secondary phase in BY powder and avoid formation of other secondary phases, pre-calcination of the powder mixture was performed. The mixed powder was poured into a crucible and heated up to 900 or 1100 °C during 1h. Before sintering, XRD (Fig. II.24), showed the presence of YAG as the major phase, and that yttria and YAP were still detectable after calcination. As alumina was not detectable anymore, it seems that pre-calcination allowed reaction between yttria and alumina but was not sufficient to have complete elimination of YAP.

All calcined powders led to samples that were completely opaque after SPS sintering (Fig. II.25).

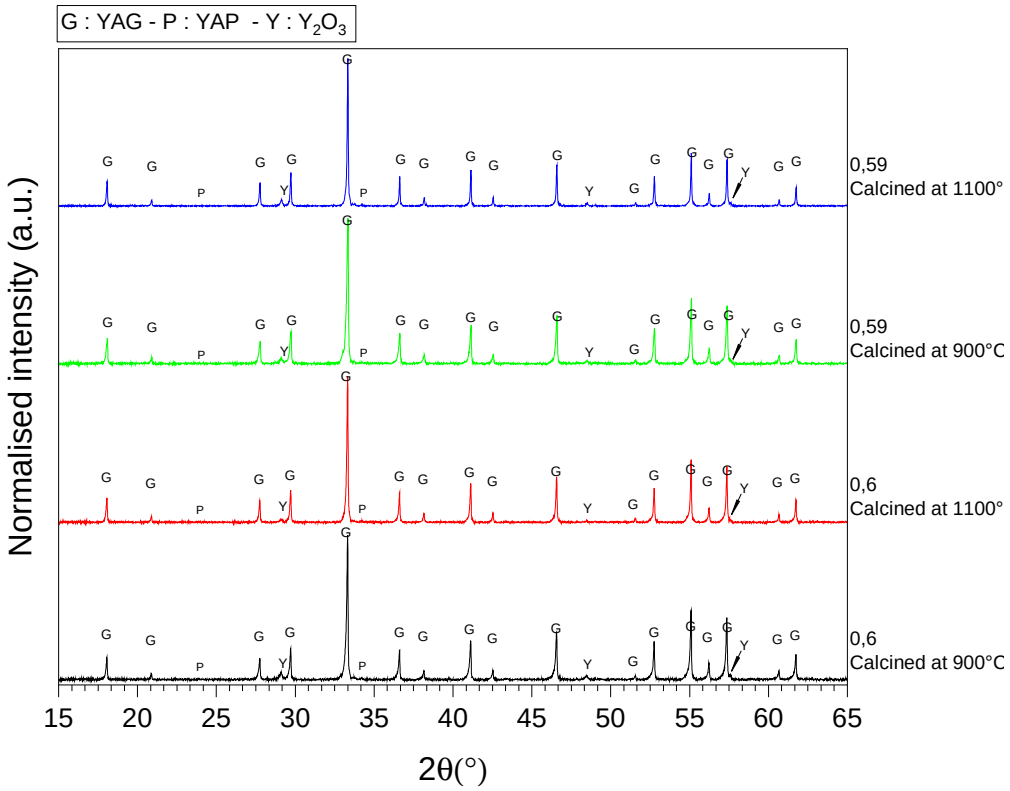

Figure II.24: X Ray Diffraction patterns of powders with various Y/Al ratios (0.590 and 0.600) calcined at 900 ° C and 1100 ° C (1 h).

For the 0.590 ratio, sample prepared with the powder pre-calcined at 900 ° C had a quite homogeneous microstructure (Fig. II.26 and II.27). Some black areas were visible but were mainly composed of carbon due to pollution from the SPS graphite tools, which was confirmed by EDX. At higher magnification, porosity was observed at triple points. For the 0.600 ratio, the powder pre-calcined at 900 ° C led to a sintered ceramic with a microstructure different from the previous sample. At low magnification, two sizes of grain were visible. The first population was composed of small grains ($\sim$ 1-2 µm) and the second was constituted of larger grains ($\sim$ 10-30 µm). A very large pore surrounded by these larger grains could be observed. On large grains, black dots were visible at the surface of grains and indicated the presence of the YAP phase as observed previously. At higher magnification, smaller pores were detected at triple points (inset on Fig. II.27).

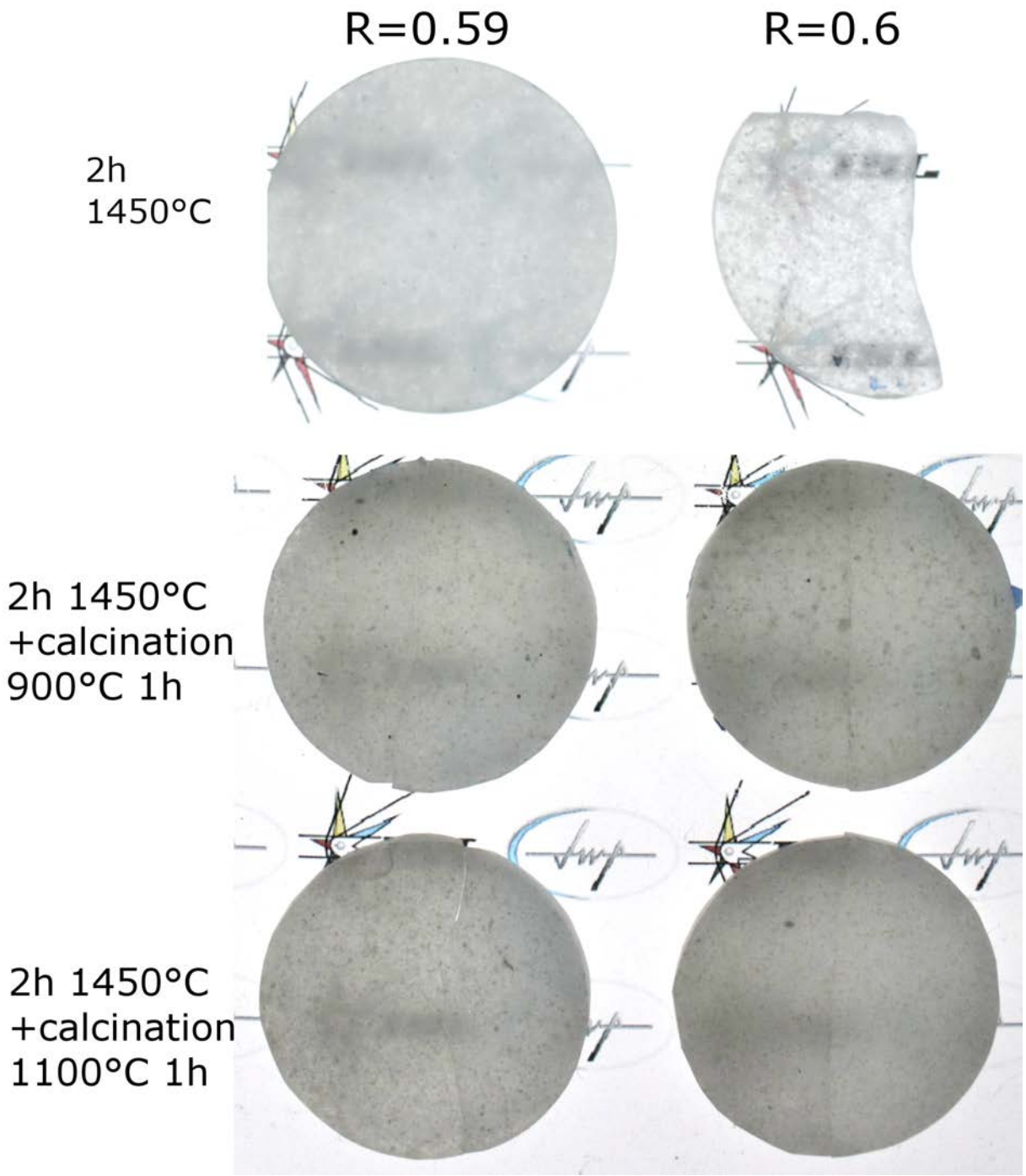

Figure II.25: SPS sintered samples of calcined powder (900 and 1100 ° C)

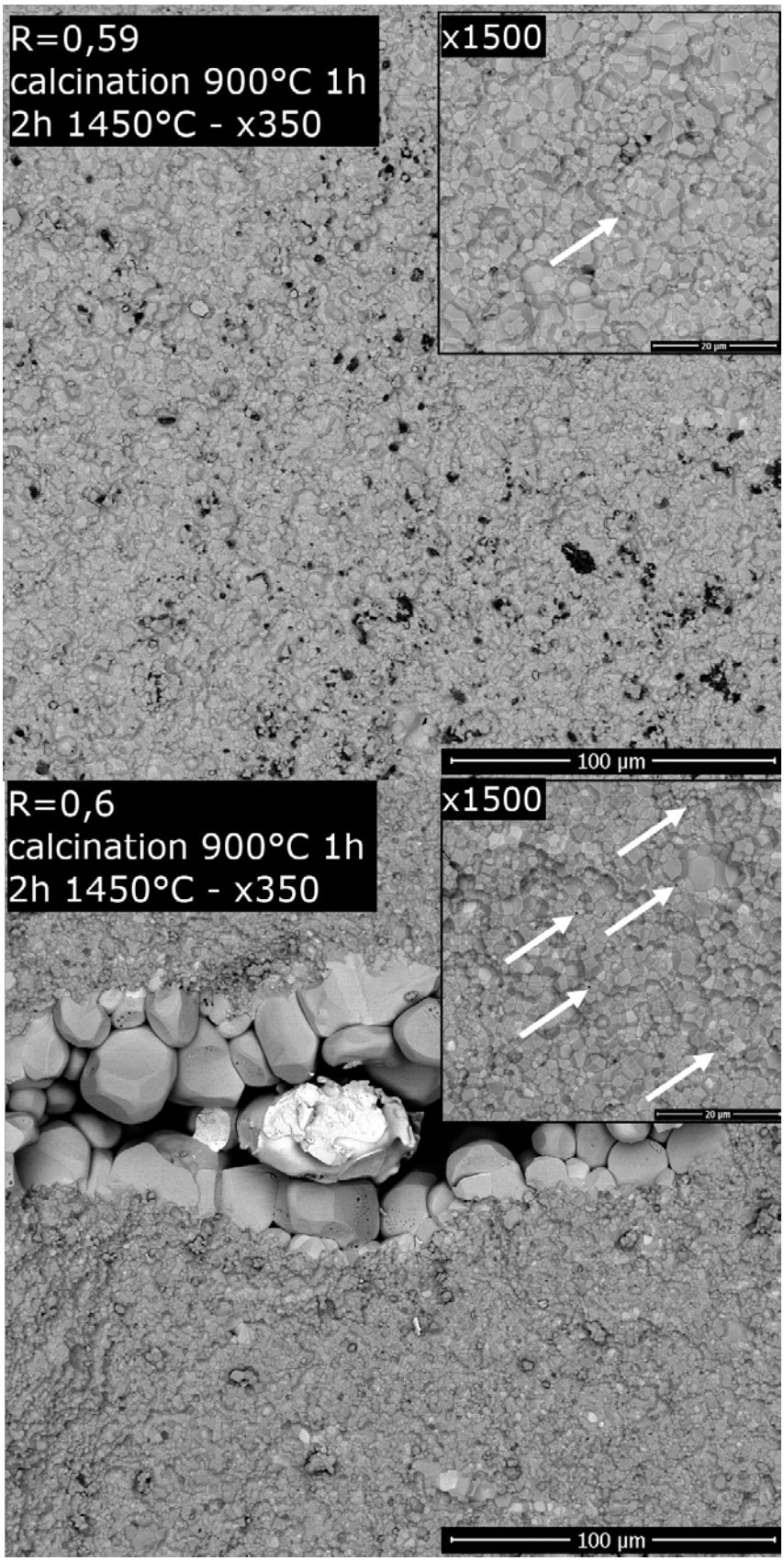

Figure II.26: SEM fracture observations of SPS sintered samples prepared with powders pre-calcined at 900 ˚C for 1h (top: Y/Al = 0.590, bottom: Y/Al = 0.600). White arrows indicate pores.

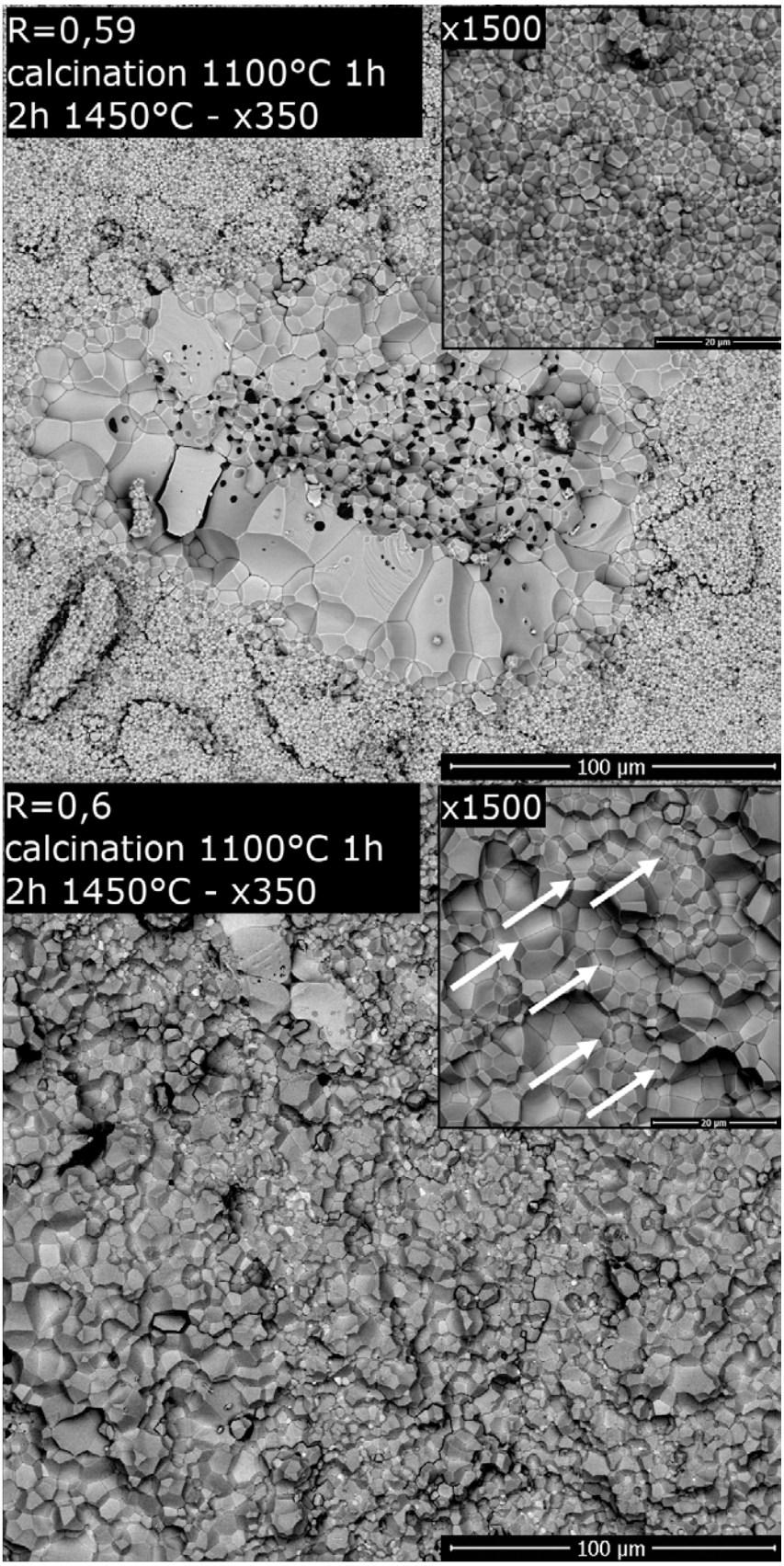

Figure II.27: SEM fracture observations of SPS sintered samples prepared with powders pre-calcined at 1100 °C for 1h (top: Y/Al = 0.590, bottom: Y/Al = 0.600). White arrows indicate pores.

For the 0.590 ratio the sample prepared with the powder pre-calcined at 1100 °C presented a heterogeneous microstructure (Fig. II.27). Three areas could be seen: one composed of micrograins of an aluminum rich phase, the second built of larger YAG grains (∼ 10-30 µm) and finally the last part made of smaller YAG grains (∼ 1-3 µm) that were more visible with higher magnification (inset on Fig. II.27). Al-rich phase was confirmed by EDX (not shown here).

For the 0.6 ratio, sintered sample of powder calcined at 1100 °C was composed of a more homogeneous microstructure. As observed before with higher magnification, small pores were still present in the sample.

In all cases of pre-calcination (at 900 or 1100 °C, for Y/Al = 0.590 or 0.600), optical results were worse than for the uncalcined YAG-yttria mixtures. As observed on SEM pictures, small pores were always present in the samples, meaning a lower reactivity of all powders. This could clearly be explained by agglomeration and grain coarsening occurring during the thermal pretreatment. During this step, larger grains were formed with the increase of inter-agglomerate porosity. This would be in agreement with results of the thermal treatments to remove sulfur shown in part 3.1.1. So the benefit of partial reactions between yttria and alumina was overcome by the deleterious effect of agglomeration and grain coarsening.

2. Conclusion about complementary work

Obtaining transparency by reaction between yttria and YAG BY powders is a quite difficult task. It involves the comprehension of all mechanisms that take place during sintering. All parameters have to be taken into account: the presence of multiple phases, their proportions, particle size and presence of agglomerates. Additionally, sintering parameters also have to be controlled to apply adapted heating rate and pressure to obtain fully dense samples.

By correcting the Y/Al ratio in a industrial experimental powder, it was possible to greatly enhance transparency, but the sample showed some opaque areas, indicating a heterogeneous microstructure. To improve homogeneity, complementary tests were performed. They consisted in modifying the thermal treatment of powders, either by calcining the yttria-YAG powder mixture before sintering or by increasing the SPS sintering dwell time. Both approaches were not very efficient. The pre-calcination induced a lower reactivity of the powder mixture, most likely linked to agglomeration and coarsening of grains. A longer holding time at sintering temperature led to an abnormal grain growth for the stoichiometric mixture (even though for Y/Al = 0.590, transparency was better for a longer dwell time).

Further experiments are still necessary to better understand the effect of calcination on the powder properties and also to optimize the sintering conditions according to powder properties. Along with this study of thermal treatments, it seems of primary importance to investigate the influence of mixing procedure (Turbula®, dry mixing, ultrasonication of suspensions...) on the homogeneity of the obtained powder. Colloidal processing could be the next step to improve mix between the alumina and BY powders.

Chapter III

Development of YAG ceramics by Solid State Reactive Sintering (SSRS)

Preface

In the previous chapter, investigations on YAG experimental industrial powder revealed the difficulty to obtain transparent ceramics after stoichiometry correction and sulfur removing treatment. Fabrication of highly transparent YAG ceramics is possible by the use of yttria and alumina powders which can come from many sources. The following chapter, presented as an article, is based on fabrication of YAG ceramics starting from Al_2O_3 and Y_2O_3. The objective of this work is to obtain a simple procedure to mix Al_2O_3 and Y_2O_3 together with a good homogeneity to promote solid state reactions during calcination of the powder and the sintering of green bodies.

Development of YAG ceramics by Solid State Reactive Sintering (SSRS)

Abstract

Obtaining YAG transparent ceramics from reactive sintering between alumina and yttria powders involves an homogeneous mixing between species to optimize the solid state reaction. Several simple and fast methods to mix Al_2O_3 and Y_2O_3 were investigated to obtain homogeneous mixing and YAG phase without use of ball-milling, source of contamination. The effect of the starting powder pre-deagglomeration, the solvent mixture, three different mixing methods and three drying steps, were investigated. To characterize these different mixtures, yield, stoichiometry measurement, relative density and EDX element map on mixed powders were carried out. For the best mixing conditions, calcination and thermal treatments in air were applied resulting to obtain 100% of YAG phase at 1500 °C for 20h for the powder and at 1500 °C for 5h for the corresponding compacted specimen. From these best mixing conditions, powder mixtures were compacted and sintered in conventional sintering in air and in high vacuum furnace. Afterwards, grain size and relative density were measured to plot a sintering map depending on sintering conditions.

1. Introduction

Er^{3+} : $Y_3Al_5O_{12}$ ceramics have been highly studied to replace Er^{3+}:YAG single crystal, as gain medium, in solid state laser. Ceramics have been considered as replacement thanks to their better thermo-mechanical properties, the possibility to have a high doping concentration and create a doping gradient, which reduces internal stresses. The use of ceramics with a doping profile allowed to increase the life time of the laser as well as the output power due to a better heat distribution inside the laser cavity. [19, 47, 192, 193]. Polycrystalline ceramics are commonly fabricated by ceramic processing [45, 121, 170]. However for laser application, full density with residual porosity under 18 ppm is at least required [71]. To reduce the formation of residual porosity high green density and adapted sintering parameters are required. Pressure assisted sintering methods such as Hot Pressing or Spark Plasma Sintering have proven their efficiency to obtain transparent ceramics.

Moreover, to be transparent, ceramics have to be free of any impurities or secondary phase, especially when used as gain medium [116].

In literature, several routes exist to fabricate YAG polycrystalline ceramics from precursors: solid state reactions (SSR) method and wet chemical routes (precipitation/co-precipitation, liquid evaporation, gel methods and non aqueous reactions) [75]. The SSR method is often used in calcination step after powder synthesis by wet-chemical route or during the sintering when the calcination step is skipped. It therefore conducts to a Solid State Reactive Sintering (SSRS) [194–196]. The main advantage of reactive sintering is to produce large and crack-free ceramics due to utilization of coarser powder than used by wet chemical approach [159].

YAG powder obtained by wet-chemical route has the advantage to allow a high control of powder characteristics during the procedure and YAG nanopowder can be obtained in a cost effective way with a high homogeneity and a low temperature of crystallization [141, 197, 198]. Nevertheless, wet chemical synthesis needs several fabrication steps and several parameters to control (pH, temperature, ...), which makes the process complex.

Ceramic powders can be provided by suppliers but the cost of the powder highly depends on the synthesis route. For example, highly pure nanosized powder synthesized

by flame spray pyrolysis is very expensive (>20 euros /g). On the contrary, less expensive powder can be provided by other suppliers with a high amount of sulfur impurity [116, 118, 121]. For instance, Goldstein *et al.* reported that in spinel powder obtained by derived sulfate route, a large amount of sulfur was detected which varies greatly from batch to batch and inside the same batch. The sulfur presence causes a yellowish tint of the sintered ceramic [199]. Villalobos *et al.* studied the absorption level of commercial powder after sintering and post treatment. They concluded that the absorption level above 21,000 ppm/cm in the 1-2 µm wavelength range is acceptable for sensor windows but is far too high for laser applications [118].

Alternatively, SSRS of oxide precursors can be performed in order to obtain transparent ceramics [120, 200]. Indeed a large number of studies show the possibility to fabricate highly transparent YAG ceramics by sintering alumina and yttria powder [120, 194, 195, 201]. For example, Kupp *et al.* have shown the possibility to synthesize highly transparent Er:YAG ceramics for laser application by tape casting using precursors powder mixed by ball milling method [112]. Oxide precursors offer the advantage of being cheaper and produced by a large number of suppliers.

In this article, we investigated the mixing of alumina and yttria powders, the influence of the different mixtures quality on the solid state reaction and the possibility to obtain YAG polycrystalline ceramics without help of sintering additives like LiF or SiO_2. Unlike Kupp *et al.*, no ball-milling was used, which reduces the process steps and moreover the potential contamination generated by overlong friction between alumina balls [202]. In this respect, simple methods such as ultrasonic and magnetic stirring were preferred to develop an accessible and fast method to mix yttria and alumina with a good homogeneity. As discussed above, a special attention was also be paid to the homogeneity of mixture, the stoichiometry, the yield, the compaction behavior and the phase evolution of powder mixtures as a function of temperature and time. Then, compacted powders obtained from best mixtures were studied by XRD, SEM and dilatometry to follow solid state reaction sintering and establish sintering trajectory.

2. Experimental

Commercially available yttria (47154, REO, <99.995% purity) and alumina (SMA6, 99.995% purity) powders were supplied by Alpha Aesar (USA) and Baikowski (France) respectively[1]. Yttria powder consists of particles of 50-70 nm (Fig. III.1-a), whereas alumina powder is composed by particles around 200 nm (Fig. III.1-b). X-Ray diffraction pattern of both powders (Fig. III.1-c) presents the pattern of the cubic phase of yttria powder and the alpha- phase for alumina powder, according to JCPDS 71-5970 and 01-0173.

[1] Technical data were provided in appendix D.

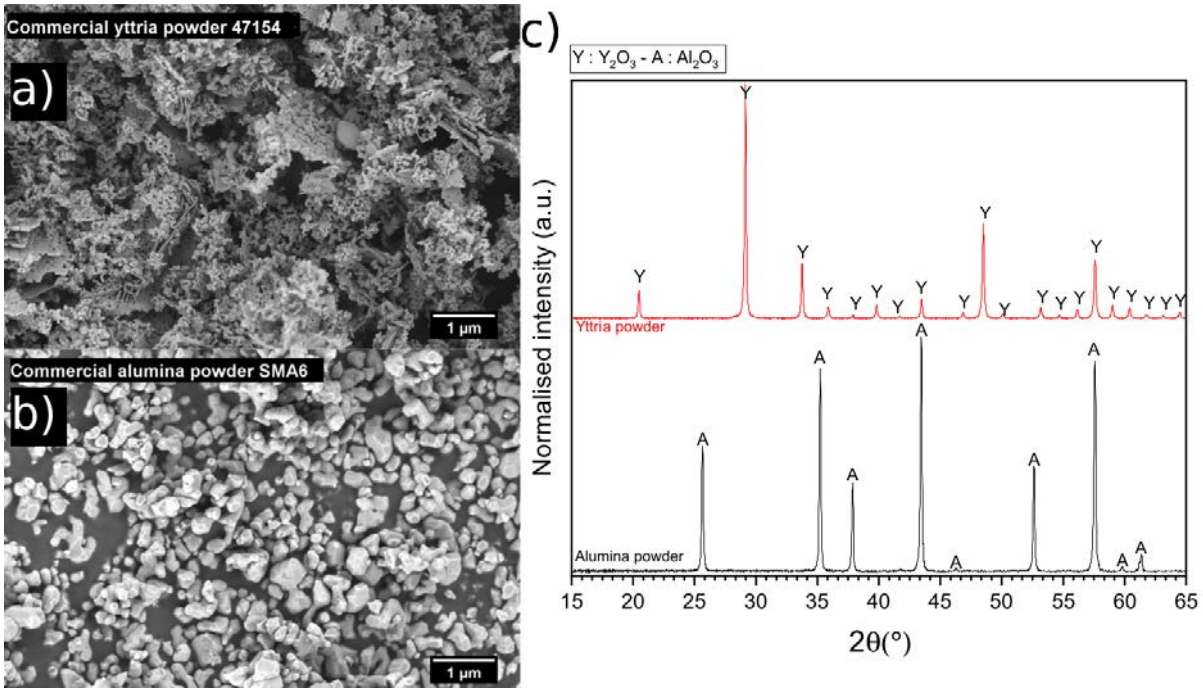

Figure III.1: a) SEM microstructure of commercial yttria and b) commercial alumina powder. c) X-Ray Diffraction of the yttria and alumina powder.

The powder was weighted according to the stoichiometric ratio R=Y/Al=0.6 and mixed together in either ethanol or 50:50 water/ethanol. The mixing was performed either by ultrasonic (US) or magnetic stirring (MS), the details of the studied mixtures are summarized in Table III.1. Optionally, an ultrasonic treatment was previously applied to deagglomerate the precursors powders before mixing together.

Condition n°	Solvent	Pre-deagglomeration	Mixing method	Drying method
1	Ethanol	Yes	Ultrasonic Prog 1	Oven
2				Freeze-drying
3				Rotary evaporator
4			Ultrasonic Prog 2	Oven
5				Freeze-drying
6				Rotary evaporator
7			Magnetic stirring	Oven
8				Freeze-drying
9				Rotary evaporator
10		No	Ultrasonic Prog 1	Oven
11				Freeze-drying
12				Rotary evaporator
13			Ultrasonic Prog 2	Oven
14				Freeze-drying
15				Rotary evaporator
16			Magnetic stirring	Oven
17				Freeze-drying
18				Rotary evaporator
19	Water / Ethanol (50/50)	Yes	Ultrasonic Prog 1	Oven
20				Freeze-drying
21				Rotary evaporator
22			Ultrasonic Prog 2	Oven
23				Freeze-drying
24				Rotary evaporator
25			Magnetic stirring	Oven
26				Freeze-drying
27				Rotary evaporator
28		No	Ultrasonic Prog 1	Oven
29				Freeze-drying
30				Rotary evaporator
31			Ultrasonic Prog 2	Oven
32				Freeze-drying
33				Rotary evaporator
34			Magnetic stirring	Oven
35				Freeze-drying
36				Rotary evaporator

Table III.1: Mixing conditions used in the current study.

A sonotrode (Bioblock Scientific, Vibracell 75042) was used to optionally deagglomerate the powder and for mixing. Thereby two sonotrode programs were chosen: 1) an ON/OFF ratio of 10 seconds /20 seconds which can be qualified as short one and the second longer 2) of an ON/OFF ratio of 20 seconds /30 seconds , while the power amplitude was 80% for both of them. The third process for mixing powder was the magnetic stirring (Fisher scientific FB 15002) at 500 rpm during 20 min at 30 °C in a glass-beaker. When precursors were deagglomerated, they were dried overnight at 80 °C in a beaker glass. Otherwise, mixtures were dried either in an oven during overnight at 80 °C (Memmert), by freeze-drying (Christ, Alpha 2-4 LD+) or by rotary evaporation (Heidolph Hei-VAP Value Digital). A manual ground was performed to homogenize the powder and break soft agglomerates formed by the drying. The powder mixtures were weighed and the yield was calculated from the mass of powder introduced at the beginning of the procedure to

estimate the losses induced by the various mixing and drying methods.

A reference sample was prepared to compare the influence of the various treatments between manual mixing and studied mixtures conditions. Therefore, yttria and alumina (R=Y/Al=0.6) powder was mixed manually in mortar and thoroughly analyzed. To be representative, three samples from the reference were analyzed by XRD and give the stoichiometry of 0.6 ±0.01.

Yttria powder has an higher density than alumina and tends to fall more easily into the bottom of the beaker. Depending on mixing conditions, yttria powder can stay stuck to the beaker walls after the drying step which could therefore impacts the stoichiometry. For this reason, XRD was performed on each powder to determine the weight percentage of alumina and yttria phase.

XRD measurements (D8 Advance, Bruker) were performed between 15 ° and 65 ° using a CuKa source (λ=1.5606 °), with a step size of 0.01 ° and 0.5 seconds for each step. Phase identification and semi-quantitative analysis were carried out using Eva software. Highest peak intensities of each phase were used to calculate the ratio of yttria and alumina in mixtures. Compaction behavior of powder mixtures was studied by uniaxial compression. Therefore, 1 g of mixed powder was poured into a 12 mm diameter steel die and compressed up to 350 MPa at 1 mm/min using a quasistatic press of Instron (5500 K9400). The density of specimen was calculated from the final specimen size according to the following equation:

$$d_{\%} = \left(\frac{m}{\pi \times r^2 \times h}\right) \div d_{theo} \times 100 \quad \text{(III.1)}$$

where r is the radius of the specimen (cm), h the height (cm), m the weight of specimen (g) and d_{theo} the theoretical density in g/cm^3. d_{theo} value is 4.51 g/cm^3 which corresponds to the theoretical density, including the stoichiometry[2].

An element map was carried out on powder mixtures by SEM (NNS-450, FEI) and EDX (QUANTAX System, Bruker) using Esprit software (Bruker) to select the most homogeneous ones.

Dilatometric measurements (Netzsch DIL 402 C) were done to analyse the shrinkage behavior of green bodies during heating up to 1700 ° C with a heating rate of 2 ° C/min between 1000 ° C and maximal temperature. In parallel, powder mixtures and their green bodies were calcined at different temperatures between 1000 ° C and 1600 ° C and different holding times, 0-20 h under air (Carbolite furnace RHF 1600), to follow changes of phase composition. The sintering cycle used for all conditions included two heating rates of 10 ° C/min and 2 ° C/m below and above 1000 ° C (Fig. III.2)

[2]Calculations are reported in the appendix.

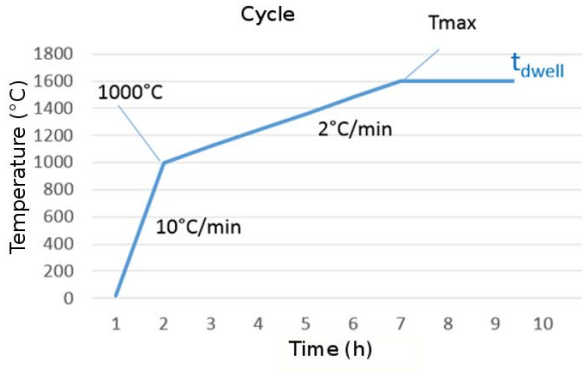

Figure III.2: Sintering cycle for sintering for green bodies under air and vacuum atmosphere.

High vacuum sintering (Lilliput, ECM Technology) was also done for three conditions: 1600 ° C for 5h, 1600 ° C for 10h and 1780 ° C for 10h to investigate the effect of vacuum conditions on final ceramic density. Post-treatment Hot Isostatic Press (HIP) (EPSI Inc.) under argon pressure of 190 MPa was applied on vacuum sintered samples to complete the densification. Afterwards, sintered specimen were mirror-polished and characterized. Relative density of sintered specimens was determined according to Archimedes principle (described in appendix) in distilled water. Intercept method on SEM pictures was used to determine the average grain size values which were plotted in function of the relative density values from Archimedes method to obtain a sintering map.

3. Results and discussion

3.1. Characterization of powder mixtures

The matter yield[3] of each mixture was calculated from the initial powder weight and plotted in Fig. III.3. As expected the reference sample has a yield of 100% and a large majority of mixture conditions were above 95%. Freeze drying method leads to drastically decrease of the yield as observed for conditions n ° 2, 5, 8, 11, 14, 17, 20, 23, 26, 29, 32 and 35. In fact, freeze drying technique induces a loss of powder due to the difficulty to collect the powder inside the freeze drying flask. On the contrary, the powder mixtures dried in the oven and the rotary evaporator have a better yield.

[3]The yield was obtained by dividing the measured weight after the drying step by the initial weight of powders introduced before the mixing step.

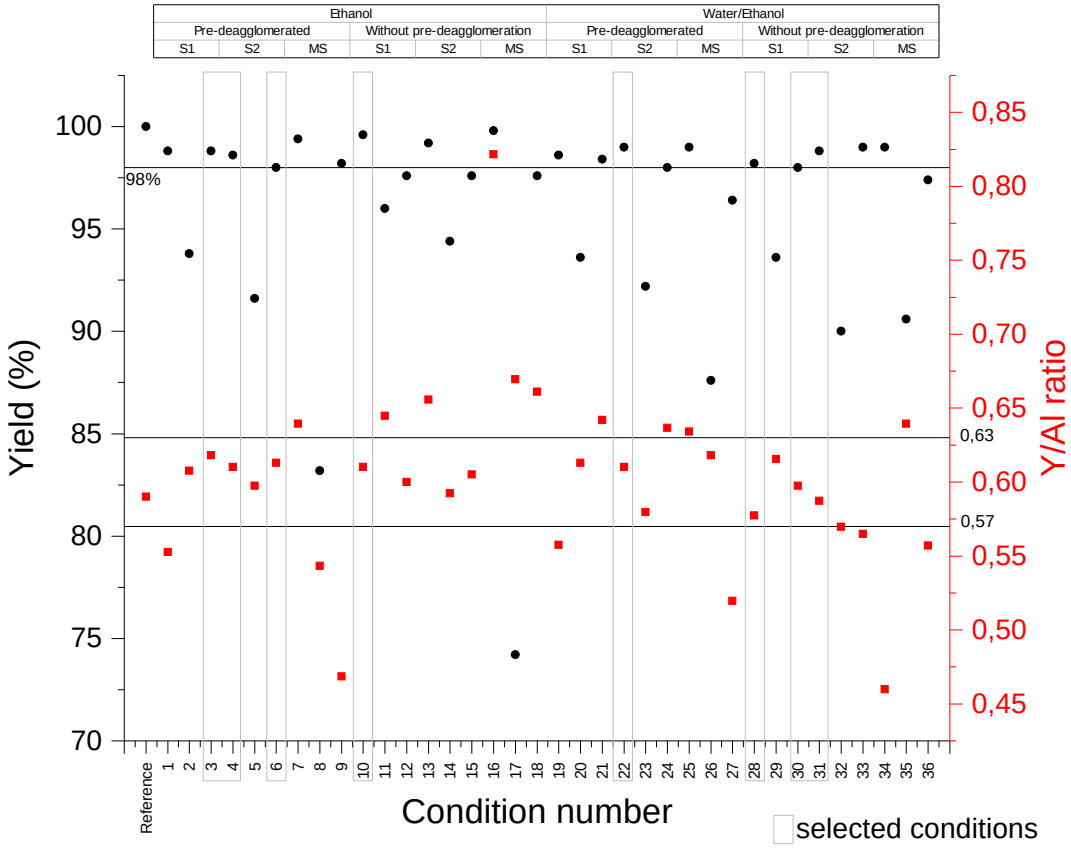

Figure III.3: Yield and stoichiometry ratio corresponding to each mixing conditions. S1 and S1 correspond to ultrasonic method for the program 1 and 2. MS stands for Magnetic Stirring mixing conditions.

Y/Al molar ratio determined by XRD is also reported in Fig. III.3. and as expected the molar ratio of the reference condition obtained a value near to 0.6 corresponding to the stoichiometry. No correlation was found between the change of Y/Al molar ratio and mixing conditions.

In the same time, the compaction behavior of all mixtures was also investigated. A high green density is important to reach the full densification. Then, relative density values obtained from the geometry of samples after compaction of 1 g of powder at 350 MPa at 1 mm/min are plotted in function of the mixing conditions (Fig. III.4).

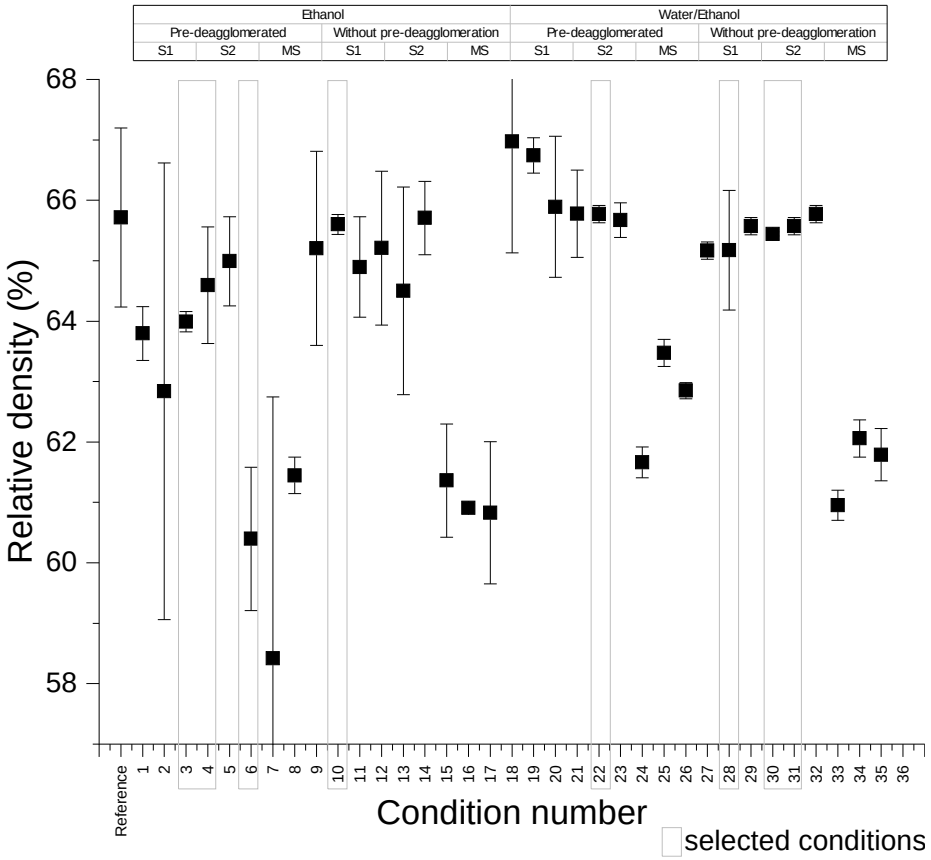

Figure III.4: Relative density after compaction of 1g of powder at 350 MPa at 1 mm/min for each conditions. S1 and S2 correspond to ultrasonic method for the program 1 and 2. MS stands for Magnetic Stirring mixing conditions.

Firstly, the type of the solvent has a low impact on the specimen compaction. However, some tendencies can be observed as the highest relative density values are obtained for mixtures with ethanol, whereas ethanol/water condition mixtures have lower densities (Fig. III.4). The addition of water to ehtanol seems to favour the compaction of powder whereas it has no influence on stoichiometry.

The pre-deagglomerated step has not particular effect on relative density for ethanol based mixtures as shown in Fig. III.4). Nevertheless, for ethanol/water solvent conditions, specimens compacted were denser when the pre-deagglomeration step is applied (n ° 19 to 27).

Considering the mixing methods used, it seems that magnetic stirring has a very negative impact on compaction as observed for conditions n ° 7, 8, 9, 16, 17, 18, 25, 26, 27, 34, 35 and 36 (Fig. III.4). In contrast, all compacted specimens from ultrasonic method present a higher relative density than magnetic stirred specimens. The possible explanation is the destruction of harder agglomerates under the action of ultrasounds which improves the particle packing. No significant difference appears between the two different ultrasound treatment programs.

For each mixing method, three drying methods were used. These methods gives roughly the same results and no particular tendency can be found between conditions belonging to

the same drying method. So, as observed before, it is quite obvious that drying methods have a huge impact on yield and the stoichiometry but not so much for the relative density of green compacts. Moreover, considering the low precision on measuring the height of the sample (±0.05 mm), relative density values can only give a general tendency.

For further investigations, mixing conditions were selected in function of the main parameter for transparency. Main criteria in order of importance are: the stoichiometry, the yield and the green relative density of specimen. Only 8 of 36 conditions met these criteria and were selected to perform EDX mapping and calcination on powder to follow the solid state reactions. The selected conditions are n ° 3, 4, 6, 10, 22, 28, 30, 31. In selected conditions, 5 of 8 conditions used the oven for drying step, half of conditions were done in ethanol/water solvent and 4 of 8 conditions had the pre-deagglomeration step. It has to be noted that freeze drying technique was not retained in the selected mixtures due to low yield obtained. Selected mixtures are reported in the following table (Table III.2).

n ° of condition	Solvent	Pre-deagglomeration	Mixing method	Drying method
3	Ethanol	yes	Ultrasonic Prog 1	Rotary evaporator
4		yes	Ultrasonic Prog 2	Oven
6		yes	Ultrasonic Prog 2	Rotary evaporator
10		no	Ultrasonic Prog 1	Oven
22	Water/Ethanol	yes	Ultrasonic Prog 2	Oven
28		no	Ultrasonic Prog 1	Oven
30		no	Ultrasonic Prog 1	Rotary evaporator
31		no	Ultrasonic Prog 2	Oven

Table III.2: Best mixtures conditions selected for SEM and EDX mapping analyses.

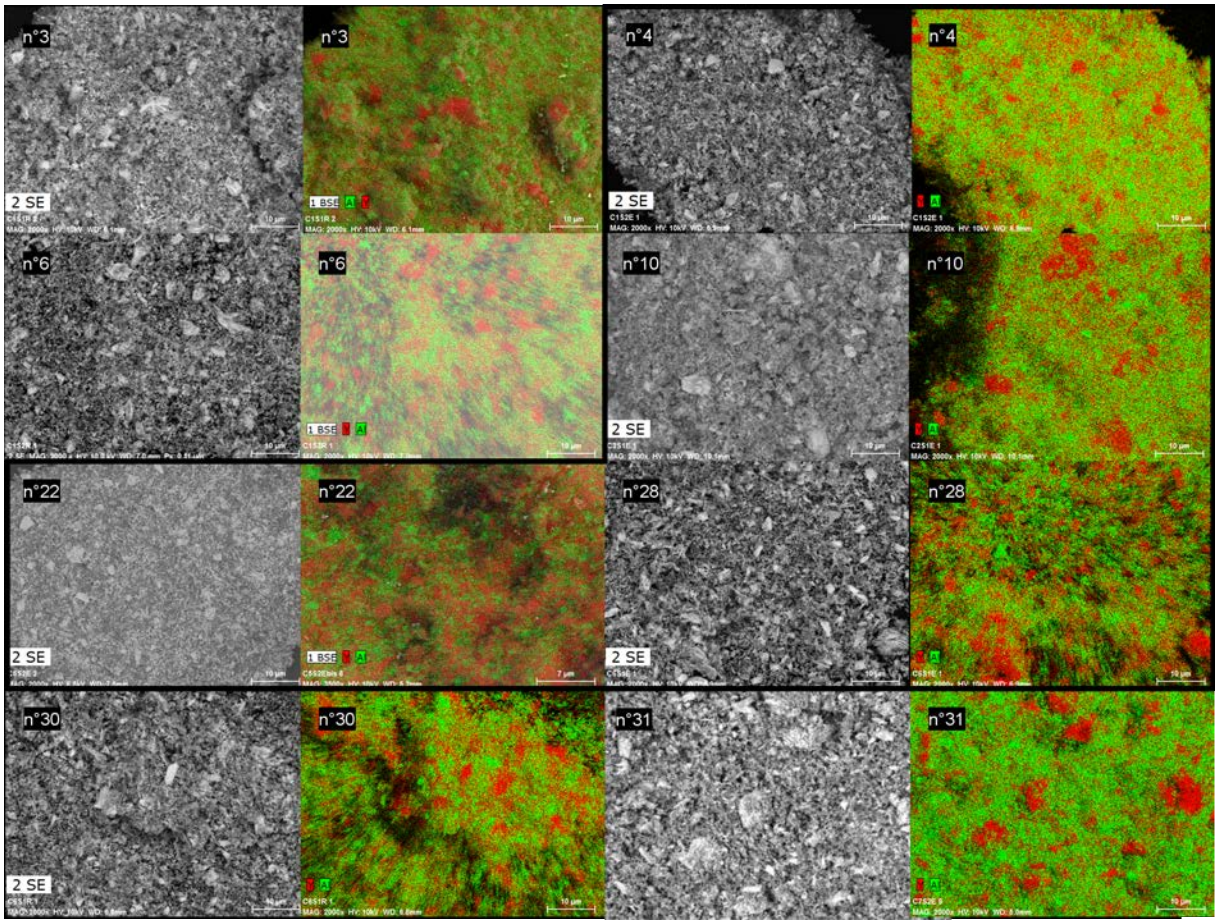

Figure III.5: SEM pictures with EDX analysis of Al (green) and Y (red) elements of 8 selected mixtures. (Enlargement of this figure is available in appendix E)

SEM imaging and EDX mapping allowed to identify the most homogeneous powder mixtures, where alumina and yttria are well dispersed in each other and without large agglomerates (> 8µm). SEM images reveal the presence of large agglomerates in the mixtures n ° 3, 6, 10, and 31 and smaller agglomerates in the n ° 28, and n ° 30. More homogeneous results such as higher species dispersion and absence of large agglomerates were obtained for samples n ° 4, 10, 22 and 28 that were dried in the oven.

A similar observation was made by Liu *et al.* for a ball-milled powder composed of Nd_2O_3, Al_2O_3 and Y_2O_3 powder. After calcination at 1100 ° C, their EDX analysis have shown no reaction between alumina and yttria particles powder at this temperature and presented same dispersion as observed in our study (without calcination).

After SEM and EDX analyses, the four most homogeneous powder mixtures, with the best dispersion of alumina in yttria were chosen (powder mixtures n ° 4, 10, 22 and 28), to follow changes in phase composition and YAG formation after thermal treatment.

3.2. Evolution of phase composition after thermal treatment of powder mixtures

For the study of the thermal treatment on the oxide powder mixtures reactivity, we have selected the powder mixtures prepared with and without pre-deagglomeration step, in ethanol or ethanol/water as dispersing medium, ultrasound dispersion and drying in oven

(batches n ° 4, 10, 22 and 28).

It is well-known that formation of YAG phase is composed of three consecutive reactions reported by Kinsman *et al.* [203]:

$$2Y_20_3 + Al_2O_3 \rightarrow Y_4Al_2O_9\ (YAM)\ (900 - 1000\,^\circ\mathrm{C}) \tag{III.2}$$

$$Y_4Al_2O_9 + Al_2O_3 \rightarrow 4YAlO_3\ (YAP)\ (1100 - 1250\,^\circ\mathrm{C}) \tag{III.3}$$

$$3YAlO_3 + Al_2O_3 \rightarrow Y_3Al_5O_{12}\ (YAG)\ (1400 - 1600\,^\circ\mathrm{C}) \tag{III.4}$$

According to literature, below 900 ° C, only alumina and yttria phases are present, YAM and YAP phases are formed at 900 and 1100 ° C respectively and the final YAG phase appears at 1400 ° C.

Fig. III.6 shows the XRD results of the n ° 4, 10, 22, 28 powder mixtures and the reference mixture before and after calcination at 1100, 1300, 1500 and 1600 ° C.

Globally, YAM and YAP phases are present at 1100 ° C for all conditions. At 1500 ° C, YAG is the major phase with 66 to 74 wt% and reaches over 80 wt% when treated at 1600 ° C for the four powder mixtures, but not for the reference sample where the YAG phase stays at 27 and 30 wt%. Phase composition between different powder mixtures is similar despite the mixing procedure but significantly different to the reference mixture: the concentration of YAG phase at 1500 and 1600 ° C is higher due to better powder mixing conditions. The highest wt% of YAG phase when treated 0 h at 1500 ° C is obtained for the condition 4 (74 wt%) (table III.1), and when treated 0h at 1600 ° C for the condition 28 (84 wt%). First observations allow to conclude here the benefit of the mixing conditions to enhance the powder reactivity and the phase appearance.

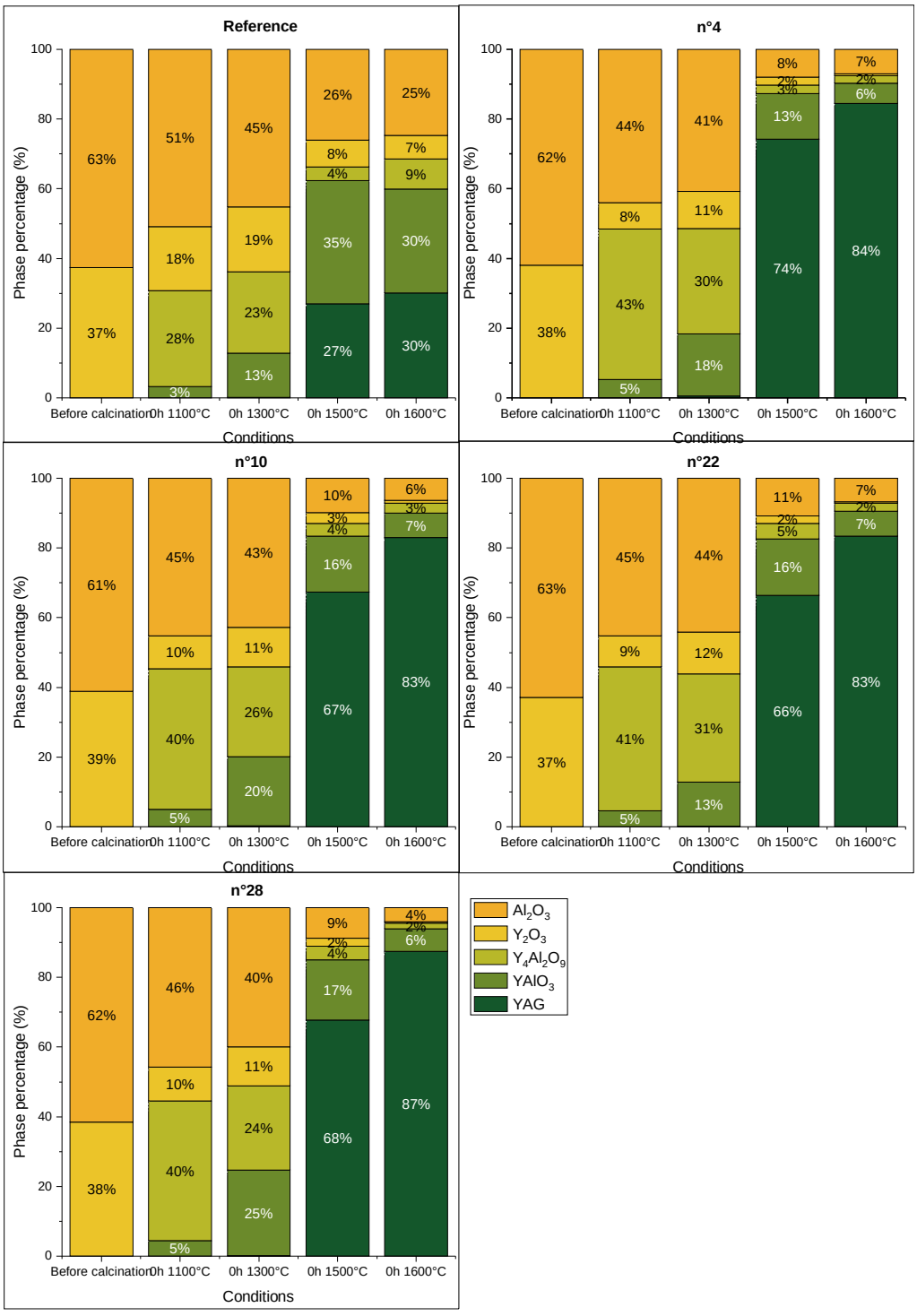

Figure III.6: Semi-quantification results after powder calcinations at 1100, 1300, 1500 and 1600 ° C.

1. Influence of a holding time on the formation of YAG phase

A holding time of 1h was applied for the temperatures 1100, 1300, and 1500 ° C and XRD semi-quantification results are presented in Fig. III.7.

For all mixing conditions, a clear improvement of the phase transformation and the YAG formation was highlighted, when a dwelling time is increased from 0 h to 1 h. On the other hand, this is not the case for the reference sample which has a lower reaction rate after 1 h at 1100 ° C. Especially at 1300 ° C, adding a dwelling step increases the YAG proportion from 0 to 1 wt% for reference sample and between 13 and 45 wt% depending on the mixing conditions.

Generally, the detected concentration of YAG phase at 1500 ° C for 1h is higher than at 1600 ° C without holding step, i.e. condition 4 presents 90% YAG phase at 1500 ° C for 1h compared to 74% at 1500 ° C for 0 h and also to 84 % at 1600 ° C for 0h. The dwelling step had a significant effect on the YAG formation and therefore longer dwelling times (3, 5, 10 and 20 h) were applied on two most reactive mixture conditions: n ° 4 and n ° 28. Results are reported in Fig. III.8.

For condition 4, when dwelling time was increased to 3h at 1500 ° C, only YAG and YAP phases were detected with 96 wt% and 4 wt%, respectively (Fig. III.8). Nevertheless, alumina is supposed to be still present in the mixture to react with YAP to form YAG but was not detected due to its low concentration. Finally, 100 wt% of YAG phase was obtained for 20 h at 1500 ° C for condition 4.

Although the phase composition conditions n ° 28 was quite similar to the n ° 4, the difference was more notable for longer holding times. Alumina was still present in the powder for 3 and 5 hours conditions with 3% and 4% respectively. For conditions n ° 4 no Al_2O_3 phase was detected for equivalent dwelling times. Between 3 and 20 h at 1500 C the YAP phases decreases from 4% down to 0 wt% at 20 h.

By comparison, 100% YAG phase was obtained at 1500 ° C by Lee *et al.* with a reactive mixture of Nd:YAG precursors ceramic with 2h of holding time [159]. This result is possible for better dispersion of alumina and yttria powders.

In the next part of this article, only two mixtures (n ° 4 and n ° 28) were kept to further investigations on densification, sintering behavior and phase evolution during sintering.

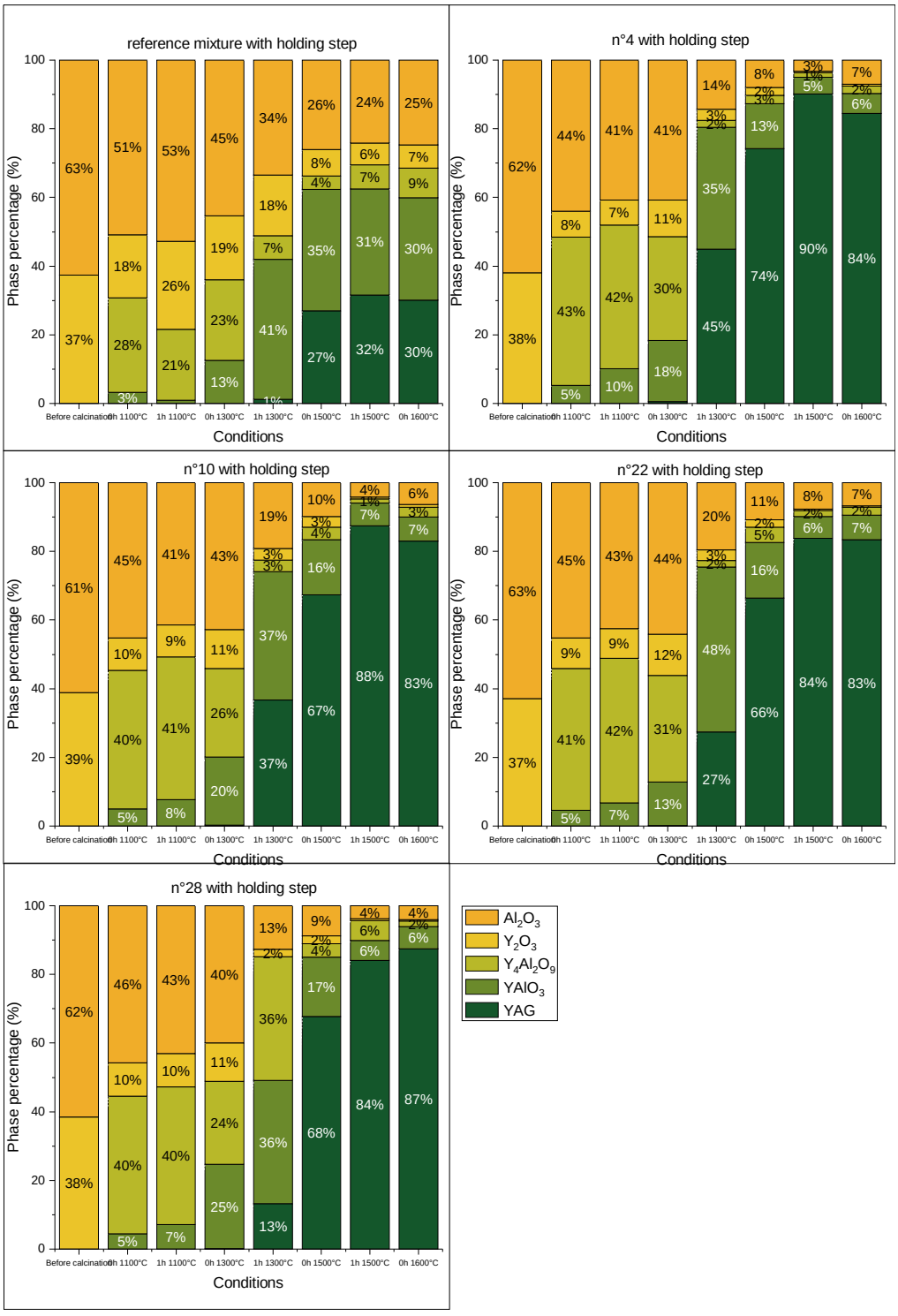

Figure III.7: Semi-quantification results after powder calcination with a dwell time of 1 hour for each condition.

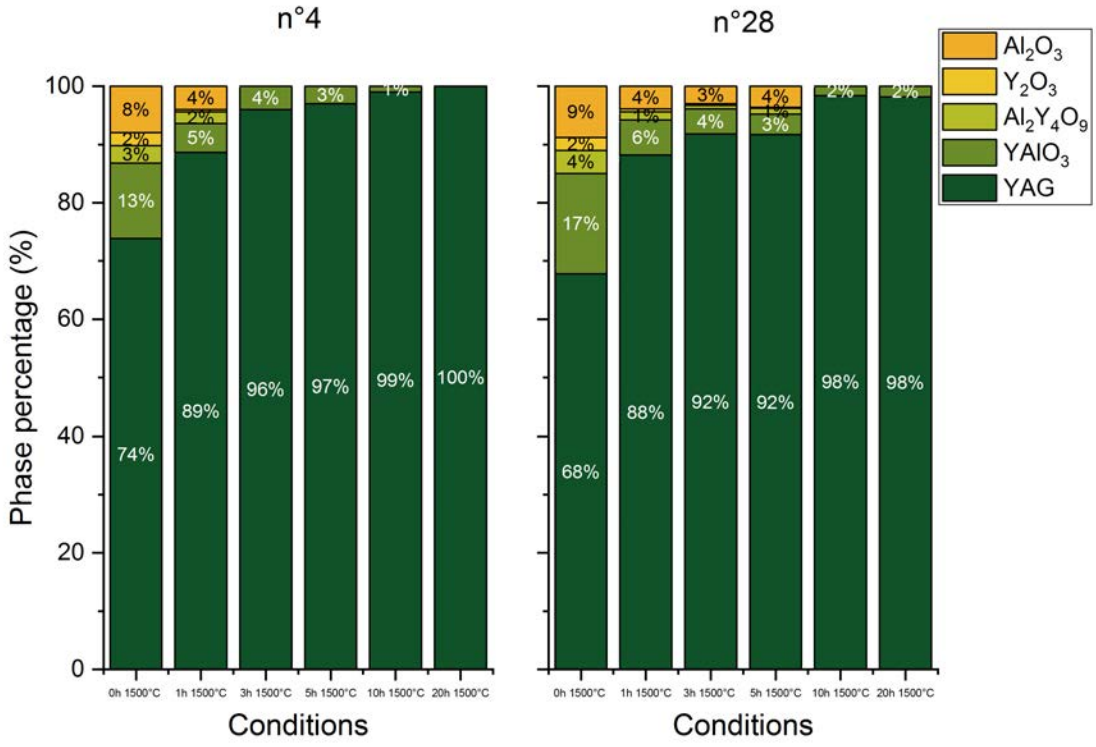

Figure III.8: Holding time impact on phase distribution for 0, 1, 3, 5, 10 and 20h for mixture n ° 4 and n ° 28.

2. Study on compacted specimens: densification, dilatometry and phase evolution

Dilatometry analysis of the green bodies of powders processed following the conditions 4 and 28 shows the same densification behavior which differs from the reference powder (Fig. III.9).[4] While the reference sample presents a classical densification behavior between 750 ° C and 1500 ° C, the 4 and 28 mixing conditions samples present several peaks corresponding to phase transformations.

For the two mixing conditions n ° 4 and n ° 28, the first phenomenon occurs at 1160 ° C with a high shrinkage of the samples followed by two expansion phenomena at 1190 ° C (2) and 1300 ° C (3). Between (3) and (4), a shrinkage takes place until 1490 ° C which corresponds to the densification of the present phases. Then, between (4) and (5), a shrinkage occurs in the two samples n ° 28 and n ° 4.

Based on literature results, in the temperature range of 900-1250 ° C, formation of YAM and YAP occurs simultaneously [204]. Above 1250 ° C, alumina reacts with the YAP to obtain YAG phase. This reaction takes place in the same time as the sintering of the newly formed YAG phase. In fact, this transformation from the perovskite structure (YAP) to garnet one (YAG) leads to a dilatation of the material due to different density values (5.35 g/cm^3 →4.55 g/cm^3)[194, 204–206]. As the expansion caused by the formation of YAG is greater than the shrinkage, a peak is observed at 1300 ° C (3) in Fig. III.9.

In order to obtain more information about phase composition in the bulk material, supplementary sinterings of reference, n ° 4 and n ° 28 samples were performed at 1000 ° C,

[4]The reference sample is obtained by a manual mixing between alumina and yttria powders.

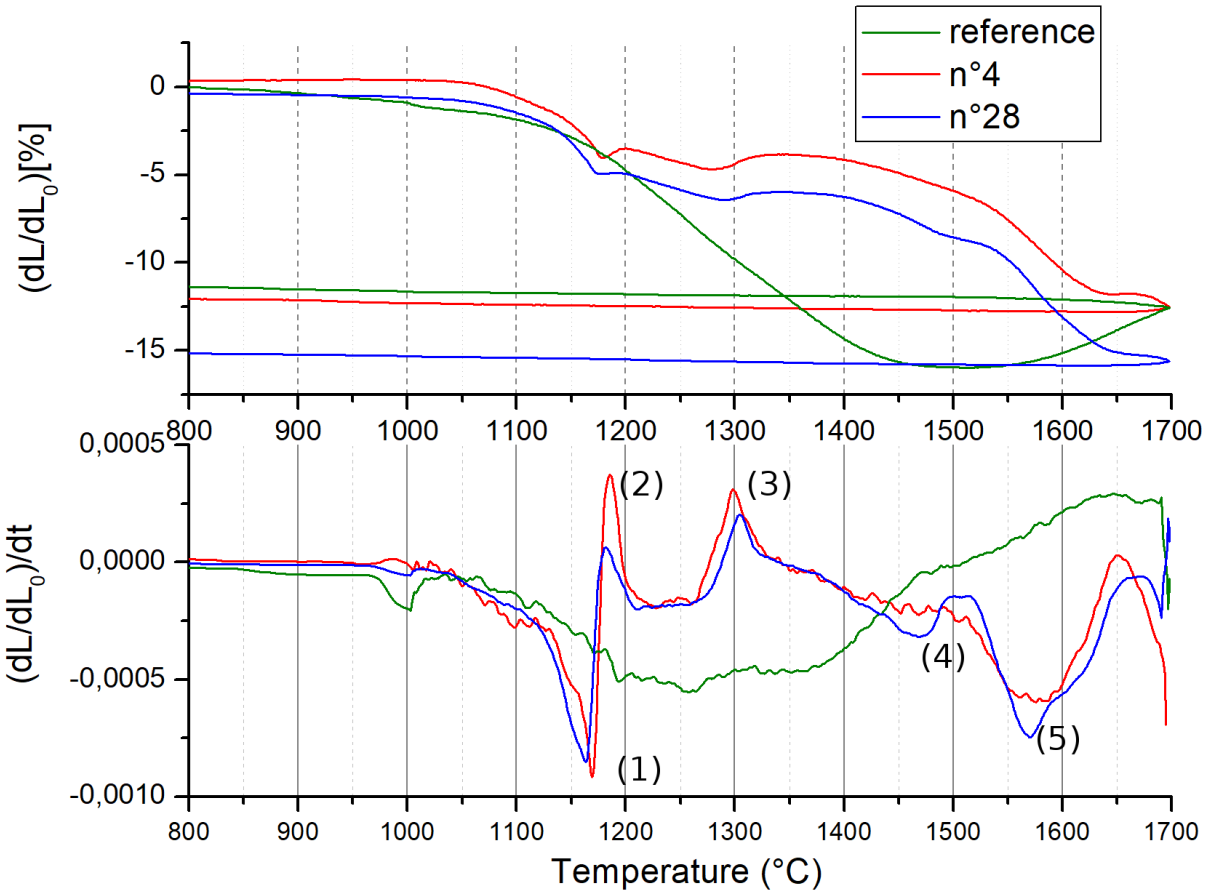

Figure III.9: Shrinkage curves (top) and derived curves (bottom) of compacted specimen from n ° 4, n ° 28 and reference condition. Numbers correspond to shrinkage rate peak.

1300 ° C and 1600 ° C. The Fig. III.10 shows the XRD results.

The reference sample was composed of multiple phases such as YAP, YAM, yttria and alumina.

The phase composition for conditions 4 and 28, sintered at 1000, 1300 and 1600 ° C are, as the dilatometric analysis already hinted, very similar. At 1000 ° C for 0h, around 7-8 wt% YAM and 54 wt% of YAP are detected for condition n ° 4 and 28. YAM phase is mainly detected at 1000 ° C and stays between 8 wt% for small dwelling times and 2 wt% for high dwelling. By increasing the dwelling time at 1000 ° C, YAP mass weight increases up to 70 wt%. When sintered at 1300 ° C, YAG is formed in specimen of both conditions. Even without dwelling time, over 40 wt% YAG is obtained and over 80 wt% YAG for 10 h at 1300 ° C. After at 1600 ° C, YAG phase is detected above 95 wt% in the both specimen from mixing conditions and the effect of the dwell time for 10h enabled to form 100 wt% YAG.

On the contrary, for the reference specimen the YAG phase reaches 14 wt% at 1600 ° C (0h) and in better case 32 wt% for 10h of holding time. In all conditions, alumina phase stays around 36 wt% in the specimen with various contents of yttria, YAG, YAP and YAM phases in function of the temperature.

So, the difference of phase transformation in the compacted specimen during the sintering shows accurately the benefit of the mixing conditions applied in this study to enhance

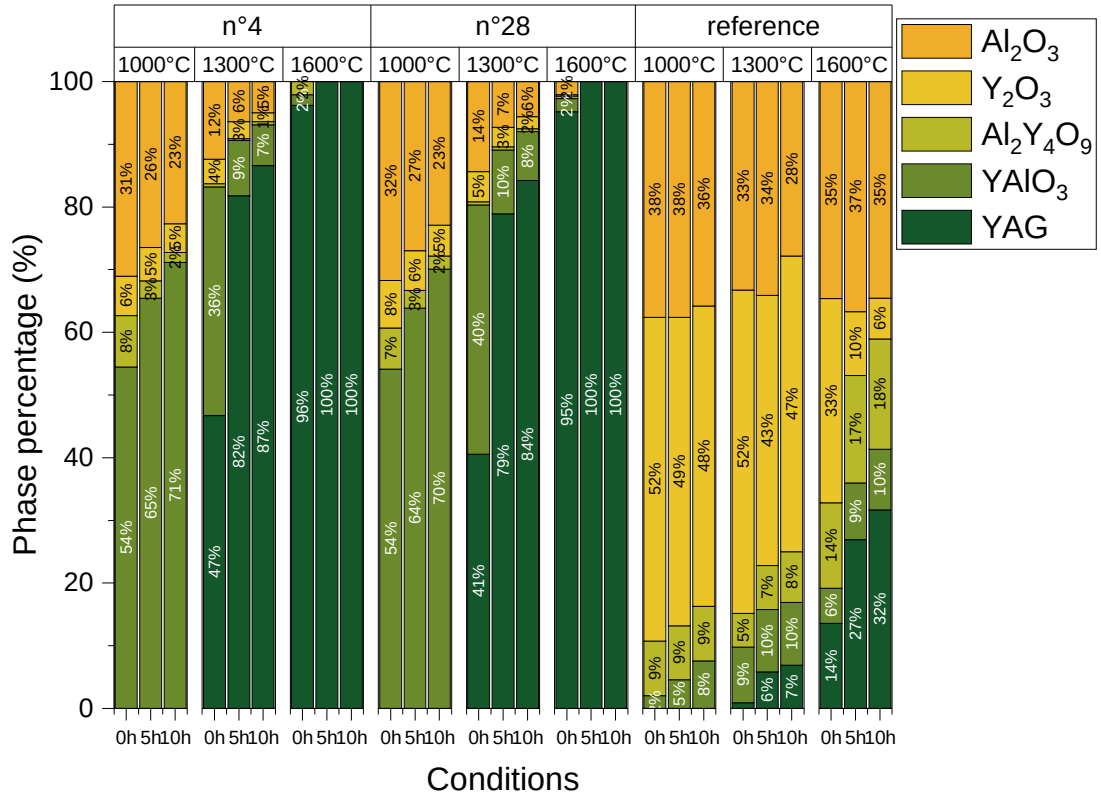

Figure III.10: Semi-quantification of ceramics specimens after sintering at 1000, 1300 and 1600 ° C with a dwell time of 0, 5, 10 hours. Standard deviation: 0.81%.

phase transformation by SSR.

According to dilatometric measurement, XRD of sintered specimen n ° 4 and n ° 28 show the formation of YAG phase between 1000 and 1300 ° C (at 0h) above 40 wt%. After 1300 ° C, the YAG formation continues and represents the major phase at 1600 ° C (Fig. III.10)

Density of specimens was measured after the different thermal treatments. Based on XRD analysis, the theoretical density of each phase composition was calculated and used as value for a 100% dense specimen (see calculation in appendix F). Considering the XRD results and dilatometric analysis, the only specimens that are discussed here are the ones which were sintered at 1600 ° C for 5 and 10 hours.

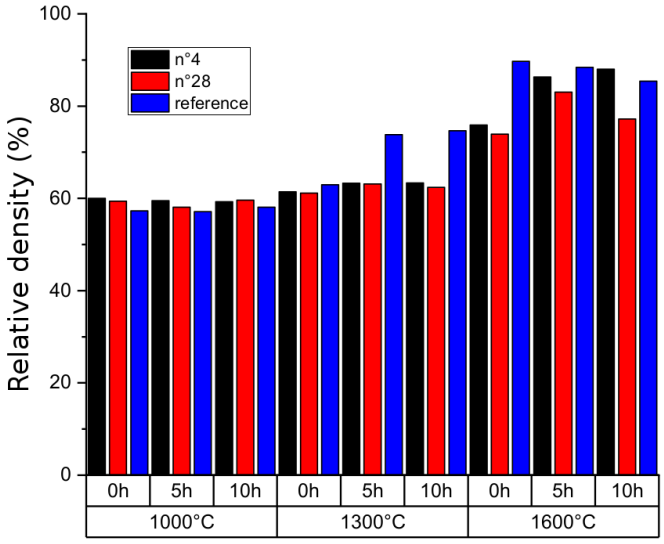

Figure III.11: Relative density of sintered specimens corresponding to conditions 4, 28 and the reference after thermal treatment.

The relative densities after sintering of the samples 4, 28 and the reference are presented in Fig. III.11 to study the evolution of the relative density as a function of the thermal conditions.

The specimen of condition 4 sintered at 1600 ° C for 10 hours reaches a density greater than 86% and the sample of condition 28 a density of about 80%. In the latter case, the density of the sample sintered for 5 hours at 1600 ° C. is 83%, which is higher than that of the specimen sintered for 10 hours at 1600 ° C. This phenomenon could be explained by the volume changes during phase formation and the resulting stresses responsible of porosity formation [207].

This led to the hypothesis that even if no secondary phase was detected by XRD for the specimen sintered for 5 h at 1600 ° C, secondary phases are present and that by increasing the duration of the heat treatment, a phase transformation occurs, modifying density and inducing pore formation. Presence of residual phases, such as YAP and alumina for example, at this step induces formation of YAG and therefore the decrease of the density [207]. The same observation can be made for the reference specimen which exhibited a loss of relative density when the sintering time increased to 1600 ° C. According to the results of DRX (Fig. III.10) and the shrinkage curve (Fig. III.9), remaining secondary phases react at high temperature which induces expansion and porosity formation.

As the formation of YAG in green bodies of conditions 4 is slightly higher than in green bodies of condition 28, further characterization was focused on specimens of condition 4.

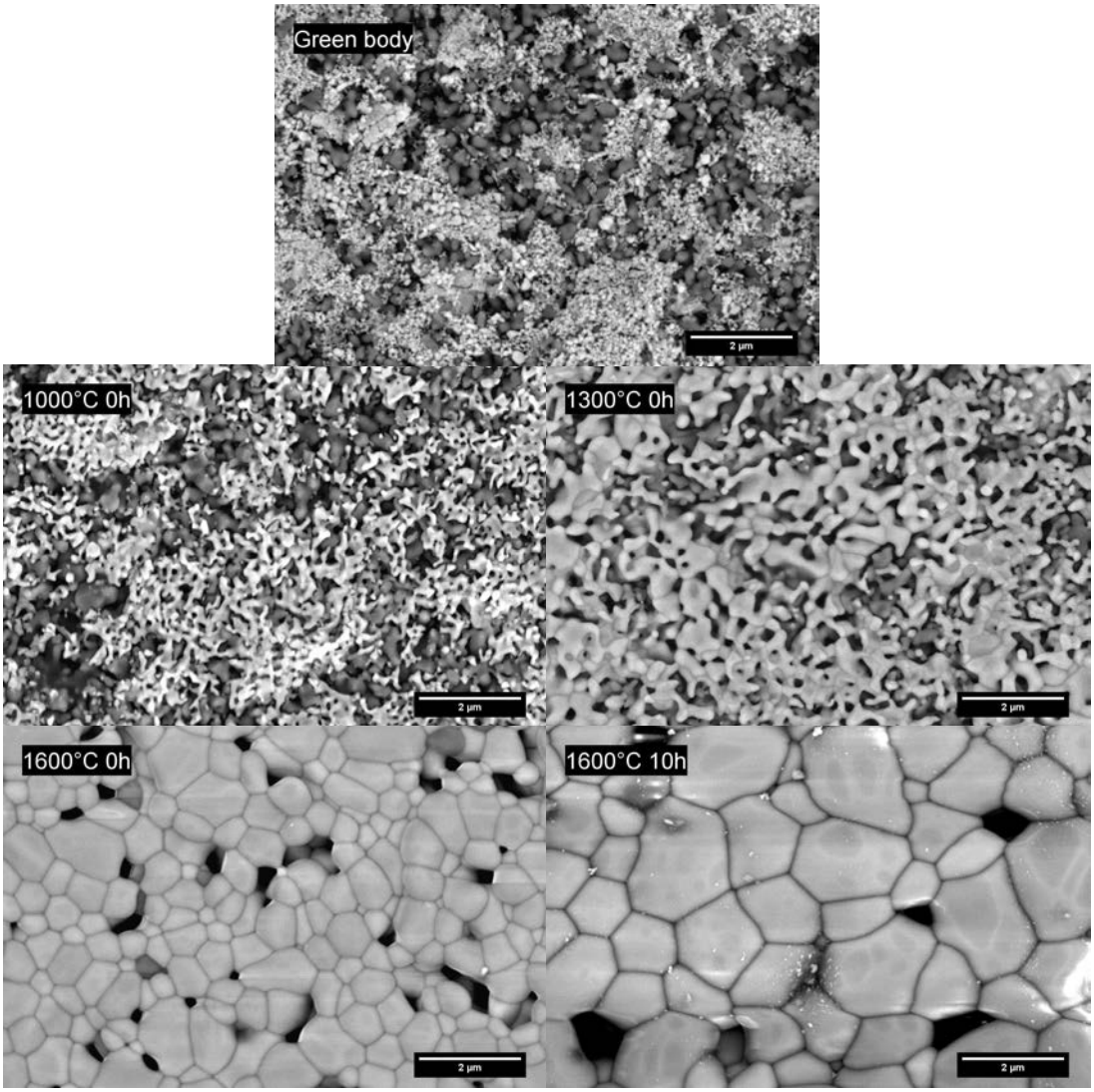

Figure III.12: SEM pictures of densification process for the specimen from n ° 4 condition powder.

SEM observations were performed at different densification stages for the specimen of condition 4, as green body and after 1000 ° C 0h, 1300 ° C 0h, 1600 ° C 0h, 1600 ° C 10h (Fig. III.12). The BSE detector allows to distinguish alumina and yttria by chemical contrast, where alumina particles are darker than yttria particles as shown in Fig. III.12.

Scanning electron microscope images revealed a vermicular arrangement between the particles at temperatures of 1000 and 1300 ° C. The contrast of the images suggests a multi-phase system which is confirmed by XRD analysis, showing that the sample is composed of alumina, yttria, YAM, YAP and YAG phases.

At 1600 ° C for 0h, a homogeneous microstructure is observed, but with various pores and still some chemical contrast corresponding to secondary phases. This agrees with the XRD measurements that revealed the presence of YAM and YAP in the specimen. The micrograph of the specimen sintered at 1600 ° C for 10h reveals a growth of the grains compared to the specimen sintered without dwell time at the same temperature. Furthermore, many pores are observed with a diameter of 0.5 µm. These pores can be removed by application of higher temperatures (1650-1750 ° C) with increasing the grain

size [204, 205]. Based on thermodynamic analysis of Kingery and Francis, if the number of grains surrounding pores (N) is below N_c=5 it induces the shrink of pores at higher temperatures ($N \leq N_c$) [205, 208]. The critical number N_c was evaluated by Boulesteix *et al.* for Nd:YAG ceramic [209]. In our case, N is equal to 5 (Fig. III.12) and therefore a pore will be expected to shrink at temperature higher than 1600 ° C.

SEM-EDX observations of surface specimen of condition n ° 4 and n ° 28 show the presence of YAM and YAP phases. Phase identification was performed by calculation of weight percentage of each element after EDX profile analysis. Then each phase was deduced by the theoretical weight percentage contained in YAG, YAP and YAM phases. These phases were present in a very low quantity in all samples sintered up to 1650 ° C.

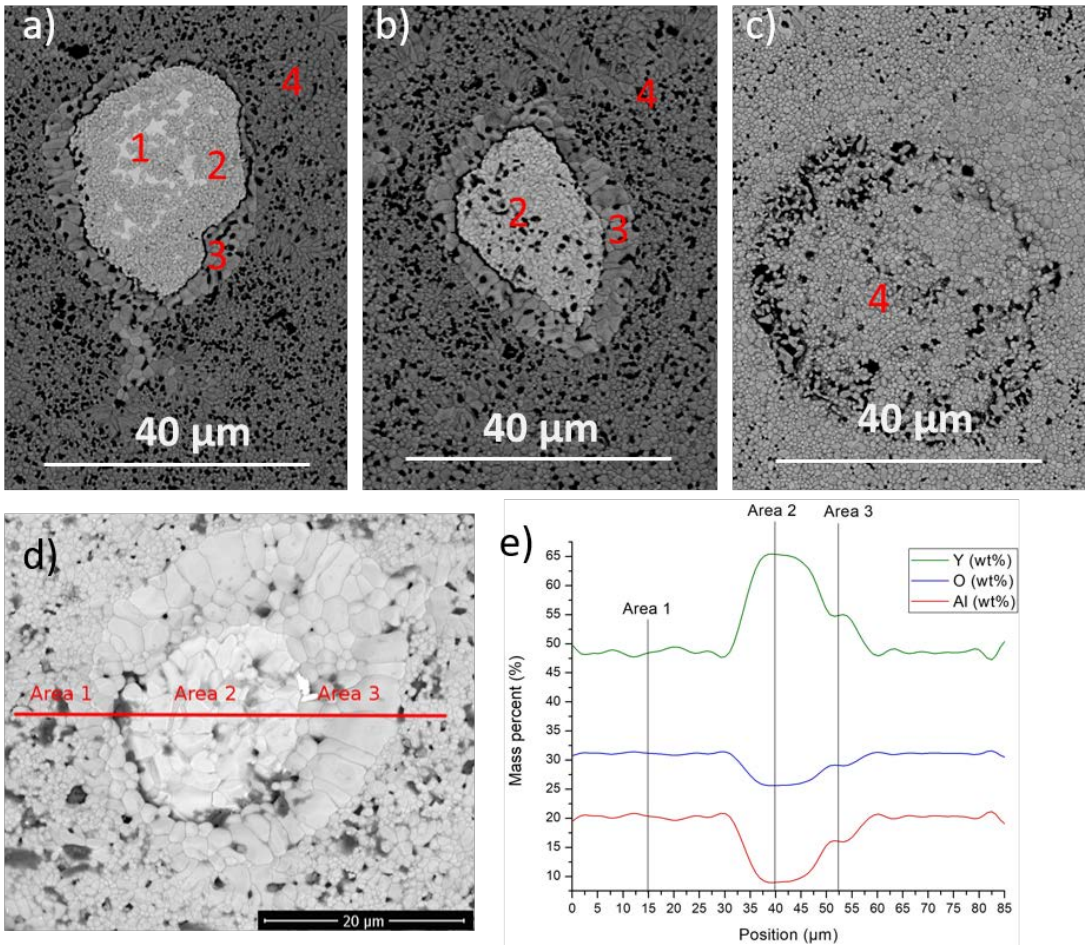

Figure III.13: a), b), c) SEM picture in back back scatter mode of n ° 4 sintered specimen at 1650 ° C at 3 different areas. d) SEM images for the EDX profile analysis and e) the element profile analysis by EDX.

The various steps of the reactive sintering are revealed by SEM (Fig. III.13) on sample n ° 4 sintered at 1650 ° C. As shown in Fig. III.13, different grain sizes, morphologies and chemical contrast are revealed by the SEM-BSE detector. Darker areas might be aluminum rich phases and brighter ones yttrium rich phases. Thereby, yttria can be attributed to phase 1, YAM to phase 2, YAP to phase 3 and YAG to phase 4 in Fig. III.13 (a) to (c).

EDX analysis was performed on similar area (Fig. III.13-(d)) to confirm previous

observations on a, b and c SEM pictures.

The EDX profile results of the (d) SEM picture are presented in Fig. III.13-(e) and the following table allows to assign the corresponding phase to each area in Fig. III.13-(d).

	Y (wt%)	Al (wt%)	O (wt%)
Area 1	0.495	0.197	0.309
YAG	0.45	0.23	0.32
Area 2	0.649	0.093	0.258
YAM	0.64	0.1	0.26
Area 3	0.547	0.162	0.291
YAP	0.54	0.17	0.29

Table III.3: Theoretical weight percentages of Y, Al and O element in YAG, YAP and YAM phases and measured composition in areas 1,2 and 3 in (d) picture and (e) EDX profile of the Fig. III.13

According to the table III.3, the central phase is composed of YAM (Area 2) embedded in a YAP phase (Area 3) and finally the YAG phase (Area 1), which is around the YAP phase. Thereby, the grains of YAG are large and elongated with lot of porosity around. The creation of additional porosity (compared to already present in the material after the compaction) can come from the expansion which takes place when the YAG phase is formed. Then, above 1350 °C the expansion ends and sintering of YAG reduces the porosity. The difficulty of reactive sintering is that alumina reacts with YAM to form YAP but also react with YAP to give YAG phase.

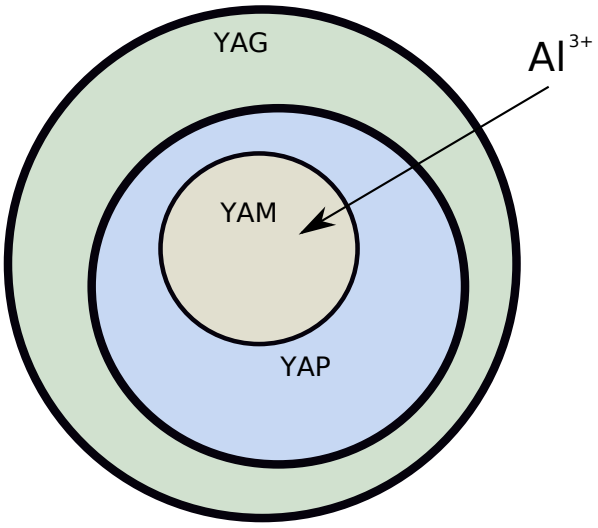

Figure III.14: Schematic representation of Al^{3+} diffusing through YAG and YAP phase to react with YAM.

Al^{3+} ions (Fig. III.14) have to migrate through YAG phase (4) and YAP phase (3) to reach the YAM phase (1) thanks to lighter mass and smaller size of the Al^{3+} ions than Y^{3+} ones [194]. During the reactions described above (eq. III.2-4), the created porosity is difficult to remove. Therefore, a longer holding time might allow the migration of Al^{3+} in the ceramic and hence the reaction of the different species leading to the formation of YAG before the end of the densification.

After the promising results of thermal treatment in air furnace, green bodies of condition 4 have been sintered in a vacuum furnace, which allowed to reach > 99% density at 1600 ˚ C and fully dense specimen after sintering at 1700 ˚ C.

Ceramics sintered under high vacuum are shown in Fig. III.15. It is clearly notable that even if dense (>99%) the ceramics are opaque. The ceramic sintered for 5 h at 1600 ˚ C (Fig. III.15) presents two translucent areas. These regions were in contact with the alumina crucible, used for sintering. It is supposed that the alumina crucible reacted with the remnant phases such as YAP and form translucent region already visible in the Fig. III.15-a). Even when holding time was increased to 10 h, the fully dense ceramic is opaque after sintering (Fig. III.15-b). Although specimen was on alumina crucible, any translucent area was found on the sample.

Finally, when ceramic was sintered at 1780 C for 10 h, both opaque and translucent regions are visible (Fig. III.15 c). The translucent and transparent parts consist of large grains. SEM observations revealed the presence of secondary phases, which can explain the optical heterogeneity.

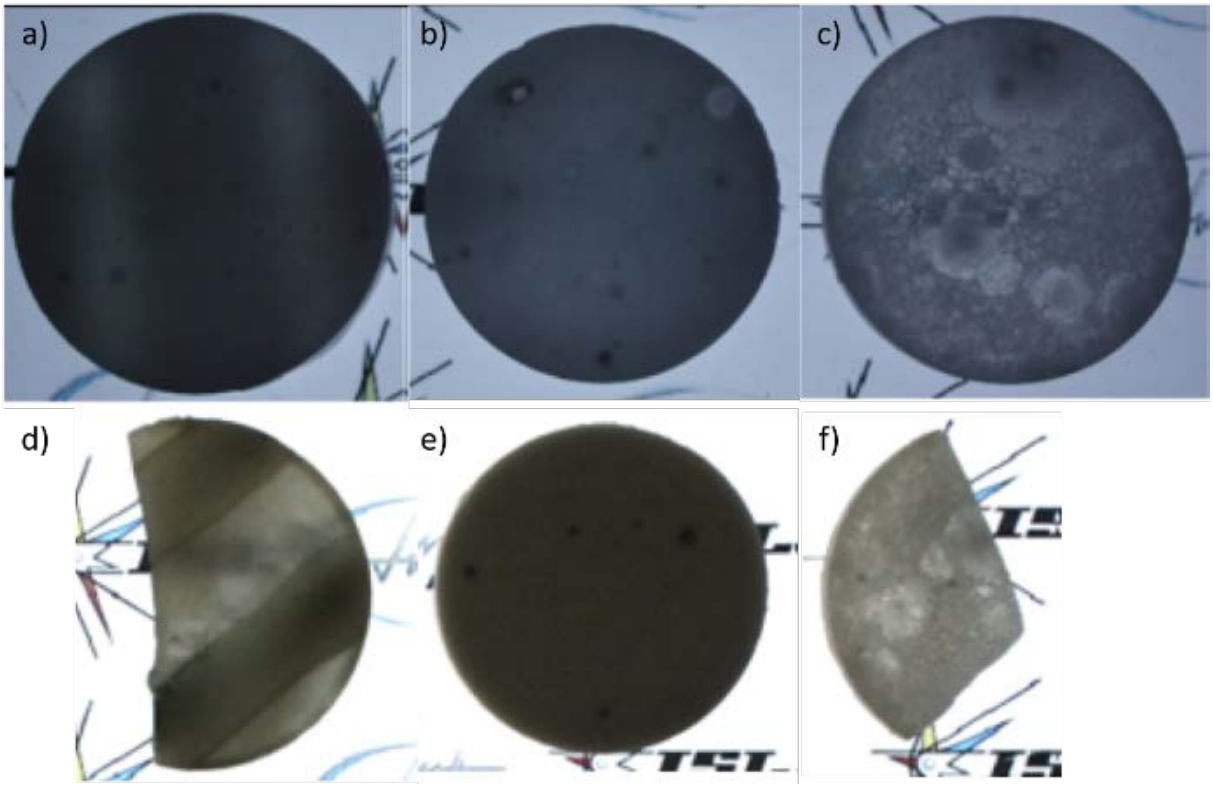

Figure III.15: Samples obtained after high vacuum sintering at a) 1600 ˚ C for 5h b) 1600 ˚ C for 10h c) 1780 ˚ C for 10h and HIP post treatment of 1650 ˚ C for 6h (1900 bars) d, e and f corresponding to a,b,c samples.

Samples underwent a HIP post-treatment at 1650 ˚ C for 6h in a powder bed to prevent any carbon pollution from the carbon furnace. Specimens after HIP are presented in the Fig. III.15 where the sample d corresponds to the specimen a) shows a higher transparency after the HIP process. Regions in contact with the alumina crucible during the sintering process, are more transparent after HIP post-treatment. Nevertheless, the same behavior is not reported in the case of specimen b) although an alumina crucible

was also used. The sample stay opaque even after the HIP procedure. The last sample c), which presents a transparent part at the center of the specimen was not homogeneous. Several macro grains are visible at the surface of the specimen which highlights the heterogeneous microstructure. Even after HIP post-treatment, the transparency is not improved and sample is still opaque.

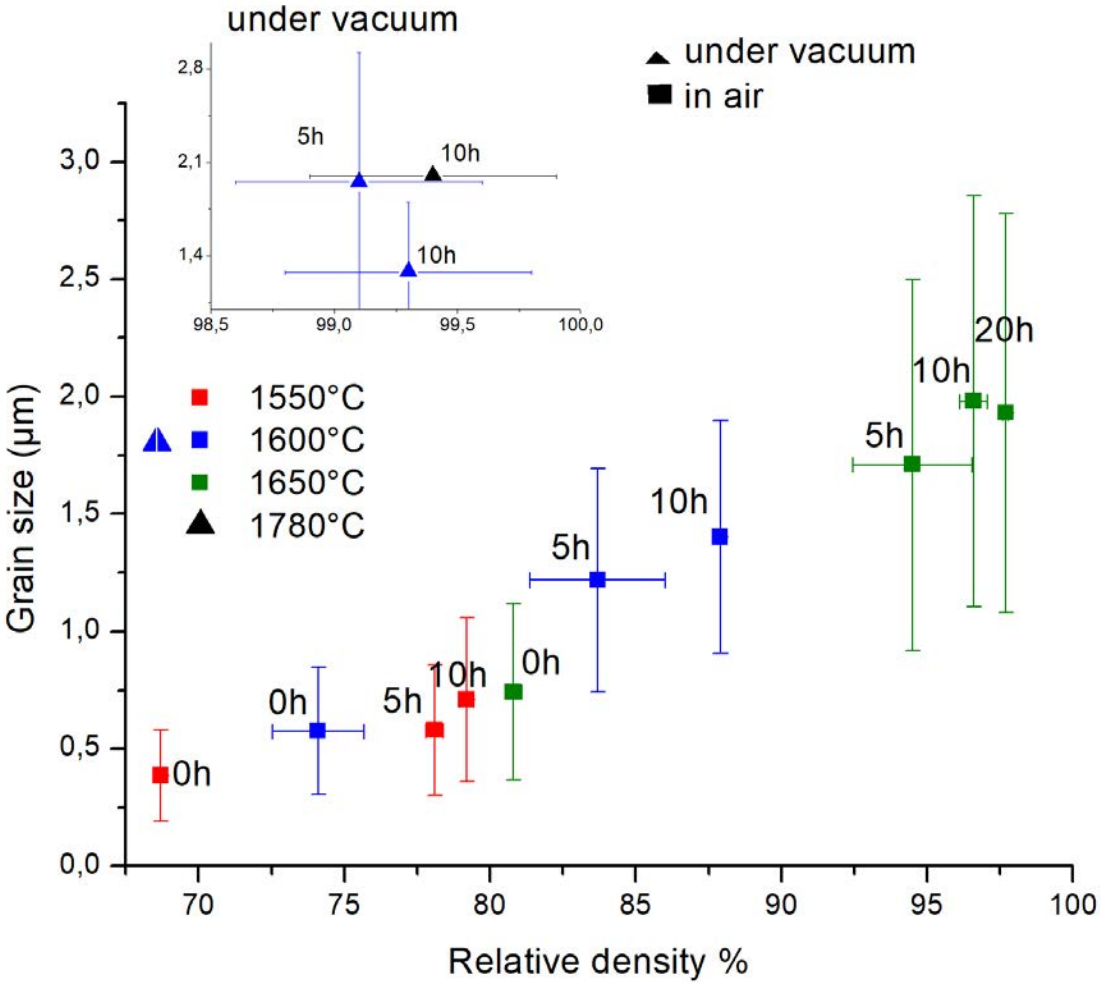

Figure III.16: Sintering map for Al_2O_3 and Y_2O_3 mixture from the n ° 4 procedure.

Based on the grain sizes and densities, a sintering map was realized for the ceramics sintered in air and under vacuum conditions. As expected the density increases with the increase of sintering temperature and dwelling time. As discussed above, the ceramics sintered beyond 5 h at 1600 ° C are not 100% composed of YAG phase. The grain size of these ceramics ranges between 0.4 and 1.1 µm, while the density does not exceed 81%. The dwelling time was increased up to 20 h at 1650 ° C which allows to increase the density value up to 97%. These sintering parameters were not sufficient to reach a fully dense specimen. The average grain size increases with the temperature and with dwelling times over 5 h. However, it seems that the temperature has a greater impact on the grain size than the dwelling time. For instance, the average grain size of ceramics sintered at 1600 ° C for 5 and 10 h is 1.2 and 1.4 µm, respectively. In general, the grain size is small and does not exceed 2.5 µm.

Comparatively to other studies, grain size obtained in the present work is lower. For

instance, a Nd:YAG mixture compacted at 300 MPa presents a grain size of 0.85, 1.6 and 2 µm at 1550 ° C for respectively 0, 5 and 10h of dwell time under vacuum condition. In our case, we obtain smaller grain size (0.38, 0.57 and 0.70) for the same conditions but with lower relative density values. At 1550 ° C for 10h and 20h, around 78% of relative density is obtained in our case against 92 and 94 % in the Ge *et al.* results [204]. This difference can be explained by the use of vacuum sintering which allows to reach higher density than conventional sintering method at same temperature.

The same observations were found for another study with a reactive powder to synthesis Nd:YAG. The authors reported a value of 94% for relative density at 1650 ° C for 2h with an average grain size between 3 and 3.5 µm under high vacuum sintering [205]. In our study, we performed the same result of relative density with a longer dwell time of 5h at 1650 ° C in air but with a smaller mean grain size only at 1.71 µm.

4. Conclusion

The goal of this study was to fabricate YAG ceramics by mixing alumina and yttria powder and determine the optimal parameters to obtain a good dispersion of species in the mixture. Through this study, 36 conditions of mixing and drying were tested and investigated by XRD, EDX and compacting leading to finally two best homogeneous mixtures.

After compaction, dilatometry study revealed the sintering behavior of the alumina and yttria mixture and solid reactive reactions occurred between 1000 and 1500 ° C followed by densification process after 1550 ° C. Finally, only the most dispersed mixture was selected to perform sintering under air and vacuum environment in order to obtain a sintering map. Alongside, phase composition was followed to know which phase is present in the specimen. The composition of specimen sintered in air at 1600 ° C for 5 h was only composed of YAG phase but the highest relative density value of 97 % was obtained after sintering at 1650 ° C for 20h.

Complementary sintering assays in high vacuum furnace were performed at 1600 ° C (5 and 10h) and 1780 ° C (10h). Denser specimens than specimen sintered in air furnace were obtained (99.3 % vs 88 % at 1600 ° C 10h). After high vacuum sintering, the porosity was still present in the specimen (≈1 %) and specimen was only opaque and translucent, depending on the sintering conditions. Additional HIP post-treatment was not adapted to improve the transparency on the density on previous samples.

To further improve the procedure, several solutions can be intended to improve solid state reactions and final density of the ceramic: improvement of the mixing method, optimization of sintering parameters in air or under vacuum condition, pre-calcination of powder to start SSRs, and the use of a sintering aid to improve sintering trajectory and reach higher level of density.

Chapter IV

Er:YAG composite ceramics processed by Spark Plasma Sintering

Preface

For the last years, yttrium aluminum garnet polycrystalline ceramics were used for laser applications owing to their interesting properties such as higher mechanical properties than glasses and single crystals, easier process for high dimensions parts than single crystals and especially the possibility to obtain doping gradient structure.

The occurrence of a high thermal gradient inside the homogeneous doped ceramic decreases the laser beam quality and limits the output power otherwise breaking of the laser slab occurs. It is why YAG composite ceramics presenting dopant gradient have recently been the focus of many research works since they could reduce the thermal gradient and improve the performance of high-average power lasers.

Several methods to manufacture composite ceramics have been reported in the literature such as dry pressing, slip casting, tape casting, crystal bonding or even the polycrystalline bonding as described in chapter 1.

The objective of our work was to test some of these methods and to apply them to Er:YAG ceramics. This chapter has been divided into 2 parts:

The first part presents the results obtained using the direct bonding of sintered samples with different dopant contents using high vacuum furnace and hot isostatic press techniques.

The second part is composed of an article draft on composite ceramics obtained by using the SPS method. Three different approaches were tested: i) stacking of various dopant contents powders, ii) stacking of pre-sintered specimens and iii) stacking of fully dense ceramics. Limitations and perspectives are discussed depending on the Er cation diffusion distances and the feasibility of the bonding method.

Direct bonding process in high vacuum furnace

The direct bonding process was inspired from laser crystal technology used to improve the contact strength in the optical contact process [210]. The two part surfaces are previously activated by chemical treatment or ion beam or plasma sputtering etching to favor a bonding at atomic level. The two parts bonding is carried out by ion diffusion during heat treatment.

Following this bonding technique, Fujioka *et al.* have fabricated a YAG/Yb^{+3}:YAG composite from two dense ceramics [175]. After mirror polishing, the sintered transparent ceramics were etched by Ar-FAB for 3 minutes. Samples were stacked and heated at 1400 °C under vacuum (2.10^{-3} Pa) during 10 hours and after bonding, the transparency was preserved [175]. Based on this publication, bonding experiments were performed studying bonding parameters and cohesion.

N °	Temperature (°C)	Holding time (h)	Heating rate (°C/min)	Weight applied	Cohesion
1	1400	10	10	no	no
2	1600	10	10	no	1 couple of sample was cohesive
3	1600	10	10	yes	yes

Table IV.1: Table resuming experiments of bonding sample in High Vacuum Furnace.

Several tests were done to check if cohesion between fully dense ceramics can occur in high vacuum furnace, but without previous surface activation between fully dense ceramics. As listed in Table IV.1, two temperatures (1400 and 1600 °C) and one holding time (10 hours) were used. For each experiment, 3 couples of previous 30-mm-diameter SPS sintered specimens were chosen for the stacking method. After mirror polishing (polishing procedure available in appendix), these fully dense specimens were stacked and placed on alumina crucible supports in the furnace. The sample stacks were heated up to dwell temperature with heating rate of 10 °C/min under vacuum between 10^{-1} to 10^{-5} Pa.

No cohesion between stacked specimens was observed after the thermal treatment at 1400 °C for 10 hours. The temperature was increased up to 1600 °C for the second attempt but only one couple of the stacks was cohesive. In order to improve the cohesion, the influence of load application by placing a weight of 220 g on the sample stacks was tested. After procedure, all assemblies were cohesive, as presented in the photograph in Fig. IV.1. The specimen in the center was cut in two to observe the cross-section of the bonding. Before the thermal treatment, the stack (c) was composed of one complete sample and the upper sample already broken in two pieces. During the treatment a weight was put on the sample stack to favor bonding. However, after the treatment only half of the upper sample was bonded to the lower one. An inhomogeneous applied load could explain the half cohesive sample (Fig. IV.1-c3).

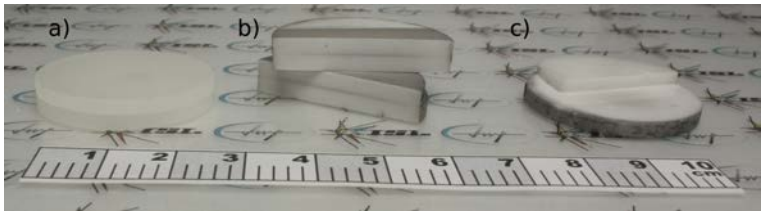

Figure IV.1: Photograph of the 3 couples of samples which are bonded after the 1600 ° C 10h treatment in High Vacuum Furnace.

In conclusion, this serie of experiments has shown the interest to add a pressure, even a low one on the sample stacking to favor the cohesion during the vacuum thermal treatment.

In order to test the bonding technique with fully dense samples, the HIP technology seemed interesting owing to the isostatic way to apply the pressure which guarantees a pressure uniformity.

Direct bonding process in hot isostatic press

Three couples of fully dense samples previously sintered by SPS were placed in the HIP furnace.

The isostatic pressure was fixed at 1900 bars under Ar atmosphere in a graphite furnace, the temperature was increased to 1800 ° C and was maintained during 10h to ensure the cohesion between samples. After the cycle, all obtained assemblies were cohesive and the result is shown in the Fig. IV.2. Samples were named from left to right: C1, C2 and C3 corresponding to each specimen couple. The upper row shows samples after HIP treatment and the lower after additional annealing for 1 h at 900 ° C under air atmosphere.

After assembling by HIP, samples were darker than before possibly due to the carbon contamination. The difference of coloration between before and after HIP treated samples is illustrated in the Fig. IV.2 C2, where the white part is the sample before the HIP treatment. Further observations showed that sample surface in contact with the support presented large grains as shown in the Fig. IV.3. The temperature at the surface of the support was too high and could lead to extreme grain growth.

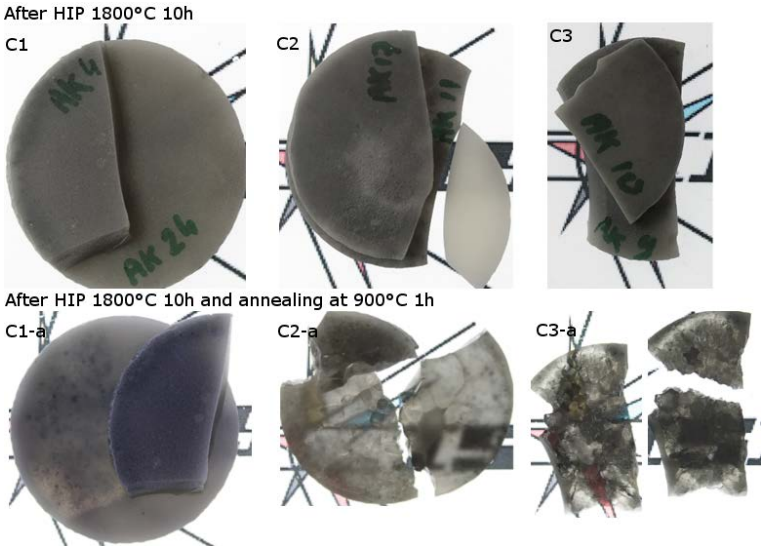

Figure IV.2: HIP experiment to bond samples at 1800 ˚ C 10h and the annealing result at 900 ˚ C 1h.

A post-treatment in air was applied on samples to remove the carbon pollution. The annealing was performed at 900 ˚ C during 1h in air (Fig. IV.2 lower row). After this thermal treatment, C2-a and C3-a samples were found completely broken in multiple parts. The two samples of C1 stack were entire but detached and the shape of the on-top sample is still visible on the sample below. The C2-a sample is translucent and cracks seem to be formed at the surface of the sample. The last sample C3-a is completely broken after annealing but the transparency was improved.



Figure IV.3: Picture of the sample C2, the side in contact with HIP support.

The reason of the sample breakage can be due to a rough sample surface resulting in trapped Ar bubbles at the interface between the two samples during HIP treatment. Zhang *et al.* have shown the formation of of Ar bubbles located in triple junction of grain in Nd:LuAG ceramics after a HIP post-treatment in argon [132]. These bubbles can be

responsible of the breaking of the sample: during the annealing process, the dilation of the Ar gas trapped between the interface lead to the break of the assembly.

The HIP process is effective to apply a isostatic pressure and ensure the cohesion of samples.

In conclusion, this first series of experiments tested the possibility of directly bonding the sintered samples. Several lessons can be drawn from these tests: the first is the application of a pressure contributes to obtaining cohesive samples. Secondly, applying a HIP post-processing allows a cohesive sample but can trap Ar bubbles at the interface. From these observations, the combination of a high vacuum that avoids the formation of gas bubbles and the application of pressure could promote cohesion. Thus, the use of Spark Plasma Sintering makes it possible to achieve these two conditions. The bonding of sintered samples by SPS is presented in the second part of the chapter. The article presented is devoted to different methods to obtain Er: YAG composite ceramics by SPS technology.

Er:YAG composite ceramics processed by Spark Plasma Sintering

Abstract

Multiple approaches were used to obtain Er:YAG ceramics with dopant gradient by Spark Plasma Sintering starting from different raw materials: powders, presintered ceramics and fully dense ceramics. Adapted SPS experimental parameters allowed the achievement of Er:YAG/YAG ceramics presenting a transparency of 81 % at 2550 nm and a thickness of 4.3 mm by powder approach. Fully dense ceramics and pre-sintered ceramics approaches were also investigated and led to obtain a polycrystalline ceramic with a doping gradient with a high transparency. EPMA analysis were performed on composite structure to measure grain-boundary diffusion of Er ions. Lengths of diffusion of 12, 141, and 194 µm were obtained for fully dense, powder and pre-sintered approaches, respectively.

1. Introduction

For the last few decades, the interest in transparent ceramics (TCs) has been growing due to their multiple applications such as armoured windshields, detector domes or gain media for High Energy Laser (HEL) [79, 211]. Especially, in the laser domain, efforts were made to replace currently used crystal host matrix by transparent ceramics to improve laser performances. In this specific area, Er:YAG ($Er^{3+} : Y_3Al_5O_{12}$) polycrystalline ceramics have several advantages: better thermo-mechanical properties, a lower synthesis temperature and higher doping contents compared to single crystal. Besides the cubic structure, Er:YAG is an interesting material due to its emission at 1.6 µm, a so-called "eye safe" wavelength, which allows numerous uses *i.e.* in defense, surgery or metal cutting [52, 212]. Nowadays, Er:YAG single crystals used as gain medium have limited performances due to thermal lenses created in the laser cavity. This effect impacts the beam quality and the laser performances [25]. To overcome this problem and obtain better performances, the solution is to develop a gain medium with a doping gradient, which is possible with TCs. In addition, this TC must possess an optimal quality close to the theoretical transparency. Ikesue *et al.* have shown a better heat distribution during the lasing time with a doping gradient in a Nd:YAG ceramic in comparison to the homogeneous doped one [45]. Multiple approaches such as tape casting [169, 171, 213], hot molding [214], pressure assisted sintering [215], laser cladding [216], or field assisted sintering [217] have been used to fabricate this type of composite structures.

A previous study has shown the successfully sintering of transparent Er:YAG ceramics by Spark Plasma sintering (SPS) with a slope efficiency of $\sim 31\%$ [176]. In this present work, different approaches were investigated to fabricate Er:YAG doping gradient ceramics by SPS, starting either from powders, pre-sintered samples or fully dense ceramics.

The first approach consists in stacking several layers of undoped and doped YAG powders in different configurations into the SPS graphite die. The second route deals with presintered samples previously obtained by a first SPS cycle with a temperature lower than the sintering temperature. The third approach involves stacking fully dense ceramics directly into the SPS die and applying pressure and during a second SPS treatment to generate cohesion. The general strategy of this study is illustrated in Fig. IV.4. These approaches will be compared in terms of feasibility and transparency of the obtained composite ceramics.

2. Experimental

Commercial YAG and Er:YAG powders (>99.999%, batches #2AM104C, #2AM152A) were supplied by Nanocerox (USA). These powders were used for the presintered samples and the powder assembly approach. For fully dense sample approach, powder from Baïkowski (batch #20238, 21998) or Nanocerox were used. These two batches of Baïkowski powder showed a stoichiometry that is not suitable to reach a very good transparency, but as the aim of this study was to assess the feasibility of the process, this choice seemed appropriate for first experiments. The powder was mixed and crushed in a mortar with LiF as sintering aid (Sigma aldrich, 99.995%) and introduced into a graphite die. The amount of LiF was set at 0.25 wt% in all assays [27]. SPS cycles were performed under vacuum using a HP D 125 SPS facility from FCT Systeme GmbH (Rauenstein, Germany). The temperature was controlled by an optical pyrometer focused on the upper graphite punch. The inner diameter of the SPS graphite matrix is 30 mm and graphite foils were inserted to facilitate the ejection of the sintered ceramic and in addition avoid the reaction between the powder and the graphite tools. The SPS cycle used in this study was optimized in a previous work with a sintering temperature of 1450 ° C [67] and called thereafter reference cycle.

After SPS cycle, a HIP post-treatment (EPSI, Inc.) at 1400 ° C for 15h under 1900 bars was performed, which lead to a transparency of 84%±1.5% (2.1 mm thickness) for an homogeneous doped ceramic [20].

Three approaches were explored:

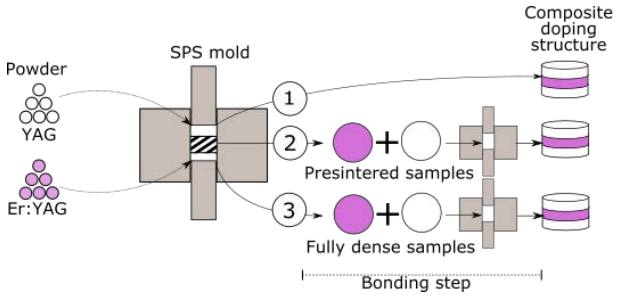

Figure IV.4: General strategy used in this study.

- For the powder assembly approach, the ground LiF-YAG-powder or LiF-Er:YAG-powder was directly poured in the graphite die. For the bi-layer (Fig. IV.5- specimen a) or the sandwich like structure (Fig. IV.5- specimen b), the different layers of powder were poured and gently smoothed with a vibrating table. For half sided specimen (Fig. IV.5- specimen c) or clad-core design (Fig. IV.5- specimen d), a brass foil was used as separator to obtain a sharp separation between doped and undoped powders and was removed before sintering. Powder assemblies were sintered with the reference cycle and mirror polished with the procedure described in appendix G. Specimen were cut in half by an automatic saw (Buehler isomet 4000). Different HIP post-treatments were applied on the sintered specimens: 1) 1400 ° C for 10h, 2) 1400 ° C for 15h and 3) 2x1400 ° C for 15h to further improve the optical quality. The condition 3) corresponds to the application of a second HIP post-treatment on the specimen, which underwent condition 2).

- For presintered samples, ceramics were firstly pre-sintered with a derived SPS cycle from the reference one. Instead of applying the whole SPS reference cycle, ceramics were sintered up to 1320 ˚ C without dwell time. This temperature corresponds to the maximum shrinkage rate peak of the reference cycle. Each sample was made of either YAG powder or Er:YAG. Samples were mirror polished and the diameter of samples was reduced by polishing the edges of sample, which facilitates the introduction of the specimen inside the SPS matrix. Samples with various dopant contents were stacked in the graphite die between punches and a second SPS treatment was conducted up to 1450 ˚ C for 2 hours, in order to bind the different pre-sintered samples. This time, a cycle without intermediate dwell time at 950 and 1200 ˚ C was performed, the final holding time at 1450 ˚ C for 2h was kept to finish the densification.
- The last approach involved assembly of fully-dense samples. Each YAG or Er:YAG sample was prepared according to the procedure described in the "pre-sintered assembly" approach, but sintered with reference cycle. SPS sintered samples were mirror polished and stacked in the graphite matrix and a second SPS cycle was applied. Several final assembling temperatures were tested: 1100, 1200, 1300 and 1450 ˚ C in parallel the dwell time was also varied from 0, 15 and 240 min.

Archimedes method was used to determine the density of final samples. In-Line Transmission (ILT) measurements were performed from 300 to 3000 nm with a UV-vis-IR spectrophotometer (Cary 7000 UMS, Agilent Technologies). To determine the Er ions diffusion between Er:YAG and YAG ceramics, EPMA measurement was performed at Institut Jean Lamour at Nancy (France).

3. Results and discussion

3.1. Powder assembly

Multiple architectures were tested following the approach presented in the schema in the upper row of Fig. IV.5.

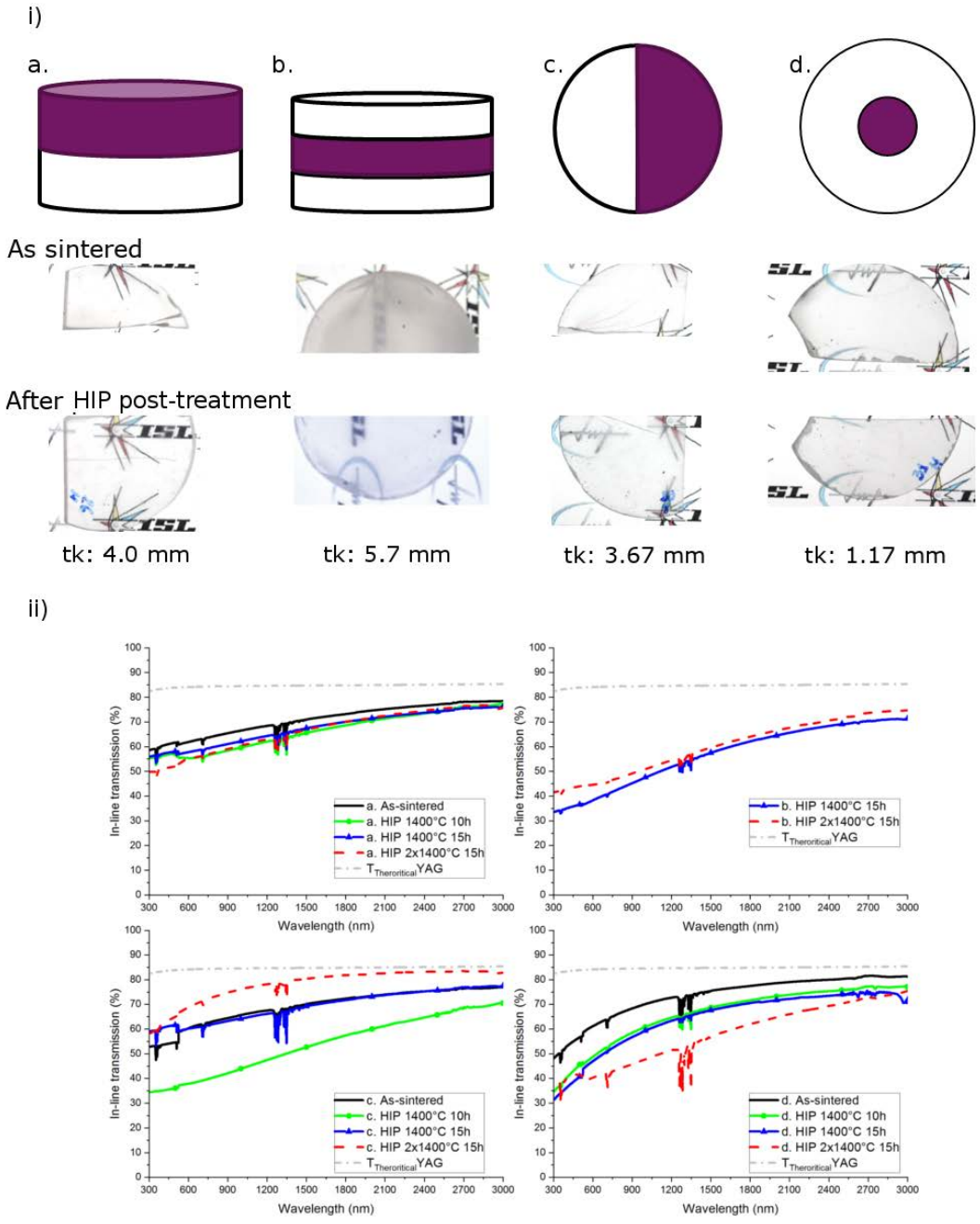

Figure IV.5: i) Different designs tested with the powder assembly approach: a. bilayer b. sandwich like c. half sided and d. clad core design, corresponding to samples after sintering (line), after a first HIP post treatment (blue and green line) and after twice HIP post-treatments at 1400 °C 15h (dashed line). ii)In-line transmission corresponding to powder assembly approach.

Results are illustrated on the same figure by pictures of the samples after sintering and HIP post-treatment with the corresponding thicknesses. A summary of HIP post-treatment is provided in Table IV.2.

3 of 4 samples were transparent directly after the SPS cycle: the bilayer, the half sided and the clad core specimens. The translucent specimen corresponds to the sandwich layer and is also the thickest one (Fig. IV.5- specimen b)).

Sample	Post-treatment cycle		
	1) 1400 °C 10h	2) 1400 °C 15h	3) 2× 1400 °C 15h
a) bilayer	x	x	x
b) sandwich		x	x
c) half sided	x	x	x
d) clad-core	x	x	x

Table IV.2: Summary of HIP post-treatement on powder assemblies.

Pictures of the samples after HIP post-treatment with condition 3 (2 × 1400 °C for 15 h) are shown in the second line in Fig. IV.5. In-Line transmission results after HIP post-treatments are plotted in Fig. IV.5.

After thorough visual observations of the specimen b) some white clouds are noticed in the bulk material and on the surface. These defects may be caused by non-adapted SPS cycle. Parameters during the sintering such as the heating rate, intermediate dwell time, temperature of pressure application and pressure are crucial to let the LiF escape from the specimen before pore closure and the final densification as reported by Katz *et al.* [67]. Optimization of sintering parameters leads to reduce defect occurrence and contributes to decrease absorption phenomena and scattering effect in the final ceramic. When the thickness of the ceramic is more important (>4 mm), defects can be present caused by a thermal gradient in the sample during sintering due to non adapted dwell times to let escapade the sintering aid LiF [20]. Heating rate and dwell time of the reference cycle were adapted to obtain a high transparent ceramic with a thickness of 3 mm. The non-adapted SPS cycle could explain the visual aspect of the thicker sample (Fig. IV.5- specimen b). Additionally, SPS method uses uniaxial pressure to consolidate the powder and facilitate the densification. More the amount of powder is important in the graphite mold more the compaction will lead to formation of density gradient and therefore different sintering behavior inside the green body.

Residual LiF can be responsible for defects due to local abnormal grain growth [218]. A low proportion of LiF entrapped in grain boundaries locally impacts the chemical composition and has an influence on grain growth, resulting in a loss of transparency [67]. To overcome this problem, the first solution is to adapt the amount of LiF and improve the homogeneity of the mixture between the YAG powder and the sintering aid.

Each sample was cut in two pieces to perform post-treatments on each side.

For the sample a) in Fig. IV.5, HIP post-treatment did not eliminate all defects present in the ceramic. The first HIP treatment (10h) tends to decrease the transmittance, whereas the HIP treatment with a longer holding time (15h) lead to comparative result as "as sintered" sample. The supplementary post-treatment (2x HIP 1400 °C 15h) downgradded ILT results compared to as sintered samples IV.5.

In the case of the specimen b), the thickest sample, only condition 3 HIP post-treatment

with two successive HIPs at 1400 ° C for 15h was applied. This condition slightly improves the transparency of the ceramic but only 60 % of ILT was measured (Fig. IV.5- specimen b).

For the specimen c), there was no improvement of ILT after HIP condition 1 and 2 and HIP post-treatment number 3 was beneficial to reach higher transparency. The post-treatments at 1400 ° C during 10h and 15h did not improve the transparency.

For the specimen d), ILT measurements were already elevated after SPS and additional HIP was detrimental to the transparency.

Globally, a shorter post-treatment can lead to a more homogeneous distribution of the defects in the bulk material and a longer treatment can favor the diffusion and the coalescence of residual small pores whose are responsible for the loss of ILT [219]. The post-HIP treatment has an important role to decrease defects and the combination between temperature and holding time is crucial. If post-treatment conditions are not adapted such as an overlong process or too high temperatures, it tends to create defects and therefore impacts the final transmission of the ceramic.

Several hypotheses can be exposed here to explain ILT measurements. HIP post-treatment can impact the transparency of specimen for different reasons. Pore coalescence due to high temperature and long dwell time leads to bigger pores and increases the scattering effect, which drastically impacts the transparency [71]. Another possible explanation could be the creation of porosity at the interface between the two powder layers. Indeed, the Er:YAG powder seems to present higher flowability than undoped one which could contribute to form two different particle arrangements once the compaction is applied.

Finally, a thick sample was fabricated by powder approach with 18 g of Nanocerox Er:YAG and YAG powders. The structure composed of 3 layers of 6 g of powder from 0.47 wt%, 0.235 wt% to 0 wt% of Er^{3+} doping is represented in Fig. IV.6.

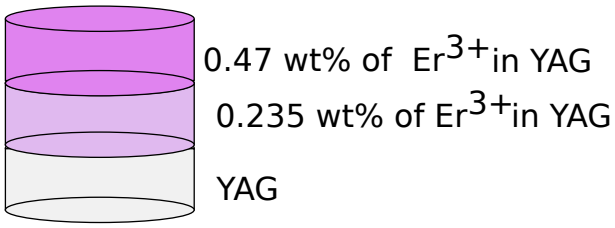

Figure IV.6: Scheme of organization of 3 layers of different doped powders for the powder approach.

The intermediate layer at 0.235 wt% of Er was obtained by mixing Er:YAG and YAG powders at 50:50 mass ratio. Each of the powder was independently mixed with 0.25 wt% of LiF to guarantee the distribution of LiF sintering aid in all layers of powder. Graphite die was filled alternatively with one of the three powders and reference SPS cycle was performed. After sintering, the sample is translucent and presents white opaque spots inside the bulk (Fig. IV.7).



Figure IV.7: SPS sintered specimen obtained from the 3 layers of powder (0.47 wt% / 0.235 wt% / 0 wt%). (30 mm diameter, thickness: 4.3 mm).

A considerable improvement of the transparency is achieved by post-processing HIP with condition 2 (Fig. IV.8). The transparency increased from 2% to 63% at 500 nm and from 67% to 79% at 2000 nm after post-HIP. The highest transmission of 81% was obtained at 2550 nm.

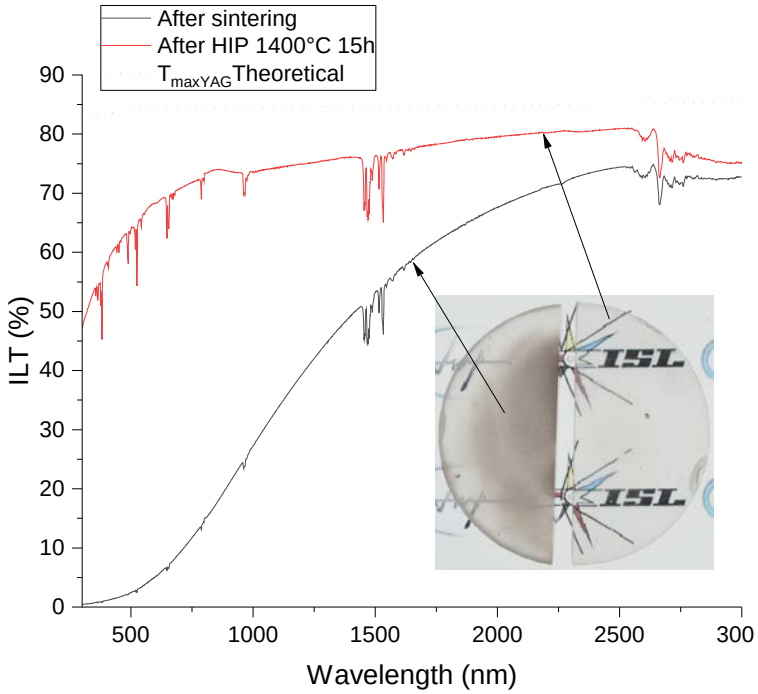

Figure IV.8: ILT measurements after SPS and after HIP post-treatment at 1400 ° C for 15h with attached picture of the corresponding specimen. (thickness: 4.3 mm)

The table IV.3 presents a comparison of results obtained in the literature for YAG homogeneous doped ceramics with the result obtained in this study. In 2016, Katz obtained first thick Er:YAG ceramics with high transparency by SPS approach [20]. In this

study, a good optical quality with composite doping structure was obtained. Nevertheless, slightly lower ILT values than for homogeneous doped YAG specimens was obtained. This means that the bonding of 3 layers of powder with different dopant concentration sintered by the SPS powder is very promising. To improve a better transparency, several parameters can be optimized during the preparation of the powder, the SPS cycle and the HIP post-treatment.

Authors	Ceramic	Specimen size (mm)	ILT at 1100 nm (%) for normalized thickness at 3 mm
Zhou *et al.* (2011)	Er:YAG	diameter:=20, tk: 2	84
Li*et al.* (2012)	Nd:YAG	diameter=23, tk: 3.5	83
Qin*et al.* (2012)	Er:YAG	diameter=15, tk: 3	84.1
Cavalli*et al.* (2013)	Er:YAG	diameter=10, tk: 2-3	79.8
Liu*et al.* (2014)	Nd:YAG	diameter=16, tk: 4.8	83
Katz (2016)	Er:YAG	**diameter=30, tk: 3.4**	**81±1.5**
This study	Er:YAG / YAG	diameter=30, tk: 4.3	77±1.5

Table IV.3: ILT measurements for Er:YAG ceramics obtained by SPS (Katz and this study) and other from the literature by conventional sintering. All transmission values were normalized at 3 mm.

Bilayer, sandwich, half sided and clad core architecture were successfully obtained by SPS approach. It was shown that transparent composite ceramics can be achieved in one step procedure. Further improvements could be done concerning the filling of the powders into the graphite mold and adjusting of the SPS parameters in order to increase the thickness and the diameter of the sample. A scale-up to increase thickness and diameter (30-50-80 mm) is possible.

3.2. Presintered samples

After the first SPS cycle, two opaque A and B samples with a relative density close to 99% were obtained and are presented in Fig. IV.9. It is noteworthy that the samples had a transparent periphery due to higher density in this area. This indicates that defects were probably caused by temperature gradient and the applied pressure by punches. Previously, computer simulation of SPS sintering revealed the possible presence of a temperature gradient of 34 °between the center and the edge of the specimen [20]. Graphite punches and matrix are generally hotter than the specimen which explains the higher temperature at sample periphery and the transparent aspect.

After the second SPS cycle, where the assembling and the final densification of presintered ceramics took place, a translucent ceramic with 2.8 mm in thickness and 30 mm in diameter was obtained. After annealing at 1100 °C for 1h in air, the obtained sample was transparent but some defects were also visible (Fig. IV.9-c). These defects have hypothetically formed at the interface between the two assembled samples. Black dots inside the ceramic can be due to the preparation step, as pieces of graphite foil might have fallen between the two samples when they were stacked in the graphite matrix. We can also observe some fibers coming from the graphite felt on the same figure. The ILT measurement revealed a transmission of 59.9 % at 1064 nm in the center of the sample.

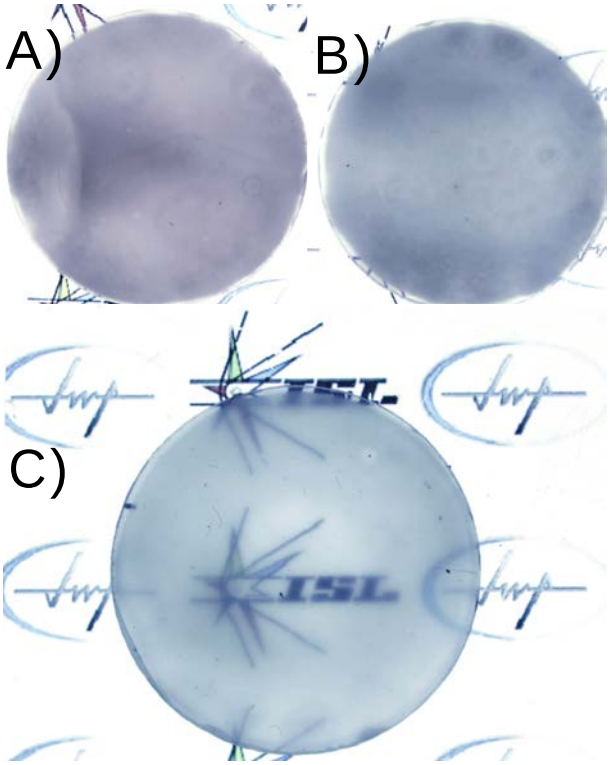

Figure IV.9: A and B pre-sintered samples by SPS and C sample obtained by assembly of the 2 previous samples by a second SPS (30mm diameter).

3.3. Fully dense ceramics

Fully dense ceramics are used to prepare Er:YAG/YAG bilayer ceramics. The tested conditions are summarized in Table IV.4 and corresponding samples are presented in Fig. IV.10.

A first series of bonding experiments were carried out with SPS samples processed with the Baïkowski powder presenting a lower purity level than Nanocerox one.

Sample	Final temperature (°C)	Holding time (min)	Conditions	Powder origin	Cohesion	Entire
A	1450	240	polishing until 3µm	Baïkowski	yes	no
B	1100	15	polishing until 3µm	Baïkowski	no	no
C	1200	15	polishing until 3µm	Baïkowski	partial	yes
D	1200	15	+V.T.	Baïkowski	yes	no
E	1200	30	+V.T.	Baïkowski	yes	no
F	1200	30	+V.T. + thick and thin samples	Baïkowski	yes	no
G	1300	0	+VT	Baïkowski	yes	yes
H	1300	0	+VT	Nanocerox	yes	no
I	1200	30	+V.T.+adapted sintering tools	Nanocerox	yes	no
J	1300	0	+V.T.+adapted sintering tools	Nanocerox	yes	yes

Table IV.4: Experimental conditions for fully dense ceramic assembly. (V.T. = Vibrating Table))

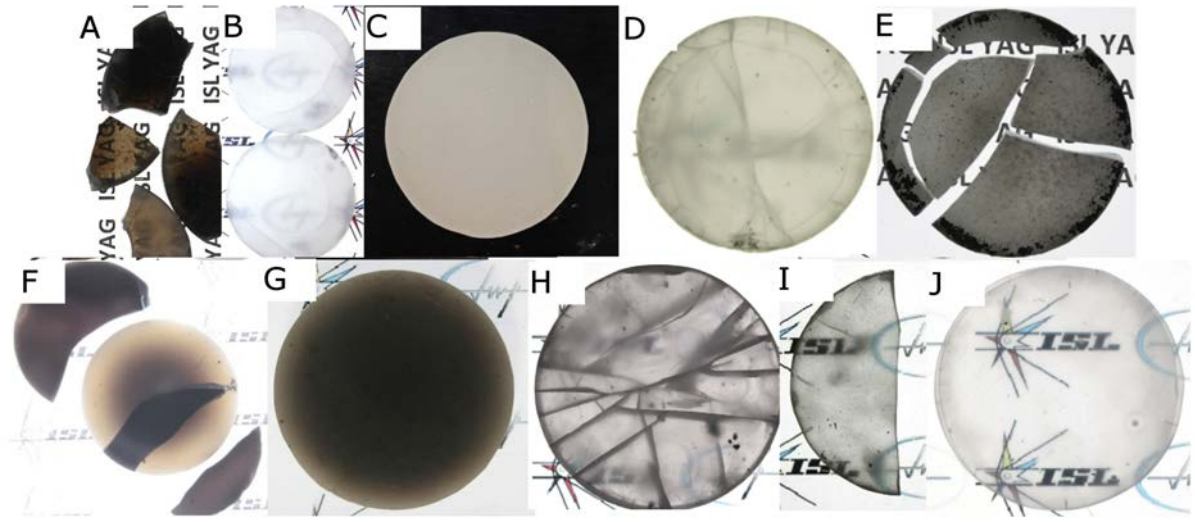

Figure IV.10: Pictures of SPS assembled with 30-mm-diameter fully dense sample.

The first assay was conducted at 1450 ˚ C for 240 minutes with a pressure of 40 MPa applied between 1000 and 1200 ˚ C to ensure the cohesion. This treatment was not suitable, as the sample was completely shattered (see Fig. IV.10-A). Therefore, lower temperatures were used for the two following experiments to check the minimal temperature and time with 1100 ˚ C-15 min-40 MPa and 1200 ˚ C-15 min-40 MPa respectively for samples B and C (Fig. IV.10). For B , no cohesion was observed at 1100 ˚ C, whereas for C the two samples was bonded together and entire. After further analysis by cutting the sample in two, only a small bonded area was observed (circle in Fig. IV.11).

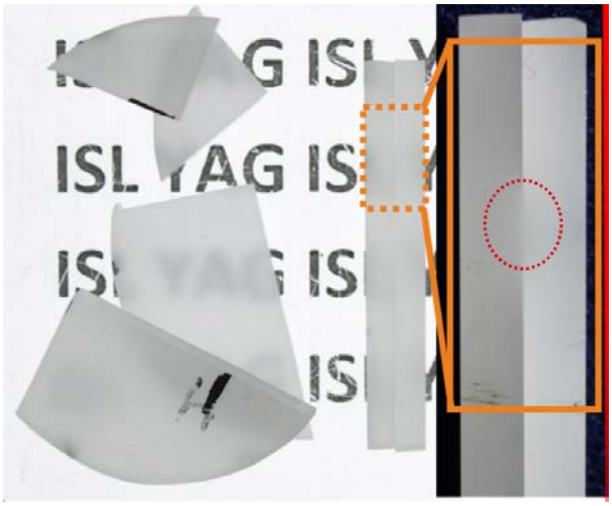

Figure IV.11: Sample C after cutting. One point of cohesion was observed.

So, to improve the surface quality of the samples, a supplementary polishing step by vibrating table was added for following samples[1]. For sample D, the added polishing step allowed to obtain an unbroken and completely bonded sample. Nevertheless, some cracks appeared on the surface despite the fact that the two ceramics are bonded. The

[1]The complete polishing procedure is described in appendix G

poor mechanical resistance of the sample is certainly due to uniaxial constraints generated during the SPS cycle. Two phenomena can be destructive:

- The uniaxial pressure applied by graphite SPS tools is not perfectly homgeneous. Indeed, the graphite punch is pierced in its center to allow the temperature measurement by the pyrometer at a distance as close as possible to the specimen. At this area, the graphite thickness is only 3 mm (Fig. IV.12 and Fig. IV.13-A). Another explanation of cracks formation could be parallelism defects (caused by the polishing step) between the two sample surfaces which could cause a non-homogeneous pressure application (Fig. IV.13-B).
- The thermal expansion mismatch between YAG and graphite induces stresses at high temperature. Moreover, as the sample is not perfectly round only some parts of the sample edge are likely to be in contact with the matrix which generates additional stresses.

For the specimen E, the dwell time was increased from 15 to 30 min, which resulted into a bonded but broken sample. The punch geometry seems to have been the main cause of the breakage in view of the particular shape of cracks.

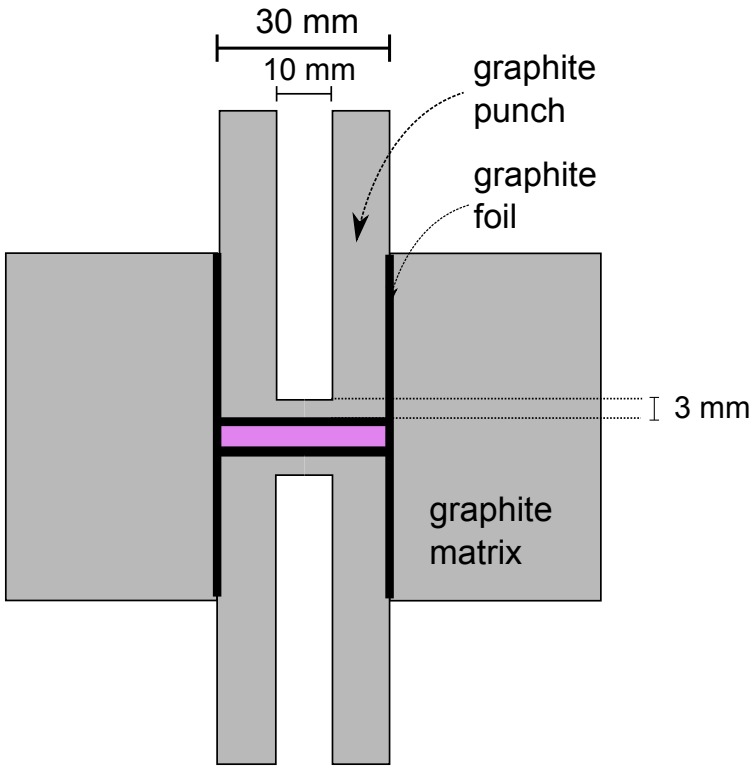

Figure IV.12: Schema of graphite punches and matrix used in this study.

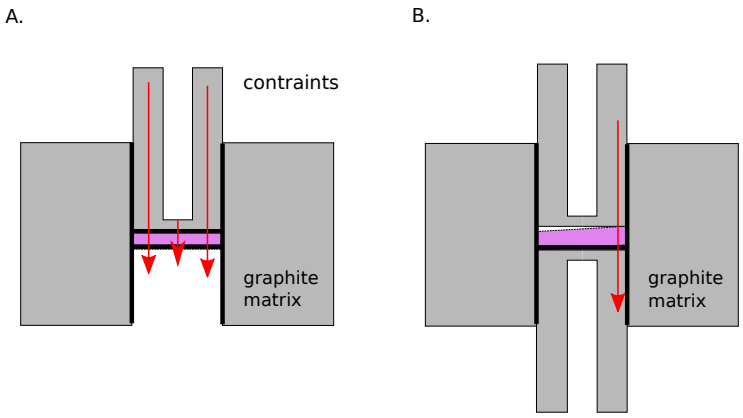

Figure IV.13: Scheme of possible explanation of cracks formation due to A. inhomogeneous pressure application and differential expansion of graphite and B. bad parallelism between the two surfaces of the sample.

A higher thickness can be helpful to sustain the load during the pressing. Therefore, the same SPS cycle was applied on a sample composed of stacking of a thicker layer (5 mm) and a thin layer (2 mm). During bonding, the small sample broke but the thick one stayed entire. A small part of the thin sample is bonded to the thicker sample but other parts are completely broken and not linked to the other part. It shows that applied constraints were too high during SPS cycles for the thin layer (2 mm) whereas the thicker layer could sustain high pressure without cracking.

The temperature was increased up to 1300 ° C for the G sample but without dwell time (Fig. IV.10). An entire and completely cohesive specimen was successfully obtained.

A second serie of bonding experiments were processed with fully dense transparent samples prepared from the high purity powder (Nanocerox). The optimized temperature and pressure conditions of the cycle G of the first serie of experiments were used for the specimen H (Fig. IV.10), which resulted in a cohesive but shattered sample. Visually, the breaking path was different from previous broken samples. Cracks are now transverse through the sample and no more circular around the graphite punch.

Two last conditions at 1200 ° C for 30' and 1300 ° C without dwell time were tested with an adaptation of sintering tools to avoid constraints exerted on the dense ceramics. Furthermore, the edges of ceramics were polished to allow a good introduction into the die. An improvement was reached for the sample I, bonded at 1200 ° C as the sample was only broken in two equal parts. Nevertheless, the two parts were cohesive and moreover the sample was transparent, despite some defects and grey color due to carbon contamination. As shown for the assembly at 1300 ° C (Specimen J in Fig. IV.10.), higher temperature (1300 ° C) was beneficial to obtain a transparent sample. However, small cracks are visible on the specimen periphery which shows the presence of compression load at these areas during the cycle, as shown in Fig. IV.14 (red circles). A transparency of 50 % was obtained by ILT measurement at 1100 nm.

A possible explanation of the formation of cracks can be the thermal gradient existence revealed in the previous approaches (presintered and powder). The temperature is higher around the sample than in the center which results to a differential expansion. These differences of expansion may lead to explain crack formation at the periphery of the

sample J.

In conclusion, the development of a constraint-free assembly of SPS parts is difficult because of the thermal expansion of graphite tools and long preparation steps are needed to prepare the bonding surface.

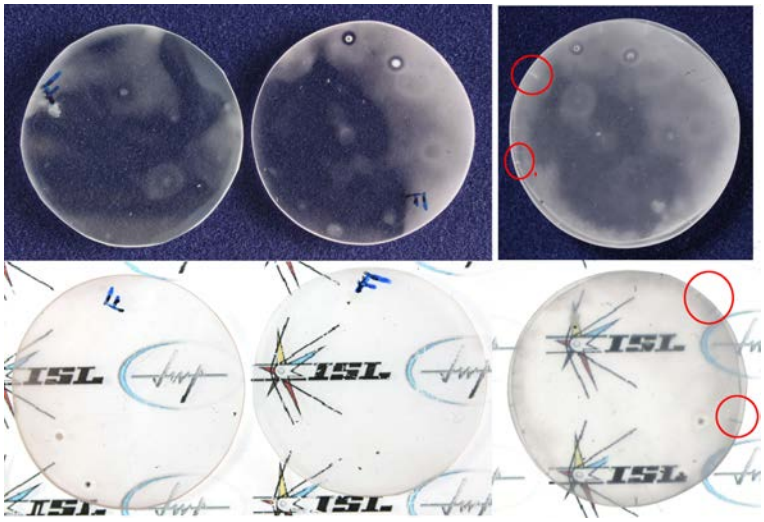

Figure IV.14: Sample J : Two left samples before bonding, and after the bonding at the right, on dark background and on light table. (F mark stands for the polished side before the stacking step). Red circles highlight cracks formed at the periphery of the specimen.

3.4. Limitations and advantages

Development of composite structures by SPS exhibits some limitations and advantages, dependent on the chosen approach. An overview of improvement and perspectives will be discussed in this part.

The assembling of presintered and fully sintered samples by SPS led to samples not uniformly transparent or with cracks in most cases. The load application on samples was not homogeneous due to geometry of punches as revealed by sample E in Fig. IV.10.

Another important fact, which has to be taken into account, is the thickness of the used ceramics for the assembly. As high pressure can be sustained by thicker samples (>5 mm, specimen E, Fig. IV.10), thinner samples were too fragile to resist. For presintered samples, a closer observation showed some cracks in the periphery of the sample. These cracks can find their origin in combination of the thermal gradient and the pressure exerted by punches.

Contrary to presintered and fully sintered sample approaches, the approach by powder assembly was not limited to process thin specimens. Highly transparent specimens with 1 mm of thickness were successfully obtained (sample d in Fig. IV.5) from powder but in case of obtaining thicker samples (>3.5 mm), some optical defects were observed. The increase of thickness leads to bad heat distribution inside the specimen. These differences in terms of temperature or pressure is shown by the different optical qualities of the specimens obtained by the powder approach. The thickness of the specimens ranges from 1.17 mm to 5.7 mm. As shown by Katz *et al.*, SPS cycle has to be optimized to obtain

a homogeneous transparent ceramic, when either thickness or diameter of the ceramics is increased (specimen b Fig. IV.5).

The solution to overcome the formation of opaque area in thick samples after the SPS, without additional post-treatment, is to adapt the SPS cycle. By this way, reducing the heating rate and increasing the dwell time will potentially improve the transparency of sintered specimens. A longer dwell time at 1450 °C should be a more interesting alternative but it has to take into account the carbon diffusion which is more important at high temperature. The proposed method in this work is also attractive due to sintering 2h at 1450 °C followed by HIP at 1400 °C for 15 h to finish the densification in a carbon-free environment (powder bed).

In conclusion, to process thick composite samples with the powder approach, SPS can be used to obtain in a first step 3-mm-thick samples (or a bit thicker) and in combination with HIP process in a second step.

Fabrication of Er^{3+}:YAG/YAG composite by SPS was successful and despite the limitation of the thickness of the composite sample, the powder assembly approach presents several advantages:

- It is a one step process.
- It is not necessary to polish the presintered or sintered samples before bonding operation
- In contrary to other approaches, less steps are needed to achieved a composite and less pollution is induced.
- Powder assembly is more suitable for fabricating complex architectures such as sandwich or clad-core design. However, the achievement of these particular designs needs some accessories in order to get a distinct separation between the different powder layers. In the case of fully dense or pre-sintered samples approaches, complex architectures are more difficult to obtain due to the control of each step of development from the sintering, cutting and stacking.

A summary of the discussed arguments is presented in Table IV.5.

Arguments	Fully dense samples	Pre-sintered samples	Powders
Bonding of thick samples (>3mm)	yes	no	no
Bonding of thin samples (<2mm)	no	no	yes
Preparation step before stacking	yes	yes	no
One step process	no	no	yes
Variety of architecture	no	no	yes

Table IV.5: Arguments of different doping gradient routes.

Diffusion of Er^{3+} ions at Er:YAG /YAG interface

For laser applications, the specimen should present a gradient of the doping element as smooth as possible, in order to obtain a better heat dissipation in the gain medium. In the general strategy, the chosen approach has to consider the profile of doped ions diffusion to conclude the comparison between the 3 approaches. Most promising samples

were chosen to perform EPMA measurements in order to determine the diffusion lengths at the interface.

For the powder approach, the 3 powder layer design with 3g/3g/3g of Er:YAG and YAG powders (Nanocerox) were chosen. This design was the same as presented in section 3.1. and is represented in Fig. IV.16. The three layers are constituted of 0.47 wt%Er (0.25 at%)/ 0.235 wt%Er (0.125 at%)/ pure YAG respectively. The intermediate layer was obtained by mixing together the two commercial powders (0.25 at% and YAG pure) to obtain a doping level at 0.235 wt%. The amount of LiF used is the same as used previously (0.25 wt%). The transparent sample obtain by SPS is presented in the Fig. IV.15. ILT measurements indicated a transparency of 77% ±1% at 1100 nm. The sample is thin with a thickness around 1.85 mm and presents some cloudy area and black spots. The sample was obtained by the same SPS reference cycle optimized for 3 mm thick ceramic. Indeed, SPS conditions are not adapted for a final thickness of 1.85 mm and result in an increase of C pollution in the sintered ceramics after the complete elimination of LiF. In other words, SPS cycle has to be adapted to the amount of LiF, to be not too short to let the whole sintering aid escapes from the ceramics and not too long to remove the LiF and let the carbon diffuse in the material. Here, the SPS cycle was a little too long and darker shades are visible corresponding to the presence of carbon.

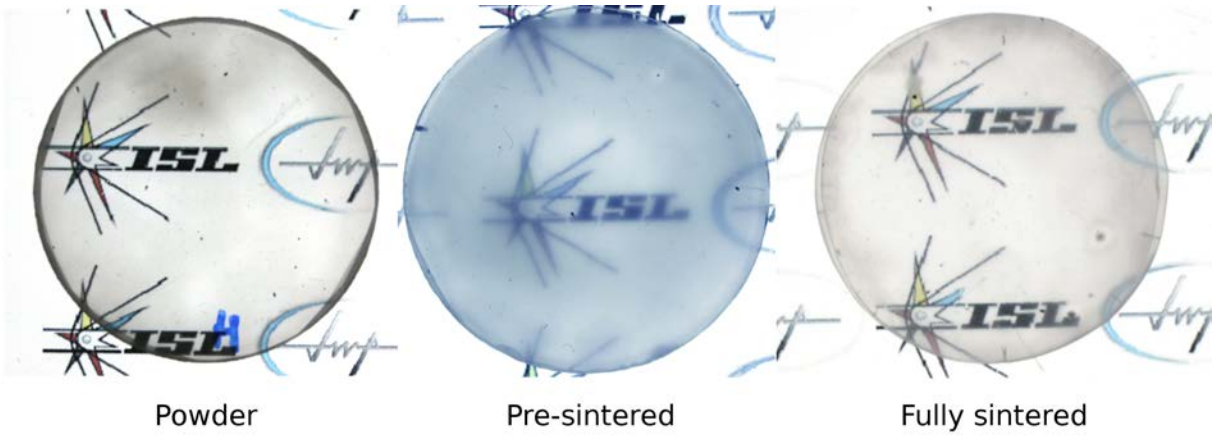

Figure IV.15: Picture of the samples selected for the EPMA measure. (30 mm diameter)

The following EPMA measurement presented in Fig. IV.16. shows the distribution of Er ions through the two different interfaces: 0.47 wt%/0.235 wt% and 0.235 wt%/0 wt%. From the measured point (Er concentration), the length of diffusion can be determined from the last point of doped region to the first point of undoped ceramic. In this case, the length of diffusion is evaluated at 140 and 120 µm from the two steps (between 0.47 wt%/0.235 wt% and 0.235 wt%/0 wt%). As observed, the intermediate step is not constant and fluctuation of the Er ions is visible. This is certainly due to the filling step and the non-planarity of the powder layer when the second or third layer is poured into the mold.

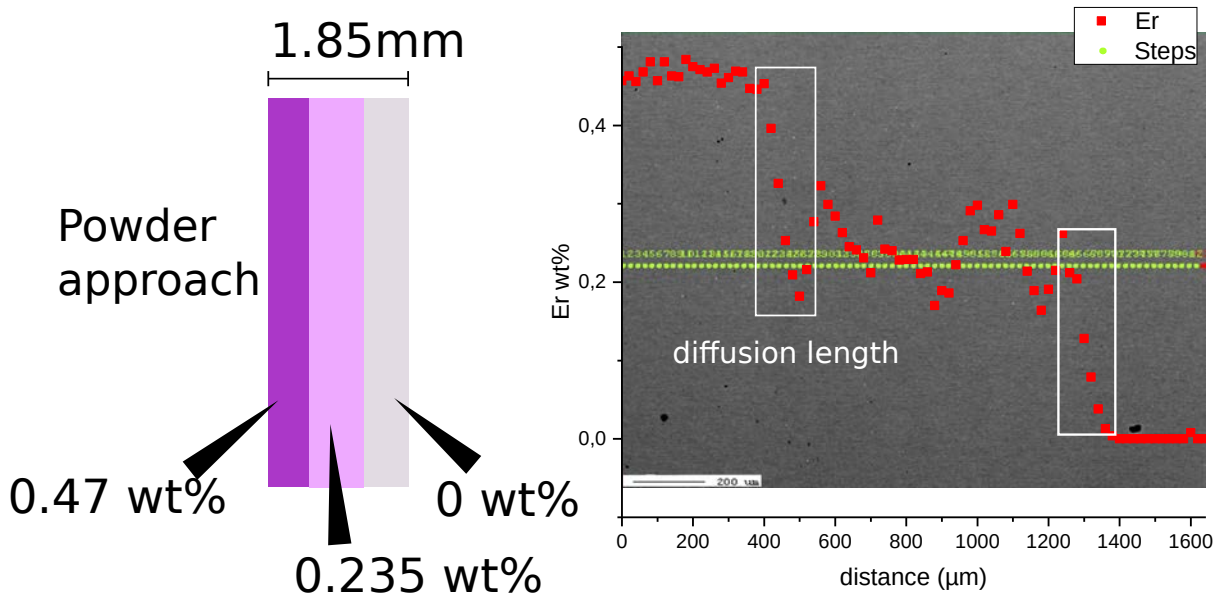

Figure IV.16: EPMA measurements of specimen from the powder approach.

For the presintered route, the bi-layer composite (0.47 wt% Er / pure YAG Nanocerox powder) sample was chosen, as presented in Fig. IV.9.

The corresponding results of EPMA measurement of the pre-sintered sample is presented in Fig. IV.17. The measure of the length of diffusion is around 194 µm.

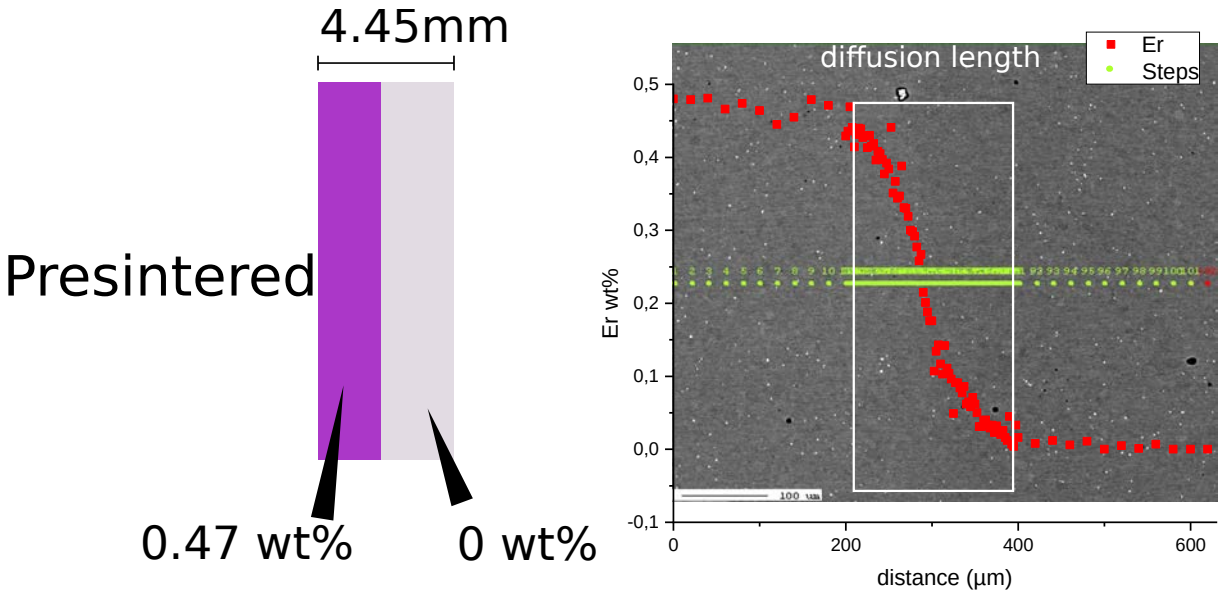

Figure IV.17: EPMA measurement of specimen from the pre-sintered approach.

For the fully dense specimen assembly, the sample used for the EPMA measurement is the condition J presented in Table IV.4 (Fig. IV.10). This specimen was obtained with the Nanocerox Er:YAG (0.47 wt%) and YAG powder. In Fig. IV.18, the EPMA measurements showed a gap between the Er content in the two ceramic layers. The

length of diffusion was about 12.1 µm, shorter than for the stacking obtained by the other assembly routes.

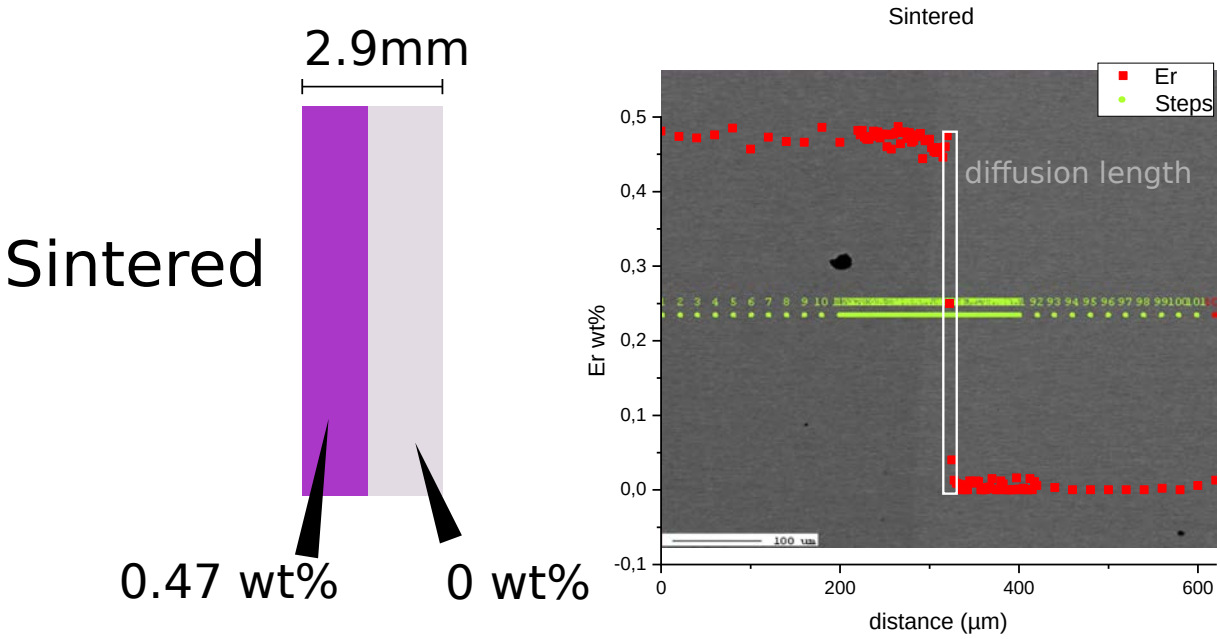

Figure IV.18: EPMA measurement of specimen from the fully dense approach

A second EPMA analysis confirms the dependence of the length of diffusion on assembling conditions. Performed on sample E (Fig. IV.10), the length of diffusion is clearly reduced when the bonding temperature is reduced by 100 ° C (1200 ° C 30min vs 1300 ° C 0 min). The diffusion length is decreased down to 4.8 µm.

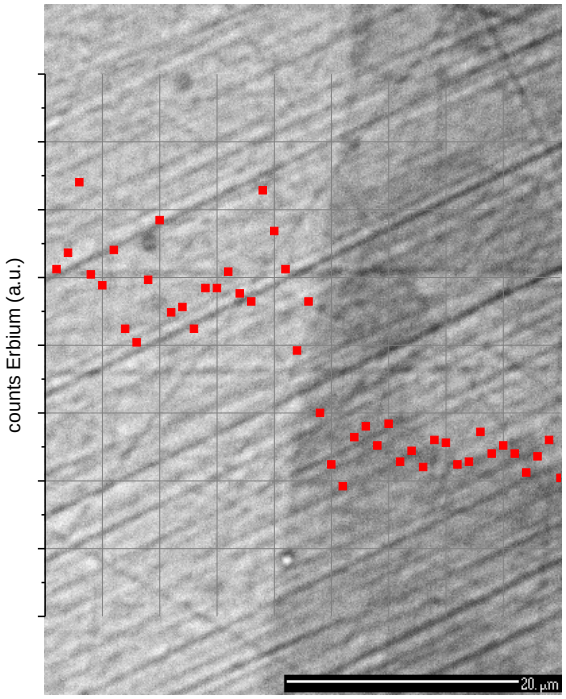

Figure IV.19: EPMA measurement for the E sample at the interface.

As shown by Fujioka *et al.*, when assembling two fully sintered samples, mobility of doping ions is very low (interdiffusion length between 1 and 15 µm in their case) [175]; which is in agreement with EPMA results on Fig. IV.19.

To have a complete comparison between these three approaches, the first Fick's law was applied to determine the bulk diffusion coefficient (in m^2/s). The first Fick's law was used for one direction and with the semi-infinite diffusion couple [220]. Distribution of Er ions ($C_{Er}(x,t)$) can be plotted in function of the distance (x) for a fixed time (t) which represents the time of diffusion.

$$C_{Er}(x,t) = \frac{C_{Er,0}}{2}\left[1 - \left(\frac{x}{2\sqrt{D_v t}}\right)\right] \tag{IV.1}$$

where $C_{Er,0}$ is the initial density of Er ions from the source corresponding in the left side of the EPMA curve. In our case, $C_{Er,0}$ is equal to 0.47 (wt%). D_v is the bulk diffusion coefficient (m^2/s) and t, the time in second. EPMA measurements were exported in Origin pro 2018 software and smoothed with an average of 8 adjacent points to obtain a corrected profile and avoid measurement variations. Measurement were centered in zero and fitted by the equation (IV.1) to determine $2\sqrt{D_v t}$ term. Fitting curves are presented in Fig. IV.20. Time was calculated from 1200 °C to be more representative on each conditions[2].

[2]Onsager's equations were maybe more suitable in this case to have a thermal dependency of bulk diffusion coefficient. First Fick's law was chosen to be comparable to the Fujioka *et al.* work.

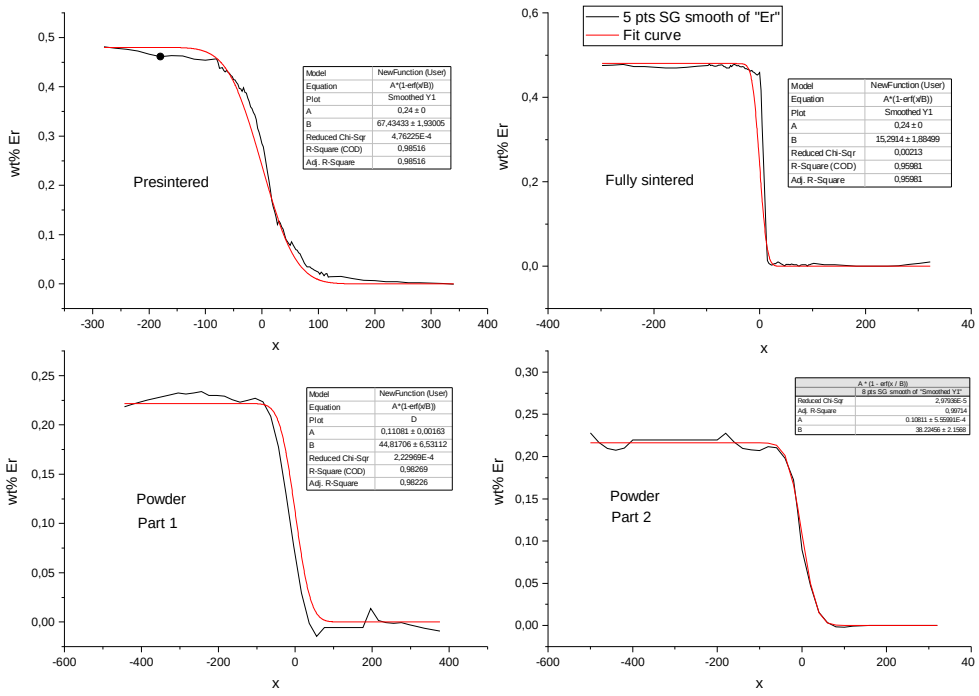

Figure IV.20: Fittings curves corresponding to each approach. For the powder, EPMA measurements were separated in 2 to simplify the fitting conditions with the Fick's law.

	Powder approach		Pre-sintered approach	Fully dense approach
	part 1	part 2		
Length of diffusion (µm)	140 ± 10	120 ± 10	194 ± 10	12.1 ± 1
t (sec)	18300		14700	3000
D_v(m²/s)	2.74×10^{-14}	2.00×10^{-14}	7.73×10^{-14}	1.94×10^{-14}

Table IV.6: Comparison of length of Er ions diffusion in function of approach chosen for SPS assembling with corresponding values of t and D_v from EPMA measures curves.

The table IV.6 summarizes the diffusion results of the 3 covered approaches: the powder approach had a D_v at 2.74×10^{-14} and 2.00×10^{-14} m²/s which is lower compared to obtained one for the presintered approach. This difference is explained by the difference of the doping gradient, the powder approach had 3 layers with an intermediate level of doping, leading to decrease the value of the coefficient of diffusion. The first Fick's law implies that a high difference of concentration leads to a higher diffusion coefficient. So, relative to the time considered, these two approaches seem correct.

For the shortest time of bonding, the fully dense approach, a relatively low D_v value is obtained which is coherent with the Fick's law.

As-sintering approach results show a high length of diffusion of 194 µm with a bulk

diffusion coefficient of 7.73×10^{-14} m^2/s which is the highest value obtained from the series. This could be explained by the relative high time of treatment and the difference of concentration of Er^{3+} between the two interfaces. Pre-sintered sample were not fully dense and the mobility of Er ions was possible compared to fully dense ceramics.

In comparison, Fujioka *et al.* had obtained a length of diffusion of 1 and 15 µm for Yb and Y ions after a pressureless treatment in a high vacuum furnace for Yb:YAG ceramics [175]. These results were in agreement with the fully dense approach.

4. Conclusion

Considering the different approaches to fabricate a doping gradient in ceramics by a SPS facility shown in this study, it appears that the route using powders allows to fabricate transparent materials with different composite architecture in a single processing step. The only limitation in terms of transparency is the adaptation of SPS condition in function of the final thickness of the ceramic and elimination of LiF before final densification. The powder approach leads to an easy process, with a time cost saving and good optical results for first attempts. Only limitations are due to the filling of the graphite matrix in order to obtain complex doping profile.

Presintered sample approach has led to a cohesive composite sample with a good ion interdiffusion at the interface but with low transparency (ILT 59.9%). An improvement of the SPS cycle and the polishing step are needed. At each step, a pollution of the sample is possible by the dust or graphite when samples are stacked together.

The fully dense approach was the less promising approach in terms of processing of composite sample. Several limitations are due to the high density of samples such as a very low interdiffusion of ions at the interface, a difficulty to obtain crack free samples due to thermal gradient and the uniaxial pressure applied during the cycle. Further investigations will be inclined towards crack apparition by reducing constraints by adapting graphite punches to allow a uniform pressure application on samples. Further investigations could also be done to study the influence of HIP post-treatments on microstructure and transmission results to understand the phenomena occurring after successive treatments.

5. Acknowledgment

The authors would like to thank Christine Gendarme for EPMA analysis (Institut Jean Lamour, Nancy).

Conclusions and perspectives

The main goal of the thesis was to develop Er:YAG transparent ceramics with an optical quality similar to single crystals and higher laser performances. For this purpose, the ceramic powder processing method and more specifically the Spark Plasma Sintering technique were used to process more quickly and at a less expensive cost transparent polycrystalline ceramics presenting doping gradient.

Three main topics were discussed to improve polycrystalline ceramics properties for laser application.

The first research topic was to determine the main defects responsible for the transparency lack in two YAG commercial powders.

- The first YAG powder had a high sulfur content that was reduced through several thermal and chemical treatments. Heat treatment was beneficial in reducing sulfur but involved an increase in particle size that modified the sintering behavior of the powder. A grain coalescence provoked by the heat treatments has created porosity and decrease sinterability of the samples. Although heat treatments were effective in lowering the sulfur content, they had deleterious effect on the transparency by porosity creation. With regard to the chemical treatments, several trends are observed: on the one hand, the acidic conditions decreased the sulfur content but impacted the YAG stoichiometry by reducing the yttrium. On the other hand, the basic solutions also made it possible to reduce the sulfur content, but in the case of NaOH, sodium contaminated the powder, making the sample worse than the untreated commercial powder. Only the treatment with water slightly improved the transparency and reduced the amount of sulfur (583 vs 662 ppm of sulfur). In order to really know if the water washing has an effect on the powder sinterability, a study on the combination of drying and hydration of the powders would be interesting to highlight the possible role of hydroxide groups in the sintering step.
- The second commercial experimental YAG powder had an yttrium deficit revealed by ICP-OES measurements. So, it was decided to add and mix yttria powder with commercial YAG powder to correct this stoichiometry defect. In view of the samples after SPS sintering, the improvement of optical quality was gradual as the theoretical stoichiometry of the YAG R = Y / Al = 0.6 was approached and reached. However, the transparency of the sample at 0.6 is not perfect as several white spots are visible. These areas may have resulted from secondary phase due to a bad mixing between yttria and YAG powder. Optimization of the mixture is always possible in order to facilitate the reaction between the species. Moreover, testing a regrinding process or a comminution of the powder with yttria could allow better mixing, reduce the particle size and increase the reactivity of the powders.

The second topic of the thesis was to test the possibility to fabricate YAG ceramics from a reactive mixture of yttria and alumina. The goal was to obtain a homogeneous mixture between these two powders by developing a simple and fast mixing method and to determine the phase transformation temperatures in the powder and green bodies. A total of 36 mixing and drying conditions were tested and through measurements of yield, stoichiometry and purity of various powder mixtures, the most homogeneous mixtures were selected to perform the calcination and sintering steps. Pure YAG phase was obtained for the powder treated under air at 1500 ° C for 15 h and for the compacted sample sintered at 1600 ° C for 5 hours. After sintering, the relative density and grain size values were used to plot a sintering map showing sintering trajectories. Between 1550 ° C and 1600 ° C, the sintered parts presented a grain size between 0.4 and 1 micron and a relative density below 83% . For higher sintering temperatures, at 1650 ° C for 10 and 20 h, a relative density between 96 and 97% was obtained which was still far from a total densification which explain the non-transparency of samples. However, this sintering map also showed that the grain size was lower than in some other studies. To obtain higher relative density values, vacuum sintering tests were performed at 1600 ° C and 1780 ° C. These non-optimized conditions made it possible to obtain a density between 99.1 and 99.4% , which is encouraging for preliminary assays. This study demonstrated it is possible from precursor oxide mixtures to obtain pure YAG phase with fine microstructure by using vacuum sintering without any sintering aids addition. Nevertheless, the residual porosity did not allow the transparency achievement. An improvement of the process could be possible by using some sintering aids such as TEOS to increase the sintering kinetics and favor the full densification conditioning the transparency. The other point of improvement concerns the sintering conditions optimization for vacuum sintering or SPS.

The last topic was the development of YAG composite ceramics by SPS from YAG commercial powders. For this study, several ways to realize the assembly of different dopant content samples were discussed: the powder approach, the pre-sintered specimens approach and the dense ceramics approach. Each of these approaches could lead to a transparent composite ceramic but each approach has pro and cons.

- Regarding the powder approach where the powders were poured directly into the SPS mold and co-sintered, it was possible to obtain very good optical quality thin ceramics. A transparency of 81% at 2550 nm was obtained for a three layers approach after a HIP post-treatment. Unfortunately, when the thickness of the sample was larger (amount of powder higher than 18 g), the temperature distribution in the sample was not homogeneous and the resultant thermal gradient provoked a differential sintering. The three-layer design (0.47 wt% / 0.235 wt% / 0 wt% Er) led to length of diffusion between 120 and 140 µm for a transparency of 81% at 2500 nm. Although an important thickness is obtained (4.3 mm), the transparency was relatively high for a non-optimized process. Despite this size limitation, the powder approach presents as advantages a fast transparent ceramic composite production within less than 10 hours and the ability to develop several forms of architectures (sandwich, layer-by-layer, clad-core). In this study, it was demonstrated that the application of HIP post-processing made it possible to increase the transparency of a sample with three doping layers. To further improve the optical quality and obtain thicker ceramics for a scale-up, it would be possible to pre-sinter the dry pressed powders by SPS and

finish the densification by a HIP post-treatment at a temperature between 1400 and 1450 ˚ C with a long holding time (15 to 25 h).

- The second approach with pre-sintered ceramics consisted in a first sintering of the powders at a temperature below the temperature leading to full densification, followed by a second SPS treatment at high temperature for assembling. Presintered samples were polished between the two thermal treatments. This method was successfully applied to obtain transparent composite ceramics with a length of diffusion measured at 194±10 µm. However, an optimization of the temperatures during presintering and then during assembly could be carried out in order to improve the transparency.
- The last approach consisted in assembling dense samples by SPS. After several attempts to optimize the pressure and temperature for assembling the ceramics, a transparent sample was obtained (50 % at 1100 nm) with a 12.1 ±1 µm length of diffusion. This fabrication method is very delicate because of the fragility of dense ceramics inducing breaking of samples during the SPS, although this method is more appropriate to make thick sample assemblies.

To increase the thickness of the transparent composite ceramics, the idea would be to proceed in several steps: i) first the production of samples with a very good transparency at the output of the SPS with an intermediate thickness (between 3 and 6 mm). This work has demonstrated the feasibility of the SPS approach to fabricate doping gradient ceramics. Beyond this 5-6 mm of thickness, the making of transparent samples is very difficult because of the thermal gradients and compaction gradients due to uniaxial pressing which become more pronounced when the thickness increases. ii) secondly, a second SPS cycle on the stacking of these different samples to assemble them. To conclude, SPS approach is a promising road to fabricate composite Er:YAG/YAG ceramics but some improvements have to be done to reach in same time a smooth gradient and a high transparency.

Appendix A

Appendix

Semi-quantification of the commercial powder

Sample	YAG (%)	YAP (%)	YAM (%)	Y_2O_3(%)
P1	90.85	2.23	1.82	5.10
P2	91.42	2.36	1.78	4.43
P3	91.43	2.32	1.66	4.60
P4	91.51	2.38	1.55	4.57
P5	91.73	2.69	1.33	4.26
P6	89.20	2.50	3.70	4.60
P7	91.30	2.20	2.00	4.50
P8	91.38	2.24	1.97	4.41
P9	91.40	2.37	1.65	4.58
Average	**91.13**	**2.37**	**1.94**	**4.56**
Standard deviation	**0.76**	**0.15**	**0.69**	**0.23**

Table A.1: Semi-quantification by XRD of phases present in 9 samples of the commercial BS powder.

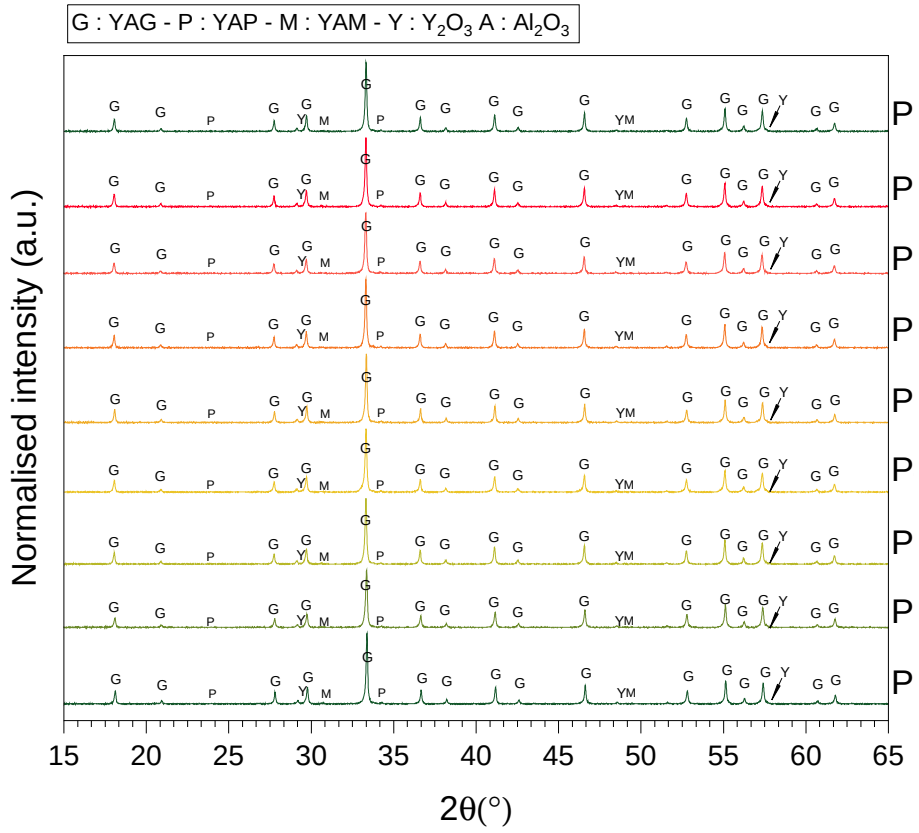

Figure A.1: XRD patterns of 9 samples of the BS commercial powder.

Appendix B

SEM observations of powders after thermal and chemical treatments.

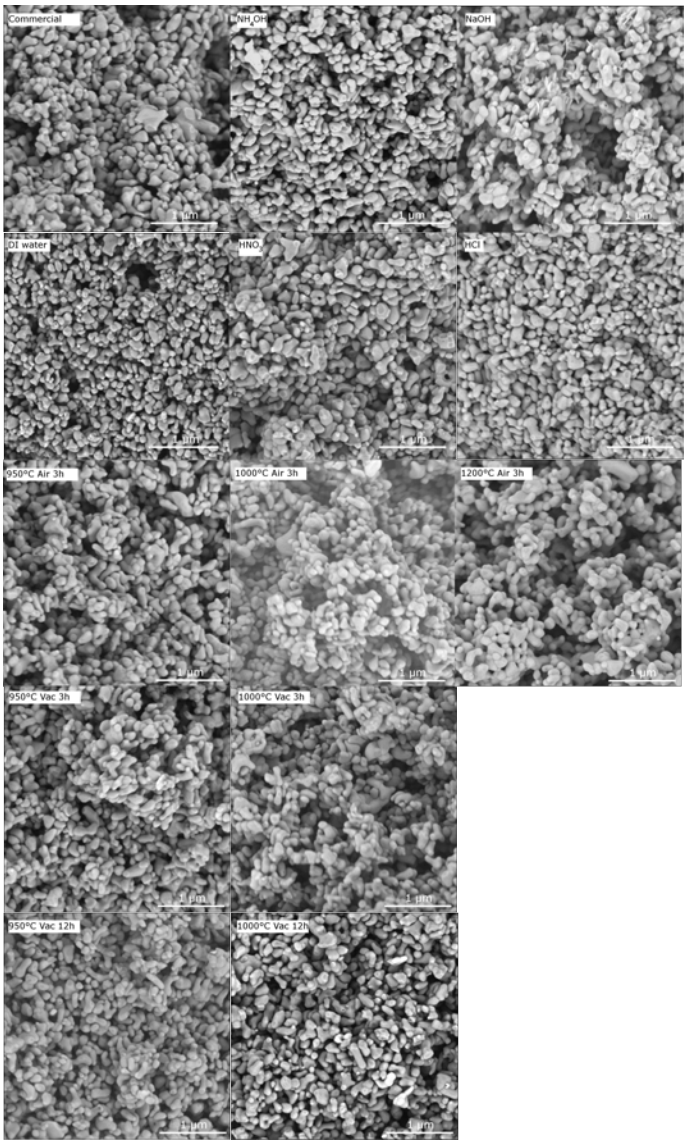

Figure B.1: SEM observations of powder particles after thermal and washing treatments.

Appendix C

XRD enlargement of 35-45 ˚2 θ for samples A to F

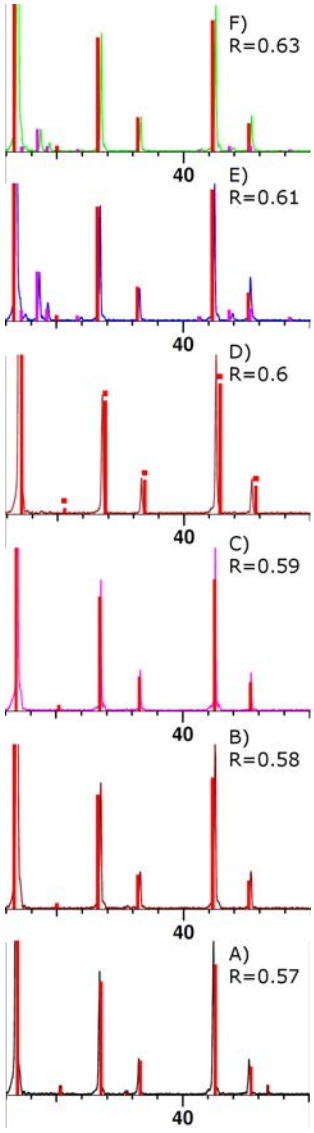

Figure C.1: XRD patterns of A to F ceramics. Red, brown and pink sticks correspond to YAG, Al_2O_3 and YAP diffraction peaks respectively.

Appendix D

Yttria and alumina supplier technical data

Alfa Aesar

Certificate of analysis

Product No.: 47154

Product: Yttrium(III) oxide, nanopowder, 99.995% (REO)

Lot No.: T22C032

CeO_2	< 2
Dy_2O_3	< 0.5
Er_2O_3	0.7
Eu_2O_3	< 0.2
Gd_2O_3	< 1
Ho_2O_3	1
La_2O_3	< 1
Lu_2O_3	< 0.2
Nd_2O_3	< 1
Pr_6O_{11}	< 1
Sm_2O_3	< 1
Tb_4O_7	< 1
Tm_2O_3	< 0.2
Yb_2O_3	< 0.2
CaO	70
CuO	< 2
NiO	< 2
Fe_2O_3	13
PbO	2
SiO_2	70

All values in ppm unless otherwise stated.

This document has been electronically generated and does not require a signature.

Order our products online **www.alfa.com**

ThermoFisher SCIENTIFIC



SMA6

TYPICAL **VALUES**

BET Specific Surface Area (m^2/g)		6
Crystal Structure		Alpha
TEM Ultimate Particle Size (nm)		200
Particle Size Distribution (µm)	d20	0.15
	d50	0.20
	d90	0.55
Bulk Density (g/cm^3)		1.00
Tapped Density (g/cm^3)		1.20
Green Density (g/cm^3)		2.28
Fired Density (g/cm^3)		3.96

CHEMICAL **ANALYSIS**

ICAP values (ppm)

Fe	6
Na	12
Si	10
Ca	2
K	20

Main applications



Colored ceramics – watch parts



Orthopedic & dental ceramics



Ceramic coatings – sensors

Typical values are given by Baikowski as an indication only. Such values are not contractual

FRANCE BP 501- F-74339 LA BALME DE SILLINGY CEDEX | Tel +33 (0)4 50 22 69 02 I Fax +33 (0)4 50 22 28 92
USA 6601 Northpark Blvd Suite H – CHARLOTTE NC 28216 | Tel +1 704 587 71 00 I Fax +1 704 587 71 06
JAPAN 6-17-13 Higashinarashino - Narashino-shi - CHIBA-KEN 275-0001 | Tel +81 474 738 150 I Fax +81 474 738 153
CHINA Room 1502 - Harbour Ring Plaza - 18 Middle XiZang Road - 200001 SHANGHAI | Tel +(86) 21 6289 2883 I Fax +(86) 21 6289 2615
WWW.BAIKOWSKI.COM

Appendix E

Enlargement of EDX map results of the number 3, 4, 6, 10, 22, 28, 30 and 31 conditions

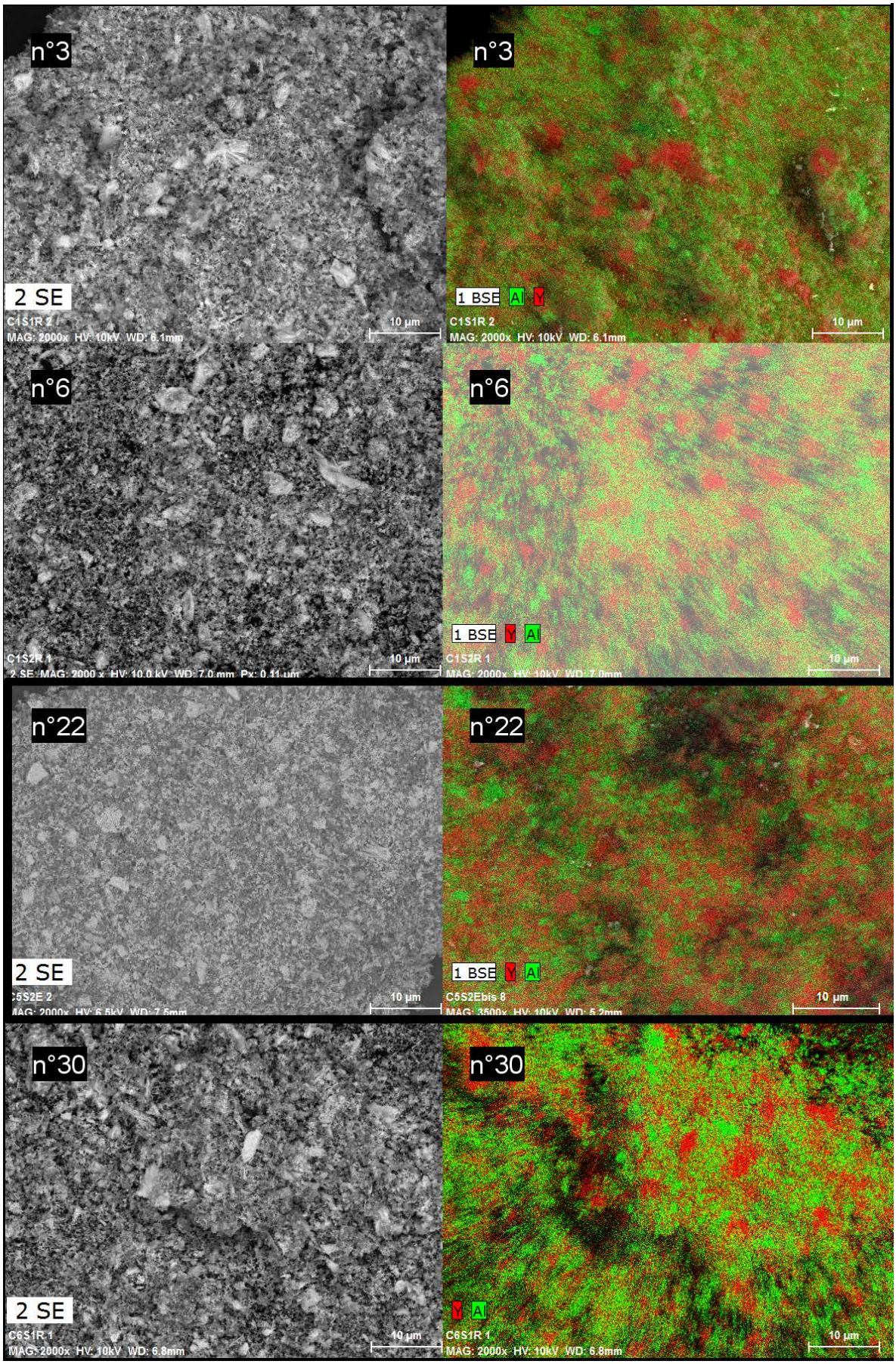

Figure E.1: EDX map of conditions n ° 3, 6, 22 and 30.

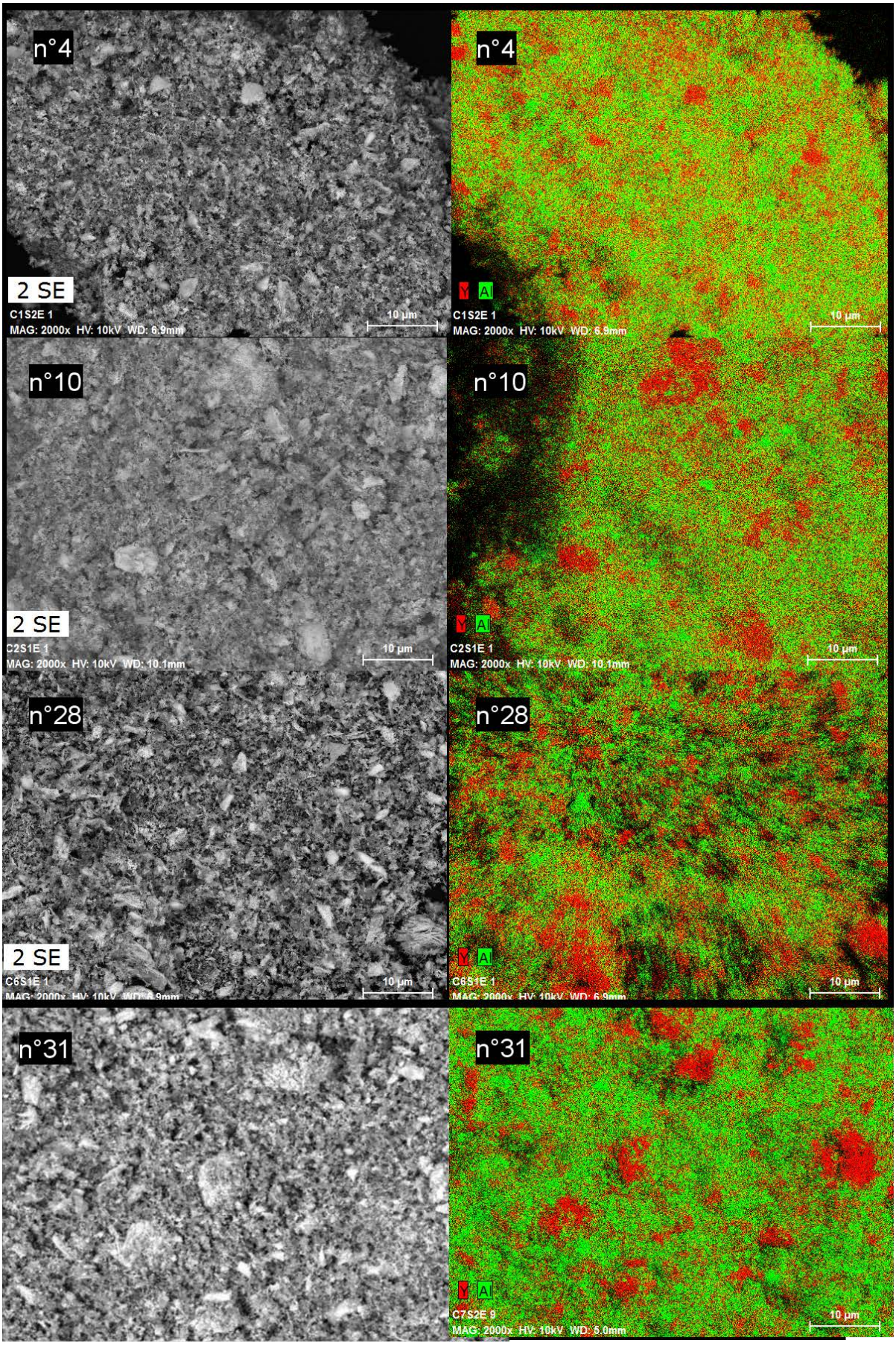

Figure E.2: EDX map of conditions n ° 4, 10, 28 and 31.

Appendix F

Determination of the porosity and relative density by Archimedes method

Three unknown parameters have to be done:

- The bulk volume of the specimen V_m
- The open porosity volume V_{po}
- The closed porosity volume V_{pc}

And the sum of these three parameters give the total volume of the specimen V_t.

To obtain these parameters, three measures have to be determined: dry, wet and immersed weight (in solvent) of the specimen. $V_m$is obtained by the division of the dry weight m_s by the theoretical density d_{theo}. The wet weight m_w allows to calculate the liquid weight present in open porosity by difference between the dry and the wet weight. The immersed weight m_i enables the possibility to obtain the closed porosity by Archimedes principle.

$$V_m = \frac{m_s}{d_{theo}} \tag{F.1}$$

$$V_{po} = \frac{m_w - m_s}{d_{solvent}} \tag{F.2}$$

$$m_s - m_i = (V_m + V_{pc}) \times d_{solvent} \tag{F.3}$$

$$V_t = V_m + V_{pc} + V_{po} \tag{F.4}$$

Following (4), (3), (2) and (5):

$$V_t = \frac{m_w - m_i}{d_{solvent}} \tag{F.5}$$

Following (2) and (5), the relative density (d_{rel}), the open ($\%po$) and closed porosity $\%pc$ can be expressed :

$$d_{rel} = \frac{m_s}{m_w - m_i} \times \frac{d_{solvent}}{d_{theo}} \tag{F.6}$$

Following (3) and (5), then the closed porosity is expressed by:

$$\%pc = 1 - d - d_{rel} - \%po \tag{F.7}$$

The procedure: sintered specimen were weighted to determine the dry weight, then immersed in water for 4 h under vacuum into a desiccator. for 4h to ensure the water penetrate into the open pores. After, specimens were weighted in water to obtain the immersed weight m_i. Finally after drying specimen by an absorbent paper, the wet weight m_w was measured.

In the case of the specimen has multiple phase (alumina, yttria, YAM, YAP and YAG), the use of YAG theoretical density to obtain the open and closed porosity is not correct. So, the theoretical density corresponding to the sum of all phases that compose the sample was calculated as follow:

$$\sum d_{theo_{phase}} \times \%phase_{XRD_{phase}} \div 100 = d_{theo_{specimen}} \tag{F.8}$$

Appendix G

Polishing procedure

Ceramics were mirror polished with an automatic Polisher machine (Buehler Ecomet 300 Pro) in 4 steps:

Step	Grain size (µm)	Pressure (N)	Time of process (min)	Grinding disk nomination
1	35	10	10	DGD color
2	9	40	4	Top (Presi)
3	3	40	4	Verdutex (Buehler)
4	1	40	4	Supra (Buehler)

Table G.1: Polishing steps to obtain a mirror polished surface

After polishing the surface by these 4 steps, the final step consists in a vibrating table (VibroMet 2, Buehler) where samples were placed on a grinding disk (RAM, Presi) with two polishing suspension solutions: Master Met 2 (0.02 µm, colloidal solution, Buehler) and Master Prep (0.05 µm, Buehler) mixed in 50:50 volume ratio. A weight was placed on the top of the sample to be more efficient during the polishing treatment. The amplitude of vibrating table was fixed at 80% and time was set to 4 hours.

These steps can be adapted in function of the amount of LiF or if samples were HIP post-treated, which changes the hardness of the ceramic.

List of Tables

I.1 Comparison of process and properties of glasses, single crystals and ceramics for solid state laser applications (from [34]. Experimental values were taken for Nd^{3+} doped materials. 10
I.2 Properties of the most widely used solid matrices as gain medium for laser applications. 14
I.3 Comparison between Y^{+3} ion characteristics and rare earth candidates for replacement in YAG matrix as active ion. 15
I.4 Spectroscopy comparison between high and low doping from [22]. 16
I.5 Summary of requirements for highly transparent samples. 24
I.6 Powder characteristics of Er:YAG-P, and YAG -P from Nanocerox and Er:YAG-S and YAG-S for Baikowski powders. S_{BET} correspond to specific surface of particles measured by BET method. From [121]. 31

II.1 Y/Al molar ratio and sulfur content in the starting powders. 42
II.2 BS powder characteristics after thermal treatments (vac. : under vacuum). . . 44
II.3 BS powder characteristics after chemical treatments. 50

III.1 Mixing conditions used in the current study. 79
III.2 Best mixtures conditions selected for SEM and EDX mapping analyses. . . . 84
III.3 Theoretical weight percentages of Y, Al and O element in YAG, YAP and YAM phases and measured composition in areas 1,2 and 3 in (d) picture and (e) EDX profile of the Fig. III.13 96

IV.1 Table resuming experiments of bonding sample in High Vacuum Furnace. . . 102
IV.2 Summary of HIP post-treatement on powder assemblies. 111
IV.3 ILT measurements for Er:YAG ceramics obtained by SPS (Katz and this study) and other from the literature by conventional sintering. All transmission values were normalized at 3 mm. 114
IV.4 Experimental conditions for fully dense ceramic assembly. (V.T. = Vibrating Table)) 115
IV.5 Arguments of different doping gradient routes. 120
IV.6 Comparison of length of Er ions diffusion in function of approach chosen for SPS assembling with corresponding values of t and D_v from EPMA measures curves. 125

A.1 Semi-quantification by XRD of phases present in 9 samples of the commercial BS powder. 131

G.1 Polishing steps to obtain a mirror polished surface 147

List of Figures

I.1 Scheme of laser system principle. 4
I.2 Principle of (left) spontaneous emission and (right) stimulated emission [7]. . 4
I.3 Crystal growth by a) Bridgman-Stockbarger [16] and b) by Czochraslki [17]. . 7
I.4 a) Experimental setup b) CW output power versus incident pump power with different HR curvatures from [25]. 8
I.5 Dependence of the output power on the input pump power for the 0.9 at. % Nd:YAG single crystal and the 3.4 and 2.3 at. % Nd:YAG ceramics [28]. . . . 9
I.6 Thermal conductivity of polycrystalline ceramics doped with different Nd concentration and single crystal from [29]. 9
I.7 Evolution of the power for diode-pumped solid-state laser versus years: Mercury, SSHCL, Textron, JHPSSL and four combined fiber laser from [43]. . . . 11
I.8 Comparison between output power of different configurations of composite gradient PCs: two-layers, three-layers and clad-core [46]. 12
I.9 a) Schematic distribution of Neodymium ions in a heterogeneous doping profile b) Comparison of thermal distribution between conventional Nd:YAG single crystal with uniform doping of Neodymium sample (top) and a smooth gradient doped sample by neodymium ions in a ceramic material (bottom) from [45]. 12
I.10 Three different solid state configurations for laser demonstration from [47] corresponding to (a) heat capacity laser (Lawrence Livermore Labs), (b) end pumped slab laser (Northrop Grumman Corp.) and (c) thinzag slab laser (Textron). 13
I.11 a) Energy-level diagrams for different host matrices doped with Er^{3+} ion. b) Calculation of emission-to-absorption cross section ratio and lower laser level population of Er^{3+} in different hosts as a function of the crystal temperature from [1]. 15
I.12 Comparison of different transparencies depending on the positioning for a translucent material, a medium transparency from Al_2O_3 ceramic and a fully transparent spinel from [64]. 18
I.13 Phenomena which take place when light hits a surface (From [65]). 19
I.14 Ceramic defects which cause a loss of transparency. 20
I.15 Phase diagram for system Y_2O_3-Al_2O_3 from [49]. 21

I.16 Simulation of RIT in function of the pore size diameter for YAG ceramics for 10, 100 and 1000 ppm of residual porosity (from top to bottom). Wavelength considered: 1031 nm. Several expressions were considered for the simulation: R-scaling, Rayleigh, Fraunhofer, maximum function, van de Hust, and Mie solution from [69]. 23
I.17 Size and morphology influence on apparent and tapped density, adapted from [107]. 28
I.18 Intergranular and intra granular pores formation from [109]. 29
I.19 Influence of ball-milling on optical result for Nd:YAG from [110]. 29
I.20 Transmittance measurements versus the stoichiometry default in the YAG system. x corresponds to the stochiometry shift of $Y_{3(1+x)}Al_5O_{12}$ formula from [120]. 30
I.21 SEM pictures of Er:YAG and YAG powders from Nanocerox (Er:YAG-P and YAG-P) and Baikowski (Er:YAG-S and YAG-S) suppliers. 31
I.22 (a) SPS setup and (b) scheme of the SPS die and the result of compacted powder after sintering. For instance, (c) a slab of the ceramic can be cut to laser applications. From [133]. 32
I.23 SEM micrographs of Nd:YAG fracture surfaces. (A) Vacuum sintered before annealing, (B) HIP-sintered specimen before annealing (C) Vacuum sintered specimen after annealing (D) HIP-sintered specimen after annealing (E) gas chromatography-mass measurement of HIPed specimen from [132]. 34
I.24 Polycrystalline multilayer ceramic obtained by dry pressing method. Effect of HIP treatment under 200 MPa was shown on sintered ceramics (from left to right): 1750 ° C 4h, 1650 ° C 4h and as-sintered (9.5 mm diameter, 1.5 mm thick) from [143]. 35
I.25 Composite 0.1% Nd:YAG/YAG obtained by slip casting method from [167]. . 36
I.26 Schematics of tape cast composites (a) stacked and (b) co-cast with corresponding pictures specimen from [170]. 36
I.27 (a) Schematic diagram of layer-by-layer composite before and after the bonding. (b) Cross observation of the specimen after thermal treatment at 1720 ° C 5h from [46]. 37
I.28 Composite ceramics Yb:YAG from fully dense sample after heat treatment (when ceramics were in contact) in high vacuum furnace at (a) 1400 ° C 10h (b) 1400 ° C 50h and (c) 1600 ° C 50h from [175]. 37

II.1 SEM pictures of the untreated commercial BS powder (left) and of the powder washed with a NaOH solution (right). Black circles indicate flake-like particles. 44
II.2 X-Ray Diffraction patterns of BS powder as-received and after various thermal treatments. 45
II.3 Shrinkage curves of samples prepared with thermally treated powders during sintering by SPS. 46
II.4 Visual aspect of polished YAG ceramics prepared with thermally treated powders after SPS sintering. Diameter of samples: 30 mm. Thickness of samples: 2.7 mm. 47
II.5 In-Line Transmission of YAG ceramics prepared with thermally treated powders after SPS sintering. 47

II.6 X Ray Diffraction patterns of YAG ceramics prepared with thermally treated powders after SPS sintering. 48
II.7 Surface observations by SEM of raw polished YAG ceramics prepared with thermally treated powders after SPS. 49
II.8 X-Ray Diffraction patterns of the powders after washing treatments. 51
II.9 Shrinkage curves of samples prepared with chemically treated powders during sintering by SPS. 52
II.10 X-Ray Diffraction patterns of YAG ceramics prepared with chemically treated powders after SPS sintering. 53
II.11 SEM fracture observations of samples prepared with chemically treated powders after SPS. 54
II.12 EDX analysis of the HCl-treated sample after sintering. 55
II.13 EDX analysis of the NaOH treated sample after sintering. a) SEM picture of the sample fracture b) EDX measurements. 56
II.14 Sintered specimens obtained with chemically treated powders. Diameter: 30mm. Thickness: 2.7 mm. 56
II.15 In-Line Transmission of YAG SPS after chemical treatment. 57
II.16 SEM observation of the BY (a) and yttria (b) powders and their X Ray Diffraction patterns (c and d). 58
II.17 Sintered specimens obtained after optimized SPS cycle with different amounts of Y_2O_3 added to the BY powder. (Ratios were calculated starting from the measured Y/Al ratio of the BY powder and the amount of yttria added). . . . 59
II.18 XRD patterns of A, B, C, D, E and F samples. 61
II.19 SEM fracture surface of A,C,D and E of sintered samples at two magnifications. Inter-granular fracture in all conditions. Arrows show areas of Al-rich phase embedded in YAG grain. 62
II.20 EDX measurement of the sample A fracture. (a) SEM image (b) Al (c) O (d) Y element map. 63
II.21 a) SEM fracture observation of the sample E and EDX profiles for the YAP (b) and YAG (c) grains. Table summarizes atomic percentages obtained from EDX measures for yttrium, aluminum and oxygen elements. 64
II.22 Visual comparison between polished sample sintered during 2 and 4 hours by SPS. 66
II.23 SEM fracture observations of samples sintered at 1450 °C during 4h. White arrows show the porosity at triple points. Red circles indicate small spherical pores on YAG grain surfaces in the inset. 67
II.24 X Ray Diffraction patterns of powders with various Y/Al ratios (0.590 and 0.600) calcined at 900 °C and 1100 °C (1 h). 69
II.25 SPS sintered samples of calcined powder (900 and 1100 °C) 70
II.26 SEM fracture observations of SPS sintered samples prepared with powders pre-calcined at 900 °C for 1h (top: Y/Al = 0.590, bottom: Y/Al = 0.600). White arrows indicate pores. 71
II.27 SEM fracture observations of SPS sintered samples prepared with powders pre-calcined at 1100 °C for 1h (top: Y/Al = 0.590, bottom: Y/Al = 0.600). White arrows indicate pores. 72

III.1 a) SEM microstructure of commercial yttria and b) commercial alumina powder. c) X-Ray Diffraction of the yttria and alumina powder. 78
III.2 Sintering cycle for sintering for green bodies under air and vacuum atmosphere. 81
III.3 Yield and stoichiometry ratio corresponding to each mixing conditions. S1 and S1 correspond to ultrasonic method for the program 1 and 2. MS stands for Magnetic Stirring mixing conditions. 82
III.4 Relative density after compaction of 1g of powder at 350 MPa at 1 mm/min for each conditions. S1 and S2 correspond to ultrasonic method for the program 1 and 2. MS stands for Magnetic Stirring mixing conditions. 83
III.5 SEM pictures with EDX analysis of Al (green) and Y (red) elements of 8 selected mixtures. (Enlargement of this figure is available in appendix E) . . . 85
III.6 Semi-quantification results after powder calcinations at 1100, 1300, 1500 and 1600 ° C. 87
III.7 Semi-quantification results after powder calcination with a dwell time of 1 hour for each condition. 89
III.8 Holding time impact on phase distribution for 0, 1, 3, 5, 10 and 20h for mixture n ° 4 and n ° 28. 90
III.9 Shrinkage curves (top) and derived curves (bottom) of compacted specimen from n ° 4, n ° 28 and reference condition. Numbers correspond to shrinkage rate peak. 91
III.10 Semi-quantification of ceramics specimens after sintering at 1000, 1300 and 1600 ° C with a dwell time of 0, 5, 10 hours. Standard deviation: 0.81%. . . . 92
III.11 Relative density of sintered specimens corresponding to conditions 4, 28 and the reference after thermal treatment. 93
III.12 SEM pictures of densification process for the specimen from n ° 4 condition powder. 94
III.13 a), b), c) SEM picture in back back scatter mode of n ° 4 sintered specimen at 1650 ° C at 3 different areas. d) SEM images for the EDX profile analysis and e) the element profile analysis by EDX. 95
III.14 Schematic representation of Al^{3+} diffusing through YAG and YAP phase to react with YAM. 96
III.15 Samples obtained after high vacuum sintering at a) 1600 ° C for 5h b) 1600 ° C for 10h c) 1780 ° C for 10h and HIP post treatment of 1650 ° C for 6h (1900 bars) d, e and f corresponding to a,b,c samples. 97
III.16 Sintering map for Al_2O_3 and Y_2O_3 mixture from the n ° 4 procedure. 98

IV.1 Photograph of the 3 couples of samples which are bonded after the 1600 ° C 10h treatment in High Vacuum Furnace. 103
IV.2 HIP experiment to bond samples at 1800 ° C 10h and the annealing result at 900 ° C 1h. 104
IV.3 Picture of the sample C2, the side in contact with HIP support. 104
IV.4 General strategy used in this study. 108

IV.5 i) Different designs tested with the powder assembly approach: a. bilayer b. sandwich like c. half sided and d. clad core design, corresponding to samples after sintering (line), after a first HIP post treatment (blue and green line) and after twice HIP post-treatments at 1400 ° C 15h (dashed line). ii)In-line transmission corresponding to powder assembly approach. 110
IV.6 Scheme of organization of 3 layers of different doped powders for the powder approach. 112
IV.7 SPS sintered specimen obtained from the 3 layers of powder (0.47 wt% / 0.235 wt% / 0 wt%). (30 mm diameter, thickness: 4.3 mm). 113
IV.8 ILT measurements after SPS and after HIP post-treatment at 1400 ° C for 15h with attached picture of the corresponding specimen. (thickness: 4.3 mm) . . 113
IV.9 A and B pre-sintered samples by SPS and C sample obtained by assembly of the 2 previous samples by a second SPS (30mm diameter). 115
IV.10 Pictures of SPS assembled with 30-mm-diameter fully dense sample. 116
IV.11 Sample C after cutting. One point of cohesion was observed. 116
IV.12 Schema of graphite punches and matrix used in this study. 117
IV.13 Scheme of possible explanation of cracks formation due to A. inhomogeneous pressure application and differential expansion of graphite and B. bad parallelism between the two surfaces of the sample. 118
IV.14 Sample J : Two left samples before bonding, and after the bonding at the right, on dark background and on light table. (F mark stands for the polished side before the stacking step). Red circles highlight cracks formed at the periphery of the specimen. 119
IV.15 Picture of the samples selected for the EPMA measure. (30 mm diameter) . . 121
IV.16 EPMA measurements of specimen from the powder approach. 122
IV.17 EPMA measurement of specimen from the pre-sintered approach. 122
IV.18 EPMA measurement of specimen from the fully dense approach 123
IV.19 EPMA measurement for the E sample at the interface. 124
IV.20 Fittings curves corresponding to each approach. For the powder, EPMA measurements were separated in 2 to simplify the fitting conditions with the Fick's law. 125

A.1 XRD patterns of 9 samples of the BS commercial powder. 132

B.1 SEM observations of powder particles after thermal and washing treatments. . 134

C.1 XRD patterns of A to F ceramics. Red, brown and pink sticks correspond to YAG, Al_2O_3 and YAP diffraction peaks respectively. 136

E.1 EDX map of conditions n ° 3, 6, 22 and 30. 142
E.2 EDX map of conditions n ° 4, 10, 28 and 31. 143

Communications

Communications (Chronological view):

Speaker

2016/03/22, GFC, Valenciennes, FRANCE, Poster
Transparent polycrystalline Er:YAG ceramic development for Laser application
Maxime LAGNY, Judith BOEHMLER, Sébastien LEMONNIER, Elodie BARRAUD (ISL) Yannick LORGOUILLOUX and Anne LERICHE (LMCPA, Valenciennes)

2016/06/23, PhD Student, Saint-Louis, FRANCE, Poster
Transparent Ceramic with doping profile for Laser Application
Maxime LAGNY, Judith BOEHMLER, Sébastien LEMONNIER, Elodie BARRAUD (ISL) Yannick LORGOUILLOUX and Anne LERICHE (LMCPA, Valenciennes)

2016/07/18, Shaping VI, Montpellier, FRANCE, Poster
Transparent polycrystalline Er :YAG ceramic development for Laser application
Maxime LAGNY, Judith BOEHMLER, Sébastien LEMONNIER, Elodie BARRAUD (ISL) Yannick LORGOUILLOUX and Anne LERICHE (LMCPA, Valenciennes)

2016/11/28, 12th Laser Ceramics Symposium, Saint-Louis, FRANCE, Oral
Assembly of transparent polycrystalline Er:YAG ceramics by SPS
Maxime LAGNY, Judith BOEHMLER, Sébastien LEMONNIER, Elodie BARRAUD (ISL) Yannick LORGOUILLOUX and Anne LERICHE (LMCPA, Valenciennes)

2017/03/07, Journée jeunes chercheurs, Mons, BELGIQUE,Poster
Developpement de ceramiques transparentes pour des applications LASER et balistiques
Maxime LAGNY, Judith BOEHMLER, Sébastien LEMONNIER, Elodie BARRAUD (ISL) *Yannick LORGOUILLOUX* and Anne LERICHE (LMCPA, Valenciennes)

2017/03/14, Axes ISL Saint-Louis, FRANCE, Oral
Assembly of transparent polycrystalline Er:YAG ceramics by SPS
Maxime LAGNY, Judith BOEHMLER, Sébastien LEMONNIER, Elodie BARRAUD (ISL) Yannick LORGOUILLOUX and Anne LERICHE (LMCPA, Valenciennes)

2017/03/21, GFC, Rennes, FRANCE, Oral
Elaboration de ceramiques transparentes pour des applications LASER et protection balistique
Maxime LAGNY, Caroline GAJDOWSKI, Aurélien KATZ, Judith BOEHMLER, Sébastien LEMONNIER, Marc EICHHORN, Elodie BARRAUD (ISL) Yannick LORGOUILLOUX and *Anne LERICHE* (LMCPA, Valenciennes)

2017/04/10, Materials2017, Aveiro, PORTUGAL, Oral
Presentation of two different approaches to elaborate transparent ceramics for LASER and ballistic protection applications

Maxime LAGNY, Caroline GAJDOWSKI, *Judith BOEHMLER*, Sébastien LEMONNIER, Elodie BARRAUD, Marc EICHHORN (ISL) Yannick LORGOUILLOUX and Anne LERICHE (LMCPA, Valenciennes)

2017/05/22, PACRim, Hawaï, USA, Oral
Processing of transparent ceramics for LASER and ballistic applications

Maxime LAGNY, Caroline GAJDOWSKI, Judith BOEHMLER, Sébastien LEMONNIER, Elodie BARRAUD (ISL) Yannick LORGOUILLOUX and *Anne LERICHE* (LMCPA, Valenciennes)

2017/06/21, PhD Student Saint-Louis, FRANCE, Oral
Transparent Ceramic with doping profile for Laser Application

Maxime LAGNY, Judith BOEHMLER, Sébastien LEMONNIER, Elodie BARRAUD (ISL) Yannick LORGOUILLOUX and Anne LERICHE (LMCPA, Valenciennes)

2017/07/09, ECERS, Budapest, HUNGARY, Poster
Transparent polycrystalline Er:YAG ceramic development for Laser application by Spark Plasma Sintering

Maxime LAGNY, Stefano BIGOTTA, Judith BOEHMLER, Sébastien LEMONNIER, Marc EICHHORN, Elodie BARRAUD (ISL) Yannick LORGOUILLOUX and Anne LERICHE (LMCPA, Valenciennes)

2017/09/26, ICube Workshop Saint-Louis, FRANCE, Oral
Ceramiques Laser

Maxime LAGNY, Judith BOEHMLER, Sébastien LEMONNIER, Elodie BARRAUD (ISL) Yannick LORGOUILLOUX and Anne LERICHE (LMCPA, Valenciennes)

2017/10/23, JA SF2M 2017, Lyon, FRANCE,Poster
Transparent polycrystalline Er:YAG ceramic development for Laser application by Spark Plasma Sintering

Maxime LAGNY, Judith BOEHMLER, Sébastien LEMONNIER, Elodie BARRAUD (ISL) Yannick LORGOUILLOUX and Anne LERICHE (LMCPA, Valenciennes)

2018/06/07, CIMTEC2018, Perugia, ITALY, Oral
Comparison of different methods for polycrystalline Er:YAG ceramics

Maxime LAGNY, Judith BOEHMLER, Sébastien LEMONNIER, Elodie BARRAUD (ISL) Yannick LORGOUILLOUX and Anne LERICHE (LMCPA, Valenciennes)

2019/01/28, ICACC 2019, Daytona, USA, Oral
Transparent Er :YAG ceramics with doping gradient by SPS

Maxime LAGNY, Aurélien KATZ Judith BOEHMLER, Sébastien LEMONNIER, Yannick LORGOUILLOUX and *Anne LERICHE* (LMCPA, Valenciennes)

2019/03/14, Axes ISL Saint-Louis, FRANCE, Oral
Development of transparent ceramics for solid-state laser sources

Maxime LAGNY, Sébastien LEMONNIER, Florence MOITRIER, Thierry BOURRE, *Judith BOEHMLER* (ISL)

Bibliography

[1] M. Eichhorn, "Quasi-three-level solid-state lasers in the near and mid infrared based on trivalent rare earth ions," *Applied Physics B*, vol. 93, pp. 269–316, Nov. 2008.

[2] F. G. Gebhardt, "High power laser propagation," *Appl. Opt.*, vol. 15, pp. 1479–1493, Jun 1976.

[3] R. Cook, M. Kochis, I. Reimanis, and H.-J. Kleebe, "A new powder production route for transparent spinel windows: powder synthesis and window properties," in *Window and dome technologies and materials IX*, vol. 5786, pp. 41–48, International Society for Optics and Photonics, 2005.

[4] J. A. Wagner, U. Paasch, M. O. Bodendorf, J. C. Simon, and S. Grunewald, "Treatment of keloids and hypertrophic scars with the triple-mode Er:YAG laser: A pilot study," *Medical Laser Application*, vol. 26, pp. 10–15, 2011.

[5] E. Bornstein, "Proper use of Er:YAG lasers and contact sapphire tips when cutting teeth and bone: scientific principles and clinical application," *Dent Today.*, vol. 23, no. 8, pp. 86–89, 2004.

[6] R. Paschotta *et al.*, *Encyclopedia of laser physics and technology*, vol. 1. Wiley-vch Berlin, 2008.

[7] "Electronics and electrical engineering rankine building, university of glasgow." `http://userweb.eng.gla.ac.uk/douglas.paul/QCL/stimulated.html`. Accessed: 2019-02-26.

[8] P. Aubry, *Elaboration de céramiques transparentes fluorées activées à l'ytterbium pour application laser*. PhD thesis, Université Pierre et Marie Curie (Paris VI), 2009.

[9] C. Marlot, *Elaboration de ceramiques transparentes Er:YAG : Synthèse de poudre par co-precipitation et frittage SPS*. PhD thesis, Université de Bourgogne, 2013.

[10] "RP-photonics,www.rp-photonics.com." Accessed: 2018-04-21.

[11] N. Manuilov and P. Peshev, "Bridgman-Stockbarger growth and spectral characteristics of vanadium-doped yttrium-aluminium garnet (YAG) single crystals," *Materials Research Bulletin*, vol. 24, pp. 1549–1555, Dec. 1989.

[12] M. Yoshimura, S.-i. Sakata, H. Iba, T. Kawano, and K. Hoshikawa, "Vertical Bridgman growth of Al2o3/YAG:Ce melt growth composite," *Journal of Crystal Growth*, vol. 416, pp. 100–105, 2015.

[13] S. Kostić, Z. Ž. Lazarević, V. Radojević, A. Milutinović, M. Romčević, N. Ž. Romčević, and A. Valčić, "Study of structural and optical properties of YAG and Nd:YAG single crystals," *Materials Research Bulletin*, vol. 63, pp. 80–87, 2015.

[14] D. E. Eakins, M. Held, M. G. Norton, and D. F. Bahr, "A study of fracture and defects in single crystal YAG," *Journal of Crystal Growth*, vol. 267, no. 3–4, pp. 502–509, 2004.

[15] J. Banerjee and K. Muralidhar, "Role of internal radiation during Czochralski growth of YAG and Nd:YAG crystals," *International Journal of Thermal Sciences*, vol. 45, no. 2, pp. 151–167, 2006.

[16] Cepheiden, "Bridgman-Stockgarer image,"

[17] "Czochralski crystal growth." `http://www.scientificmaterials.com/capabilities/czochralski-crystal-growth.php`. Accessed: 2019-02-26.

[18] T. Taira, "Ceramic YAG lasers," *Comptes Rendus Physique*, vol. 8, pp. 138–152, 2007.

[19] M. Richardson, "The future of solid state lasers - Photonics.com," Oct. 2018.

[20] A. Katz, *Elaboration de céramiques polycristallines Er^{3+}:YAG transparentes par Spark Plasma Sintering pour applications laser de puissance*. PhD thesis, Université de Valenciennes, 2016.

[21] I. Kamińska, K. Fronc, B. Sikora, M. Mouawad, A. Siemiarczuk, M. Szewczyk, K. Sobczak, T. Wojciechowski, W. Zaleszczyk, R. Minikayev, W. Paszkowicz, P. Stępień, P. Dziawa, K. Ciszak, D. Piątkowski, S. Maćkowski, M. Kaliszewski, M. Włodarski, J. Młyńczak, K. Kopczyński, M. Łapiński, and D. Elbaum, "Upconverting/magnetic: Gd_2O_3:(Er^{3+},Yb^{3+},Zn^{2+}) nanoparticles for biological applications: effect of Zn^{2+} doping," *RSC Adv.*, vol. 5, no. 95, pp. 78361–78373, 2015.

[22] http://www.scientificmaterials.com/products/er-yag.php, 2013.

[23] K. Kuhn, *Laser Engineering*. Prentice Hall, 1998.

[24] R. Iffländer, *Solid-State Lasers for Materials Processing*. No. 77 in Springer Series in Optical Sciences, Springer-Verlag Berlin Heidelberg, 2001.

[25] M. Eichhorn, "Thermal lens effects in an Er^{3+}:YAG laser with crystalline fiber geometry," *Applied Physics B*, vol. 94, no. 3, pp. 451–457, 2008.

[26] H. Yagi, K. Takaichi, K. Ueda, Y. Yamakasi, T. Yanagitani, and A. Kaminskii, "The physical properties of composite YAG ceramics," *Laser Physics*, vol. 15, pp. 1338–1344, 2004.

[27] C. Marlot, *Elaboration de céramiques transparentes Er:YAG : Synthèse de poudre par co-précipitation et frittage SPS*. PhD thesis, Université de Bourgogne, 2013.

[28] I. Shoji, S. Kurimura, Y. Sato, T. Taira, A. Ikesue, and K. Yoshida, "Optical properties and laser characteristics of highly Nd $^{3+}$-doped $Y_3Al_5O_{12}$ceramics," *Applied Physics Letters*, vol. 77, no. 7, pp. 939–941, 2000.

[29] T. Taira, A. Ikesue, and K. Yoshida, "Diode-pumped Nd: YAG ceramics lasers," in *Advanced Solid State Lasers*, p. CS4, Optical Society of America, 1998.

[30] W. Koechner, *Solid-state laser engineering*, vol. 1. Springer, 2013.

[31] G. Q. (VLOC), "Spectroscopic and laser evaluation and comparison of rare-earth doped ceramics for directed energy applications," (Paris), 3 rd LCS, 2007.

[32] H. Yagi, T. Yanagitani, T. Numazawa, and K. Ueda, "The physical properties of transparent y3al5o12: Elastic modulus at high temperature and thermal conductivity at low temperature," *Ceramics international*, vol. 33, no. 5, pp. 711–714, 2007.

[33] Y. Kalisky, *The physics and engineering of solid state lasers*, vol. TT71 of *The International Society for Optical Engineering*. SPIE, 2006.

[34] P. Aubry, *Elaboration de céramiques transparentes fluorées activées à l'yterbium pour application laser*. PhD thesis, Université Paris VI, 2009.

[35] S. Hatch, W. Parsons, and R. Weagley, "Hot-Pressed Polycrystalline CaF_2:Dy^{2+} Laser," *Applied Physics Letters*, vol. 5, no. 8, pp. 153–154, 1964.

[36] J. C. C. Greskovich, "Improved polycrystalline ceramic laser," *Journal of Applied Physics*, vol. 44, p. 4599, 1973.

[37] G. Toda, I. Matsuyama, and Y. Tsukuda, "Method for producing highly pure sintered polycrystalline yttrium oxide body having high transparency," 1975.

[38] C. Greskovich and C. O'Clair, "Yttrium oxide ceramic body," 1988.

[39] S. Dutta and G. Gazza, "Method for production of transparent yttrium oxide," 1975.

[40] A. Ikesue, T. Kinoshita, K. Kamata, and K. Yoshida, "Fabrication and Optical Properties of High-Performance Polycrystalline Nd:YAG Ceramics for Solid-State Lasers," *Journal of the American Ceramic Society*, vol. 78, no. 4, pp. 1033–1040, 1995.

[41] J. Lu, H. Yagi, K. Takaichi, T. Uematsu, J. F. Bisson, Y. Feng, A. Shirakawa, K. I. Ueda, T. Yanagitani, and A. A. Kaminskii, "110 W ceramic Nd^{3+}: $Y_3Al_5O_{12}$ laser," *Applied Physics B*, vol. 79, pp. 25–28, July 2004.

[42] J. Lu, K.-i. Ueda, H. Yagi, T. Yanagitani, Y. Akiyama, and A. A. Kaminskii, "Neodymium doped yttrium aluminum garnet $Y_3Al_5O_{12}$ nanocrystalline ceramics—a new generation of solid state laser and optical materials," *Journal of Alloys and Compounds*, vol. 341, no. 1–2, pp. 220–225, 2002.

[43] B. Le Garrec, "Challenges of high power diode-pumped lasers for fusion energy," *High Power Laser Science and Engineering*, vol. 2, 2014.

[44] A. Ikesue, Y. L. Aung, T. Taira, T. Kamimura, K. Yoshida, and G. L. Messing, "Progress in Ceramic Lasers," *Annu. Rev. Mater. Res.*, vol. 36, pp. 397–429, 2006.

[45] A. Ikesue and Y. L. Aung, "Ceramic laser materials," *Nature Photonics*, vol. 2, no. 12, pp. 721–727, 2008.

[46] A. Ikesue and Y. L. Aung, "Synthesis and Performance of Advanced Ceramic Lasers," *Journal of the American Ceramic Society*, vol. 89, pp. 1936–1944, 2006.

[47] J. Sanghera, W. Kim, G. Villalobos, B. Shaw, C. Baker, J. Frantz, B. Sadowski, and I. Aggarwal, "Ceramic Laser Materials," *Materials*, vol. 5, pp. 258–277, 2012.

[48] L. Laversenne, *Nouvelle méthode de chimie combinatoire pour l'optimisation des propriétés spectroscopiques des ions terres rares laser Yb^{3+}, Er^{3+} et Ho^{3+} dans des fibres monocristallines de sesquioxydes réfractaires M_2O_3 (M=Y, Sc, Lu, Gd).* PhD thesis, Université Claude Bernard-Lyon 1, 2002.

[49] L. B. Kong, Y. Huang, W. Que, T. Zhang, S. Li, J. Zhang, Z. Dong, and D. Tang, "Transparent Ceramic Materials," pp. 29–91, 2015.

[50] A.-C. Bravo, *Elaboration de céramiques transparentes de Yb:Sc_2O_3 pour applications laser.* PhD thesis, Université de Limoges, 2008.

[51] G. Boulon, "Sources lasers à l'état solide. Fondements," *Techniques de l'ingénieur : Optique physique*, 2006.

[52] M. Eichhorn, "First investigations on an Er^{3+}:YAG SSHCL," *Applied Physics B*, vol. 93, no. 4, pp. 817–822, 2008.

[53] M. Eichhorn, S. Fredrich-Thornton, E. Heumann, and G. Huber, "Spectroscopic Properties of Er3+:YAG at 300-550 K and their Effects on the 1.6 μm Laser Transitions," *Applied Physics B*, vol. 91, no. 2, pp. 249–256, 2008.

[54] M. Eichhorn, "Numerical Modeling of Diode-End-Pumped High-Power Er^{3+}: YAG Lasers," *IEEE Journal of Quantum Electronics*, vol. 44, no. 9, 2008.

[55] K. Li and D. Xue, "Estimation of Electronegativity Values of Elements in Different Valence States," *The Journal of Physical Chemistry A*, vol. 110, no. 39, pp. 11332–11337, 2006.

[56] M. L. Saladino, E. Caponetti, D. C. Martino, S. Enzo, and G. Ibba, "Effect of the dopant selection (Er, Eu, Nd or Ce) and its quantity on the formation of yttrium aluminum garnet nanopowders," *Optical Materials*, vol. 31, no. 2, pp. 261–267, 2008.

[57] "webelements.com."

[58] "periodictable.com," Aug. 2018.

[59] X. Xu, Z. Zhao, P. Song, J. Xu, and P. Deng, "Growth of high-quality single crystal of 50 at.% Yb:YAG and its spectral properties," *Journal of Alloys and Compounds*, vol. 364, no. 1, pp. 311 – 314, 2004.

[60] G. Spina, *Transparent YAG and composite ceramic materials in the system Alumina-YAG-Zirconia*. PhD thesis, Politecnico di Torino, 2012.

[61] M. Bass and O. S. o. America, *Handbook of Optics: Fundamentals, techniques, and design*. No. vol. 1 in Handbook of Optics, McGraw-Hill, 1995.

[62] A. Goldstein, "Correlation between $MgAl_2O_4$-spinel structure, processing factors and functional properties of transparent parts (progress review)," *Journal of the European Ceramic Society*, vol. 32, no. 11, pp. 2869–2886, 2012.

[63] G. Spina, *Transparent YAG and composite ceramic materials in the system Alumina-YAG-Zirconia*. PhD thesis, Université de Lyon, MATEIS UMR CNRS 5510, 2012.

[64] A. Krell, T. Hutzler, and J. Klimke, "Transmission physics and consequences for materials selection, manufacturing, and applications," *Journal of the European Ceramic Society*, vol. 29, pp. 207–221, 2009.

[65] "Mr. wayne's class.com." `www.mrwaynesclass.com`. Accessed: 2019-05-29.

[66] R. Apetz and M. P. B. van Bruggen, "Transparent Alumina: A Light-Scattering Model," *Journal of the American Ceramic Society*, vol. 86, no. 3, pp. 480–486, 2003.

[67] A. Katz, E. Barraud, S. Lemonnier, E. Sorrel, M. Eichhorn, S. d'Astorg, and A. Leriche, "Role of LiF additive on spark plasma sintered transparent YAG ceramics," *Ceramics International*, vol. 43, no. 17, pp. 15626–15634, 2017.

[68] Y. Kodera, C. L. Hardin, and J. E. Garay, "Transmitting, emitting and controlling light: Processing of transparent ceramics using current-activated pressure-assisted densification," *Scripta Materialia*, vol. 69, pp. 149–154, 2013.

[69] W. Pabst, J. Hostaša, and L. Esposito, "Porosity and pore size dependence of the real in-line transmission of YAG and alumina ceramics," *Journal of the European Ceramic Society*, vol. 34, pp. 2745–2756, 2014.

[70] A. Ikesue and K. Yoshida, "Influence of pore volume on laser performance of Nd:YAG ceramics," *Journal of Materials Science*, vol. 34, pp. 1189–1195, Mar. 1999.

[71] R. Boulesteix, A. Maitre, J.-F. Baumard, Y. Rabinovitch, and F. Reynaud, "Light scattering by pores in transparent Nd: YAG ceramics for lasers: correlations between microstructure and optical properties," *Optics express*, vol. 18, no. 14, pp. 14992–15002, 2010.

[72] H. N. Yoshimura and H. Goldenstein, "Light scattering in polycrystalline alumina with bi-dimensionally large surface grains," *Journal of the European Ceramic Society*, vol. 29, no. 2, pp. 293–303, 2009.

[73] M. Suárez, A. Fernández, J. L. Menéndez, M. Nygren, R. Torrecillas, and Z. Zhao, "Effect of freeze-drying treatment on the optical properties of SPS-sintered alumina," *Ceramics International*, vol. 39, pp. 6669–6672, 2013.

[74] M. G. Randall, *Powder metallurgy science*. second edition ed., 1994.

[75] L. B. Kong, Y. Huang, W. Que, T. Zhang, S. Li, J. Zhang, Z. Dong, and D. Tang, *Transparent Ceramic Materials*, pp. 29–91. Cham: Springer International Publishing, 2015.

[76] A. Ikesue, T. Kinoshita, K. Kamata, and K. Yoshida, "Fabrication and Optical Properties of High-Performance Polycrystalline Nd:YAG Ceramics for Solid-State Lasers," *Journal of the American Ceramic Society*, vol. 78, pp. 1033–1040, 1995.

[77] H.-L. Li, X.-J. Liu, and L.-P. Huang, "Fabrication of transparent cerium-doped lutetium aluminum garnet (LuAG: Ce) ceramics by a solid-state reaction method," *Journal of the American Ceramic Society*, vol. 88, no. 11, pp. 3226–3228, 2005.

[78] I. Ganesh, B. Srinivas, R. Johnson, B. P. Saha, and Y. R. Mahajan, "Microwave assisted solid state reaction synthesis of $MgAl_2O_4$ spinel powders," *Journal of the European Ceramic Society*, vol. 24, no. 2, pp. 201–207, 2004.

[79] I. Ganesh, "A review on magnesium aluminate ($MgAl_2O_4$) spinel: synthesis, processing and applications," *International Materials Reviews*, vol. 58, no. 2, pp. 63–112, 2013.

[80] L. B. Kong, T. Zhang, J. Ma, and F. Boey, "Progress in synthesis of ferroelectric ceramic materials via high-energy mechanochemical technique," *Progress in Materials Science*, vol. 53, no. 2, pp. 207–322, 2008.

[81] V. Šepelák, A. Düvel, M. Wilkening, K.-D. Becker, and P. Heitjans, "Mechanochemical reactions and syntheses of oxides," *Chemical Society Reviews*, vol. 42, no. 18, pp. 7507–7520, 2013.

[82] X. Chen, T. Lu, N. Wei, Z. Lu, L. Chen, Q. Zhang, G. Cheng, and J. Qi, "Systematic optimization of ball milling for highly transparent Yb:YAG ceramic using co-precipitated raw powders," *Journal of Alloys and Compounds*, vol. 653, pp. 552–560, 2015.

[83] H. Gong, D. Tang, H. Huang, and J. Ma, "Fabrication of yttrium aluminum garnet transparent ceramics from yttria nanopowders synthesized by carbonate precipitation," *Journal of electroceramics*, vol. 23, no. 1, pp. 89–93, 2009.

[84] M. Serantoni, A. Piancastelli, A. L. Costa, and L. Esposito, "Improvements in the production of Yb: YAG transparent ceramic materials: Spray drying optimisation," *Optical Materials*, vol. 34, no. 6, pp. 995–1001, 2012.

[85] J. Marchal, T. John, R. Baranwal, T. Hinklin, and R. M. Laine, "Yttrium aluminum garnet nanopowders produced by liquid-feed flame spray pyrolysis (lf-fsp) of metalloorganic precursors," *Chemistry of materials*, vol. 16, no. 5, pp. 822–831, 2004.

[86] R. Geidobler and G. Winter, "Controlled ice nucleation in the field of freeze-drying: fundamentals and technology review," *European Journal of Pharmaceutics and Biopharmaceutics*, vol. 85, no. 2, pp. 214–222, 2013.

[87] M. Shojaie-Bahaabad, E. Taheri-Nassaj, and R. Naghizadeh, "An alumina–yag nanostructured fiber prepared from an aqueous sol–gel precursor: preparation, rheological behavior and spinnability," *Ceramics International*, vol. 34, no. 8, pp. 1893–1902, 2008.

[88] K. Zhang, W. Hu, J. Li, Y. Tang, and H. Liu, "Matrix induced synthesis of $Y_3Al_5O_{12}$: Ce phosphor through the pechini method," *International Journal of Materials Research*, vol. 100, no. 2, pp. 238–242, 2009.

[89] J. Li, Y. Pan, F. Qiu, Y. Wu, and J. Guo, "Nanostructured nd: Yag powders via gel combustion: the influence of citrate-to-nitrate ratio," *Ceramics International*, vol. 34, no. 1, pp. 141–149, 2008.

[90] J. Toniolo, M. Lima, A. Takimi, and C. Bergmann, "Synthesis of alumina powders by the glycine–nitrate combustion process," *Materials research bulletin*, vol. 40, no. 3, pp. 561–571, 2005.

[91] C. Baker, W. Kim, J. Sanghera, R. Goswami, G. Villalobos, B. Sadowski, and I. Aggarwal, "Flame spray synthesis of Lu_2O_3 nanoparticles," *Materials Letters*, vol. 66, no. 1, pp. 132–134, 2012.

[92] J. G. Li and X. Sun, "Synthesis and sintering behavior of a nanocrystalline α-alumina powder," *Acta Materialia*, vol. 48, no. 12, pp. 3103–3112, 2000.

[93] W. L. Suchanek, "Hydrothermal synthesis of alpha alumina (α-Al_2O_3) powders: study of the processing variables and growth mechanisms," *Journal of the American Ceramic Society*, vol. 93, no. 2, pp. 399–412, 2010.

[94] M. Nyman, J. Caruso, M. J. Hampden-Smith, and T. T. Kodas, "Comparison of solid-state and spray-pyrolysis synthesis of yttrium aluminate powders," *Journal of the American Ceramic Society*, vol. 80, no. 5, pp. 1231–1238, 1997.

[95] I. Claussen, T. Ustad, I. Strommen, and P. Walde, "Atmospheric freeze drying—a review," *Drying Technology*, vol. 25, no. 6, pp. 947–957, 2007.

[96] L. Qian and H. Zhang, "Controlled freezing and freeze drying: a versatile route for porous and micro-/nano-structured materials," *Journal of Chemical Technology & Biotechnology*, vol. 86, no. 2, pp. 172–184, 2011.

[97] K. Guo, H.-H. Chen, X. Guo, X.-X. Yang, F.-F. Xu, and J.-T. Zhao, "Morphology investigation of yttrium aluminum garnet nano-powders prepared by a sol–gel combustion method," *Journal of Alloys and Compounds*, vol. 500, no. 1, pp. 34–38, 2010.

[98] M. Galceran, M. Pujol, M. Aguiló, and F. Díaz, "Synthesis and characterization of nanocrystalline Yb: Lu_2O_3 by modified pechini method," *Materials Science and Engineering: B*, vol. 146, no. 1-3, pp. 7–15, 2008.

[99] R. Marin, G. Sponchia, P. Riello, R. Sulcis, and F. Enrichi, "Photoluminescence properties of yag: Ce $^{3+}$, pr $^{3+}$ phosphors synthesized via the pechini method for white leds," *Journal of Nanoparticle Research*, vol. 14, no. 6, p. 886, 2012.

[100] R. Wiglusz, T. Grzyb, S. Lis, and W. Strek, "Preparation and spectroscopy characterization of Eu: $MgAl_2O_4$ nanopowder prepared by modified pechini method," *Journal of nanoscience and nanotechnology*, vol. 9, no. 10, pp. 5803–5810, 2009.

[101] N. Wang, X. Zhang, Z. Bai, H. Sun, Q. Liu, L. Lu, X. Mi, and X. Wang, "Synthesis of nanocrystalline ytterbium-doped yttria by citrate-gel combustion method and fabrication of ceramic materials," *Ceramics International*, vol. 37, no. 8, pp. 3133–3138, 2011.

[102] Nanocerox, "Flame Spray Pyrolysis-Nanocerox," 2011.

[103] T. Rudin, K. Wegner, and S. E. Pratsinis, "Uniform nanoparticles by flame-assisted spray pyrolysis (fasp) of low cost precursors," *Journal of Nanoparticle Research*, vol. 13, no. 7, pp. 2715–2725, 2011.

[104] A. Krell, T. Hutzler, J. Klimke, and A. Potthoff, "Fine-Grained Transparent Spinel Windows by the Processing of Different Nanopowders," *Journal of the American Ceramic Society*, vol. 93, pp. 2656–2666, 2010.

[105] H. Abdizadeh, *Elaboration et caractérisation de composites duplex "Composites laminaires tri-couches à base d'alumine"*. PhD thesis, Université de Lyon, 1997.

[106] B. P. Saha, V. Kumar, S. Joshi, A. Balakrishnan, and C. L. Martin, "Investigation of compaction behavior of alumina nano powder," *Powder technology*, vol. 224, pp. 90–95, 2012.

[107] D. Bouvard, *Métallurgie des poudres*. Lavoisier, 2002.

[108] T. J. Mroz, T. M. Hartnett, J. M. Wahl, L. M. Goldman, J. Kirsch, and W. R. Lindberg, "Recent Advances in Spinel Optical Ceramic," vol. 5786, 2005.

[109] M. G. Randall, *Sintering: Theory and Practice*. Wiley, 1996.

[110] J. Liu, L. Lin, J. Li, J. Liu, Y. Yuan, M. Ivanov, M. Chen, B. Liu, L. Ge, T. Xie, H. Kou, Y. Shi, Y. Pan, and J. Guo, "Effects of ball milling time on microstructure evolution and optical transparency of Nd:YAG ceramics," *Ceramics International*, vol. 40, no. 7, Part A, pp. 9841–9851, 2014.

[111] P. Boch, *Matériaux et processus céramiques*. Hermès Science, 2001.

[112] E. R. Kupp, G. L. Messing, J. M. Anderson, V. Gopalan, J. Q. Dumm, C. Kraisinger, N. Ter-Gabrielyan, L. D. Merkle, M. Dubinskii, V. K. Simonaitis-Castillo, and G. J. Quarles, "Co-casting and optical characteristics of transparent segmented composite Er:YAG laser ceramics," *Journal of Materials Research*, vol. 25, pp. 476–483, 2011.

[113] A. Goldstein, "Transparent ceramics at 60: Materials,applications and progress in engieneering," June 2018.

[114] M. Trunec and K. Maca, "Advanced Ceramic Processes," pp. 123–150, 2014.

[115] W. Liu, W. Zhang, J. Li, H. Kou, Y. Shen, L. Wang, Y. Shi, D. Zhang, and Y. Pan, "Influence of pH values on (Nd + Y):Al molar ratio of Nd:YAG nanopowders and preparation of transparent ceramics," *Journal of Alloys and Compounds*, vol. 503, pp. 525–528, 2010.

[116] M. Rubat du Merac, I. E. Reimanis, C. Smith, H.-J. Kleebe, and M. M. Müller, "Effect of Impurities and LiF Additive in Hot-Pressed Transparent Magnesium Aluminate Spinel," *International Journal of Applied Ceramic Technology*, vol. 10, pp. E33–E48, 2013.

[117] A. Kundu and M. Harmer, "Methods for decontamination of powders," 2013.

[118] G. Villalobos, S. Bayya, W. Kim, C. Baker, J. Sanghera, M. Hunt, B. Sadowski, F. Miklos, and I. Aggarwal, "Low absorption magnesium aluminate spinel windows for high energy laser applications," *Journal of Materials Research*, vol. 29, no. 19, pp. 2266–2271, 2014.

[119] M. Zarzecka-Napierała, M. M. Bućko, and K. Haberko, "The effect of non-stoichiometry on microstructure and selected properties of YAG polycrystals," *Ceramics International*, vol. 38, pp. 2589–2592, 2012.

[120] J. Liu, X. Cheng, J. Li, T. Xie, M. Ivanov, X. Ba, H. Chen, Q. Liu, Y. Pan, and J. Guo, "Influence of non-stoichiometry on solid-state reactive sintering of YAG transparent ceramics," *Journal of the European Ceramic Society*, vol. 35, pp. 3127–3136, 2015.

[121] A. Katz, E. Barraud, S. Lemonnier, E. Sorrel, J. Boehmler, A. Blanc, M. Eichhorn, S. d'Astorg, and A. Leriche, "Influence of powder physicochemical characteristics on microstructural and optical aspects of YAG and Er: YAG ceramics obtained by SPS," *Ceramics International*, vol. 43, no. 14, pp. 10673–10682, 2017.

[122] A. Vivet, F. Paday, and L. Bonneau, "Design des matières premières poudres au regard des propriétés recherchées pour la transparence," 2015.

[123] M. R. du Merac, *The role of impurities, LiF, and processing on the sintering, microstructure and optical properties of transparent polycrystalline magnesium alluminate $MgAl_2O_4$ spinel*. PhD thesis, 2014.

[124] K. Morita, B.-N. Kim, H. Yoshida, H. Zhang, K. Hiraga, and Y. Sakka, "Effect of loading schedule on densification of $MgAl_2O_4$ spinel during spark plasma sintering (SPS) processing," *Journal of the European Ceramic Society*, vol. 32, no. 10, pp. 2303–2309, 2012.

[125] P. Palmero, B. Bonelli, G. Fantozzi, G. Spina, G. Bonnefont, L. Montanaro, and J. Chevalier, "Surface and mechanical properties of transparent polycrystalline YAG fabricated by SPS," *Materials Research Bulletin*, vol. 48, pp. 2589–2597, 2013.

[126] M. Sokol, S. Kalabukhov, M. P. Dariel, and N. Frage, "High-pressure spark plasma sintering (SPS) of transparent polycrystalline magnesium aluminate spinel (PMAS)," *Journal of the European Ceramic Society*, vol. 34, pp. 4305–4310, 2014.

[127] A. Goldstein, J. Raethel, M. Katz, M. Berlin, and E. Galun, "Transparent MgAl 2 O 4 /LiF ceramics by hot-pressing: Host–additive interaction mechanisms issue revisited," *Journal of the European Ceramic Society*, vol. 36, no. 7, pp. 1731–1742, 2016.

[128] J. Sanghera, G. Villalobos, W. Kim, S. Bayya, B. Sadowski, and I. Aggarwal, "Hot-pressed transparent ceramics and ceramic lasers," 2012.

[129] M. Rubat du Merac, I. E. Reimanis, and H.-J. Kleebe, "Electrochemical Impedance Spectroscopy of Transparent Polycrystalline Magnesium Aluminate (MgAl2o4) Spinel," *Journal of the American Ceramic Society*, vol. 98, pp. 2130–2138, 2015.

[130] C. Gajdowski, J. Böhmler, Y. Lorgouilloux, S. Lemonnier, S. d'Astorg, E. Barraud, and A. Leriche, "Influence of post-HIP temperature on microstructural and optical properties of pure $MgAl_2O_4$ spinel: From opaque to transparent ceramics," *Journal of the European Ceramic Society*, vol. 37, no. 16, pp. 5347–5351, 2017.

[131] S.-H. Lee, E. R. Kupp, A. J. Stevenson, J. M. Anderson, G. L. Messing, X. Li, E. C. Dickey, J. Q. Dumm, V. K. Simonaitis-Castillo, and G. J. Quarles, "Hot Isostatic Pressing of Transparent Nd:YAG Ceramics," *Journal of the American Ceramic Society*, vol. 92, pp. 1456–1463, 2009.

[132] Y. Zhang, M. Cai, B. Jiang, J. Fan, C. Zhou, X. Mao, and L. Zhang, "Micro-structure of grain boundary in post-annealed Sinter plus HIPed Nd:$Lu_3Al_5O_{12}$ ceramics," *Optical Materials Express*, vol. 4, p. 2182, Oct. 2014.

[133] F. Kaiser, P. Simon, U. Burkhardt, B. Kieback, Y. Grin, and I. Veremchuk, "Spark plasma sintering of tungsten oxides wox: Phase analysis and thermoelectric properties," *Crystals*, vol. 7, no. 9, 2017.

[134] R. Orrù, R. Licheri, A. M. Locci, A. Cincotti, and G. Cao, "Consolidation/synthesis of materials by electric current activated/assisted sintering," *Mater. Sci. Eng., R*, vol. 63, no. 4–6, pp. 127–287, 2009.

[135] M. Suárez, A. Fernández, J. L. Menéndez, M. Nygren, R. Torrecillas, and Z. Zhao, "Hot isostatic pressing of optically active Nd:YAG powders doped by a colloidal processing route," *Journal of the European Ceramic Society*, vol. 30, no. 6, pp. 1489–1494, 2010.

[136] G. Mata-Osoro, J. S. Moya, and C. Pecharroman, "Transparent alumina by vacuum sintering," *Journal of the European Ceramic Society*, vol. 32, pp. 2925–2933, 2012.

[137] L. Esposito and A. Piancastelli, "Role of powder properties and shaping techniques on the formation of pore-free YAG materials," *Journal of the European Ceramic Society*, vol. 29, no. 2, pp. 317–322, 2009.

[138] M. Shimada, T. Endo, T. Saito, and T. Sato, "Fabrication of transparent spinel polycrystalline materials," *Materials Letters*, vol. 28, no. 4-6, pp. 413–415, 1996.

[139] N. Benameur, *Elaboration et caractérisations d'un spinelle polycristallin à grains fins transparent dans le visible et l'infrarouge*. PhD thesis, Lille, Université de Lille, 2009.

[140] G. de and H. J. A. v. Dijk, "Translucent Y3al5o12 ceramics," *Materials Research Bulletin*, vol. 19, no. 12, pp. 1669 – 1674, 1984.

[141] J. W. G. A. Vrolijk, S. Cruysem, van den, and R. Metselaar, "The influence of MgO and SiO_2 dopants on the sintering behaviour of yttrium aluminium garnet ceramics," in *Ceramic processing science and technology : [proceedings of the Fifth International Conference on Ceramic Processing Science and Technology, Friedrichshafen, Germany]* (H. Hausner, G. L. Messing, and S.-I. Hiarno, eds.), Ceramic Transactions, (United States), pp. 573–577, American Ceramic Society, 1995.

[142] T. Frueh, E. R. Kupp, C. Compson, J. Atria, and G. L. Messing, "The Effects of Na_2o and SiO_2 on Liquid Phase Sintering of Bayer Al_2O_3," *Journal of the American Ceramic Society*, vol. 99, no. 7, pp. 2267–2272, 2016.

[143] J. P. Hollingsworth, J. D. Kuntz, F. J. Ryerson, and T. F. Soules, "Nd diffusion in YAG ceramics," *Optical Materials*, vol. 33, pp. 592–595, 2011.

[144] N. Ter-Gabrielyan, L. D. Merkle, M. Dubinskii, E. Kupp, and G. L. Messing, "Efficient Resonantly-Pumped Eye-Safe Composite Ceramic Er: YAG Laser," in *Advanced Solid-State Photonics*, p. AWB1, Optical Society of America, 2010.

[145] M. Sokol, S. Kalabukhov, V. Kasiyan, A. Rothman, M. P. Dariel, and N. Frage, "Mechanical, thermal and optical properties of the SPS-processed polycrystalline Nd:YAG," *Optical Materials*, vol. 38, pp. 204–210, 2014.

[146] I. E. Reimanis and H.-J. Kleebe, "Reactions in the sintering of $MgAl_2O_4$ spinel doped with LiF," *International Journal of Materials Research*, vol. 98, pp. 1273–1278, Dec. 2007.

[147] J.-L. Huang, S.-Y. Sun, and Y.-C. Ko, "Investigation of High-Alumina Spinel: Effect of LiF and CaCO3 Addition," *Journal of the American Ceramic Society*, vol. 80, no. 12, pp. 3237–3241, 1997.

[148] A. Krell, K. Waetzig, and J. Klimke, "Influence of the structure of $MgO \cdot nAl_2O_3$ spinel lattices on transparent ceramics processing and properties," *Journal of the European Ceramic Society*, vol. 32, no. 11, pp. 2887–2898, 2012.

[149] A. Ikesue, K. Yoshida, T. Yamamoto, and I. Yamaga, "Optical scattering centers in polycrystalline Nd: YAG laser," *Journal of the American Ceramic Society*, vol. 80, no. 6, pp. 1517–1522, 1997.

[150] S. Meir, S. Kalabukhov, N. Froumin, M. P. Dariel, and N. Frage, "Synthesis and Densification of Transparent Magnesium Aluminate Spinel by SPS Processing," *Journal of the American Ceramic Society*, vol. 92, pp. 358–364, 2009.

[151] N. Frage, S. Kalabukhov, N. Sverdlov, V. Ezersky, and M. P. Dariel, "Densification of transparent yttrium aluminum garnet (YAG) by SPS processing," *Journal of the European Ceramic Society*, vol. 30, no. 16, pp. 3331–3337, 2010.

[152] L. Esposito, A. Piancastelli, P. Miceli, and S. Martelli, "A thermodynamic approach to obtaining transparent spinel $MgAl_2O_4$ by hot pressing," *Journal of the European Ceramic Society*, vol. 35, no. 2, pp. 651–661, 2015.

[153] K. G. Rozenburg, *An investigation on the role of lithium fluoride in the sintering of magnesium aluminate spinel*. PhD thesis, Colorado school of Mines, 2009.

[154] K. Rozenburg, I. E. Reimanis, H. J. Kleebe, and R. L. Cook, "Chemical Interaction Between LiF and $MgAl_2O_4$ spinel During Sintering," *Journal of the American Ceramic Society*, vol. 90, no. 7, pp. 2038–2042, 2007.

[155] I. E. Reimanis and H.-J. Kleebe, "Reactions in the sintering of $MgAl_2O_4$ spinel doped with LiF," *International Journal of Materials Research*, vol. 98, pp. 1273–1278, Dec. 2007.

[156] M. M. Müller, H.-J. Kleebe, and H. Chan, "Sintering Mechanisms of LiF-Doped Mg-Al-Spinel," *Journal of the American Ceramic Society*, vol. 95, pp. 3022–3024, 2012.

[157] G. R. Villalobos, J. S. Sanghera, and I. D. Aggarwal, "Degradation of Magnesium Aluminum Spinel by Lithium Fluoride Sintering Aid," *Journal of the American Ceramic Society*, vol. 88, pp. 1321–1322, 2005.

[158] M. Suárez, A. Fernández, J. L. Menéndez, M. Nygren, R. Torrecillas, and Z. Zhao, "Hot isostatic pressing of optically active Nd:YAG powders doped by a colloidal processing route," *Journal of the European Ceramic Society*, vol. 30, pp. 1489–1494, 2010.

[159] S.-H. Lee, S. Kochawattana, G. L. Messing, J. Q. Dumm, G. Quarles, and V. Castillo, "Solid-State Reactive Sintering of Transparent Polycrystalline Nd:YAG Ceramics," *Journal of the American Ceramic Society*, vol. 89, pp. 1945–1950, 2006.

[160] W. Liu, Y. Zeng, J. Li, Y. Shen, Y. Bo, N. Zong, P. Wang, Y. Xu, J. Xu, D. Cui, Q. Peng, Z. Xu, D. Zhang, and Y. Pan, "Sintering and laser behavior of composite YAG/Nd:YAG/YAG transparent ceramics," *Journal of Alloys and Compounds*, vol. 527, pp. 66–70, 2012.

[161] W. Liu, J. Li, B. Jiang, D. Zhang, and Y. Pan, "2.44kw laser output of Nd:YAG ceramic slab fabricated by a solid-state reactive sintering," *Journal of Alloys and Compounds*, vol. 538, pp. 258–261, 2012.

[162] J. Li, Y. Wu, Y. Pan, W. Liu, L. Huang, and J. Guo, "Laminar-structured yag/nd:yag/yag transparent ceramics for solid-state lasers," *International Journal of Applied Ceramic Technology*, vol. 5, no. 4, pp. 360–364, 2008.

[163] K. Yoshida, A. Ikesue, and Y. Okamoto, "All ceramic composite with layer by layer and clad-core structure by advanced ceramic technology," in *Conference on Lasers and Electro-Optics*, p. CTuT3, Optical Society of America, 2004.

[164] J. P. Hollingsworth, J. D. Kuntz, and T. F. Soules, "Neodymium ion diffusion during sintering of Nd : YAG transparent ceramics," *Journal of Physics D: Applied Physics*, vol. 42, no. 5, p. 052001, 2009.

[165] F. Sommer, F. Kern, H. F. El-Maghraby, M. A. El-Ezz, M. Awaad, R. Gadow, and S. M. Naga, "Effect of preparation route on the properties of slip-casted Al_2O_3/YAG composites," *Ceramics International*, vol. 38, pp. 4819–4826, 2012.

[166] J. Lu, T. Murai, K. Takaichi, T. Uematsu, K.-i. Ueda, Y. Akiyama, H. Yagi, and T. Yanagi, "Development of nd: Yag ceramic lasers," in *Advanced Solid State Lasers*, p. WE1, Optical Society of America, 2002.

[167] H. Yagi, K. Takaichi, K. Ueda, Y. Yamasaki, T. Yanagitani, and A. A. Kaminskii, "The Physical Properties of Composite YAG Ceramics," *Laser Physics*, vol. 15, no. 9, pp. 1338–1344, 2005.

[168] H. Yagi, T. Yanagitani, T. Numazawa, and K. Ueda, "The physical properties of transparent $Y_3Al_5O_{12}$," *Ceramics International*, vol. 33, no. 5, pp. 711–714, 2007.

[169] J. Hostaša, "Transparent layered YAG ceramics with structured Yb doping produced via tape casting," 2017.

[170] E. R. Kupp, G. L. Messing, J. M. Anderson, V. Gopalan, J. Q. Dumm, C. Kraisinger, N. Ter-Gabrielyan, L. D. Merkle, M. Dubinskii, V. K. Simonaitis-Castillo, and others, "Co-casting and optical characteristics of transparent segmented composite Er: YAG laser ceramics," *Journal of Materials Research*, vol. 25, no. 3, pp. 476–483, 2010.

[171] C. Ma, F. Tang, H. Lin, W. Chen, G. Zhang, Y. Cao, W. Wang, X. Yuan, and Z. Dai, "Fabrication and planar waveguide laser behavior of YAG/Nd:YAG/YAG composite ceramics by tape casting," *Journal of Alloys and Compounds*, vol. 640, no. 0, pp. 317–320, 2015.

[172] F. Tang, Y. Lin, W. Wang, X. Yuan, J. Chen, J. Huang, C. Ma, Z. Dai, W. Guo, and Y. Cao, "High efficient Nd:YAG laser ceramics fabricated by dry pressing and tape casting," *Journal of Alloys and Compounds*, vol. 617, pp. 845–849, 2014.

[173] V. V. Osipov, V. A. Shitov, V. I. Solomonov, K. E. Lukyashin, A. V. Spirina, and R. N. Maksimov, "Composite Nd:YAG/Cr4+:YAG transparent ceramics for thin disk lasers," *Ceramics International*, vol. 41, pp. 13277–13280, 2015.

[174] V. V. Osipov, K. E. Lukyashin, V. A. Shitov, and R. N. Maksimov, "Two-step thermal diffusional bonding of transparent Nd:YAG ceramics," *Materials Letters*, vol. 167, pp. 81–84, 2016.

[175] K. Fujioka, A. Sugiyama, Y. Fujimoto, J. Kawanaka, and N. Miyanaga, "Ion diffusion at the bonding interface of undoped YAG/Yb:YAG composite ceramics," *Optical Materials*, vol. 46, pp. 542–547, 2015.

[176] S. Bigotta, L. Galecki, A. Katz, J. Böhmler, S. Lemonnier, E. Barraud, A. Leriche, and M. Eichhorn, "Resonantly pumped eye-safe Er $^{3+}$: YAG SPS-HIP ceramic laser," *Optics express*, vol. 26, no. 3, pp. 3435–3442, 2018.

[177] K. N. LaFortune, R. L. Hurd, S. N. Fochs, M. D. Rotter, P. H. Pax, R. L. Combs, S. S. Olivier, J. M. Brase, and R. M. Yamamoto, "Technical challenges for the future of high energy lasers," vol. 6454, pp. 64540O–64540O–11, 2007.

[178] H. Yagi, K. Takaichi, K. Ueda, Y. Yamakasi, T. Yanagitani, and A. A. Kaminskii, "The physical properties of composite YAG ceramics," *Laser Physics*, vol. 15, pp. 1338–1344, 2004.

[179] A. Goldstein and A. Krell, "Transparent ceramics at 50: progress made and further prospects," *Journal of the American Ceramic Society*, vol. 99, no. 10, pp. 3173–3197, 2016.

[180] V. Gritsyna, Y. Kazarinov, A. Moskvitin, and I. Reimanis, "Point Defects in Magnesium Aluminates Spinel Ceramics Doped with Lithium Fluoride," *ACTA PHYSICA POLONICA A*, vol. 117, pp. 161–165, 2010.

[181] G. P. Summers, G. White, K. Lee, and J. Crawford Jr, "Radiation damage in $MgAl_2O_4$," *Physical Review B*, vol. 21, no. 6, p. 2578, 1980.

[182] G. White, R. Jones, and J. Crawford Jr, "Optical spectra of $MgAl_2O_4$ crystals exposed to ionizing radiation," *Journal of Applied Physics*, vol. 53, no. 1, pp. 265–270, 1982.

[183] G. Bernard-Granger, N. Benameur, C. Guizard, and M. Nygren, "Influence of graphite contamination on the optical properties of transparent spinel obtained by spark plasma sintering," *Scripta Materialia*, vol. 60, no. 3, pp. 164–167, 2009.

[184] *Multi-kW near-diffraction -limited single-frequency Nd:YAG*, (CLEO Europe), 2005.

[185] S. Pandey, *Quantification of Non-stoichiometry andImpurities in Transparent YAG Ceramics by Laser-induced Breakdown Spectroscopy (LIBS)*. Phd thesis, University of Florida, The address of the publisher, 2017.

[186] A. Lapucci, M. Ciofini, L. Esposito, P. Ferrara, L. Gizzi, J. Hostaša, L. Labate, A. Pirri, G. Toci, and M. Vannini, "Characterization of Yb: YAG active slab media based on a layered structure with different doping," vol. 8780, p. 87800J, 2013.

[187] M. I. Mendelson, "Average grain size in polycrystalline ceramics," *Journal of the American Ceramic society*, vol. 52, no. 8, pp. 443–446, 1969.

[188] W. Kim, C. Baker, G. Villalobos, S. Bayya, M. Hunt, B. Sadowski, I. Aggarwal, and J. Sanghera, "Low-loss spinel windows for high-energy lasers," in *Window and Dome Technologies and Materials XIV*, vol. 9453, p. 945303, International Society for Optics and Photonics, 2015.

[189] H. Qin, J. Jiang, H. Jiang, Y. Sang, D. Sun, X. Zhang, J. Wang, and H. Liu, "Effect of composition deviation on the microstructure and luminescence properties of Nd: YAG ceramics," *CrystEngComm*, vol. 16, no. 47, pp. 10856–10862, 2014.

[190] A. Patel, M. Levy, R. Grimes, R. Gaume, R. Feigelson, K. McClellan, and C. Stanek, "Mechanisms of nonstoichiometry in $Y_3Al_5O_{12}$," *Applied Physics Letters*, vol. 93, no. 19, p. 191902, 2008.

[191] M. M. Kuklja, "Defects in yttrium aluminium perovskite and garnet crystals: atomistic study," *Journal of Physics: Condensed Matter*, vol. 12, no. 13, p. 2953, 2000.

[192] G. Boulon, "Fifty years of advances in solid-state laser materials," *Optical Materials*, vol. 34, no. 3, pp. 499–512, 2012.

[193] J. Lu, M. Prabhu, K. Ueda, H. Yagi, T. Yanagitani, A. Kudryashov, and A. A. Kaminskii, "Potential of Ceramic YAG Lasers," *Laser Physics*, vol. 11, no. 10, pp. 1053–1057, 2001.

[194] B. Liu, J. Li, M. Ivanov, W. Liu, L. Ge, T. Xie, H. Kou, S. Zhuo, Y. Pan, and J. Guo, "Diffusion-controlled solid-state reactive sintering of Nd:YAG transparent ceramics," *Ceramics International*, vol. 41, pp. 11293–11300, 2015.

[195] E. R. Kupp, S. Kochawattana, S.-H. Lee, S. Misture, and G. L. Messing, "Particle size effects on yttrium aluminum garnet (YAG) phase formation by solid-state reaction," *Journal of Materials Research*, vol. 29, no. 19, pp. 2303–2311, 2014.

[196] Y. Wu, J. Li, F. Qiu, Y. Pan, Q. Liu, and J. Guo, "Fabrication of transparent Yb,Cr:YAG ceramics by a solid-state reaction method," *Ceramics International*, vol. 32, pp. 785–788, 2006.

[197] D. Sordelet, M. Akinc, M. Panchula, Y. Han, and M. Han, "Synthesis of yttrium aluminum garnet precursor powders by homogeneous precipitation," *Journal of the European Ceramic Society*, vol. 14, no. 2, pp. 123 – 130, 1994.

[198] K. Sarath Chandra, M. Monalisa, G. Ulahannan, D. Sarkar, and H. S. Maiti, "Preparation of yag nanopowder by different routes and evaluation of their characteristics including transparency after sintering," *Journal of the Australian Ceramic Society*, vol. 53, pp. 751–760, Oct 2017.

[199] A. Goldstein, A. Shames, A. J. Stevenson, Z. Cohen, and M. Vulfson, "Parasitic light absorption processes in transparent polycrystalline $MgAl_2O_4$ and YAG," *Journal of the American Ceramic Society*, vol. 96, no. 11, pp. 3523–3529, 2013.

[200] L. Chrétien, R. Boulesteix, A. Maître, C. Sallé, and Y. Reignoux, "Post-sintering treatment of neodymium-doped yttrium aluminum garnet (Nd:YAG) transparent ceramics," *Optical Materials Express*, vol. 4, pp. 2166–2173, Oct. 2014.

[201] J. Li, J. Zhou, Y. Pan, W. Liu, W. Zhang, J. Guo, H. Chen, D. Shen, X. Yang, and T. Zhao, "Solid-State Reactive Sintering and Optical Characteristics of Transparent Er:YAG Laser Ceramics," *Journal of the American Ceramic Society*, vol. 95, pp. 1029–1032, 2012.

[202] W. Liu, B. Liu, J. Li, J. Liu, Y. Pan, and J. Guo, "Effects of characteristics of Y_2O_3 commercial powders on structural and optical properties of Nd:YAG ceramics," *Ceramics International*, vol. 40, no. 7, Part B, pp. 11399–11404, 2014.

[203] K. M. Kinsman, J. McKittrick, E. Sluzky, and K. Hesse, "Phase Development and Luminescence in Chromium-Doped Yttrium Aluminum Garnet (YAG:Cr) Phosphors," *Journal of the American Ceramic Society*, vol. 77, no. 11, pp. 2866–2872, 1994.

[204] L. Ge, J. Li, Z. Zhou, B. Liu, T. Xie, J. Liu, H. Kou, Y. Shi, Y. Pan, and J. Guo, "Nd:YAG transparent ceramics fabricated by direct cold isostatic pressing and vacuum sintering," *Optical Materials*, vol. 50, Part A, pp. 25–31, 2015.

[205] M. Liu, S. W. Wang, D. Y. Tang, L. D. Chen, and J. Ma, "Fabrication and microstructures of YAG transparent ceramics," *Science of Sintering*, vol. 40, pp. 311–317, 2008.

[206] A. Maître, C. Sallé, R. Boulesteix, J.-F. Baumard, and Y. Rabinovitch, "Effect of silica on the reactive sintering of polycrystalline Nd: YAG ceramics," *Journal of the American Ceramic Society*, vol. 91, no. 2, pp. 406–413, 2008.

[207] R. S. Hay, "Kinetics and deformation during the reaction of yttrium-aluminum perovskite and alumina to yttrium-aluminum garnet," *Journal of the American Ceramic Society*, vol. 77, no. 6, pp. 1473–1485, 1994.

[208] W. Kingery, "The sintering of crystalline oxides, i. interactions between grain boundaries and pores," *Sintering and Related Phenomena*, pp. 471–498, 1967.

[209] R. Boulesteix, A. Maitre, L. Chrétien, Y. Rabinovitch, and C. Sallé, "Microstructural evolution during vacuum sintering of yttrium aluminum garnet transparent ceramics: toward the origin of residual porosity affecting the transparency," *Journal of the American Ceramic Society*, vol. 96, no. 6, pp. 1724–1731, 2013.

[210] R. Stengl, T. Tan, and U. Gösele, "A model for the silicon wafer bonding process," *Japanese Journal of Applied Physics*, vol. 28, pp. 1735–1741, oct 1989.

[211] M. Rubat du Merac, H.-J. Kleebe, M. M. Müller, and I. E. Reimanis, "Fifty Years of Research and Development Coming to Fruition; Unraveling the Complex Interactions during Processing of Transparent Magnesium Aluminate (MgAl2o4) Spinel," *Journal of the American Ceramic Society*, vol. 96, pp. 3341–3365, 2013.

[212] M. Eichhorn, "Multi-kW-class 1.64 μm Er^{3+}:YAG lasers based on heat-capacity operation," 2011.

[213] F. Tang, Y. Cao, J. Huang, W. Guo, H. Liu, Q. Huang, and W. Wang, "Multilayer YAG/Re:YAG/YAG laser ceramic prepared by tape casting and vacuum sintering method," *Journal of the European Ceramic Society*, vol. 32, no. 16, pp. 3995–4002, 2012.

[214] N. Cai, C.-W. Nan, J. Zhai, and Y. Lin, "Large high-frequency magnetoelectric response in laminated composites of piezoelectric ceramics, rare-earth iron alloys and polymer," *Applied Physics Letters*, vol. 84, no. 18, pp. 3516–3518, 2004.

[215] R. A. Islam, Y. Ni, A. G. Khachaturyan, and S. Priya, "Giant magnetoelectric effect in sintered multilayered composite structures," *Journal of Applied Physics*, vol. 104, no. 4, p. 044103, 2008.

[216] Y. T. Pei and J. T. M. De Hosson, "Functionally graded materials produced by laser cladding," *Acta materialia*, vol. 48, no. 10, pp. 2617–2624, 2000.

[217] P. Palmero, A. Simone, C. Esnouf, G. Fantozzi, and L. Montanaro, "Comparison among different sintering routes for preparing alumina-YAG nanocomposites," *Journal of the European Ceramic Society*, vol. 26, pp. 941–947, 2006.

[218] M. Rubat du Merac, I. E. Reimanis, C. Smith, H.-J. Kleebe, and M. M. Müller, "Effect of Impurities and LiF Additive in Hot-Pressed Transparent Magnesium Aluminate Spinel," *International Journal of Applied Ceramic Technology*, vol. 10, pp. E33–E48, 2013.

[219] W. Zhang, T. Lu, B. Ma, N. Wei, Z. Lu, F. Li, Y. Guan, X. Chen, W. Liu, and L. Qi, "Improvement of optical properties of Nd:YAG transparent ceramics by post-annealing and post hot isostatic pressing," *Optical Materials*, vol. 35, no. 12, pp. 2405–2410, 2013.

[220] J. Crank *et al.*, *The mathematics of diffusion*. Oxford university press, 1979.